Technische Universität München
TUM School of Engineering and Design

Modeling and Control of Electric Heat Pump Systems for Power System Frequency Response

Ruihao Song

Complete reprint of the dissertation approved by the TUM School of Engineering and Design of the Technical University of Munich for the award of the

Doktor der Ingenieurwissenschaften (Dr.-Ing.).

Chair: Prof. Dr.-Ing. Dirk Weuster-Botz

Examiners:

1. Prof. Dr. Thomas Hamacher
2. Prof. Dr. Marcelo Lobo Heldwein

The dissertation was submitted to the Technical University of Munich on 23.01.2024 and accepted by the TUM School of Engineering and Design on 17.09.2024.

Abstract

As the global power system transforms, a salient trend towards low-inertia configurations has become evident. This evolution is predominantly driven by integrating renewable energy generations, like wind and solar, which inherently lack the mechanical inertia traditionally provided by synchronous generators in conventional power systems. Consequently, the susceptibility of the system to frequency deviations escalates, elevating the importance of effective frequency response mechanisms. Efficient and rapid frequency control is vital to ensure system stability, reliability, and resilience in this new era of power generation and distribution. Recognizing and addressing this emergent need for enhanced frequency response is essential, as it lays the foundation for a sustainable and reliable power grid that is equipped to handle stochastic energy generation and demands.

Similar to power systems, heating systems are also evolving from the previously centralized combustion-based system into distributed electricity-based systems. This trend enables new opportunities for frequency response services as heating grids have a continuously growing inertia because of the increasing heat storage capacity. This thesis explores the potential of heating systems, specifically heat pumps, in augmenting frequency response services within the power system framework. The main focus of this thesis can be divided into two research threads, which are introduced as follows.

The first research thread offers a deep dive into using heat pumps to enhance frequency stability and reduce frequency nadir/peak in future low-inertia scenarios, typically through fast frequency response services. Emphasis is placed on non-linear dynamic modeling rooted in fundamental physics and robust controller design for resisting uncertain working conditions. The second research thread targets using heat pumps for the frequency recovery stage, typically through primary and secondary frequency response services, where the focus shifts to tracking a dispatched power reference under uncertain working conditions in a practical and versatile way.

In summary, this thesis systematically analyzes how to model and control heat pumps for different levels of frequency response services. The findings of this thesis are potentially valuable for grid operators to establish new business models for frequency response services that involve more heat pumps on the demand side and for manufacturers to upgrade heat pump controllers to participate in frequency response services.

Zusammenfassung

Im Zuge der global voranschreitenden Energiewende ist hinsichtlich des Stromsektors ein signifikanter rückläufiger Trend in Bezug auf die inhärente Trägheit des Netzes zu beobachten. Hauptursache dieser Entwicklung ist die zunehmende Integration erneuerbarer Energieträger wie Wind- und Solarenergie, deren mechanische Trägheit technologiebedingt nicht in der Größenordnung liegt, wie sie traditionell von Synchrongeneratoren in konventionellen Stromsystemen bereitgestellt wird. Infolgedessen steigt die Anfälligkeit des Systems für Frequenzabweichungen, weshalb effektive Mechanismen zur Frequenzstabilisierung zunehmend an Bedeutung gewinnen. Um die Stabilität, Zuverlässigkeit und Widerstandsfähigkeit des Netzes in dieser neuen Ära der Stromerzeugung und -verteilung weiterhin zu gewährleisten, ist eine effiziente und schnelle Frequenzregelung essentiell. Das Erkennen und Bereitstellen dieses aufkommenden Bedarfs an verbesserten Regelungsmechanismen ist von entscheidender Bedeutung, da es den Grundstein für ein nachhaltiges und zuverlässiges Stromnetz legt, das für die zunehmend volatile Energieerzeugung und -nachfrage gerüstet ist.

Analog zum Stromnetz entwickeln sich auch Heizungssysteme von den zuvor zentralisierten, auf fossilen Energieträgern beruhenden Systemen, hin zu verteilten, elektrizitätsbasierten Systemen weiter. Dieser Trend eröffnet neue Möglichkeiten hinsichtlich der Frequenzregelung, da die zunehmende Verbreitung dieser Heizsysteme ein kontinuierlich wachsendes Trägheitsreservoir zur Verfügung stellt. Diese Dissertation bietet eine umfassende Untersuchung des Potenzials von Heizsystemen, insbesondere von Wärmepumpen, zur Steigerung der Stabilität der Netzfrequenz im Stromnetz. Die Kernthematik der Arbeit ist in zwei Forschungsschwerpunkte untergliedert, die im Folgenden vorgestellt werden.

Der erste Forschungsaspekt behandelt eingehend den potenziellen Beitrag von Wärmepumpen zur Unterstützung in der Frequenzerhaltung und zur Reduzierung von Frequenzabweichungen in zukünftigen Netzszenarien mit geringer Momentanreserve, wobei schnelle Frequenzregelungs-dienste eingesetzt werden. Im Mittelpunkt stehen dabei zum einen die nichtlineare, dynamische Modellierung, basierend auf physikalischen Grundlagen, zum anderen die Robustheit des Regelungsentwurfs, um den unbeständigen Betriebsbedingungen standzuhalten. Der zweite Schwerpunkt konzentriert sich auf die Verwendung von Wärmepumpen für die Frequenz-rückgewinnung, wobei diese Anlagen primäre und sekundäre Regelleistung bereitstellen. Das Hauptaugenmerk der Untersuchungen verlagert sich hierbei auf die Einhaltung einer vorgegebenen Leistungsreferenz bei unbeständigen Einsatzbedingungen auf eine praxisorientierte und anpassungsfähige Art und Weise.

Zusammenfassend bietet diese Arbeit eine systematische Analyse, wie Wärmepumpen auf verschiedene Ebenen zum Einsatz in Frequenzreaktionsdiensten modelliert und gesteuert werden können. Die Ergebnisse dieser Arbeit bieten einen Mehrwert sowohl für Netzwerkbetreiber, um neue Geschäftsmodelle zu etablieren und dabei die Heizsysteme in den Regelmarkt einzubeziehen, als auch für Hersteller der Anlagen, um deren Wärmepumpenregler entsprechend für die Teilnahme am Regelleistungsmarkt zu entwerfen.

Acknowledgment

Completing a doctoral thesis is never an easy task, and many attribute it solely to the personal dedication of the candidate. However, I believe no significant achievement is the product of a single individual's efforts. I have journeyed over 8,000 kilometers, now sitting in this very office, writing this thesis, because of the unwavering support from my beloved family. I am merely the one harvesting the fruit of a collective effort.

I want to thank my grandparents, who worked tirelessly to lift our family out of our rural village. Their sacrifices ensured my father could complete his bachelor's degree during those harsh times when even basic needs were considered a luxury. In addition, my deepest gratitude goes to my parents, who created a safe environment that enabled me to advance in my career.

My deepest thanks go to my wife, who has been my constant companion in this academic journey. As two doctoral candidates, we have supported one another through challenging moments of research, looked after each other during all the deadlines, and most importantly, loved each other from the bottom of our hearts. I feel blessed to have you in my life.

I also sincerely appreciate my supervisors, Prof. Hamacher and Dr. Peric. Thank you for taking me in during a difficult period in my life when I was struggling with my career, and thank you for providing all the financial support during this thesis. Special thanks to Dr. Peric, whose consistent guidance has been significant in refining my papers. This thesis would not have been possible without your care and patience.

To all my friends in Germany and back home, our cherished moments together have been a source of joy and motivation. I wish you all a successful career and happy life. May our paths cross again in the future!

Song, Ruihao

12. Oct. 2023

Garching, Germany

致谢

人生如登山，二十又九年，走过的每一步似乎都还在眼前若隐若现。如今我已完成博士论文，足迹遍布全球，也算是小有成就。古人云人生不如意十之八九，我回望来路，荆棘遍地，好在是有惊无险。作为一名工程师，我是不相信运气的人。我这一路，有太多人的人和事需要感谢了，谨以此文略表一二。

家庭一直是我这一路最大的助力。尽管我的祖父母只是穷苦的农民，但他们深谙教育的重要性。他们奋斗一生，培养了四个孩子完成大学学业，完成了在那个缺衣少粮的年代中几乎不可能的任务。我的父母踩在他们的肩膀上，成为了工程师，并乘着祖国高速工业化的东风，将我家带进了相对富足的生活。没有他们的付出与铺垫，我之今日何在？实际上，这篇博士论文是我家三代人艰苦奋斗的成果之一。作为最后摘果子的那个人，我回想往昔，不禁感慨万分。

我要感谢一直和我同甘共苦的妻子。我之所以会深造读博，在很大程度上是受她的影响。相识十余载，我们互相勉励批评，最终相互成就，这实为人生之一大幸事！希望我们能长长久久，相伴一生。

我要感谢指导我研究的教授们。他们在我人生之谷底给了我来读书的机会，并且提供给我经济支持，使我能全身心地投入到研究课题中。没有他们的倾力协助，我不可能完成本篇博士论文。我衷心祝他们身体健康，家庭和睦，并且能在各自领域内更上一层楼。

致我所有的朋友们：人生尚早，我们江湖再见！

宋瑞皓

2023 年 10 月 12 日于慕尼黑

Table of Contents

List of Figures

List of Tables

Chapter 1: Introduction

The global energy landscape has significantly transformed in recent years, with a growing emphasis on reducing global warming. Fossil fuel combustion, a major source of CO2 and other greenhouse gas emissions, has been a prime contributor to global warming [1]. Renewable energy generation (REG), with its negligible carbon footprint, has been seen as a viable solution to counteract the emission challenge. Historically, fossil fuels, such as coal and natural gas, have dominated power generation due to cost competitiveness. However, the falling costs of photovoltaic (PV) and wind turbines have made REG increasingly viable for large-scale applications. A 2020 report from the International Renewable Energy Agency (IRENA) highlighted that over half of the REG capacity added in 2019 achieved lower power costs than the cheapest new coal plants [2]. The reduced costs push the global REG penetration level on a rapidly rising track from 10% in 2010 to nearly 30% in 2023 [3]. This overhaul of the generation side brings a series of transitions to traditional power systems, which covers aspects such as grid dynamic characteristics, ancillary services, and multi-energy integration.

1.1 Frequency Fluctuations Caused by the Falling Grid Inertia

As the penetration of renewables in power grids increases, it challenges the operation and control aspects of power systems. One of the critical challenges is the reduction in power system inertia, which refers to the ability of a system to resist changes in frequency in the context of power systems [4][5][6]. Traditional power systems, dominated by large-scale synchronous generators (SG), inherently possess high levels of inertia through the rotating masses that store kinetic energy. When there is a sudden change in the grid's active power balance, the stored energy helps to resist rapid changes in system frequency, giving operators time to take corrective actions. This feature is characterized by the swing equation, which is shown in:

$$H\frac{df}{dt} = \frac{f_n^2}{2S_n f}(P_m - P_e), \tag{1.1}$$

where H is the inertia constant of the combined turbine-generator system, f is the frequency at the output, f_n is nominal grid frequency, S_n is the rated apparent power of the turbine-generator system, P_m is the turbine's mechanical power, and P_e is the electrical power of the generator. Through (1.1), it is evident that the rate of change of frequency is determined by the active power imbalance and the inertia constant of the turbine-generator system. In reality, the power grid can also contain some frequency-dependent loads. If we

consider these loads, the following transfer function (1.2) between active power imbalance and the resulting frequency disturbance can be obtained:

$$\Delta f = G_{grid}(s)\Delta P = \frac{f_n}{S_n(2H_{grid}s + kf_n)}\Delta P, \tag{1.2}$$

where H_{grid} is the combined inertia constant of the whole grid, k is the frequency-dependency coefficient of loads. A simulation result documented in [7], which is shown in Fig. 1-1, illustrates how generator size impacts the frequency transients on a 36-Gigawatt (GW) grid. As the kinetic energy capacity reduces (a smaller rotating mass), the frequency nadir decreases, and the frequency transient slope gets steeper. As REGs connect to power grids via power electronic devices rather than synchronous generators, the rotating mass of grids, i.e., the grid inertia, is decreasing sharply [8]. A sharp decrease in the grid inertia can lead to faster frequency change rates when there are active power imbalances, making the system vulnerable to instability if not managed correctly.

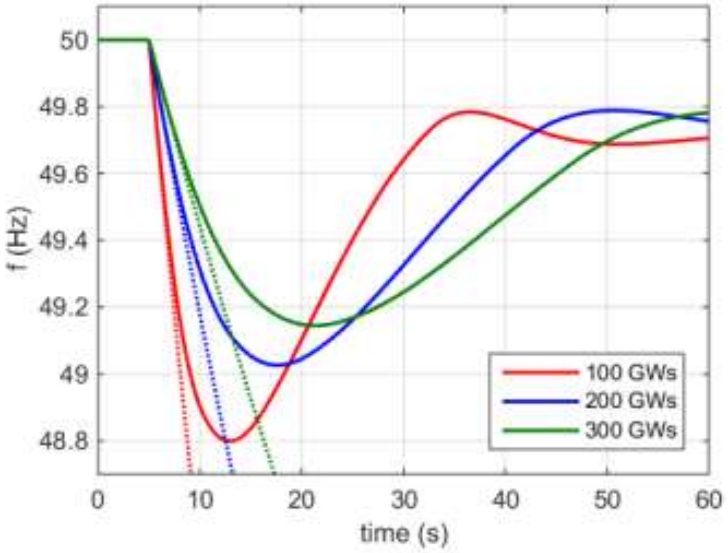

Figure 1-1 The effect of the amount of kinetic energy on the behavior of frequency after a loss of production [7] (GWs = GW seconds).

Currently, inertia reduction in power systems has been reported globally as a common problem by grid operators. Australia, the United Kingdom, and Nordic countries generally have more severe problems regarding inertia reduction as the scale of their grids is relatively small. In [9], the Australian Energy Market Operator (AEMO) anticipated a significant inertia drop of over 30% in the power system of New South Wales and Queensland by 2028, as shown in Fig. 1-2. A similar percentage of inertia reduction is predicted in [10] by the United Kingdom's national grid operator. As a result, the frequency fluctuation becomes more volatile than before. In Fig. 1-3, the frequency deviation caused by a loss of major generation units in the Nordic region was documented by the European Network of Transmission System Operators for Electricity (ENTSO-e), where we see that the frequency fell significantly for 0.25 Hz within 10 seconds [11]. These large variations can potentially disable or damage power system equipment and disturb normal grid operations.

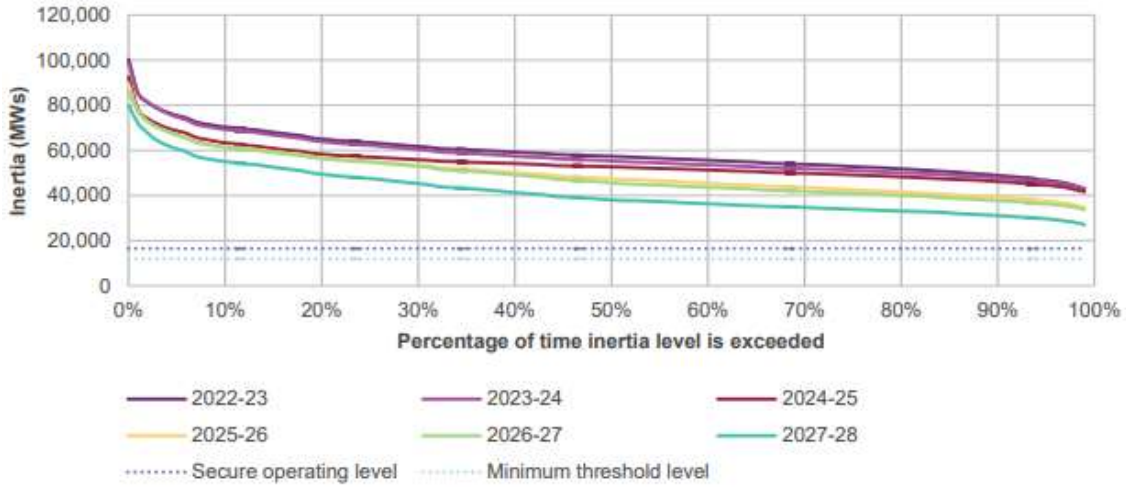

Figure 1-2 Projected inertia for New South Wales and Queensland's five-year outlook, step change scenario [9].

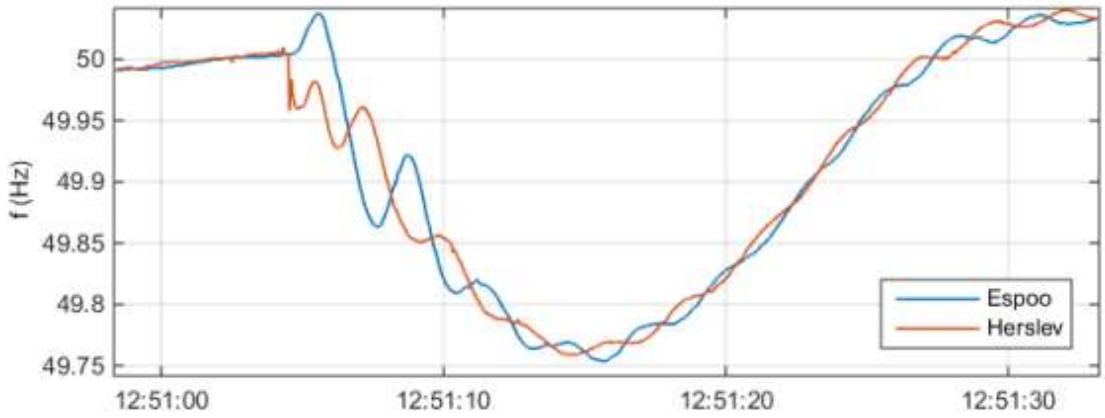

Figure 1-3 Frequency in Espoo (southern Finland) and Herslev (Denmark) after a loss of 580 MegaWatts (MW) generation [11].

In order to deal with the upcoming challenges of inertia drop and maintain a constantly healthy frequency in power systems, frequency ancillary services are mandatory. As shown in Fig. 1-4, the ENTSO-e summarized that over 6 billion Euros were spent on grid frequency response across Europe in 2022 [12]. Although the ancillary service market size is still not comparable to the electricity wholesale market, it is anticipated to grow with the percentage of REG penetration. The essence of these ancillary services is to regulate the active power of the subject equipment according to the current frequency measurements. For instance, if the frequency is too low, then the active power consumption of a load equipment will be tuned lower, and vice versa for the equipment on the generation side. Nevertheless, the challenging part is to develop a systematic multi-level service structure to include various equipment on both the generation and demand sides, as different equipment has distinct dynamic characteristics in terms of power response, such as modulation depth, settling time, and efficiency preferences. The following subsection of this thesis introduces the existing structure of frequency ancillary services in detail.

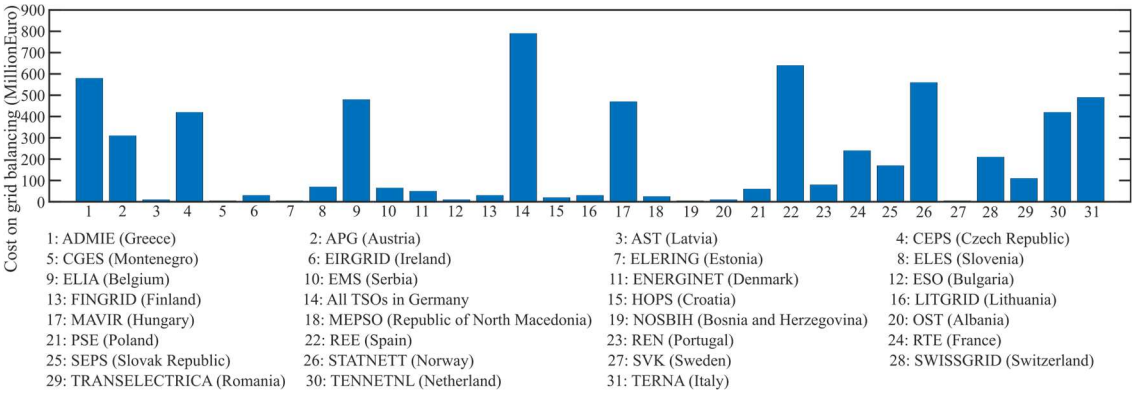

Figure 1-4 Total costs of frequency response for different transmission system operators across Europe in 2022 (data from [12]).

1.2 Frequency Ancillary Services

Current frequency ancillary services are categorized by their response speed. From fast to slow, there are fast frequency response (FFR), primary frequency response (PFR), secondary frequency response (SFR), and tertiary frequency response (TFR) services. Generally, a faster service means higher service costs, as the number of available equipment for the target service is reduced. Therefore, from FFR to TFR services, the goal gradually shifts from short-term frequency stabilization to economic recovery. This thesis mainly focuses on the FFR, PFR, and SFR services, as the TFR service is more related to day-ahead planning and optimizations.

1.2.1 Fast Frequency Response

FFR services are designed to tackle rapid frequency changes. Unlike traditional frequency response services that act with minute-level speed, FFR services are designed to act within seconds (often less than 2 seconds) after an anomalous frequency event. This level of response speed is crucial, especially when considering the sharp frequency drops that can occur with the expanding low-inertia power systems.

Limited by the harsh response requirement, the application scope of FFR services is often restricted to battery energy storage systems (BESS) [13][14][15][16] and flexible REGs [17][18][19] as they do not have a major rotating mass that limits the power response capability. The concept of FFR services is relatively new compared to PFR and SFR services, and they were recently introduced to counter the recent drops in power system inertia. High service costs currently hinder the development of FFR services since most conventional power plants cannot achieve the required response speed. BESSs and flexible REGs can satisfy the harsh response speed requirement, but expanding their capacity will significantly increase the capital and maintenance costs of the grid. Besides, as the frequency stability can be affected by FFR services, the controller testing and validation procedures are also more complex than PFR and SFR services [20][21]. This often leads to equipment-specific controller designs, and the results are hard to generalize for other equipment types and rating levels.

The market of FFR services is only at the starting phase, as traditional PFR and SFR services can still manage the current REG penetration level in most countries, except for some with relatively weak grids. As one of the main initiators, the Nordic region implemented a service called "Fast Frequency Reserve", and the maximum activation time ranges from 0.7 to 1.3 seconds [22]. In the United Kingdom, new FFR services called "Dynamic Containment" and "Dynamic Moderation" have been implemented in the financial year of 2023/24. They have a reaction time limit of 0.5 seconds, a response time limit of 1 second, and a minimum bid of 1 MW [23]. Similarly, the AEMO recently initiated a new type of service called "Very Fast Raise/Lower" for FFR-level grid balancing on the 9th of October 2023, also with a minimum bid of 1 MW and a response time of 1 second [24].

1.2.2 Primary Frequency Response

Before the rise of REGs and the inertia shortage, the frequency stability of conventional SG-based power systems was maintained mainly by PFR services. In modern and future high REG scenarios, standalone PFR becomes unsatisfactory; thus, its role in maintaining frequency stability becomes less critical. PFR services react much slower than FFR services, and a typical response time threshold is 30 seconds.

The application scope of PFR services is significantly broader than that of FFR services, as most conventional power plants are available under the PFR response time limit. Grid operators worldwide have mandated minimum PFR requirements in speed governors of conventional power plants such as coal, gas, nuclear, and hydro types, which means PFR is an inherent functionality of large-scale SGs [25][26][27]. A considerable portion of BESSs and flexible REGs are also considered in PFR services [28][29], while the possibility of involving demand-side response (DSR) resources has also been investigated in recent years [30][31][32].

Market regulations of PFR services are standardized and mature in modern power systems, but the market size is still relatively small as the body part of PFR services is often done with major power plants by default without market procurement. In Europe, the ENTSO-e implemented PFR as "Frequency Containment Reserves (FCR)", which has a response time requirement of 30 seconds [33] and a minimum bid of 1 MW. In the United Kingdom, there are two services in operation within the range of PFR services. The first one is "Dynamic Regulation" with an initiation time of 2 seconds, a response time of 10 seconds, and a minimum bid of 1 MW. The second is the "Static Response" service, which has the same requirement as the FCR launched by the ENTSO-e. As in Australia, the AEMO established "Slow Raise/Lower" for PFR services, with a response time of 60s and a minimum bid size of 1 MW for both directions [34].

1.2.3 Secondary Frequency Response

While FFR and PFR services quickly respond to frequency anomalies, they are contingency measures that are not designed for long-term operations because of the high costs. SFR services step in as slow recovery measures to gradually relieve and replace FFR and PFR services, ensuring a sustained return to the nominal frequency through a re-dispatch with economical equipment selected by either the grid operator or an

optimization strategy [35][36]. A typical response time range for SFR services is 5-15 minutes, which is significantly more relaxed than FFR and PFR services.

Similar to PFR services, SFR services have been widely used for decades. Before the inertia shortage problem emerges, traditional power systems often adopt SFR services through Automatic Generation Control (AGC) [37][38], which is essentially a centralized control scheme that calculates re-dispatch signals for selected SGs based on observed frequency deviation at the control center. In modern power systems, where the grid operator tends to include more flexibility sources to reduce the SFR costs, a large amount of BESSs [39][40], DSR resources [41][42], and flexible REGs [43] are also allowed to participate, which means their equipment coverage is much broader than PFR and FFR services.

A significant portion of SFR services is sourced through market procurement, ensuring a larger market size than FFR and PFR services. For instance, the ENTSO-E has rolled out a Europe-wide "Automated Frequency Restoration Reserves (aFRR)" market dedicated to SFR services, characterized by a 5-minute response time and a 1 MW minimum bid [44]. A smaller market, known as the "Manual Frequency Restoration Reserves (mFRR)", was created for a specific region that includes Germany, Austria, and Czechia, which extends the response time threshold to 15 minutes [44]. Australia launched the "Delayed Raise/Lower" services with a 5-minute response time and a 1 MW minimum bid criterion [34]. In contrast, the United States Pennsylvania-NewJersey-Maryland (PJM) interconnection developed the "Regulation A" market for SFR services, forcing a 5-minute response time limit and a notably smaller minimum bid of 100 kilowatts (kW) [45].

1.3 Sector Coupling with the Heat (Thermal) Sector

1.3.1 An Electrified Heating Sector

Heating systems, particularly those that rely on fossil fuels, are pivotal contributors to global carbon emissions. Discussions around carbon emissions in the past were often predominantly anchored to electricity generation, yet the heating systems, especially in residential and commercial areas, cannot be overlooked. Heating loads are the predominant energy demand within buildings. The International Energy Agency (IEA), in its 2022 report, highlighted that approximately 30% of the global energy consumption was marked for building operations. If we explore these statistics, around 50% of the building energy consumption was used for space and water heating [46][47]. A critical observation in the IEA data was the persistent dependence on combustion-based heating, with a large portion of 63% of the building-related heating demand still tethered to fossil fuels [46]. This highlights an obstacle in emission reduction and hinders more REG integration.

The shift towards a low-carbon heat sector naturally encourages electrification on heat generation [48], as power-to-heat (PtH) systems are carbon-free if they are supplied by REGs. From the efficiency perspective, PtH systems like electric heat pumps are more efficient than combined-heat-and-power (CHP) and condensing boiler units, which also bring down the total energy demand for heating purposes. As the capital costs of heat

pumps continue to fall, they become increasingly popular. Reports from the IEA showed that sales of air-to-water heat pumps in Europe grew by nearly 50% in 2021 and 2022, while the global average annual growth was 24% [49]. Given these trends, it is clear that heat pumps are promising to gradually replace traditional CHPs and condensing boilers for heat generation in the heat sector [50].

1.3.2 Frequency Ancillary Services through Modulating Heat Pumps

In the context of a highly electrified heating sector, a large amount of power flexibility opportunities can be unlocked through sector coupling and smart grid operations [51], which is pivotal for solving the inertia challenges in power systems. As heating grids utilize water, which is a fluid with high thermal capacity, the temperature variations are often not significant when heat pumps modulate their capacity for short-term flexible operations [52]. Furthermore, as thermal storage systems are much more affordable than BESSs [53], there is a possibility for their mass adoption, which further weakens the negative effect of flexible operations on sector coupling equipment such as heat pumps. These features suggest that a considerable amount of unused flexibility exists in heating grids, which can be potentially used to fill the flexibility gap in power systems.

Because the heat sector is not sensitive to short-term production-consumption imbalances, the operating cost for heat pumps to participate in frequency response services is not significant. As for the capital cost, since there is no need for additional infrastructure investment but just an upgrade of the heat pump controller, the capital cost is also minimal. Therefore, using existing heat pumps for frequency response services is a low-cost measure to contain frequency variations and thus reduces the service reliance on BESSs and flexible REGs. This expansion of frequency response capacity can further enhance the integration of REGs into power systems [54] because of the increased capability for handling discontinuous power generation. Such integration, in turn, causes a downward trend in electricity prices, amplifying the attraction of heat pumps as a heat generator, thus establishing a positive synergy. Moreover, participation in frequency response services can offer property owners and industrial manufacturers financial advantages as compensation for grid support services.

The process of designing frequency response controllers for heat pumps should be tailored to specific applications. It is vital to choose the optimal modeling and control strategies based on the target heat pump's physical characteristics and the response requirement of the desired service. The focus of controller design varies for services like FFR, PFR, and SFR. FFR services demand precise dynamic modeling and robust control, with less emphasis on design versatility [55]. In contrast, the control design of PFR and SFR services prioritizes high versatility instead of control stability and transient performance, as these services typically have a much broader equipment coverage and relatively relaxed response time requirements [56][57].

1.4 Thesis Outline

In this doctoral thesis, we focused on heat pumps as they are a promising solution for the heating sector to reach carbon-neutral goals. The feasibility of their participation in different levels of frequency response services is thoroughly analyzed, and possible

control strategies are proposed. The core content of this thesis is written by raising and answering the following research questions with a clear structure, as shown in Fig. 1-5.

Research question 1: What is the state-of-the-art in using heating systems for frequency response services and the related future trends?

Research question 2: How to model the heat pump systems for different frequency response services that have diverged design focus?

Research question 3: How to design stable and robust heat pump controllers for future FFR services in order to provide inertia support in a low-inertia power grid?

Research question 4: How to design relatively universal and practical heat pump controllers for PFR and SFR services in order to perform economical frequency recovery?

Chapter 2 provides a foundational literature review for this thesis. It systematically investigates and summarizes equipment capabilities, control strategies, related studies, and future trends. This Chapter highlights the significance of heat pumps and identifies challenges for control design due to uncertainties in heat pump operations.

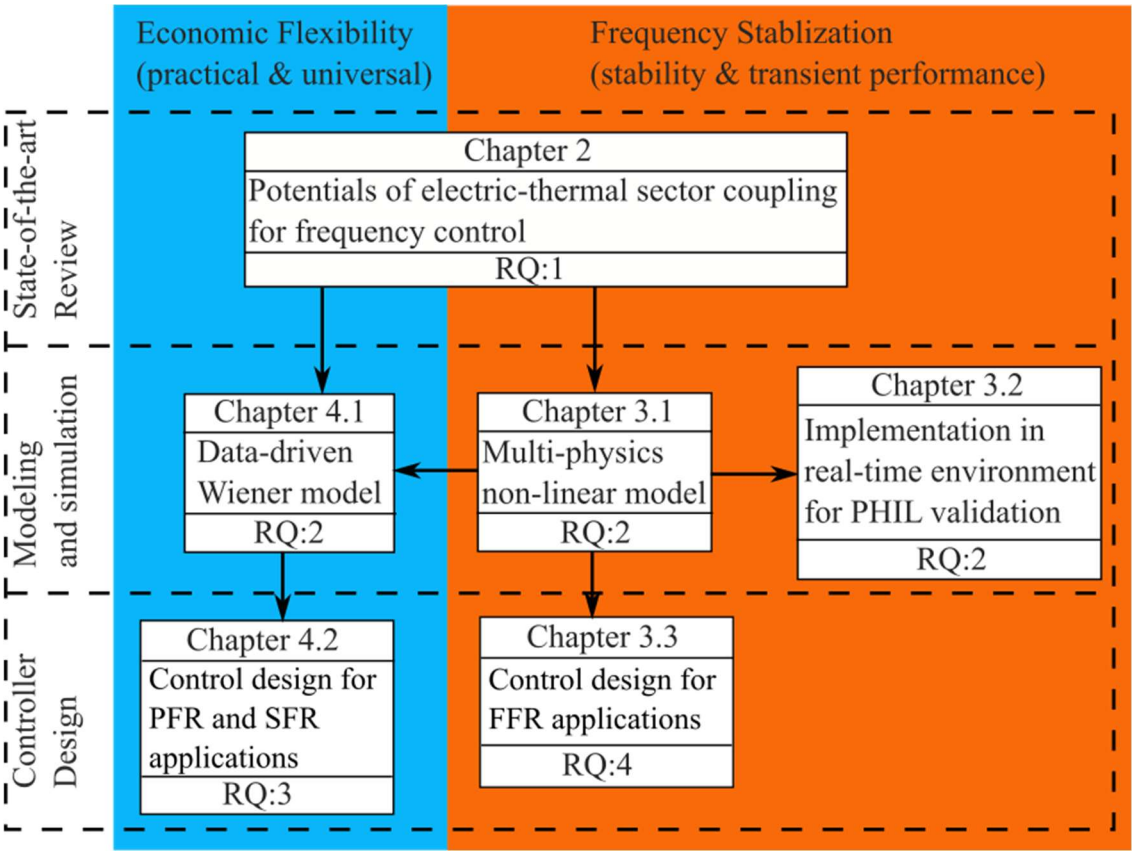

Figure 1-5 Graphic illustrations of the thesis structure.

Chapter 3 delves into rapid modulation scenarios, such as using distributed air-source heat pumps to enhance frequency stability in FFR services. This Chapter considers a future low-inertia grid background, and heat pumps are assumed to be used with their maximum physical potential. Section 3.1 starts by modeling heat pump non-linear dynamics based on fundamental physics and mathematics, forming the bedrock of this thesis in understanding heat pump characteristics. Then, Section 3.2 introduces how the developed model can be implemented on real-time Power-Hardware-in-the-Loop (PHIL) emulators, creating a close-to-reality environment for heat pump control validation in standard power system laboratories. Section 3.3 presents one possible way to design a grid-level robust FFR control strategy for integrating distributed air-source heat pumps, considering the stability impact of uncertain heat pump operating conditions.

Chapter 4 focuses on PFR and SFR scenarios, such as using a wide range of heat pumps for economic power flexibility. Unlike the previous Chapter, which leans heavily on theory and simulations, this Chapter prioritizes real-world applications and the versatility of proposed solutions. Section 4.1 outlines a data-driven modeling method for scenarios like PFR and SFR services to balance model accuracy and versatility. The derived model structure is validated in our laboratory on a 4 kW commercial air-source heat pump. Section 4.2 introduces a novel open-loop control strategy to enhance heat pumps' power reference tracking capability in PFR and SFR scenarios under uncertain operating conditions.

Finally, Chapter 5 wraps up the thesis content by answering the key research questions in Section 5.1 and suggesting potential future research directions in Section 5.2.

1.5 List of Publications during the Doctoral Program

The full publication record related to this thesis is shown as follows. Each paper is presented in its corresponding Chapter, along with a summary and description of each author's contribution.

1. **R. Song***, T. Hamacher, V. Terzija and V. S. Perić, "Potentials of Using Electro-thermal Sector Coupling for Frequency Control: A Review," *International Journal of Electrical Power & Energy Systems,* 2023.
   doi: https://doi.org/10.1016/j.ijepes.2023.109194.
2. **R. Song*,** A. Mohapatra, T. Hamacher and V. S. Perić, "Power-Hardware-in-the-Loop Validation of Air-Source Heat Pump for Fast Frequency Response Applications," Electric Power Systems Research, 2024.
   doi: 10.1016/j.epsr.2024.110754.
3. **R. Song***, V. Terzija, T. Hamacher and V. S. Perić, " Integrating Air-Source Heat Pumps into the Demand-side Fast Frequency Response Service: A Study Based on Thermal Dynamic Uncertainty," *IEEE Transactions on Sustainable Energy*, 2024.
   doi: 10.1016/j.epsr.2024.110754.
4. **R. Song***, G. Yon, T. Hamacher and V. S. Perić, "Data-Driven Model Reduction of the Moving Boundary Heat Pump Dynamic Model," *2022 IEEE Power &*

Energy Society General Meeting (PESGM), 2022.
doi: 10.1109/PESGM48719.2022.9916823.

5. **R. Song***, D. Zinsmeister, T. Hamacher, H. Zhao, V. Terzija and V. S. Perić, "Adaptive Control of Practical Heat Pump Systems for Power System Flexibility based on Reinforcement Learning," *2023 International Conference on Power System Technology (POWERCON)*, 2023.
doi: 10.1109/PowerCon58120.2023.10331231.

Besides the publications above, there are also publications listed below that is not directly related to this thesis.

6. **R. Song***, T. Hamacher and V. S. Perić, " Impact of hydraulic faults on the electric system in an integrated multi-energy microgrid," *the 9th Workshop on Modeling and Simulation of Cyber-Physical Energy Systems (MSCPES)*, 2021.
doi: 10.1145/3470481.3472709.

Chapter 2: A Review on Frequency Response Services through Sector Coupling

Scientific Context

The increasing focus on lowering carbon emissions has led to a significant shift towards electrifying traditional heat sources. This transition fosters more interaction between the heat (thermal) and power (electro) sectors. In the context of reduced grid inertia and a lack of flexibility in power systems, it is evident that power-heat sector coupling equipment will play a crucial role in providing frequency response services. This development marks a step towards more integrated energy operations in the future. Historically, the emphasis on integrated power-heat energy operations was often placed on hourly or sub-hourly dispatch strategies for the sector coupling equipment, as highlighted in various papers such as [58][59][60][61]. Moreover, several review contributions have encapsulated the state-of-the-art in this research domain, including [62] and [63]. However, there is a noticeable gap in organizing research contributions related to short-term flexibility, particularly in the area of frequency response services. To address this gap, our study comprehensively summarized the current research on frequency response services utilizing power-heat sector coupling equipment. We presented our survey through three key perspectives as follows:

- Equipment capabilities: we summarized and compared the power modulation capabilities of power-heat sector coupling equipment in terms of modulation depth, response speed, and efficiency based on existing research papers and industrial documentation.
- Control algorithms: we reviewed the existing grid-following frequency control strategies and list example research that shows how these strategies can be implemented on power-heat sector coupling equipment.
- Challenges and trends: we showed the current barriers that hinder the large-scale integration of power-heat sector coupling equipment into frequency response services. Besides, future possible opportunities were also identified.

Publication #1: Potentials of using electro-thermal sector coupling for frequency control: A review

Authors: Ruihao Song, Thomas Hamacher, Vladimir Terzija, Vedran Peric

Publication: International Journal of Electrical Power and Energy Systems (IJEPES)

Digital object identifier: 10.1016/j.ijepes.2023.109194

Author	Contribution	Tasks
Ruihao Song	75%	• Conceptualization • Methodology • Investigation • Writing-original draft • Writing-review & editing
Thomas Hamacher	5%	• Supervision • Funding acquisition
Vladimir Terzija	5%	• Writing-review & editing
Vedran Peric	15%	• Conceptualization • Supervision • Writing-review & editing

Electrical Power and Energy Systems 151 (2023) 109194

Contents lists available at ScienceDirect

International Journal of Electrical Power and Energy Systems

journal homepage: www.elsevier.com/locate/ijepes

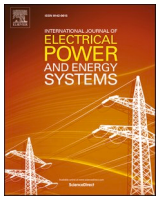

Review

Potentials of using electric-thermal sector coupling for frequency control: A review

Ruihao Song [a,*], Thomas Hamacher [a], Vladimir Terzija [b], Vedran S. Perić [a]

[a] Technical University of Munich, Lichtenbergstr. 4a, 85748 Garching, Germany
[b] Skolkovo Institute of Science and Technology, Bol'shoy Bul'var, 30, стр 1, 121205 Moscow, Russia

ARTICLE INFO

Keywords:
Combined heat and power
Power to heat
Microgrid
Sector coupling
Frequency control
Power flexibility

ABSTRACT

Power and heat are the two most important sectors in modern energy systems. Microgrid, as the basic block of the future power sector, is turning into a low-inertia system as the renewable energy penetration level continues to rise. Since battery energy storage systems are still costly, the flexibility in microgrids is currently limited, which makes frequency control challenging. On the contrary, as a result of the high thermal inertia and affordable thermal energy storage systems, the heat sector has a large amount of unused flexibility. With the trend of decarbonization, the heat sector is increasingly being electrified, granting the opportunity for combined operation between the power and heat sectors. Utilizing the flexibilities in heating systems for microgrid frequency control is an essential step toward sector coupling and multi-energy operations. This paper analyzes the flexibilities of combined-heat-and-power (CHP) and power-to-heat (PtH) systems through several key performance indicators. In addition, the available control strategies and existing practices of frequency control based on CHPs and PtH systems are reviewed. Finally, future research directions on sector-coupled frequency control are provided based on the gathered information.

1. Introduction

The penetration of renewable energy generation (REG) has recently increased dramatically worldwide. In 2020, the overall statistical data showed that the percentages of REG in the European Union, China, and the United States, have reached 22.1, 26, and 19.8 %, respectively [1–3]. With the increasing adoption of intermittent REGs, power systems are also transforming from centralized to distributed structures. Microgrids are one of the most accepted solutions for renewable energy integration [4,5]. However, with the increased penetration of REGs and decreased number of synchronous generators, the inertia level of microgrids is weakened, causing the system to be sensitive to active power imbalances leading to larger frequency fluctuations. In order to stabilize the microgrid, it is crucial to have fast-responding systems from the customer side that can vary their power level as requested and hence provide "flexibility". Battery energy storage systems (BESS) are typically adopted for this purpose, yet their mass installation is obstructed by the high costs [6]. Therefore, how to fill the flexibility gap for microgrids has become a challenge of high priority.

In recent years, as the traditional heat sector is transforming from a centralized, combustion-based, and high-temperature network [7] to a distributed, electrified, and low-temperature network [8–11], microgrid researchers have started to investigate the possibility of using potentials in the heat sector to improve microgrid's performance [12]. Unlike low-inertia microgrids, heating systems are generally not sensitive to sudden generation-demand imbalances because it has significant thermal inertia. In addition, a thermal energy storage system is much cheaper [13] than a BESS in microgrids, which boosts the heating system's tolerance of short-time heat imbalances. On the other hand, with the massive adoption of combined-heat-and-power (CHP) and power-to-heat (PtH) systems, power and heat sectors are becoming more integrated, creating the need for coordinated operation of both systems [14]. In the past, the research on electric-thermal sector coupling focused heavily on finding the optimal dispatching of CHP or PtH systems in diverse application scenarios [15,16]. Some of these methods consider a detailed heat grid model [17–21], while others neglect the impact of the heat grid [22–28]. The dispatching is determined through the day-ahead optimization, [17,21,23,27], while sometimes intra-day adjustments have been treated with a two-level optimization approach as in [18–20,22,24,25,26,28]. Besides optimizing the minimum

* Corresponding author.
E-mail address: ruihao.song@tum.de (R. Song).

https://doi.org/10.1016/j.ijepes.2023.109194
Received 6 October 2022; Received in revised form 23 February 2023; Accepted 20 April 2023
Available online 1 May 2023

operating costs as in [17,20–24,26–28], there have been approaches to consider the trade-off between risks and costs [18,19,25]. On the other hand, sector coupling that considers short-time dynamics, such as fast dispatch, control design, and fault propagation analysis, also starts to attract attention [29,30]. Using short-time flexibilities within heating systems for frequency control (see Fig. 1), one of the vital ancillary services in microgrids, can be seen as a practical example of sector-coupled operation in the real-time domain.

In the past, various control strategies for electric-thermal sector-coupled frequency control have been reported in the open literature. However, there are limited attempts to review and summarize the existing findings. This paper intends to provide a clear picture of the state-of-art in heat sector-based frequency control. To be specific, we analyze the progress from the following key aspects:

- We review the existing industrial documentation and summarize the key performance indicators of CHPs and PtH systems on flexibility.
- We extract existing mainstream control strategies for grid-following frequency control from the open literature and review the merits and shortcomings of each configuration.
- We review existing applications of grid-following frequency control strategies on CHPs and PtH systems and provide an assessment of the current focus.

Finally, the paper identifies several possible development directions for sector-coupled frequency control from policy-making and control design perspectives.

This paper is organized as follows. Section two summarizes the flexibility critical performance data of different CHP and PtH technologies and assess their suitability for participating in frequency control. In this context, we document the existing control strategies for grid-following frequency control in section three, and existing practices of frequency control on CHP and PtH systems are reviewed in section four. Besides, we show the possible future development directions in section five. Finally, the conclusion of this paper is given in Section six.

2. Opportunities in sector coupling

The main types of CHP in the heat sector are steam turbines (ST), combined cycle gas turbines (CCGT), simple cycle gas turbines (SCGT), aero-derivative turbines (AGT), and internal combustion engines (ICE), while PtH systems include electric boilers (EB) and heat pumps (HP). Currently, heat demands or temperature set points mainly constrain these CHP and PtH systems. However, they possess a large amount of unused short-time power variation ability, which can potentially satisfy the response speed requirement (<30 s [31]) for frequency stabilization. This review will analyze the flexibility opportunities within CHP and PtH systems for frequency control at three levels: centralized, community, and domestic. Table 1 summarizes the characteristics of all analyzed equipment. We review the flexibility opportunities through the following key performance indicators [32]:

- Rating and modulation range: this indicator shows the magnitude of possible power flexibilities.
- Response speed: this shows how quickly the flexibilities can be provided.
- Costs and modulation preferences are affected by fuel, efficiency, and system characteristics.

2.1. Centralized level resources: MW-GW

Centralized level heat sources generally include ST, CCGT, and AGT. These heat sources produce electric and heat power in the range of several MW to several hundreds of MW. In terms of frequency control, these major CHPs are inherently involved due to the droop characteristic programmed in speed governors.

The STs mainly use a water boiler to generate high-pressure steam for torque. Common fuel types for STs can be coal, nuclear, or biomass. The power modulation range for STs can vary with the fuel types, but they generally do not have large modulation range as the efficiency of turbine systems reduces at the partial load. From the dynamic

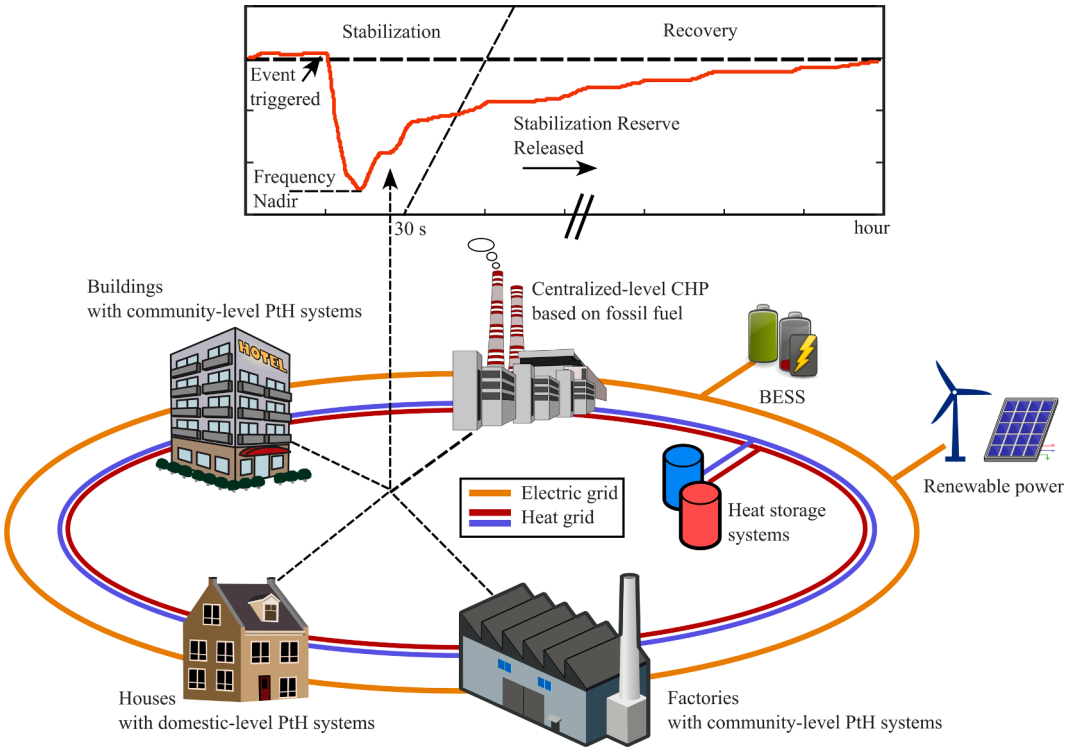

Fig. 1. Graphic illustration of the electric-thermal sector coupled frequency control.

Table 1
Power flexibility potentials comparison of main heat sources in the heat sector (Hot start, commodity price 2015 (EU import). Reference: [33–47]). O&M: operating and maintenance; Elec.: electricity.

Type	Power Magnitude (kW)	Response Speed (%/30 s)	General Min Load (%)	O&M Cost (€/MWh)	Fuel cost (€/MWh)	Electricity efficiency (%)	Heat efficiency (%)	Control Delay	Control Difficulty
ST	10^3-10^5	0.3–1.5	35–50	2–4	10.10 (Coal)	46–51	49–54	High	High
CCGT	10^3-10^5	1.5–6	30	3–7	29.43 (Gas)	48–56	44–52	Medium	Medium
AGT	10^3-10^5	30–60	5	≈1.8	34.21 (Oil)	44	56	Low	Low
ICE	10-10^3	24–100	30	4–12	34.21/29.43	41–45	55–59	Low	Low
SCGT	10^2-10^4	3–15	25	4–7	29.43	28–40	60–72	Low	Low
EB	1-10^3	100	≈ 0	≈1	68 (Elec.)	0	100	≈ 0	Low
HP	1-10^4	30–100	25	1–3	68	0	300–500	Low	Medium

perspective, because of the complexity of fuel processing, thermal interaction, steam pressurizing, and turbine operation, the ST system is highly inert, nonlinear, and uncertain in transients. Therefore, the power responses of STs are often relatively slow. From an economic point of view, the overall costs for STs to generate flexibility are attractive as they can use fuels with various specifications.

CCGT has a simple cycle gas turbine (SCGT) as the main torque source and a ST for auxiliary torque production from the exhaust gas. Compared to STs, their power modulation depth is slightly improved. From the transient perspective, the power response is also improved from the ST level because most torque production directly results from fuel combustion. However, as the CCGT system still has a secondary ST for increasing electrical efficiency, the response speed is generally lower than the SCGT and AGT types. CCGTs require a stable gas input with strict quality control in purity and pressure, so their overall cost is higher than STs.

The last type of high-power-rating turbine is the AGT. They are lightweight and specialized SCGTs that only use exhaust gas for heat production. AGTs offer the best power modulation depth at the centralized level, and their transient characteristics are significantly better than STs and CCGTs. As they typically use gasoline as a fuel and generally have lower efficiency, they tend to be used for an emergency reserve only.

2.2. Community-level resources: kW to MW

The community-level heat sources include ICE, SCGT, HP, and electrode boiler (EB). These sources are often decentralized and built with medium power that ranges from tens of kW to several MW levels. At this level, participation in frequency control is not common practice. The main reason is that the current regulatory framework of frequency control hardly considers these medium-level sources. As both the power and heat sectors become increasingly distributed, the community-level sources will take a more important role in the frequency control market.

On the generation side, ICE is more popular than SCGT at the community level because of its low capital cost and relatively higher electrical efficiency. On the other hand, ICEs and SCGT share a similar level of power modulation depth. From the transient perspective, ICEs directly use fuel combustion to push pistons instead of a turbine to generate torque, suggesting a much-reduced inertia compared with SCGTs. However, there are trade-offs in comparing economic values between ICEs and SCGTs. Although ICEs generally have higher efficiency, SCGTs have lower fuel and maintenance costs. Besides, ICEs also generate more pollutants in exhaust gas than SCGTs.

On the demand side, EBs currently count for a larger share than HPs at the community level. As the capital cost of HP systems continues to drop, the market share of HPs will gradually take over the EBs' place in the heat sector. Compared with EBs, HPs have much worse power modulation depth and response speed. The transient performance of the HP system is limited by the thermal interactions within the refrigerant loop, and it is also affected by the source and sink temperatures, while the performance of the EB is stable and mainly constrained by the electrical stress on power electronics. However, from the economic perspective, the efficiency of HPs for low-temperature water heating (20–70 °C) is several times larger than the EB, which implies an outstanding economic value in residential heating scenarios.

2.3. Domestic level resources: W to kW

The domestic-level electric-thermal equipment includes EBs and HPs at the demand side of the power grid. These house appliances usually rate from hundreds of W to several kW, often in large quantities. The controllability of these equipment at the domestic level is far lower than at the community level, and binary control based on thermostats is often the default option for cost-saving reasons. The lack of sensing and control gear makes these appliances hard to be utilized in frequency control. However, with a robust communication network, these domestic-level EBs and HPs can be involved in frequency control through load aggregation. Given the current cost of such communication systems, it is still not economically feasible to use these low-power units for frequency control. As the frequency control market continues to grow over the world and new business models are being established, domestic-level appliances could be a potentially valuable flexibility source for frequency control in the future [48].

3. Control strategies

In order to add frequency control function to the CHPs and PtH, grid-following control strategies are typically assumed. In the past, several frequency control strategies have been proposed by researchers over the world, where the control goals are as follows:

- Tuning the active power of individual equipment to restore the grid frequency under load disturbances.
- Sharing the regulating power among all participating equipment according to a predefined ratio.
- Making the transient process as smooth as possible (lower oscillations, faster convergence, etc.).

Generally, the existing control strategies for grid-following frequency control can be divided into three categories, namely decentralized, centralized, and distributed strategies, as shown in Fig. 2. Decentralized strategies only contain the primary control layer, while centralized and distributed strategies contain both primary and secondary layers. We will first review the theoretical basis and principle for each category, then summarize commonly used strategies and application possibilities for CHP and PtH systems, as shown in Table 2.

3.1. Decentralized strategies

The root of decentralized strategies is the concept of droop control. Currently, the power-frequency droop characteristic is widely implemented in speed governors of AC generators and controllers of inverter-interfaced renewables for forming the voltage in microgrids [49,50]. In

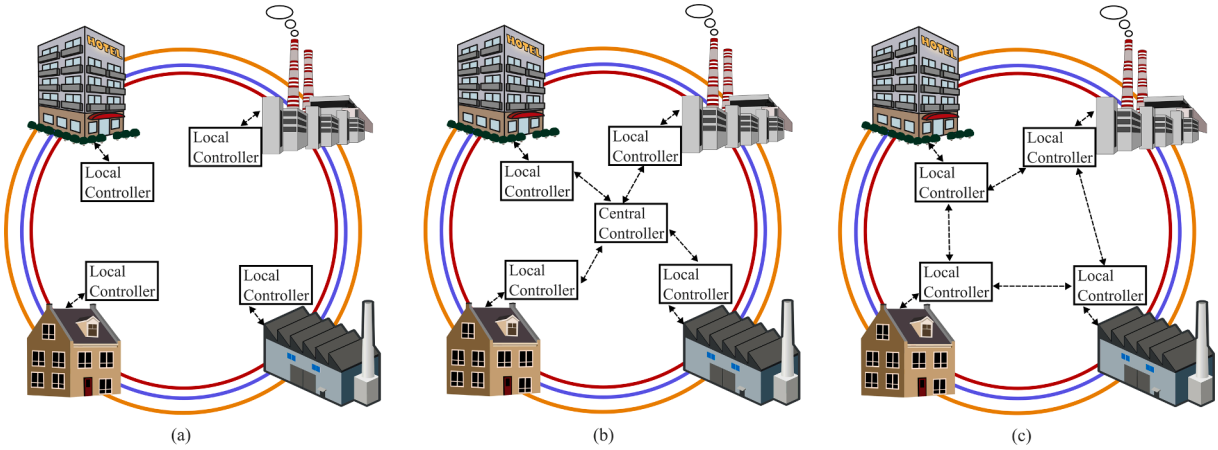

Fig. 2. Comparison of main frequency control strategy categories: (a) decentralized; (b) centralized; (c) distributed.

Table 2
Comparison of mainstream strategies for frequency control under grid-following scenarios.

Ref.	Type	Strategy		Communication	Advantages	Disadvantages	Suitable Application	
		Secondary	Primary					
[51–53]	Decentralized	N/A	Rule-based switching	N/A	• Customizable rule • Plug-and-play	• Poor transient behavior • Steady-state deviation • Frequent On/Off damages		• EB • HP
[54–57]	Decentralized	N/A	f-P droop	N/A	• Light computation • Plug-and-play	• Steady-state deviation • Trade-off: deviation – transient	• ST • CCGT • SCGT • AGT • ICE	• EB • HP
[58–60]	Decentralized	N/A	Synthetic Inertia	N/A	• Customizable inertia • Light computation • Plug-and-play	• Steady-state deviation • Potential noise amplification	• AGT • ICE	• EB • HP
[61–66]	Centralized	Optimal deviation restoration	f-P droop or N/A	• Bi/Uni-direction • Star • Inflexible • High bandwidth	• No steady-state deviation • Results are normally economically optimal	• Fragile to communication faults • Stability affected by communication	• ST CCGT • SCGT • AGT	
[67–70]	Distributed	Consensus searching	f-P droop or N/A	• Peer-to-peer • Flexible topology • High bandwidth	• No steady-state deviation • Good transient behavior • Plug-and-play	• Stability and transient behavior affected by communication topology and delay	• ST • CCGT • SCGT • AGT • ICE	• EB • HP
[71–73]	Distributed	Distributed optimization	f-P droop or N/A	• Peer-to-peer • Flexible bandwidth • Flexible topology	• No steady-state deviation • Ability to include economic concerns • Plug-and-play	• Transient behavior affected by communication topology and delay • Trade-off: communication burden – convergence speed • Measurement errors can cause oscillations	• ST • CCGT • SCGT • AGT • ICE	• EB • HP

this context, a strong relationship between frequency and power is established. Therefore, the basic principle of decentralized strategies for grid-following sources/loads is to calculate the required active power injection/consumption from the local frequency measurement. In addition, since the frequency is a global variable in AC grids, no communication link is needed to share the responsibility among all participating units. The decentralized strategies are often considered the most robust, cost-saving, and practical among all existing solutions for frequency control. Nevertheless, their control performance is generally not comparable to distributed and centralized strategies.

Basic decentralized strategies include rule-based control, frequency-power (f-P) droop, and synthetic inertia. The rule-based [51–53] control is often straightforward: turn ON or OFF specific equipment if the local frequency measurement satisfies the rule or not, and thus has the advantages of minimum hardware requirements, low costs, and simplicity, but the frequency control and transient performance are inferior compared with other strategies. There are many low-power thermal appliances in households, such as impedance-based water/space heaters, fridges, and air-source HPs (conditioners), which can be economically involved in frequency control through simple rule-based control. The f-P droop [54–57] requires the target system to have higher sensing and processing capability than the rule-based strategy, but the resulting frequency control and transient performance are significantly improved. However, the choice of the droop coefficient introduces a trade-off between frequency control and transient performance. Typically, a small droop coefficient suggests a slow converging speed during transients and a slight steady-state deviation, while a large one produces the opposite. The f-P droop can be applied to any CHPs and PtH systems discussed in the previous section on the condition that continuous frequency measurement and power control capability are guaranteed. However, it is often recommended for at least community-level systems considering the hardware cost to build the implementation

Table 3
Summary of existing application of using CHP or PtH systems for frequency control. LLS: Lumped linear system; SPG: Simulated physical grid; Exp.: Experiment.

Ref.	Year	Target	Communication	Strategy Details		Equipment	Power Grid	Heat Grid
				Secondary	Primary	Model	Model	Model
[80]	2005	Centralized CCGT	N/A	N/A	f-P droop	LLS	N/A	N/A
[81]	2013	Centralized CCGT	N/A	N/A	f-P droop	LLS	LLS	N/A
[82]	2020	Centralized CCGT	N/A	N/A	f-P droop	LLS	LLS	N/A
[83]	2017	Centralized CCGT	N/A	N/A	f-P droop	LLS	LLS	N/A
[84]	2017	Community ICE	N/A	N/A	f-P droop	LLS	LLS	N/A
[85]	2022	Centralized ST	N/A	N/A	f-P droop	LLS	N/A	N/A
[86]	2021	Community SCGT	N/A	N/A	Synthetic inertia	LLS	LLS	N/A
[87]	2012	Domestic EB & HP	N/A	N/A	Rule-based switching	LLS	LLS	N/A
[88]	2011	Domestic EB & HP	N/A	N/A	Rule-based switching	LLS	LLS	N/A
[89]	2018	Community HP	N/A	N/A	Rule-based switching	Static	N/A	LLS
[90]	2007	Domestic HP	N/A	N/A	Rule-based switching	Static	LLS	LLS
[91]	2016	Community EB	N/A	N/A	Rule-based switching	Static	LLS	LLS
[92]	2017	Domestic EB & HP	N/A	N/A	Rule-based switching	Static	SPG	N/A
[93]	2018	Domestic HP	N/A	N/A	Rule-based switching	Static	SPG	LLS
[94]	2019	Community EB	N/A	N/A	Rule-based switching (cluster f-P droop)	Static	N/A	LLS
[95]	2020	Domestic HP	N/A	N/A	Rule-based switching (cluster f-P droop)	Static	SPG	LLS
[96]	2019	Community EB	N/A	N/A	f-P droop	Static	N/A	N/A
[97]	2021	Domestic EB & HP	N/A	N/A	f-P droop	Static	SPG	LLS
[98]	2019	Domestic EB	N/A	N/A	f-P droop	Static	SPG	LLS
[99]	2020	Domestic HP	N/A	N/A	f-P droop	Static	N/A	LLS
[100]	2020	Community HP	N/A	N/A	f-P droop	Static	N/A	LLS
[101]	2015	Community HP	N/A	N/A	Synthetic inertia	Static	LLS	LLS
[102]	2021	Community HP	N/A	N/A	Synthetic inertia	LLS	SPG	N/A
[103]	2022	Domestic HP	N/A	N/A	Multi-objective optimization	Static	LLS	Static
[104]	2021	Domestic HP	N/A	N/A	Sliding-mode control	LLS	SPG	N/A
[105]	2018	Domestic HP	Center ↔ unit	Dead band calculation	Rule-based switching (cluster f-P droop)	Static	LLS	LLS
[106]	2015	Community HP	Center → unit	PCC-based deviation restoration	N/A	LLS	SPG	LLS
[107]	2016	Domestic HP	Center → unit	PCC-based deviation restoration	N/A	Exp.	Exp.	Exp.
[108]	2013	Community HP (Fan)	Center → unit	PCC-based deviation restoration	N/A	Static	N/A	SPG
[109]	2015	Domestic HP (Fan)	Center → unit	PCC-based deviation restoration	N/A	LLS	N/A	LLS
[110]	2016	Community HP (Fan)	Center → unit	PCC-based deviation restoration	N/A	LLS	N/A	LLS
[113]	2018	Domestic HP	Center ↔ unit	Synthetic inertia-based deviation restoration	N/A	Exp.	Exp.	Exp.

environment. The synthetic inertia control [58–60] can be seen as a modified f-P droop by replacing the constant gain with a designed transfer function. A common type of synthetic inertia is the proportional-derivative function, generally to provide extra damping during frequency transients in low-inertia grids. Nevertheless, synthetic inertia may also bring disadvantages, such as increased noise amplification. The synthetic inertia control is generally suitable for sources with high power but relatively low inertia. In the heat sector, this often applies to AGTs, ICEs, EBs, and HPs. In particular cases, their relatively fast responding speed can cause the grid frequency to have problematic oscillations. Therefore, the necessity of synthetic inertia control is scenario-based, and the inertia terms should be tailored with customized objectives.

3.2. Centralized strategies

The centralized strategies assume the control algorithm that makes the decisions based on all available information. Usually, the central controller is located at a higher hierarchy level and provides reference set-points to the decentralized layer. In case of frequency control, the centralized strategies calculate control signals from the frequency deviation at critical buses and send results to all DGs and controllable loads via communication links to eliminate the deviation [74]. The advantage of centralized strategies is that they have the potential to calculate a global optimum control action. However, the centralized strategies can be costly as the high control rate for frequency control requires high-bandwidth communication links and a powerful processor to handle the star information traffic [75].

In the open literature, centralized strategies are achieved at the Power Control Center (PCC) through optimizations; however, the method used can be disparate. Some researchers adopted relatively complex methods, such as model predictive control based on an established grid dynamic model [61]. Although the results are highly optimal, these methods are hard to be implemented in reality as they require bi-directional communication and knowledge of the electric grid. On the other hand, the traditional proportional-integral (PI) algorithm with optimal-amended gains for each unit [62–66] is much more practical and popular because of the simple implementation and low computational burden. Nevertheless, considering the high demand for communication, the mentioned centralized strategies are only suggested for significant power sources such as heavy turbines. Involving community and domestic level systems will increase the communication burden and decrease reliability.

3.3. Distributed strategies

The distributed strategies are designed for a multi-agent system (MAS) connected by a relatively sparse communication network . Like centralized strategies, distributed strategies are often built on top of decentralized strategies as a performance-boosting layer. The theoretical basis of such MAS control is “Reynold’s Rule” [77], which is well-accepted for describing animal flock movements. The “Reynold’s Rule” can also be extended to power grids by considering each distributed generation (DG) or load as one individual in the flock. All units in the power grids seek matching in active power, while some leader units seek alignment on regular voltage frequency. Therefore, the principle of distributed strategies is to use a specific method to process the information that an agent gathers from its neighbors. An elementary demonstration for frequency control can be found in [78], as shown in (1) and (2):

$$\textit{Matching power and frequency}: \quad \boldsymbol{u}_{i,1} = \sum_{j\in N_i \wedge j\notin N_i^c} b_i\left(P_j - P_i\right) + c_i\left(\omega_j - \omega_i\right), \tag{1}$$

$$\textit{For leaders}: \ \textit{Achieving normal frequency}: \quad \boldsymbol{u}_{i,2} = b_i\left(\omega_{ref} - \omega_i\right). \tag{2}$$

where i represents a specific unit, P represents the active power, ω represents the angular frequency, N^c represents the collision neighborhood, N represents the full sensible neighborhood, $\boldsymbol{u}_{1/2}$ is two different parts of the control input vector, a, b, and c are gains. The main advantage of decentralized strategies is that they have fewer oscillations and a faster converging speed during transients. Besides, although they demand a high-bandwidth communication network, the communication topology is flexible, and the communication burden is distributed among agents. However, the control performance of distributed strategies is affected by the number of communication links in the network. As communication becomes fast and stable, distributed strategies become increasingly attractive for implementation.

One common distributed strategy is building an active PI-based consensus searching layer on top of f-P droop control [67–70], which directly implements Reynold’s rule by considering power as the position and frequency as the movement speed. Several units within the grid are configured as leaders, and they always converge to the regular frequency in steady-state, and the rest followers seek to synchronize with the leaders. Although with many positive features, the PI-based consensus searching method is still as demanding as the centralized strategies regarding communication bandwidth, which limits the application range to major equipment. Another strategy for MAS control of grid-following resources is developed based on distributed sub-gradient optimization [79]. The developed strategies normally seek convergence of a specific artificial variable, which can be diverse for different scenarios. For example, the convergence variable in [71] is chosen as the utilization level of specific DG, while in [72] and [73], it becomes the increment rate which is directly proportional to the power level and generation cost. The major advantage of subgradient optimization-based MAS control is that the communication bandwidth is reduced significantly and relatively flexible. In practical applications, the bandwidth should be chosen to balance the communication burden and converging speed.

4. Existing research directions

A summary table of current research development in frequency control based on CHPs and PtH systems is shown in Table 3. From the table, we can first identify that most research focuses on utilizing PtH systems for frequency control. Inside the PtH category, HPs (air-conditioners included) receive the most significant attention from researchers, followed by EBs, while the investigated power range is highly concentrated at the domestic and community levels (with or without aggregation) as expected, considering that the large units are already providing frequency control. As for the CHP category, CCGTs and STs are the main targets. Faster CHP types like AGTs, ICEs, and SCGTs only receive little attention.

Decentralized control strategies currently have the dominating position among all equipment types. The strategies developed for CHP systems are very consistent, and the f-P droop is often implemented in the speed governors by default [80–85]. The majority of research in the CHP category emphasizes the inner-loop power modulation performance of highly inert systems such as CCGTs and STs. An idea of combining micro-turbine and BESS operations for frequency control is proposed in [86], in which the synthetic inertia strategy is used to distribute control signals with different bandwidths among the turbine and BESS. Unlike the CHP category, the research in the PtH category is more about proposing new schemes and feasibility assessments as they are generally not used for frequency control at the moment. It is also noteworthy that thermal comfort is being considered as one of the control design objectives for PtH systems rather than neglected in the CHP category. The adopted strategies are very diverse for PtH

equipment. The majority of papers use traditional rule-based switching, f-P droop, or centralized strategies for frequency control. This is because the equipment controllability (digital or analogy) and the available infrastructures for PtH systems can be very different. The authors in [87] designed the switching signal of domestic water heaters and refrigerators based on frequency disturbance magnitude only, while the disturbance duration factor is included in [88], and the temperature control factor is included in [89–93]. For a large cluster of binary loads, the rule-based strategy is also used to approximate analogy f-P droop control by manipulating the number of activated units [94,95]. Traditional f-P droop is the predominately adopted strategy for equipment with analogy controllability. Authors in [96] investigated the feasibility of f-P droop from the electrical side only, while authors in [97–100] proved that the heat supply of PtH systems would not be interrupted significantly by frequency control. Besides the f-P droop, references [101] and [102] proposed control based on synthetic inertia with a goal to force HPs only to react to high-frequency signals, which can smooth the sharp frequency disturbances and leave a minimum interruption in heat supply. In recent years, more advanced decentralized strategies have been used. In [103], a local multi-objective optimization problem for individual HPs is developed to deal with the trade-off between frequency control performance and thermal comfort. Authors in [104] try to solve the response uncertainty problem and maintain the ideal f-P droop curve through sliding-mode control, where the used model for calculating the sliding variable is trained through online deep learning.

Besides decentralized strategies, centralized strategies are also proposed for PtH equipment, but the number of existing applications is not comparable with decentralized strategies. In [105], the dead band of the f-P droop for HP clusters is tuned on a minute basis at the central controller based on forecasted temperatures from the room model. Reference [106–110] focus on applications within the Pennsylvania-NewJersey-Maryland Interconnection (PJM) [111] and propose to directly use the fast regulation signal (RegD [112]) from the PJM dispatch center to modulate the fan speed of building air-conditioning systems. Authors in [113] try to combine the HP and BESS operations by dividing the RegD signal into low and high-frequency components. Here, the low-frequency control signals are sent to HPs, and high-frequency ones are sent to BESSs, which is similar to the structure documented in [86].

From the implementation perspective, almost all listed papers choose to verify the control performance through simulations, but the tests are implemented with also disparate configurations. For equipment power response modeling, we see the same consistency as the regulation strategy for CHPs: they are generally modeled by a series of component-level lumped linear dynamics, and the model structure is roughly the same. On the other hand, the power response dynamics of PtH systems are often neglected, and many papers modeled them with only static functions. Nevertheless, systems like HPs can have considerable inertia in power response and strongly nonlinear behavior. This reveals a challenge that the currently used models of PtH systems are generally over-simplified. For validating the PFR performance, the majority of papers tend to model a grid environment, either by using standard linear transfer functions to represent the grid inertia between power and frequency, or by modeling a physical multi-bus grid on the chosen simulation platform (with Simulink, PSCAD, Modelica, etc.), while others validate the PFR performance by only showing a fast power-tracking capability. Unlike the PFR capability, thermal comfort is not treated as a common control objective. The most used validation method for thermal comfort is to model an enclosed air or water storage environment with lumped thermal mass systems, and the heat losses are usually calculated through a thermal resistance–capacitance (RC) equivalent model. For both electrical and thermal side performances, only limited papers involved experiments, suggesting a considerable lack of practical validations.

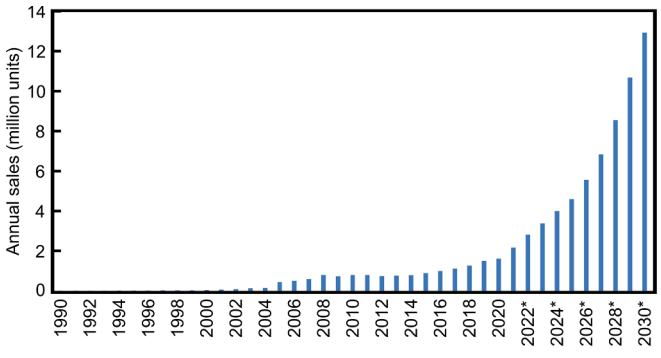

Fig. 3. Annual sales amount of HPs in Europe from 1990 to 2030 (Source: [128]).

Based on our review, we can summarize the current development as follows.

- PtH systems are the key rather than CHPs, and the research is concentrated on developing controls for domestic and community-level equipment.
- Decentralized strategies are in the dominant position, which may be caused by the systems' currently limited communication capability at domestic and community levels.
- A large portion of research on PtH systems treats thermal comfort as a vital control objective, while for CHPs, the interruption in heat supply is rarely analyzed.
- The dynamic modeling of PtH systems is based on a high level of simplification, which overlooks the fact that HPs can be inert and nonlinear.
- Most papers only validate their control strategies through simulations, suggesting a significant lack of experimental verification.

5. Challenges and future development directions

Reviewing the existing research on sector-coupled frequency control system design reveals the limitations of policy-making and control. In this section, we discuss the currently existing challenges for sector-coupled frequency control and what can be done to improve the performance of the service.

5.1. Uncertainties brought by heat pumps

We are currently experiencing a significant shift towards electric HPs in the heat sector [114]. Take Europe as an example, a sharp rising in HP development can be noticed in a rapidly growing market, as shown in Fig. 3, where the annual sales amount is expected to be nearly six times larger in 2030. From the policy perspective, the "REPowerEU" plan launched by the European Union in 2022 aims to increase the installation of HPs to 30 million units by 2030 [115,116]. Across Europe and Asia, the Chinese and German governments signed a Sino-German Energy Partnership and co-drafted a white paper for aligning the HP industrial standards between China and Germany for future close collaborations [117]. In North America, subsidy bills for electric HPs are also proposed in the United States in 2022, which cover both the manufacturers and customers [118]. According to the recent trend, the Heat Roadmap Europe (HRE4) project studied the future of the European heating system and predicted that HPs will dominate the heat sector by a factor of 47.3 % in the year 2050 with an assumption of high renewable penetration, as shown in Fig. 4 [119]. Therefore, HPs will become a major source of flexibility for frequency control in the coming decades. However, the trend of adopting HPs will bring uncertainty problems to the electric sector, especially if our power grids are evolving into microgrids. According to Fig. 5, the most cost-efficient HPs worldwide are air-source HPs, which implies a potential massive installation in the future. In Europe, the statistics have shown that the newly installed HPs

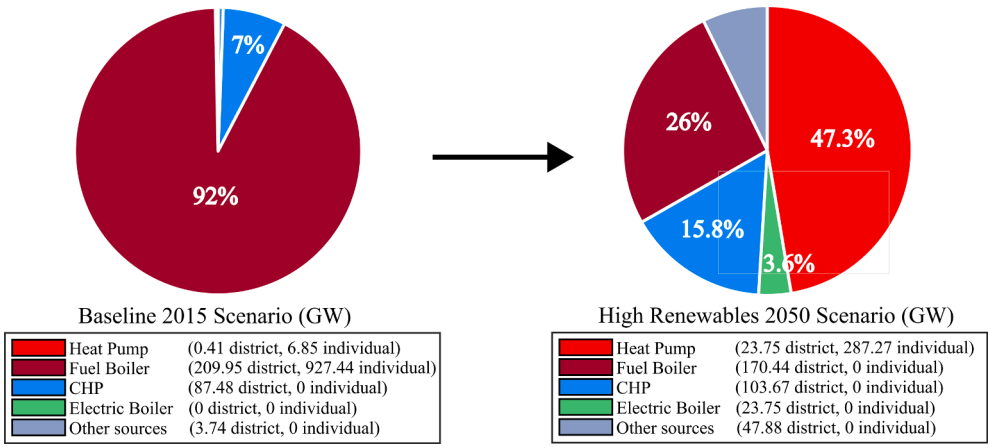

Fig. 4. The share of HP in the heat sector from the "BaseLine2015″ to "High Renewables 2050″ scenario, in GW (Source: [119]).

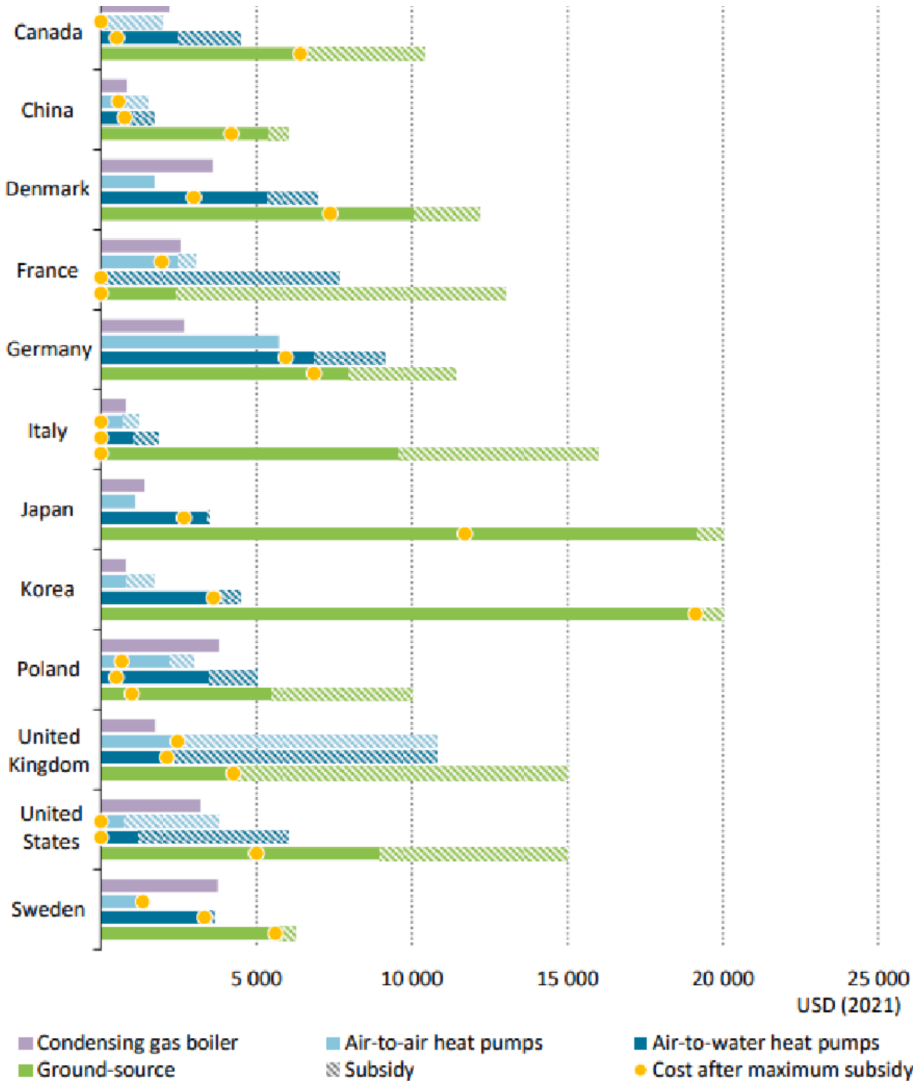

Fig. 5. Equipment and installation cost of the cheapest model of main residential heating technologies in selected countries, 2022. (Source: [116], License: CC BY 4.0).

are already dominated by the air-source type, as shown in Fig. 6. Although with high economic values, air-source HPs are susceptive to work environment changes. The uncertainty in ambient air (source/sink) can cause a shifting thermal equilibrium in the refrigerant loop, eventually leading to a changing dynamic and steady-state behavior. From the perspective of the heat sector, these fluctuations do not significantly impact water temperature because of the inertia in thermal storage and pipelines. Besides, as the settling time of temperature

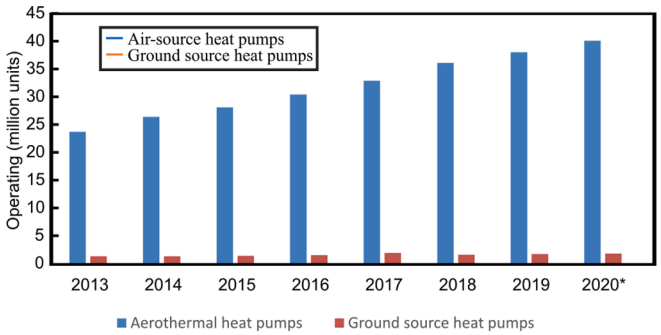

Fig. 6. The number of operating HPs in Europe by type from 2013 to 2020 (Source: [129]).

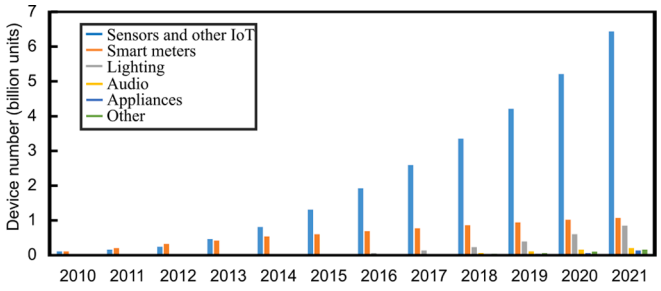

Fig. 7. The global stock of digitally enabled automated devices 2010–2021 (Source: [130], Licence: CC BY 4.0).

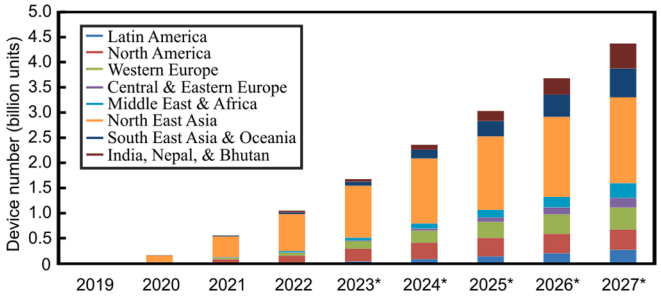

Fig. 8. 5G mobile subscriptions worldwide 2019–2027, by region (Source: [131]).

control is often at least minute-level, there is also little impact on control stability. However, from the microgrid perspective, the grid inertia is almost negligible, and control loops are executed much faster. If we want to use the power flexibility of HPs for frequency control, the control needs to be designed to fulfill the requirements from the electrical side, which means the uncertainty in ambient air can potentially create microgrid voltage fluctuations and even instability. Therefore, there is a motivation to consider the environmental uncertainties during the control design when integrating the domestic and community level-HPs [120]. This can be done either through implementing an advanced control strategy with environmental adaptivity or designing mechanical countermeasures to compensate for the environmental changes.

5.2. Move towards a distributed configuration

As mentioned before, there is a strong trend of adopting HPs in the heat sector. As the heat generation pattern becomes distributed, these HP systems are increasingly installed at domestic and community levels, while the large-scale HP market is much smaller [121]. As the equipment size decreases, the general controllability decreases for cost reduction purposes. On the other hand, the heat grid requires much less controllability if it runs independently from the electrical grid, which is caused by a large amount of thermal inertia within thermal storage and transmission pipelines. These factors reveal that many domestic and community-level PtH systems are under thermostatic control with binary switching, which can be problematic for aiding the frequency control. However, as shown in Fig. 7, we can see a clear trend of the increasing market size of sensors and the internet of things (IoT), which suggests a predictable future increment of controllability for domestic and community PtH systems that leads to the implementation of better algorithms and improved frequency transient dynamics.

As the heat sector has not yet been equipped with high-bandwidth communication capability, the research that focuses on their frequency control functionality is still concentrated on decentralized strategies, leading to limited dynamic performance and non-optimal coordination. The recently introduced fifth-generation communication (5G) technology enables remote control capability in our heat sector. From Fig. 8, we can observe that the implementation scale of 5G will increase by at least four times before 2030. Compared with previous 4G communication, the 5G network allows around 10–100 times faster speed and low latency data transfer [122]. The 5G's Massive Machine Type Communication (mMTC) service is designed for system integration of up to 1 million units per km^2 [123], which is well-suited for interfacing a large number of domestic-level sources into the control network. For community-level and centralized-level PtH systems and CHPs, the Ultra-reliable and Low-latency Communication (uRLLC) service [123], which is designed for industrial remote control and latency-sensitive systems, can be used for building the necessary communication links. These potentials in the energy sector are increasingly being investigated worldwide, resulting in pilot testing and demonstration projects. In Finland, the "Wireless for Verticals" (WIVE) project is launched to test the uRLLC and mMTC services for remote machine control under smart grid scenarios [124]. In the European Union, the "VirtualWind" project is proposed for intra-area and inter-area communication and control of windfarms, where the 5G's Software Defined Networking (SDN) and Network Function Visualization (NFV) ecosystem are used for programmable connectivity, rapid service provisioning, and service channeling [125]. In Asia, the Chinese state grid corporation launched a project to build a Ubiquitous Power IoT (UPIoT) based on 5G to enhance the power grid with state awareness and flexible demand response [126,127].

Suppose all the heat sources have improved controllability and can be integrated into a fast and reliable IoT network, the distributed strategies become the most competitive method for coordinating different participating units because of the improved transient response, reliability, and expandability. On the other hand, distributed strategies offer a platform for a distributed market scheme. Considering the requirement of clearing speed for the intra-day frequency control market and the rise of small-scale equipment, the distributed scheme is more suited than the centralized scheme. In addition, a distributed market will maximize the economic profit of individual participants, which can then attract more equipment owners to participate and thus form a positive synergy.

5.3. Business model

The lack of a suitable business model impedes the implementation of sector-coupled frequency control. As we mentioned earlier, the heat sector is heading towards a distributed grid with the majority of heat sources descending into low and medium power ranges, which means the available power flexibility will be highly scattered. However, no existing market scheme can integrate all these distributed heat sources for frequency control, which means the owners of domestic and community-level PtH systems cannot get either lower electricity tariffs or regulation payments. Therefore, the owners do not have a solid motivation to participate in the frequency control scheme, not to mention that they still have to pay a capital fee for upgrading the control system. Although the global market development of frequency control is

still at an early stage, we can notice a trend of increasing demand and decreasing participation requirements. The European Union, as a global leader in renewable energy development, launched the "frequency containment reserve" (FCR) market in 2007 to improve frequency stabilization [132]. The demand in the FCR market was around 600 MW in 2014, while it has snowballed to around 1400 MW in recent years [132,133]. In the meantime, the minimum bid size was reduced to 1 MW from 5 MW in 2011 [133]. The required supporting duration also decreased to 4 h in 2020 from one month in 2007 [132]. The mentioned data shows that the existing business model can only involve centralized CHPs in large heat plants. In the future, it is crucial that we develop an appropriate business model to attract people to participate in the frequency control. This can be done by further liberating the regulation market to allow more individuals to profit or by providing suitable aggregation plans to allow group participation.

5.4. Application of artificial intelligence (AI)

Target equipment nonlinearity, uncertainty, and unmodeled dynamics are intense challenges in designing the frequency control system. Control systems based on traditional linear methods often require the target equipment to run in a narrow band of operating conditions and may fail if the system states go beyond the designed range. For some large-scale turbine and HP systems, the control system may need to be designed several times to cover all possible operating ranges, which leads to a large amount of modeling work and non-ideal control performance. The AI-based methods can help build an adaptive and optimal control system to handle the mentioned challenges. In the early stage of development in power systems, as the computational power is still limited, AI-based methods such as genetic algorithm (GA) are primarily used for control gain optimization [134–137]. In recent years, because of the exponential growth of computational power and better communication infrastructures, reinforcement learning (RL) has become a promising algorithm in grid-following frequency control [138]. The principle of this method is to mimic the human learning process in frequency control by making and correcting mistakes. The correction is done by constructing a reward quantity based on frequency response dynamic features. In [139], the steady-state frequency deviation, control signal magnitude, and control performance standard are used to formulate the reward, while in [140], a stacked denoising auto-encoder (SDAE) is used to involve more advanced features in building the reword quantity. A two-layer distributed control structure is proposed in [141], where the upper layer is essentially a MAS consensus searching algorithm for generating area control error (ACE) signal, and the lower layer is a gain-scheduling controller based on RL to execute the ACE signal. In this way, minimum frequency deviations and unscheduled power flow between agents can be achieved. Another reference in [142] also adopted a two-layer control structure, where the lower layer is a MAS consensus searching based on the deep neural network (DNN), and the upper layer is a centralized RL for tuning the parameters of all DNNs in the control network. From the identified trend on the electrical side, AI-based methods, especially reinforcement learning, could also be implemented on the heat side systems to improve the performance of traditional distributed frequency control strategies. The learning capability of AI-based methods is a great resource to combat the uncertainties and nonlinearities of heating equipment, which should be verified in the future through equipment-focused studies.

6. Conclusions

Utilizing the flexibilities of the heat sector for frequency control is an essential step toward dynamic sector coupling and multi-energy operation. This paper reviews the current opportunities and progress of sector-coupled frequency control, aiming to provide a general picture of why and how to design a frequency control system for CHP and PtH systems. The power flexibility of this equipment is thoroughly analyzed based on a list of key performance indicators such as magnitude, response speed, and costs. The mainstream control strategies and existing practices of frequency control based on CHPs and PtH systems are also reviewed and summarized. Finally, possible future directions on sector-coupled frequency control are provided. It is shown that now the biggest obstacle to implementing sector-coupled frequency control is the lack of controllability and business model, as the future frequency control market will be dominated by domestic and community-level PtH systems, especially HPs. With the increasing adoption of advanced communication technologies, the future frequency control and market structures in the heat sector will gradually shift from decentralized to distributed MAS configuration. Besides, we also identify a trend of AI penetration in frequency control strategies for environment awareness, self-perception, and optimal decision-making. These characteristics are becoming increasingly valuable in the heat sector as the uncertainty level continues to rise.

Declaration of Competing Interest

The authors declare that they have no known competing financial interests or personal relationships that could have appeared to influence the work reported in this paper.

Data availability

No data was used for the research described in the article.

Acknowledgments

The work of Mr. Ruihao Song was supported by the Bavarian Research Foundation of Germany through the project "Sector coupling und Microgrids (STROM)" under project number AZ-1473-20. The work of Dr. Vedran S. Perić was supported by the Deutsche Forschungsgemeinschaft (DFG) of Germany through the project "Optimal Operation of Integrated Low-Temperature Bidirectional Heat and Electric Grids (IntElHeat)" under project number 450821044.

References

[1] Eurostat, "Renewable energy statistics in EU." [Online]. Available: https://ec.europa.eu/eurostat/statistics-explained/index.php?title=Renewable_energy_statistics.
[2] Wikipedia, "Renewable Energy in China." [Online]. Available: https://en.wikipedia.org/wiki/Renewable_energy_in_China.
[3] U.S. Energy Information Administration, "US renewable energy sources." [Online]. Available: https://www.eia.gov/tools/faqs/faq.php?id=92&t=4#:~:text=In 2020%2C renewable energy sources,about 19.8%25 of electricity generation.
[4] Kroposki B, Lasseter R, Ise T, Morozumi S, Papathanassiou S, Hatziargyriou N. Making microgrids work. IEEE Power Energy Mag 2008;6(3):40–53. https://doi.org/10.1109/MPE.2008.918718.
[5] Hatziargyriou N. microgrids [guest editorial]. IEEE Power Energy Mag 2008;6(3):26–9. https://doi.org/10.1109/MPE.2008.920383.
[6] Bloomberg, "Lithium-ion Battery costs and market." [Online]. Available: https://data.bloomberglp.com/bnef/sites/14/2017/07/BNEF-Lithium-ion-battery-costs-and-market.pdf.
[7] Wikipedia, "District heating." [Online]. Available: https://en.wikipedia.org/wiki/District_heating#Third_Generation.
[8] Lund H, Werner S, Wiltshire R, Svendsen S, Thorsen JE, Hvelplund F, et al. 4th generation district heating (4GDH): integrating smart thermal grids into future sustainable energy systems. Energy 2014;68:1–11. https://doi.org/10.1016/j.energy.2014.02.089.
[9] Buffa S, Cozzini M, D'Antoni M, Baratieri M, Fedrizzi R. 5th generation district heating and cooling systems: A review of existing cases in Europe. Renew Sustain Energy Rev 2019;104:504–22. https://doi.org/10.1016/j.rser.2018.12.059.
[10] Wirtz M, Kivilip L, Remmen P, Müller D. 5th generation district heating: a novel design approach based on mathematical optimization. Appl Energy 2020;260:114158. https://doi.org/10.1016/j.apenergy.2019.114158.
[11] Lund H, Østergaard PA, Nielsen TB, Werner S, Thorsen JE, Gudmundsson O, et al. Perspectives on fourth and fifth generation district heating. Energy 2021;227:120520. https://doi.org/10.1016/j.energy.2021.120520.
[12] Tan J, Wu Q, Zhang M. Strategic investment for district heating systems participating in energy and reserve markets using heat flexibility. Int J Electr

Power Energy Syst 2022;137:107819. https://doi.org/10.1016/j.ijepes.2021.107819.
[13] Bayern ZAE. Storage technology issues and opportunities. [Online]. Available: https://docplayer.net/24183430-Storage-technology-issues-and-opportunities.html.
[14] Eurostat, "Energy consumption in households." [Online]. Available: https://ec.europa.eu/eurostat/statistics-explained/index.php?title=Energy_consumption_in_households.
[15] Gu W, Wu Z, Bo R, Liu W, Zhou G, Chen Wu, et al. Modeling, planning and optimal energy management of combined cooling, heating and power microgrid: A review. Int J Electr Power Energy Syst 2014;54:26–37. https://doi.org/10.1016/j.ijepes.2013.06.028.
[16] Wang J, You S, Zong Y, Træholt C, Dong ZY, Zhou Y. Flexibility of combined heat and power plants: A review of technologies and operation strategies. Appl Energy 2019;252:113445. https://doi.org/10.1016/j.apenergy.2019.113445.
[17] Gu W, Wang J, Lu S, Luo Z, Wu C. Optimal operation for integrated energy system considering thermal inertia of district heating network and buildings. Appl Energy 2017;199:234–46. https://doi.org/10.1016/j.apenergy.2017.05.004.
[18] Li Z, Xu Y, Feng X, Wu Q. Optimal stochastic deployment of heterogeneous energy storage in a residential multienergy microgrid with demand-side management. IEEE Trans Ind Informatics 2021;17(2):991–1004. https://doi.org/10.1109/TII.2020.2971227.
[19] Li Z, Wu L, Xu Y. Risk-averse coordinated operation of a multi-energy microgrid considering voltage/Var control and thermal flow: an adaptive stochastic approach. IEEE Trans Smart Grid 2021;12(5):3914–27. https://doi.org/10.1109/TSG.2021.3080312.
[20] Li Z, Wu L, Xu Y, Moazeni S, Tang Z. Multi-stage real-time operation of a multi-energy microgrid with electrical and thermal energy storage assets: a data-driven MPC-ADP approach. IEEE Trans Smart Grid 2022;13(1):213–26. https://doi.org/10.1109/TSG.2021.3119972.
[21] Chen Y, Xu Y, Li Z, Feng X. Optimally coordinated dispatch of combined-heat-and-electrical network with demand response. IET Gener Transm Distrib 2019;13(11):2257–67. https://doi.org/10.1049/iet-gtd.2018.6992.
[22] Wang J, Zhang C, You S, Zong Yi, Træholt C, Dong ZY. Multi-timescale coordinated operation of a CHP plant-wind farm portfolio considering multiple uncertainties. Int J Electr Power Energy Syst 2021;125:106428. https://doi.org/10.1016/j.ijepes.2020.106428.
[23] Beck T, Kondziella H, Huard G, Bruckner T. Optimal operation, configuration and sizing of generation and storage technologies for residential heat pump systems in the spotlight of self-consumption of photovoltaic electricity. Appl Energy 2017;188:604–19. https://doi.org/10.1016/j.apenergy.2016.12.041.
[24] Zhang C, Xu Y, Li Z, Dong ZY. Robustly coordinated operation of a multi-energy microgrid with flexible electric and thermal loads. IEEE Trans Smart Grid 2019;10(3):2765–75. https://doi.org/10.1109/TSG.2018.2810247.
[25] Li Z, Xu Y, Wu L, Zheng X. A risk-averse adaptively stochastic optimization method for multi-energy ship operation under diverse uncertainties. IEEE Trans Power Syst 2021;36(3):2149–61. https://doi.org/10.1109/TPWRS.2020.3039538.
[26] Li Z, Xu Y, Fang S, Zheng X, Feng X. Robust coordination of a hybrid AC/DC multi-energy ship microgrid with flexible voyage and thermal loads. IEEE Trans Smart Grid 2020;11(4):2782–93. https://doi.org/10.1109/TSG.2020.2964831.
[27] Li Z, Xu Y. Optimal coordinated energy dispatch of a multi-energy microgrid in grid-connected and islanded modes. Appl Energy 2018;210:974–86. https://doi.org/10.1016/j.apenergy.2017.08.197.
[28] Li Z, Wu L, Xu Y, Zheng X. Stochastic-weighted robust optimization based bilayer operation of a multi-energy building microgrid considering practical thermal loads and battery degradation. IEEE Trans Sustain Energy 2022;13(2):668–82. https://doi.org/10.1109/TSTE.2021.3126776.
[29] Wang J, You S, Zong Yi, Cai H, Træholt C, Dong ZY. Investigation of real-time flexibility of combined heat and power plants in district heating applications. Appl Energy 2019;237:196–209. https://doi.org/10.1016/j.apenergy.2019.01.017.
[30] Song R, Hamacher T, Perić VS. Impact of hydraulic faults on the electric system in an integrated multi-energy microgrid. The 9th Workshop on Modeling and Simulation of Cyber-Physical Energy Systems, 2021, p. 1–6, doi: 10.1145/3470481.3472709.
[31] ENTSO-EU, "Load-frequency control & reserves." [Online]. Available: https://eepublicdownloads.entsoe.eu/clean-documents/pre2015/publications/ce/oh/Policy1_final.pdf.
[32] Dvorkin Y, Kirschen DS, Ortega-Vazquez MA. Assessing flexibility requirements in power systems. IET Gener Transm Distrib 2014;8(11):1820–30. https://doi.org/10.1049/iet-gtd.2013.0720.
[33] California ISO, "Variable operations and maintenance cost." [Online]. Available: http://www.caiso.com/documents/variableoperationsandmaintenancecostreport-dec212018.pdf.
[34] Heat Roadmap Europe, "EU28 fuel prices for 2015, 2030, and 2050." [Online]. Available: https://heatroadmap.eu/wp-content/uploads/2020/01/HRE4_D6.1-Future-fuel-price-review.pdf.
[35] Hidalgo Rodriguez DI, Spitalny L, Myrzik J. Development of a control strategy for mini CHP plants for an active voltage management in low voltage networks. 2012 3rd IEEE PES Innovative Smart Grid Technologies Europe (ISGT. Europe) 2012:1–8. https://doi.org/10.1109/ISGTEurope.2012.6465797.
[36] Petkovic D, Banjac M, Milic S, Petrovic MV, Wiedermann A. Modeling the transient behavior of gas turbines. J Turbomach 2020;142(8). https://doi.org/10.1115/1.4046451.
[37] Magnitude, "Technology and case studies factsheets." [Online]. Available: https://www.magnitude-project.eu/wp-content/uploads/2019/07/MAGNITUDE_D1.2_EIFER_Final_Submitted.pdf.
[38] Siemens Energy, "Large-scale industrial heat pumps." [Online]. Available: https://www.siemens-energy.com/global/en/offerings/power-generation/heat-pumps.html.
[39] Rasmussen BP, Alleyne AG. Control-oriented modeling of transcritical vapor compression systems. J Dyn Syst Meas Control 2004;126(1):54–64. https://doi.org/10.1115/1.1648312.
[40] Agora, "Flexibility in thermal power plants." [Online]. Available: https://www.agora-energiewende.de/fileadmin/Projekte/2017/Flexibility_in_thermal_plants/115_flexibility-report-WEB.pdf.
[41] Grigg C, Wong P, Albrecht P, Allan R, Bhavaraju M, Billinton R, et al. The IEEE reliability test system-1996: a report prepared by the reliability test system task force of the application of probability methods subcommittee. IEEE Trans Power Syst 1999;14(3):1010–20. https://doi.org/10.1109/59.780914.
[42] IEA Clean Coal Centre, "Increasing the flexibility of coal-fired power plant." [Online]. Available: https://usea.org/sites/default/files/092014_Increasing the flexibility of coal-fired power plants_ccc242.pdf.
[43] Siemens, "Flexibility Solutions." [Online]. Available: https://assets.siemens-energy.com/siemens/assets/api/uuid:5ca0af69-e3f8-4eb3-9e60-fe6e0cec2357/addedvalue-flexibility-final.pdf.
[44] GE Gas Power, "LM6000 Aeroderivative Gas Turbine." [Online]. Available: https://www.ge.com/content/dam/gepower-new/global/en_US/downloads/gas-new-site/products/gas-turbines/lm6000-fact-sheet-product-specifications.pdf.
[45] Advantages of aero-derivative gas turbines in industrial applications: technical, operational and financial considerations on equipment selection. 20th Symp. Ind. Appl. Gas Turbines Comm. 2013:1–15.
[46] Danish Energy Agency, "Technology data - generation of electricity and district heating." [Online]. Available: https://ens.dk/en/our-services/projections-and-models/technology-data/technology-data-generation-electricity-and.
[47] M. Wideskog and N. Wägar, "Operational flexibility with Wärtsilä 50SG," 2014, [Online]. Available: https://www.wartsila.com/docs/default-source/smartpowergeneration/content-center/conference-papers/operational_flexibility_with_wartsila_50sg.pdf.
[48] Wang J, Cai H, You S, Zong Y, Zhang C, Træholt C. A framework for techno-economic assessment of demand-side power-to-heat solutions in low-temperature district heating. Int J Electr Power Energy Syst 2020;122:106096. https://doi.org/10.1016/j.ijepes.2020.106096.
[49] De Brabandere K, et al. A voltage and frequency droop control method for parallel inverters. 2004 IEEE 35th Annual Power Electronics Specialists Conference, 2004, p. 2501–2507, doi: 10.1109/PESC.2004.1355222.
[50] Vidyanandan KV, Senroy N. Primary frequency regulation by deloaded wind turbines using variable droop. IEEE Trans Power Syst 2013;28(2):837–46. https://doi.org/10.1109/TPWRS.2012.2208233.
[51] Schweppe F, Tabors R, Kirtley J, Outhred H, Pickel F, Cox A. Homeostatic utility control. IEEE Trans on Power Apparatus and Syst 1980;99(3):1151–63. https://doi.org/10.1109/TPAS.1980.319745.
[52] Aunedi M, Kountouriotis P-A, Calderon JEO, Angeli D, Strbac G. Economic and environmental benefits of dynamic demand in providing frequency regulation. IEEE Trans Smart Grid 2013;4(4):2036–48. https://doi.org/10.1109/TSG.2013.2258047.
[53] Chassin DP, Donnelly MK, Dagle JE. Electrical power distribution control methods, electrical energy demand monitoring methods, and power management devices. US7149605B2. 2006.
[54] Kakimoto N, Takayama S, Satoh H, Nakamura K. Power modulation of photovoltaic generator for frequency control of power system. IEEE Trans Energy Convers 2009;24(4):943–9. https://doi.org/10.1109/TEC.2009.2026616.
[55] Yao W, Lee KY. A control configuration of wind farm for load-following and frequency support by considering the inertia issue. 2011 IEEE Power and Energy Society General Meeting. 2011. p. 1–6. doi: 10.1109/PES.2011.6039511.
[56] Josephine RL, Suja S. Estimating PMSG wind turbines by inertia and droop control schemes with intelligent fuzzy controller in Indian development. J Electr Eng Technol 2014;9(4):1196–201. https://doi.org/10.5370/JEET.2014.9.4.1196.
[57] Mishra S, Zarina PP, Sekhar PC. A novel controller for frequency regulation in a hybrid system with high PV penetration. 2013 IEEE Power and Energy Society General Meeting. 2013:1–5. https://doi.org/10.1109/PESMG.2013.6672143.
[58] Canevese S, Iaria A, Rapizza M. Impact of fast primary regulation and synthetic inertia on grid frequency control. 2017 IEEE PES Innovative Smart Grid Technologies. Conference Europe. 2017:1–6. https://doi.org/10.1109/ISGTEurope.2017.8260147.
[59] Guggilam SS, Zhao C, Dall'Anese E, Chen YC, Dhople SV. Optimizing DER participation in inertial and primary-frequency response. IEEE Trans Power Syst 2018;33(5):5194–205. https://doi.org/10.1109/TPWRS.2018.2798540.
[60] Morren J, Pierik J, de Haan SWH. Inertial response of variable speed wind turbines. Electr Power Syst Res 2006;76(11):980–7. https://doi.org/10.1016/j.epsr.2005.12.002.
[61] Heins T, Joševski M, Karthik Gurumurthy S, Monti A. Centralized model predictive control for transient frequency control in islanded inverter-based microgrids. IEEE Trans Power Syst 2023;38(3):2641–52. https://doi.org/10.1109/TPWRS.2022.3189958.
[62] Gil NJ, Lopes JAP. Hierarchical frequency control scheme for islanded multi-microgrids operation. 2007 IEEE Lausanne Power Tech 2007:473–8. https://doi.org/10.1109/PCT.2007.4538363.

[63] Guerrero JM, Vasquez JC, Matas J, De Vicuña LG, Castilla M. Hierarchical control of droop-controlled AC and DC microgrids - a general approach toward standardization. IEEE Trans Ind Electron 2011;58(1):158–72. https://doi.org/10.1109/TIE.2010.2066534.
[64] Savaghebi M, Jalilian A, Vasquez JC, Guerrero JM. Secondary control scheme for voltage unbalance compensation in an islanded droop-controlled microgrid. IEEE Trans Smart Grid 2012;3(2):797–807. https://doi.org/10.1109/TSG.2011.2181432.
[65] Guan Y, Vasquez JC, Guerrero JM. Coordinated secondary control for balanced discharge rate of energy storage system in islanded AC microgrids. IEEE Trans Ind Appl 2016;52(6):5019–28. https://doi.org/10.1109/TIA.2016.2598724.
[66] Daraz A, Malik SA, Azar AT, Aslam S, Alkhalifah T, Alturise F. Optimized fractional order integral-tilt derivative controller for frequency regulation of interconnected diverse renewable energy resources. IEEE Access 2022;10:43514–27. https://doi.org/10.1109/ACCESS.2022.3167811.
[67] Simpson-Porco JW, Dörfler F, Bullo F. Synchronization and power sharing for droop-controlled inverters in islanded microgrids. Automatica 2013;49(9):2603–11. https://doi.org/10.1016/j.automatica.2013.05.018.
[68] Bidram A, Lewis FL, Davoudi A, Qu Z. Frequency control of electric power microgrids using distributed cooperative control of multi-agent systems. 2013 IEEE International Conference on Cyber Technology in Automation Control and Intelligent Systems. 2013:223–8. https://doi.org/10.1109/CYBER.2013.6705449.
[69] Liu W, Gu W, Sheng W, Meng X, Wu Z, Chen W. Decentralized multi-agent system-based cooperative frequency control for autonomous microgrids with communication constraints. IEEE Trans Sustain Energy 2014;5(2):446–56. https://doi.org/10.1109/TSTE.2013.2293148.
[70] Zhang N, Sun Q, Wang J, Yang L. Distributed adaptive dual control via consensus algorithm in the energy internet. IEEE Trans Ind Informatics 2021;17(7):4848–60. https://doi.org/10.1109/TII.2020.3031437.
[71] Xu Y, Zhang W, Liu W, Wang X, Ferrese F, Zang C, et al. Distributed subgradient-based coordination of multiple renewable generators in a microgrid. IEEE Trans Power Syst 2014;29(1):23–33. https://doi.org/10.1109/TPWRS.2013.2281038.
[72] Wang Z, Wu W, Zhang B. A fully distributed power dispatch method for fast frequency recovery and minimal generation cost in autonomous microgrids. IEEE Trans Smart Grid 2016;7(1):19–31. https://doi.org/10.1109/TSG.2015.2493638.
[73] Yang Y, Lu Q, Wu S, Wang Z, Xia T. Coordinated primary frequency control for virtual power plant based on distributed subgradient-projection method. 2019 IEEE Innovative Smart Grid Technologies - Asia. 2019:1638–43. https://doi.org/10.1109/ISGT-Asia.2019.8881674.
[74] Duan S, Meng Y, Xiong J, Kang Y, Chen J. Parallel operation control technique of voltage source inverters in UPS. IEEE 1999 International Conference on Power Electronics and Drive Systems. 1999. p. 883–887. doi: 10.1109/PEDS.1999.792823.
[75] Rokrok E, Shafie-khah M, Catalão JPS. Review of primary voltage and frequency control methods for inverter-based islanded microgrids with distributed generation. Renew Sustain Energy Rev 2018;82:3225–35. https://doi.org/10.1016/j.rser.2017.10.022.
[77] Reynolds CW. Flocks, herds and schools: A distributed behavioral model. The 14th annual conference on Computer graphics and interactive techniques. 1987. p. 25–34. doi: 10.1145/37401.37406.
[78] Lewis F, Zhang H, Hengster-Movric K, Das A. Cooperative control of multi-agent systems: optimal and adaptive design approaches. Springer; 2014.
[79] Nedic A, Ozdaglar A. Distributed subgradient methods for multi-agent optimization. IEEE Trans Automat Contr 2009;54(1):48–61. https://doi.org/10.1109/TAC.2008.2009515.
[80] Lalor G, Ritchie J, Flynn D, O'Malley MJ. The impact of combined-cycle gas turbine short-term dynamics on frequency control. IEEE Trans Power Syst 2005;20(3):1456–64. https://doi.org/10.1109/TPWRS.2005.852058.
[81] Saikia LC, Sahu SK. Automatic generation control of a combined cycle gas turbine plant with classical controllers using Firefly Algorithm. Int J Electr Power Energy Syst 2013;53(1):27–33. https://doi.org/10.1016/j.ijepes.2013.04.007.
[82] Saha D, Bora P, Sarmah U. Modeling of air and fuel combustion as emission in solving AGC problem of an isolated CCGT plant." 2020 International Conference on Computational Performance Evaluation. 2020. p. 719–24. https://doi.org/10.1109/ComPE49325.2020.9200069.
[83] Wang Y, Li H, Xu Y, Tang Y. System frequency regulation in Singapore using distributed energy storage systems. 2017 Asian Conference on Energy Power and Transportation Electrification. 2017:1–6. https://doi.org/10.1109/ACEPT.2017.8168561.
[84] Bian Y, Wang H, Wyman-Pain H, Gu C, Li F. Frequency response in the GB power system from responsive CHPs. Energy Procedia 2017;105:2302–9. https://doi.org/10.1016/j.egypro.2017.03.664.
[85] Liu Z, Zheng Z, Song J, Wang C. Primary frequency regulation capacity enhancement of CHP units: control strategy combining high pressure valve adjustment and heating extraction steam adjustment. Case Stud Therm Eng 2022;35:102097. https://doi.org/10.1016/j.csite.2022.102097.
[86] Xu X, Ming W, Zhou Y, Wu J. Unlock the flexibility of combined heat and power for frequency response by coordinative control with batteries. IEEE Trans Ind Informatics 2021;17(5):3209–19. https://doi.org/10.1109/TII.2020.3012495.
[87] Samarakoon K, Ekanayake J, Jenkins N. Investigation of domestic load control to provide primary frequency response using smart meters. IEEE Trans Smart Grid 2012;3(1):282–92. https://doi.org/10.1109/TSG.2011.2173219.
[88] Molina-Garcia A, Bouffard F, Kirschen DS. Decentralized demand-side contribution to primary frequency control. IEEE Trans Power Syst 2011;26(1):411–9. https://doi.org/10.1109/TPWRS.2010.2048223.
[89] Meesenburg W, Ommen T, Elmegaard B. Dynamic exergoeconomic analysis of a heat pump system used for ancillary services in an integrated energy system. Energy 2018;152:154–65. https://doi.org/10.1016/j.energy.2018.03.093.
[90] Short JA, Infield DG, Freris LL. Stabilization of grid frequency through dynamic demand control. IEEE Trans Power Syst 2007;22(3):1284–93. https://doi.org/10.1109/TPWRS.2007.901489.
[91] Cheng M, Wu J, Galsworthy SJ, Ugalde-Loo CE, Gargov N, Hung WW, et al. Power system frequency response from the control of bitumen tanks. IEEE Trans Power Syst 2016;31(3):1769–78. https://doi.org/10.1109/TPWRS.2015.2440336.
[92] Obaid ZA, Cipcigan LM, Muhssin MT, Sami SS. Development of a water heater population control for the demand-side frequency control. 2017 IEEE PES Innovative Smart Grid Technologies Conference Europe. 2017:1–6. https://doi.org/10.1109/ISGTEurope.2017.8260113.
[93] Muhssin MT, Cipcigan LM, Jenkins N, Slater S, Cheng M, Obaid ZA. Dynamic frequency response from controlled domestic heat pumps. IEEE Trans Power Syst 2018;33(5):4948–57. https://doi.org/10.1109/TPWRS.2017.2789205.
[94] Zhou Y, Cheng M, Wu J, Long C. Decentralized control of industrial heating loads for providing multiple levels and types of primary frequency control service. Energy Procedia 2019;158:3138–43. https://doi.org/10.1016/j.egypro.2019.01.1015.
[95] Shen Y, Li Y, Zhang Q, Shi Q, Li F. State-shift priority based progressive load control of residential HVAC units for frequency regulation. Electr Power Syst Res 2020;182:106194. https://doi.org/10.1016/j.epsr.2020.106194.
[96] Melo SP, Brand U, Vogt T, Telle JS, Schuldt F. Maydell K.v. Primary frequency control provided by hybrid battery storage and power-to-heat system. Appl Energy 2019;233:220–31. https://doi.org/10.1016/j.apenergy.2018.09.177.
[97] Mendieta W, Canizares CA. Primary frequency control in isolated microgrids using thermostatically controllable loads. IEEE Trans Smart Grid 2021;12(1):93–105. https://doi.org/10.1109/TSG.2020.3012549.
[98] Shi Q, Li F, Liu G, Shi D, Yi Z, Wang Z. Thermostatic load control for system frequency regulation considering daily demand profile and progressive recovery. IEEE Trans Smart Grid 2019;10(6):6259–70. https://doi.org/10.1109/TSG.2019.2900724.
[99] Angenendt G, Zurmühlen S, Figgener J, Kairies K-P, Sauer DU. Providing frequency control reserve with photovoltaic battery energy storage systems and power-to-heat coupling. Energy 2020;194:116923. https://doi.org/10.1016/j.energy.2020.116923.
[100] Meesenburg W, Thingvad A, Elmegaard B, Marinelli M. Combined provision of primary frequency regulation from Vehicle-to-Grid (V2G) capable electric vehicles and community-scale heat pump. Sustain Energy, Grids Networks 2020;23:100382. https://doi.org/10.1016/j.segan.2020.100382.
[101] Crosa di Vergagni M, Conte F. Frequency support by distributed demand side management of building cooling systems. 2015 5th International Youth. Conference on Energy. 2015:1–5. https://doi.org/10.1109/IYCE.2015.7180742.
[102] Harild Rasmussen TB, Wu Q, Zhang M. Primary frequency support from local control of large-scale heat pumps. Int J Electr Power Energy Syst 2021;133:107270. https://doi.org/10.1016/j.ijepes.2021.107270.
[103] Zhang Di, Li C, Luo S, Luo D, Shahidehpour M, Chen C, et al. Multi-objective control of residential HVAC loads for balancing the user's comfort with the frequency regulation performance. IEEE Trans Smart Grid 2022;13(5):3546–57. https://doi.org/10.1109/TSG.2022.3171847.
[104] Xu Y, Member S, Yao L, Member S, Liao S, Li Y. Optimal frequency regulation based on characterizing the air conditioning cluster by online deep learning. CSEE J Power Energy Syst 2021; 8(5): 1373-1387. https://doi.org/10.17775/CSEEJPES.2020.05940.
[105] Wu X, He J, Xu Y, Lu J, Lu N, Wang X. Hierarchical control of residential HVAC units for primary frequency regulation. IEEE Trans Smart Grid 2018;9(4):3844–56. https://doi.org/10.1109/TSG.2017.2766880.
[106] Kim Y-J, Norford LK, Kirtley JL. Modeling and analysis of a variable speed heat pump for frequency regulation through direct load control. IEEE Trans Power Syst 2015;30(1):397–408. https://doi.org/10.1109/TPWRS.2014.2319310.
[107] Kim Y-J, Fuentes E, Norford LK. Experimental study of grid frequency regulation ancillary service of a variable speed heat pump. IEEE Trans Power Syst 2016;31(4):3090–9. https://doi.org/10.1109/TPWRS.2015.2472497.
[108] Zhao P, Henze GP, Plamp S, Cushing VJ. Evaluation of commercial building HVAC systems as frequency regulation providers. Energy Build 2013;67:225–35. https://doi.org/10.1016/j.enbuild.2013.08.031.
[109] Lin Y, Barooah P, Meyn S, Middelkoop T. Experimental evaluation of frequency regulation from commercial building HVAC systems. IEEE Trans Smart Grid 2015;6(2):776–83. https://doi.org/10.1109/TSG.2014.2381596.
[110] Beil I, Hiskens I, Backhaus S. Frequency regulation from commercial building HVAC demand response. Proc IEEE 2016;104(4):745–57. https://doi.org/10.1109/JPROC.2016.2520640.
[111] Wikipedia, "PJM interconnection." [Online]. Available: https://en.wikipedia.org/wiki/PJM_Interconnection.
[112] PJM State and Member Training Department, "PJM regulation market." [Online]. Available: https://www.pjm.com/-/media/training/nerc-certifications/markets-exam-materials/generation-itp/regulation-testing.ashx.
[113] Kim Y-J, Wang J. Power hardware-in-the-loop simulation study on frequency regulation through direct load control of thermal and electrical energy storage resources. IEEE Trans Smart Grid 2018;9(4):2786–96. https://doi.org/10.1109/TSG.2016.2620176.
[114] Rosenow J, Gibb D, Nowak T, Lowes R. Heating up the global heat pump market. Nat Energy 2022:10–3. https://doi.org/10.1038/s41560-022-01104-8.
[115] European Union, "REPowerEU." [Online]. Available: https://ec.europa.eu/commission/presscorner/detail/en/ip_22_3131.

[116] International Energy Agency, "The future of heat pumps," [Online]. Available: https://iea.blob.core.windows.net/assets/01324438-d634-4d49-95d8-3d08aaab00d5/TheFutureofHeatPumps.pdf.
[117] Energiepartnerschaft, "Promoting the application of heat pumps in China to contribute to energy decarbonization." [Online]. Available: https://www.energypartnership.cn/home/events/promoting-the-application-of-heat-pumps-in-china-to-contr/.
[118] U.S. Congress, "S.4139 - HEATR act." [Online]. Available: https://www.congress.gov/bill/117th-congress/senate-bill/4139/text?r=1&s=1.
[119] Paardekooper S, et al. Heat roadmap europe 4: quantifying the impact of low-carbon heating and cooling roadmaps. Aalborg Univ; 2018.
[120] Song R, Hamacher T, Perić V. Integrated battery and heat pump system for decentralized primary frequency control in low-inertia microgrids. TechRxiv 2022. https://doi.org/10.36227/techrxiv.21707870.v1.
[121] EurObservER, "Heat pumps barometer 2020." [Online]. Available: https://www.isi.fraunhofer.de/content/dam/isi/dokumente/ccx/2020/EurObservER-Heat-Pumps-Barometer-2020-en.pdf.
[122] Panwar N, Sharma S, Singh AK. A survey on 5G: the next generation of mobile communication. Phys Commun 2016;18:64–84. https://doi.org/10.1016/j.phycom.2015.10.006.
[123] HUAWEI Technologies, "5G network architecture." [Online]. Available: https://www-file.huawei.com/-/media/corporate/pdf/mbb/5g_nework_architecture_whitepaper_en.pdf?la=en.
[124] Engerati, "WIVE project uses 5G to increase the business value of smart grids." [Online]. Available: https://www.engerati.com/energy-retail/wive-project-uses-5g-to-increase-the-business-value-of-smart-grids/.
[125] European Union, "VirtualWind." [Online]. Available: http://www.virtuwind.eu/.
[126] Jiang A, Yuan H, Li D, Tian J. Key technologies of ubiquitous power internet of things-aided smart grid. J Renew Sustain Energy 2019;11(6):062702. https://doi.org/10.1063/1.5121856.
[127] Nokia, "Nokia optical transport selected by state grid corporation of China, bringing massive scale, security and agility to nation's power grid." [Online]. Available: https://www.nokia.com/about-us/news/releases/2022/10/26/nokia-optical-transport-selected-by-state-grid-corporation-of-china-bringing-massive-scale-security-and-agility-to-nations-power-grid/.
[128] European Heat Pump Association, "Annual sales of heat pumps in Europe from 1990 to 2020, with forecasts until 2030 (in 1,000s) [Graph]," [Online]. Available: https://www.statista.com/statistics/1191798/heat-pump-sales-europe/.
[129] EurObserv'ER, "Annual amount of heat pumps in operation in the European Union (EU) from 2013 to 2020 (in millions) [Graph]," [Online]. Available: https://www.statista.com/statistics/739745/heat-pumps-in-operation-eu/.
[130] International Energy Agency, "Global stock of digitally enabled automated devices." [Online]. Available: https://www.iea.org/data-and-statistics/charts/global-stock-of-digitally-enabled-automated-devices-2010-2021.
[131] Ericsson, "Forecast number of mobile 5G subscriptions worldwide by region from 2019 to 2027 [Graph]." [Online]. Available: https://www.statista.com/statistics/521598/5g-mobile-subscriptions-worldwide/.
[132] Regelleistung.Net. "Frequency containment reserve" [Online]. Available: https://www.regelleistung.net.
[133] Schreider A, Bucher R. An auspicious combination: fast-ramping battery energy storage and high-capacity pumped hydro. Energy Procedia 2018;155:156–64. https://doi.org/10.1016/j.egypro.2018.11.059.
[134] Chang CS, Fu W, Wen F. Load frequency control using genetic-algorithm based fuzzy gain scheduling of PI controllers. Electr Mach Power Syst 1998;26(1):39–52. https://doi.org/10.1080/07313569808955806.
[135] Talaq J, Al-Basri F. Adaptive fuzzy gain scheduling for load frequency control. IEEE Trans Power Syst 1999;14(1):145–50. https://doi.org/10.1109/59.744505.
[136] Chang-Chien L-R, Wu Y-S, Cheng J-S. Online estimation of system parameters for artificial intelligence applications to load frequency control. IET Gener Transm Distrib 2011;5(8):895. https://doi.org/10.1049/iet-gtd.2010.0654.
[137] Omar M, Soliman M, Ghany AMA, Bendary F. Optimal tuning of PID controllers for hydrothermal load frequency control using ant colony optimization. Int J Electr Eng Informatics 2013;5(3):348–60. https://doi.org/10.15676/ijeei.2013.5.3.8.
[138] Zhang Yi, Shi X, Zhang H, Cao Y, Terzija V. Review on deep learning applications in frequency analysis and control of modern power system. Int J Electr Power Energy Syst 2022;136:107744. https://doi.org/10.1016/j.ijepes.2021.107744.
[139] Yin L, Yu T, Zhou L, Huang L, Zhang X, Zheng B. Artificial emotional reinforcement learning for automatic generation control of large-scale interconnected power grids. IET Gener Transm Distrib 2017;11(9):2305–13. https://doi.org/10.1049/iet-gtd.2016.1734.
[140] Yan Z, Xu Y. Data-driven load frequency control for stochastic power systems: a deep reinforcement learning method with continuous action search. IEEE Trans Power Syst 2019;34(2):1653–6. https://doi.org/10.1109/TPWRS.2018.2881359.
[141] Singh VP, Kishor N, Samuel P. Distributed multi-agent system-based load frequency control for multi-area power system in smart grid. IEEE Trans Ind Electron 2017;64(6):5151–60. https://doi.org/10.1109/TIE.2017.2668983.
[142] Yan Z, Xu Y. A multi-agent deep reinforcement learning method for cooperative load frequency control of a multi-area power system. IEEE Trans Power Syst 2020;35(6):4599–608. https://doi.org/10.1109/TPWRS.2020.2999890.

Concluding Remarks

This paper examined the current research on using power-heat sector coupling equipment for frequency response services. The identified general state-of-the-art in the paper is used as the foundation for this thesis.

Initially, the paper explored various standard power-heat equipment within the heat sector that are capable of providing frequency response services. With the ongoing shift towards a fully REG-based network, the range of generation equipment in the heat sector has been extended from diverse CHP systems to a mix of CHP and PtH systems. Each equipment type exhibits distinct power modulation characteristics, including response speed, modulation depth, and efficiency. These are essential factors to be evaluated when selecting heating equipment for specific frequency response services.

The control strategy is pivotal when embedding frequency response functions into sector coupling equipment. We reviewed the available control strategies for frequency response services in the literature and listed application examples for each specific equipment type. We found that the current control hardware of diverse types of equipment lacks standardization. Algorithm decisions are, therefore, hinged on the hardware condition of the implementation platform, with the dominant choice being decentralized algorithms.

In addition, several conclusions have been drawn from the literature's open statistical data and development trends. Based on current IEA observations, heat pumps, especially air-source types, will gradually replace centralized CHPs and dominate the future heat sector. Frequency response services through heat pumps are also becoming increasingly popular because the number of related publications has grown quickly in recent years. Although using heat pumps for frequency response services is still immature regarding control standardization and business model, it is obvious that such applications become increasingly crucial to overcome the challenges of high renewable penetration.

Chapter 3: Rapid Frequency Stabilization: the FFR Service Scenario

This Chapter focuses on how to model and design controllers for heat pumps to enable them for FFR services. Given the growing adoption of distributed heat pumps, especially air-source heat pumps (ASHP), there is great potential for utilizing them to enhance grid inertia and stabilize grid frequency during anomaly events. These small-scale heat pumps, characterized by their inherently lower mechanical inertia than centralized units, are theoretically capable of responding to rapid modulation commands. This potential is attractive because it can significantly reduce the costs of BESSs and flexible REGs that are used for FFR services. In this context, we discuss related modeling, testing, and controller design issues to realize such an idea in this section.

3.1 Multiphysics Modeling of Distributed Air-Source Heat Pumps

Understanding the detailed dynamic behavior of heat pumps is the core step for application-specific modeling and control design. An illustration of the physical structure of a common air-to-water ASHP is shown in Fig. 3-1. ASHP systems are composed of electrical and thermal subsystems. The electrical subsystem is a variable-frequency drive (VFD) system, while the thermal subsystem is a vapor compression system. As the dynamic characteristics of these two subsystems are naturally diverse, their modeling concepts are illustrated separately in two subsections.

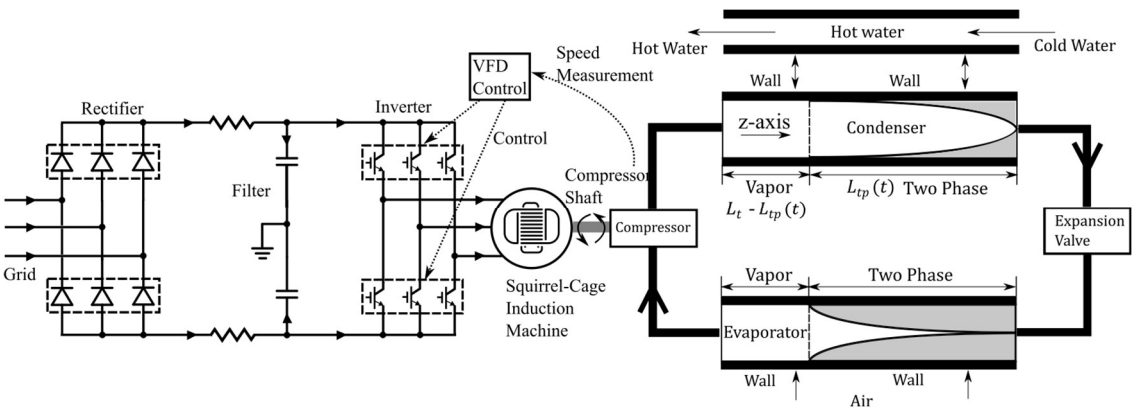

Figure 3-1 Physical structure of a typical distributed ASHP.

3.1.1 Electrical Subsystem

The electrical subsystem of typical ASHPs can be divided into four main components: rectifier, Direct Current (DC) filter, inverter with a controller, and machine. This part of modeling is standardized in power electronic research, and there are good references from Simulink Simscape Power System Library [64]. The core method for converting the full physics-based model into a control-oriented version is simplification through equivalent circuits [65]. All equations of each model component are derived as follows.

Rectifier (Diode)

Variable-speed ASHP systems generally rely on rectifiers to provide the DC link voltage for the later inverter stage. Although various types of rectifiers exist, three-phase diode bridges are dominant because of their low costs [66]. To derive a mathematical twin system for the rectifier, it is key that we understand its fundamental electrical functions, as shown in Fig. 3-2a. The positive bridge arm at the output side is always the maximum voltage among all phases, while the negative bridge arm is always the minimum one, leading to the following mathematical expression between output voltages v_{rec}^{+}, v_{rec}^{-}, and grid line-to-ground voltages $v_{g,abc}$ by (3.1)-(3.2):

$$v_{rec}^{+} = \max\left(v_{g,a}, v_{g,b}, v_{g,c}\right), \tag{3.1}$$

$$v_{rec}^{-} = \min\left(v_{g,a}, v_{g,b}, v_{g,c}\right). \tag{3.2}$$

If the current flow to later-stage systems i_{rec}^{+} and i_{rec}^{-} are known, then we can relate the rectifier grid-interfacing current $i_{g,abc}^{*}$ with i_{rec}^{+} and i_{rec}^{-} by a set of rules $g_{rec,abc}^{\pm}$ (6 in total, only phase *a* rules are listed) which describes the on/off status of each arm, as in (3.3)-(3.5):

$$i_{g,abc}^{*} = i_{rec}^{+} g_{rec,abc}^{+} + i_{rec}^{-} g_{rec,abc}^{-}, \tag{3.3}$$

$$g_{rec,a}^{+} = \begin{cases} 1 & v_{g,a} > v_{g,b} \cap v_{g,a} > v_{g,c} \\ 0 & else \end{cases}, \tag{3.4}$$

$$g_{rec,a}^{-} = \begin{cases} 1 & v_{g,a} < v_{g,b} \cap v_{g,a} < v_{g,c} \\ 0 & else \end{cases}, \tag{3.5}$$

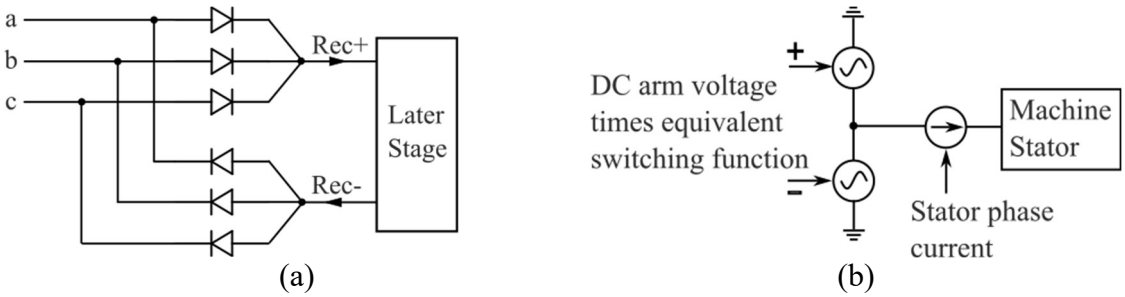

Figure 3-2 Essential function demonstration: (a) rectifier; (b) inverter (per phase).

The resulting rectifier system is a five-input-five-output system, where the inputs are $v_{g,abc}$, i_{rec}^{+}, and i_{rec}^{-}, and the outputs are v_{rec}^{+}, v_{rec}^{-}, and $i_{g,abc}^{*}$.

DC Filter (R-C Type)

The outputs of the rectifier bridge are generally filtered by a passive R-C type filter system, which can be described through Kirchhoff's Voltage and Current Laws [67]. Note that the current of both positive and negative arms should be saturated because of the diodes in the rectifier, which leads to the expressions in (3.6)-(3.7):

$$\boldsymbol{R_f i_{rec}^{\pm} = v_{rec}^{\pm} - v_{dc}^{\pm}}, \qquad \boldsymbol{i_{rec}^{+} \geq 0}, \qquad \boldsymbol{i_{rec}^{-} \leq 0}, \tag{3.6}$$

$$C_f \frac{dv_{dc}^{\pm}}{dt} = i_{rec}^{\pm} - i_{dc}^{\pm}, \tag{3.7}$$

where R_f is the filter resistance**,** C_f is the filter capacitance, v_{dc}^{+} and v_{dc}^{-} are the DC link voltages**,** and i_{dc}^{+} and i_{dc}^{-} are the DC link currents. The obtained system is a four-input-four-output system, where the inputs are v_{rec}^{+}, v_{rec}^{-}, i_{dc}^{+}, and i_{dc}^{-}, the outputs are i_{rec}^{+}, i_{rec}^{-} v_{dc}^{+}, and v_{dc}^{-}.

Inverter & Speed Controller

The key to inverter system modeling is to replace the Pulse-Width Modulation (PWM) switching process [68] with equivalent functions $g_{i,abc}^{\pm}$. For each phase in the inverter system, the electrical equivalent circuit can be simplified into Fig. 3-2b if the switching-induced harmonics are not of interest. Under such simplification, each inverter output arm is supplied by two controlled voltage sources whose references are decided by the target voltage of PWM cycles on a specific bridge arm, and each arm is also connected to a current source whose reference is decided by the machine stator phase current. In this context, the resulting supply voltages to the machine stator $v_{s,abc}$ and current drow by the stator i_{dc}^{+} and i_{dc}^{-} can be represented by (3.8)-(3.9):

$$v_{s,abc} = \frac{1}{2} g_{i,abc}^{+} v_{dc}^{+} + \frac{1}{2} g_{i,abc}^{-} v_{dc}^{-}, \tag{3.8}$$

$$i_{dc}^{\pm} = \frac{1}{2}\left(g_{i,a}^{\pm} i_{s,a} + g_{i,b}^{\pm} i_{s,b} + g_{i,c}^{\pm} i_{s,c}\right), \tag{3.9}$$

For each bridge arm, the PWM signals for top and bottom switches are complementary, which means their switching target function are in opposite polarity, as in (3.10):

$$g_{i,abc}^{+} = -g_{i,abc}^{-}. \tag{3.10}$$

The switching equivalent function $g_{i,abc}^{+}$ is decided by the VFD speed control system. If we assume a general case where the PI controller is used based on the V/f (constant flux) speed control [69], the resulting control signal for phase *a* can be generated by (3.11) and (3.12) as follows:

$$f = k_p(\omega_m^* - \omega_m) + k_i \int (\omega_m^* - \omega_m)\, dt, \tag{3.11}$$

$$g_{i,a}^{+} = \frac{k_\varphi f sin(2\pi f t)}{\bar{v}_{dc}}, \tag{3.12}$$

where f is the supply voltage frequency, ω_m^* is the angular speed reference, ω_m is the angular speed measurement, $k_{p/i}$ are controller gains, k_φ is the flux coefficient, $\bar{v}_{dc}$ is the average DC link voltage. To summarize, the inverter, along with the VFD speed control, is a seven-input-five-output system where the inputs are ω_m^*, ω_m, v_{dc}^{+}, v_{dc}^{-}, and $i_{s,abc}$, and the outputs are $v_{s,abc}$, i_{dc}^{+} and i_{dc}^{-}.

Machine

The majority of distributed ASHPs rely on squirrel-cage induction machines (SCIM) to provide torque for the vapor compression stage (thermal subsystem). The modeling of the SCIM is based on the rotating reference frame (dq) [70]. Therefore, the Park Transform is needed for both the input and output layer to translate the signal between abc and dq reference frames. If we choose the rotor field as the rotating reference frame, the principle SCIM electro-magnetic dynamics can be described by (3.13)-(3.20):

$$\frac{d\varphi_{s,q}}{dt} = v_{s,q} - R_s i_{s,q} - \omega_e \varphi_{s,d}, \tag{3.13}$$

$$\frac{d\varphi_{s,d}}{dt} = v_{s,d} - R_s i_{s,d} + \omega_e \varphi_{s,q}, \tag{3.14}$$

$$\frac{d\varphi'_{r,q}}{dt} = v'_{r,q} - R'_r i'_{r,q}, \tag{3.15}$$

$$\frac{d\varphi'_{r,d}}{dt} = v'_{r,d} - R'_r i'_{r,d}, \tag{3.16}$$

$$\varphi_{s,q} = \left(L_{ls} + L_{mg}\right) i_{s,q} + L_{mg} i'_{r,q}, \tag{3.17}$$

$$\varphi_{s,d} = \left(L_{ls} + L_{mg}\right) i_{s,d} + L_{mg} i'_{r,d}, \tag{3.18}$$

$$\varphi'_{r,q} = \left(L'_{lr} + L_{mg}\right) i'_{r,q} + L_{mg} i_{s,q}, \tag{3.19}$$

$$\varphi'_{r,d} = \left(L'_{lr} + L_{mg}\right)i'_{r,d} + L_{mg}i_{s,d}, \tag{3.20}$$

where variable φ is flux, L is inductance; subscript r represents rotor, l represents leakage, mg represents magnetization; superscript $'$ represents rotor variables referred to the stator. The mechanical part of the machine model is described by a swing system, as in (3.21)-(3.22):

$$J\frac{d\omega_m}{dt} = T_e - k_F\omega_m - \frac{P_m}{\omega_m}, \tag{3.21}$$

$$T_e = 1.5p\left(\varphi_{s,d}i_{s,q} - \varphi_{s,q}i_{s,d}\right), \tag{3.22}$$

where T_e is the produced electrical torque, k_F is the friction coefficient, p is the number of pole pairs. Note that the mechanical shaft power P_m should be provided by the connected thermal subsystem, which will be introduced in the next section of this paper. After combining the swing system and the electro-magnetic system, the resulting system is a four-input-four-output system, where the inputs are $v_{s,abc}$ and P_m, and the outputs are ω_m and $i_{s,abc}$.

3.1.2 Thermal Subsystem

The thermal subsystem of distributed ASHPs is a single-stage vapor compression system. It can be divided into four main components: evaporator, compressor, condenser, and expansion valve, where evaporator and condenser are phase-shifting heat exchangers and, therefore, relatively complex to model. This part of modeling is usually highly simplified in the area of power systems, as the non-linearity of heat pumps was considered trivial in PFR and SFR control scenarios, such as in [71][72][73]. For rapid-response scenarios such as FFR services, a comprehensive understanding of the thermal subsystem's dynamics based on fundamental physics is critical. In this thesis, we adopted an established method from the area of fluid thermal dynamics to model the thermal subsystems of distributed ASHPs. From reviewing the literature, the mainstream methods that satisfy our expectations are finite volume [74][75] and moving boundary methods [76][77][78]. The moving boundary method is by far more suitable, as the finite volume method is overqualified with redundant information on variable spatial distribution. Following this modeling method, each component model is then derived and listed separately in this subsection.

Evaporator

The modeling processes for the evaporator and condenser are similar, and we use the evaporator system to explain the core method. The fluid flow within the evaporator is governed by the conservation laws of a Newtonian fluid traveling in a one-dimensional space and the pipe wall. Since the equipment size is relatively small, we neglect the refrigerant momentum conservation and pressure drops. If no simplifications are made, the partial differential equations (PDE) of related conservation laws [79] are shown in (3.23)-(3.25):

$$Refrigerant\ mass: A_{i,c}\frac{\partial \rho}{\partial t}+\frac{\partial \dot{m}}{\partial z}=0, \tag{3.23}$$

$$Refrigerant\ energy: A_{i,c}\frac{\partial (\rho h-p)}{\partial t}+\frac{\partial (\dot{m}h)}{\partial z}=c_i\alpha_i(T_w-T_r), \tag{3.24}$$

$$Pipe\ wall\ energy: C_w\rho_w\left(A_{o,c}\text{-}A_{i,c}\right)\frac{\partial T_w}{\partial t}=c_i\alpha_i\left(T_{r,tp}\text{-}T_w\right)+c_o\alpha_o(T_a\text{-}T_w), \tag{3.25}$$

where variable ρ is the refrigerant density, $\dot{m}$ is the mass flow, z is the axial direction, h is the specific enthalpy, p is the pressure, A is the cross-section area of the pipe, c is the premiter of the pipe, α is the heat transfer coefficient, T is the temperature; subscript i represents pipe inner variables, o represents pipe outer variables, c represents cross-section, w represents the pipe wall variables, a represents ambient air, and r represents refrigerant variables. The above PDE system is too complex for a practical control design as we can only solve them through numerical approximations. Therefore, reasonable simplification towards the ordinary differential equation (ODE) system is needed. In the moving boundary method, evaporator volume is divided into different zones, where each zone is characterized by a specific refrigerant thermal state. For example, the two-zone type model separates the evaporator volume into two-phase and vapor zones. We then integrate (3.23)-(3.25) over the length of specific zones to eliminate the z-axis derivative terms. However, we need some assumptions to continue the integration.

- The refrigerant is in a thermal-equilibrium state in the two-phase zone.
- Variable and parameters are lumped in each zone.
- The refrigerant is in a thermal-equilibrium vapor state at the zone boundary.

two-phase zone: refrigerant mass conservation (start)

As the refrigerant enters the evaporator in a two-phase state, we start the integration from the two-phase zone. Let the length of the two-phase zone be $L_{tp}(t)$, which leads to the following integration in (3.26) from the mass conservation PDE:

$$A_{i,c}\underbrace{\int_0^{L_{tp}(t)}\frac{\partial \rho}{\partial t}dz}_{Terms_{tp}.1}+\underbrace{\int_0^{L_{tp}(t)}\frac{\partial \dot{m}}{\partial z}dz}_{Terms_{tp}.2}=0, \tag{3.26}$$

where variable L is the zone length; subscript tp represents two-phase zone variables. In order to proceed, the Leibniz's integration rule [80], as shown in (3.27), is needed:

$$\int_{L_1(t)}^{L_2(t)} \frac{\partial f(z,t)}{\partial t} dz = \frac{d}{dt}\left(\int_{L_1(t)}^{L_2(t)} f(z,t)\, dz\right) + f(L_1(t),t)\frac{d\left(L_1(t)\right)}{dt} - f(L_2(t),t)\frac{d\left(L_2(t)\right)}{dt}, \tag{3.27}$$

where variable $L_1(t)$ and $L_2(t)$ are the start and end points of the integration. With an average vapor fraction $\bar{\gamma}$, we can then write the density of the two-phase mixture as shown in (3.28):

$$\rho'_{tp} = \bar{\gamma}\rho'_v + (1-\bar{\gamma})\rho'_l, \tag{3.28}$$

where the subscript v represents the vapor, l represents the liquid; superscript $'$ represents thermal-equilibrium state. Since the refrigerant is assumed to be in an equilibrium state in the two-phase zone, the density of refrigerant vapor or liquid is a function of pressure. According to the chain rule in calculus [81], we can obtain (3.29):

$$\frac{d\rho'_v}{dt} = \frac{d\rho'_v}{dp}\frac{dp}{dt}, \qquad \frac{d\rho'_l}{dt} = \frac{d\rho'_l}{dp}\frac{dp}{dt}. \tag{3.29}$$

Based on (3.27)-(3.29), we then integrate (3.26) term by term as follows:

$ms_{tp}.1 = \frac{d}{dt}\int_0^{L_{tp}} \rho\, dz - \rho'_v \frac{dL_{tp}}{dt}$	Substitute (3.27)
$= \frac{d}{dt}\int_0^{L_{tp}} \rho'_{tp}\, dz - \rho'_v \frac{dL_{tp}}{dt}$	Lump $\rho(z,t)$ over the zone
$= \frac{d(\rho'_{tp}L_{tp})}{dt} - \rho'_v \frac{dL_{tp}}{dt}$	
$= \frac{d\rho'_{tp}}{dt}L_{tp} + (\rho'_{tp} - \rho'_v)\frac{dL_{tp}}{dt}$	
$= \frac{d(\bar{\gamma}\rho'_v + (1-\bar{\gamma})\rho'_l)}{dt}L_{tp} + \frac{dL_{tp}}{dt}(\bar{\gamma}\rho'_v + (1-\bar{\gamma})\rho'_l) - \rho'_v\frac{dL_{tp}}{dt}$	Substitute (3.28)
$= L_{tp}\bar{\gamma}\frac{d\rho'_v}{dt} + L_{tp}(1-\bar{\gamma})\frac{d\rho'_l}{dt} + (\rho'_l - \rho'_v)(1-\bar{\gamma})\frac{dL_{tp}}{dt}$	
$= L_{tp}\bar{\gamma}\frac{d\rho'_v}{dp}\frac{dp}{dt} + L_{tp}(1-\bar{\gamma})\frac{d\rho'_l}{dp}\frac{dp}{dt} + (\rho'_l - \rho'_v)(1-\bar{\gamma})\frac{dL_{tp}}{dt}$	Substitute (3.29)

$$= \left(\frac{d\rho_v'}{dp}\bar{\gamma} + \frac{d\rho_l'}{dp}(1-\bar{\gamma})\right) L_{tp}\frac{dp}{dt} + (\rho_l' - \rho_v')(1-\bar{\gamma})\frac{dL_{tp}}{dt},$$

$$ms_{tp}.2 = \dot{m}_b - \dot{m}_{in},$$

where subscript b represents the zone boundary. The resulting ODE of the mass conservation in the two-phase zone is then as in (3.30):

$$\left(\frac{d\rho_v'}{dp}\bar{\gamma} + \frac{d\rho_l'}{dp}(1-\bar{\gamma})\right) A_{i,c}L_{tp}\frac{dp}{dt} + (\rho_l' - \rho_v')(1-\bar{\gamma})A_{i,c}\frac{dL_{tp}}{dt} + \dot{m}_b\text{-}\dot{m}_{in} = 0. \quad (3.30)$$

In (3.30), p and L_{tp} are state variables, $\dot{m}_b$ is an intermediate variable that will be canceled when combining all components, $\dot{m}_{in}$ is an input variable. $\frac{d\rho_v'}{dp}$, $\frac{d\rho_l'}{dp}$, ρ_v', and ρ_l' are thermal dynamic property coefficients that need to be determined dynamically during calculation based on p with refrigerant data look-up-tables.

two-phase zone: refrigerant mass conservation (end)

two-phase zone: refrigerant energy conservation (start)

The mentioned energy conservations consist of two parts: one part for the refrigerant and the other part for the corresponding pipe wall. It is essential to include the wall because the thermal inertia within the metal pipe is non-negligible. We begin with the derivation for the refrigerant part. Similar to the mass conservation, we integrate (3.24) from 0 to $L_{tp}(t)$, which leads to the following results, as shown in (3.31):

$$A_{i,c}\underbrace{\int_0^{L_{tp}(t)}\frac{\partial(\rho h - p)}{\partial t}dz}_{Term\ er_{tp}.1} + \underbrace{\int_0^{L_{tp}(t)}\frac{\partial(\dot{m}h)}{\partial z}dz}_{Term\ er_{tp}.2} = \underbrace{\int_0^{L_{tp}(t)} c_i\alpha_{i,tp}(T_w - T_r)dz}_{Term\ er_{tp}.3}. \quad (3.31)$$

Similarly, We can write the refrigerant energy density of the two-phase mixture based on $\bar{\gamma}$, as shown in (3.32):

$$\rho_{tp}'h_{tp}' = \bar{\gamma}\rho_v'h_v' + (1-\bar{\gamma})\rho_l'h_l'. \quad (3.32)$$

Again, because the refrigerant is in a thermal equilibrium state, all variables are only related to pressure [82]. According to the chain rule, we can obtain (3.33):

$$\frac{d(\rho_v'h_v')}{dt} = \frac{d(\rho_v'h_v')}{dp}\frac{dp}{dt}, \qquad \frac{d(\rho_l'h_l')}{dt} = \frac{d(\rho_l'h_l')}{dp}\frac{dp}{dt}. \quad (3.33)$$

Based on (3.32) and (3.33), we then integrate (3.31) term by term as follows:

$$er_{tp}.1 = \frac{d}{dt}\int_0^{L_{tp}} \rho h \, dz - \rho_v' h_v' \frac{dL_{tp}}{dt} - L_{tp}\frac{dp}{dt}$$ Substitute (3.27)

$$= \frac{d}{dt}\int_0^{L_{tp}} \rho_{tp}' h_{tp}' \, dz - \rho_v' h_v' \frac{dL_{tp}}{dt} - L_{tp}\frac{dp}{dt}$$ Lump $\rho(z,t)$ and $h(z,t)$ over the zone

$$= \frac{d(\rho_{tp}' h_{tp}' L_{tp})}{dt} - \rho_v' h_v' \frac{dL_{tp}}{dt} - L_{tp}\frac{dp}{dt}$$

$$= \frac{d(\rho_{tp}' h_{tp}')}{dt} L_{tp} - L_{tp}\frac{dp}{dt} + \rho_{tp}' h_{tp}' \frac{dL_{tp}}{dt} - \rho_v' h_v' \frac{dL_{tp}}{dt}$$

$$= \frac{d(\bar{\gamma}\rho_v' h_v' + (1-\bar{\gamma})\rho_l' h_l')}{dt} L_{tp} - L_{tp}\frac{dp}{dt} + (\bar{\gamma}\rho_v' h_v'$$

$$+(1-\bar{\gamma})\rho_l' h_l')\frac{dL_{tp}}{dt} - \rho_v' h_v' \frac{dL_{tp}}{dt}$$ Substitute (3.32)

$$= L_{tp}\bar{\gamma}\frac{d\rho_v' h_v'}{dt} + L_{tp}(1-\bar{\gamma})\frac{d\rho_v' h_v'}{dt} - L_{tp}\frac{dp}{dt}$$

$$+(1-\bar{\gamma})(\rho_l' h_l' - \rho_v' h_v')\frac{dL_{tp}}{dt}$$

$$= L_{tp}\bar{\gamma}\frac{d(\rho_v' h_v')}{dp}\frac{dp}{dt} + L_{tp}(1-\bar{\gamma})\frac{d(\rho_l' h_l')}{dp}\frac{dp}{dt} - L_{tp}\frac{dp}{dt}$$ Substitute (3.33)

$$+(1-\bar{\gamma})(\rho_l' h_l' - \rho_v' h_v')\frac{dL_{tp}}{dt}$$

$$= \left(\left(\frac{d\rho_v'}{dp}h_v' + \frac{dh_v'}{dp}\rho_v'\right)\bar{\gamma} + \left(\frac{d\rho_l'}{dp}h_l' + \frac{dh_l'}{dp}\rho_l'\right)(1-\bar{\gamma}) - 1\right)L_{tp}\frac{dp}{dt}$$

$$+(\rho_l' h_l' - \rho_v' h_v')(1-\bar{\gamma})\frac{dL_{tp}}{dt},$$

$$er_{tp}.2 = \dot{m}_b h_b - \dot{m}_{in} h_{in},$$

$$er_{tp}.3 = A_{i,s}\frac{L_{tp}}{L_t}\alpha_{i,tp}\left(T_{w,tp} - T_{r,tp}\right),$$

where subscript t represents total. The resulting ODE for the refrigerant's energy conservation of the two-phase zone is shown in (3.34).

$$\left(\left(\frac{d\rho_v'}{dp}h_v' + \frac{dh_v'}{dp}\rho_v'\right)\bar{\gamma} + \left(\frac{d\rho_l'}{dp}h_l' + \frac{dh_l'}{dp}\rho_l'\right)(1-\bar{\gamma}) - 1\right)A_{i,c}L_{tp}\frac{dp}{dt}$$

$$+(\rho_l'h_l' - \rho_v'h_v')(1-\bar{\gamma})A_{i,c}\frac{dL_{tp}}{dt} + \dot{m}_b h_b - \dot{m}_{in}h_{in} \tag{3.34}$$

$$= A_{i,s}\frac{L_{tp}}{L_t}\alpha_{i,tp}\left(T_{w,tp} - T_{r,tp}\right).$$

In (3.34), $\dot{m}_b$ and h_b are both intermediate variables, $\dot{m}_{in}$ and h_{in} are input variables. $T_{r,tp}$ represents a lumped refrigerant mixture saturation temperature, which can be obtained from p through property look-up tables.

two-phase zone: refrigerant energy conservation (end)

two-phase zone: wall energy conservation (start)

In order to obtain the wall energy conservation for the two-phase zone, (3.25) has to be integrated over 0-$L_{tp}(t)$, which resulted in (3.35).

$$C_w\rho_w\left(A_{o,c}\text{-}A_{i,c}\right)\underbrace{\int_0^{L_{tp}}\frac{\partial T_w}{\partial t}dz}_{Term\ ew_{tp}.1} = \underbrace{\int_0^{L_{tp}}c_i\alpha_{i,tp}(T_r\text{-}T_w)dz}_{Term\ ew_{tp}.2} + \underbrace{\int_0^{L_{tp}}c_o\alpha_o(T_a\text{-}T_w)dz}_{Term\ ew_{tp}.3}. \tag{3.35}$$

If the boundary wall temperature between zones is $T_{w,b}$, equation (3.35) can be integrated as follows.

$ew_{tp}.1 = \frac{d}{dt}\int_0^{L_{tp}}T_w dz - T_{w,b}\frac{dL_{tp}}{dt}$	Substitute (3.27)
$= \frac{d}{dt}\int_0^{L_{tp}}T_{w,tp}dz - T_{w,b}\frac{dL_{tp}}{dt}$	Lump $T_w(z,t)$ over the zone
$= \frac{dT_{w,tp}}{dt}L_{tp} + T_{w,tp}\frac{dL_{tp}}{dt} - T_{w,b}\frac{dL_{tp}}{dt}$	
$= \frac{dT_{w,tp}}{dt}L_{tp},$	Let $T_{w,b} = T_{w,tp}$
$ew_{tp}.2 = A_{i,s}\frac{L_{tp}}{L_t}\alpha_{i,tp}\left(T_{r,tp} - T_{w,tp}\right),$	

$$ew_{tp}.3 = A_{o,s}\frac{L_{tp}}{L_t}\alpha_o\left(T_a - T_{w,tp}\right).$$

The resulting ODE for wall energy conservation in the two-phase zone is shown in (3.36).

$$C_w\rho_w(A_{o,c} - A_{i,c})L_{tp}\frac{dT_{w,tp}}{dt} = A_{i,s}\frac{L_{tp}}{L_t}\alpha_{i,tp}\left(T_{r,tp} - T_{w,tp}\right) + A_{o,s}\frac{L_{tp}}{L_t}\alpha_o\left(T_a - T_{w,tp}\right). \tag{3.36}$$

two-phase zone: wall energy conservation (end)

vapor zone: refrigerant mass conservation (start)

The governing ODEs of the vapor zone are derived similarly to the two-phase zone by integrating the PDE conservation equations over the subject zone length (now from $L_{tp}(t)$ to L_t). For the mass conservation in the vapor zone, the integration process is as (3.37):

$$A_{i,c}\underbrace{\int_{L_{tp}(t)}^{L_t}\frac{\partial\rho}{\partial t}dz}_{Term\,ms_v.1} + \underbrace{\int_{L_{tp}(t)}^{L_t}\frac{\partial\dot{m}}{\partial z}dz}_{Term\,ms_v.2} = 0 \tag{3.37}$$

The fundamental difference for the vapor zone is that the refrigerant is no longer in the thermal-equilibrium state. This makes its density a function of both pressure and specific enthalpy rather than just pressure, which leads to (3.38):

$$\frac{d\rho_v}{dt} = \frac{\partial\rho_v}{\partial p}\bigg|_{h_v}\frac{dp}{dt} + \frac{\partial\rho_v}{\partial h_v}\bigg|_{p}\frac{dh_v}{dt}. \tag{3.38}$$

Considering all variables are lumped, h_v can be written as the averaged version of the entry (pure thermal-equilibrium vapor) and leaving specific enthalpy, as in (3.39).

$$h_v = \frac{h_v' + h_{out}}{2}. \tag{3.39}$$

As the refrigerant is in a thermal-equilibrium vapor state at the zone boundary, the boundary-specific enthalpy is still only a function of pressure, leading to (3.40):

$$\frac{dh_v'}{dt} = \frac{dh_v'}{dp}\frac{dp}{dt}. \tag{3.40}$$

The integration process of (3.37) is then as follows.

$ms_v.1 = \frac{d}{dt}\int_{L_{tp}}^{L_t} \rho\, dz + \rho_v' \frac{dL_{tp}}{dt}$	Substitute (3.27)
$= \frac{d}{dt}\int_{L_{tp}}^{L_t} \rho_v\, dz + \rho_v' \frac{dL_{tp}}{dt}$	Lump $\rho(z,t)$ over the zone
$= \frac{d(\rho_v(L_t - L_{tp}))}{dt} + \rho_v' \frac{dL_{tp}}{dt}$	
$= \frac{d\rho_v}{dt}(L_t - L_{tp}) + (\rho_v' - \rho_v)\frac{dL_{tp}}{dt}$	
$= L_v\left(\left.\frac{\partial \rho_v}{\partial p}\right\|_{h_v} \frac{dp}{dt} + \left.\frac{\partial \rho_v}{\partial h_v}\right\|_{p} \frac{dh_v}{dt}\right) + (\rho_v' - \rho_v)\frac{dL_{tp}}{dt}$	Substitute (3.38)
$= L_v\left(\left.\frac{\partial \rho_v}{\partial p}\right\|_{h_v} \frac{dp}{dt} + \frac{1}{2}\left.\frac{\partial \rho_v}{\partial h_v}\right\|_{p} \left(\frac{dh_v'}{dt} + \frac{dh_{out}}{dt}\right)\right) + (\rho_v' - \rho_v)\frac{dL_{tp}}{dt}$	Substitute (3.39)
$= L_v\left(\left.\frac{\partial \rho_v}{\partial p}\right\|_{h_v} \frac{dp}{dt} + \frac{1}{2}\left.\frac{\partial \rho_v}{\partial h_v}\right\|_{p} \left(\frac{dh_v'}{dp}\frac{dp}{dt} + \frac{dh_{out}}{dt}\right)\right) + (\rho_v' - \rho_v)\frac{dL_{tp}}{dt}$	Substitute (3.40)
$= L_v\left(\left.\frac{\partial \rho_v}{\partial p}\right\|_{h_v} + \frac{1}{2}\left.\frac{\partial \rho_v}{\partial h_v}\right\|_{p} \frac{dh_v'}{dp}\right)\frac{dp}{dt} + \frac{1}{2}L_v \left.\frac{\partial \rho_v}{\partial h_v}\right\|_{p} \frac{dh_{out}}{dt}$ $+(\rho_v' - \rho_v)\frac{dL_{tp}}{dt},$	
$ms_v.2 = \dot{m}_{out} - \dot{m}_b.$	

Finally, the resulting ODE for the refrigerant's mass conservation of the vapor zone is shown in (3.41):

$$\left(\left.\frac{\partial \rho_v}{\partial p}\right|_{h_v} + \frac{1}{2}\left.\frac{\partial \rho_v}{\partial h_v}\right|_{p} \frac{dh_v'}{dp}\right) A_{i,c} L_v \frac{dp}{dt} + \frac{1}{2}\left.\frac{\partial \rho_v}{\partial h_v}\right|_{p} A_{i,c} L_v \frac{dh_{out}}{dt} + (\rho_v' - \rho_v) A_{i,c} \frac{dL_{tp}}{dt} + \dot{m}_{out} - \dot{m}_b = 0. \tag{3.41}$$

In (3.41), $\frac{\partial \rho}{\partial p}\Big|_h$, $\frac{\partial \rho}{\partial h}\Big|_p$ and $\frac{dh_v'}{dp}$ are all coefficients that are obtained through refrigerant data look-up-tables. Similarly, ρ_v is the lumped density which can be obtained through data tables with h_v and p.

vapor zone: refrigerant mass conservation (end)

vapor zone: refrigerant energy conservation (start)

The refrigerant energy conservation (3.25) can be integrated over the vapor zone length as in (3.42):

$$A_{i,c}\underbrace{\int_{L_{tp}}^{L_t}\frac{\partial(\rho h-p)}{\partial t}dz}_{Term\ er_v.1}+\underbrace{\int_{L_{tp}}^{L_t}\frac{\partial(\dot{m}h)}{\partial z}dz}_{Term\ er_v.2}=\underbrace{\int_{L_{tp}}^{L_t}c_i\alpha_{i,v}(T_w-T_r)dz}_{Term\ er_v.3} \tag{3.42}$$

The detailed integration process of (3.42) is shown as follows.

$$er_v.1=\frac{d}{dt}\int_{L_{tp}}^{L_t}\rho h\,dz+\rho_v'h_v'\frac{dL_{tp}}{dt}-L_v\frac{dp}{dt}$$ Substitute (3.27)

$$=\frac{d}{dt}\int_{L_{tp}}^{L_t}\rho_v h_v\,dz+\rho_v'h_v'\frac{dL_{tp}}{dt}-L_v\frac{dp}{dt}$$ Lump $\rho(z,t)$ and $h(z,t)$ over the zone

$$=\frac{d(\rho_v h_v L_v)}{dt}+\rho_v'h_v'\frac{dL_{tp}}{dt}-L_v\frac{dp}{dt}$$

$$=\frac{d(\rho_v h_v)}{dt}L_v-L_v\frac{dp}{dt}-\rho_v h_v\frac{dL_{tp}}{dt}+\rho_v'h_v'\frac{dL_{tp}}{dt}$$

$$=\left(\frac{d\rho_v}{dt}h_v+\frac{dh_v}{dt}\rho_v\right)L_v-L_v\frac{dp}{dt}-\rho_v h_v\frac{dL_{tp}}{dt}+\rho_v'h_v'\frac{dL_{tp}}{dt}$$

$$=\left(\left(\frac{\partial\rho_v}{\partial p}\Big|_{h_v}\frac{dp}{dt}+\frac{\partial\rho_v}{\partial h_v}\Big|_p\frac{dh_v}{dt}\right)h_v+\frac{dh_v}{dt}\rho_v-\frac{dp}{dt}\right)L_v-\rho_v h_v\frac{dL_{tp}}{dt}$$ Substitute (3.38)

$$+\rho_v'h_v'\frac{dL_{tp}}{dt}$$

$$=\left(\left(\frac{\partial\rho_v}{\partial p}\Big|_{h_v}h_v-1\right)\frac{dp}{dt}+\left(\frac{\partial\rho_v}{\partial h_v}\Big|_p h_v+\rho_v\right)\frac{dh_v}{dt}\right)L_v$$

$$+(\rho_v' h_v' - \rho_v h_v)\frac{dL_{tp}}{dt}$$

$$= \left(\left(\frac{\partial \rho_v}{\partial p}\Big|_{h_v} h_v - 1\right)\frac{dp}{dt} + \frac{1}{2}\left(\frac{\partial \rho_v}{\partial h_v}\Big|_{p} h_v + \rho_v\right)\left(\frac{dh_v'}{dt} + \frac{dh_{out}}{dt}\right)\right) L_v$$

Substitute (3.39)

$$+(\rho_v' h_v' - \rho_v h_v)\frac{dL_{tp}}{dt}$$

$$= \left(\left(\frac{\partial \rho_v}{\partial p}\Big|_{h_v} h_v - 1\right)\frac{dp}{dt} + \frac{1}{2}\left(\frac{\partial \rho_v}{\partial h_v}\Big|_{p} h_v + \rho_v\right)\left(\frac{dh_v'}{dp}\frac{dp}{dt} + \frac{dh_{out}}{dt}\right)\right)$$

Substitute (3.40)

$$L_v + (\rho_v' h_v' - \rho_v h_v)\frac{dL_{tp}}{dt}$$

$$= \left(\left(\frac{\partial \rho_v}{\partial p}\Big|_{h_v} + \frac{1}{2}\frac{\partial \rho_v}{\partial h_v}\Big|_{p}\frac{dh_v'}{dp}\right) h_v + \frac{1}{2}\rho_v \frac{dh_v'}{dp} - 1\right) L_v \frac{dp}{dt}$$

$$+ \frac{1}{2}\left(\frac{\partial \rho_v}{\partial h_v}\Big|_{p} h_v + \rho_v\right) L_v \frac{dh_{out}}{dt} + (\rho_v' h_v' - \rho_v h_v)\frac{dL_{tp}}{dt},$$

$$er_v.2 = \dot{m}_{out} h_{out} - \dot{m}_b h_b,$$

$$er_v.3 = A_{i,s}\frac{L_v}{L_t}\alpha_{i,v}\left(T_{w,v} - T_{r,v}\right).$$

The resulting ODE for refrigerant's energy conservation in the vapor zone is then shown in (3.43):

$$\left(\left(\frac{\partial \rho_v}{\partial p}\Big|_{h_v} + \frac{1}{2}\frac{\partial \rho_v}{\partial h_v}\Big|_{p}\frac{dh_v'}{dp}\right) h_v + \frac{1}{2}\rho_v \frac{dh_v'}{dp} - 1\right) A_{i,c} L_v \frac{dp}{dt}$$

$$+ \frac{1}{2}\left(\frac{\partial \rho_v}{\partial h_v}\Big|_{p} h_v + \rho_v\right) A_{i,c} L_v \frac{dh_{out}}{dt} + (\rho_v' h_v' - \rho_v h_v) A_{i,c}\frac{dL_{tp}}{dt} + \dot{m}_{out} h_{out} \tag{3.43}$$

$$-\dot{m}_b h_b = A_{i,s}\frac{L_v}{L_t}\alpha_{i,v}\left(T_{w,v} - T_{r,v}\right).$$

In (3.43), $\dot{m}_b$ and h_b are both intermediate variables, $\dot{m}_{out}$ and h_{out} are input variables. $T_{r,v}$ represent a lumped refrigerant vapor temperature, which can be obtained from p and h_v through data tables.

vapor zone: refrigerant energy conservation (end)

vapor zone: wall energy conservation (start)

In order to get the wall energy conservation ODE for the vapor zone, we integrate (3.26) between $L_{tp}(t)$- L_t, as in (3.44):

$$C_w\rho_w(A_{o,c}\text{-}A_{i,c}) \underbrace{\int_{L_{tp}}^{L_t}\frac{\partial T_w}{\partial t}dz}_{Term\ ew_v.1} = \underbrace{\int_{L_{tp}}^{L_t}c_i\alpha_{i,tp}(T_r\text{-}T_w)dz}_{Term\ ew_v.2} + \underbrace{\int_{L_{tp}}^{L_t}c_o\alpha_o(T_a\text{-}T_w)dz}_{Term\ ew_v.3}. \quad (3.44)$$

Following the same process and assumptions from the two-phase zone, the integration of (3.44) is shown as follows.

$ew_v.1 = \frac{d}{dt}\int_{L_{tp}}^{L_t}T_w dz + T_{w,b}\frac{dL_{tp}}{dt}$	Substitute (3.27)
$= \frac{d}{dt}\int_{L_{tp}}^{L_t}T_{w,v}dz + T_{w,b}\frac{dL_{tp}}{dt}$	Lump $T_w(z,t)$ over the zone
$= L_t\frac{dT_{w,v}}{dt} - \frac{dT_{w,v}L_{tp}}{dt} + T_{w,b}\frac{dL_{tp}}{dt}$	
$= L_t\frac{dT_{w,v}}{dt} - L_{tp}\frac{dT_{w,v}}{dt} - T_{w,v}\frac{dL_{tp}}{dt} + T_{w,tp}\frac{dL_{tp}}{dt}$	Let $T_{w,b} = T_{w,tp}$
$= L_v\frac{dT_{w,v}}{dt} + (T_{w,tp} - T_{w,v})\frac{dL_{tp}}{dt}$,	
$ew_v.2 = A_{i,s}\frac{L_v}{L_t}\alpha_{i,v}(T_{r,v} - T_{w,v})$,	
$ew_{tp}.3 = A_{o,s}\frac{L_v}{L_t}\alpha_o(T_a - T_{w,v})$.	

Finally, the resulting ODE of the wall's energy conservation in the vapor zone is shown in (3.45):

$$C_w\rho_w\left(A_{o,c}-A_{i,c}\right)L_v\left(\frac{dT_{w,v}}{dt}+\frac{dL_{tp}}{dt}\frac{T_{w,tp}-T_{wv}}{L_v}\right) = A_{i,s}\frac{L_v}{L_t}\alpha_{i,v}\left(T_{r,v}-T_{w,v}\right)+A_{o.s}\frac{L_v}{L_t}\alpha_o\left(T_a-T_{w,v}\right). \tag{3.45}$$

Compressor

The compression process in this thesis is considered isentropic [83], which means the specific enthalpy increment can be calculated with (3.46). The mass flow is calculated with (3.47) with a dynamic volumetric efficiency, which is a function of the pressure ratio between the input and output. The efficiency polynomial function is often determined empirically. Finally, the compressor mechanical power can be obtained by multiplying the mass flow rate and the specific enthalpy increment, as shown in (3.48):

$$\Delta h = \frac{k_1 R T_{in}}{k_1-1}\left[\left(\frac{p_{out}}{p_{in}}\right)^{\frac{k_1-1}{k_1}}-1\right], \tag{3.46}$$

$$\dot{m}_{out} = \frac{\omega_m}{2\pi}V\rho_{in}\eta, \tag{3.47}$$

$$P_m = \dot{m}_{out}\,\Delta h, \tag{3.48}$$

where variable ω is the rotational angular speed, and P is power; subscript m represents mechanical variable; parameter V is the volume, η is the volumetric efficiency, R is the gas constant, and k_1 is an empirical constant.

Condenser

For the condenser, the derivation of all conservation equations is similar to the evaporator. The difference is that the order of the zones is swapped, which means the refrigerant enters the vapor zone first and then goes through the two-phase zone. Besides, as the condenser exchanges heat with water, there is an additional water volume to be modeled. We skip the derivation process, and the resulting system ODEs for all the conservations are listed as follows in (3.49)-(3.55):

vapor zone: refrigerant mass conservation

$$\left(\left.\frac{\partial\rho_v}{\partial p}\right|_{h_v}+\frac{1}{2}\left.\frac{\partial\rho_v}{\partial h_v}\right|_p\frac{dh_v'}{dp}\right)A_{i,c}L_v\frac{dp}{dt}+\dot{m}_b-\dot{m}_{in}+(\rho_v-\rho_v')A_{i,c}\frac{dL_v}{dt} + \frac{1}{2}\left.\frac{\partial\rho_v}{\partial h_v}\right|_p A_{i,c}L_1\frac{dh_{in}}{dt}=0, \tag{3.49}$$

vapor zone: refrigerant energy conservation

$$\left(\left(\left.\frac{\partial\rho_v}{\partial p}\right|_{h_v}+\frac{1}{2}\left.\frac{\partial\rho_v}{\partial h_v}\right|_{p}\frac{dh_v'}{dp}\right)h_v+\frac{1}{2}\frac{dh_v'}{dp}\rho_v-1\right)A_{i,c}L_v\frac{dp}{dt}$$

$$+\left(\left.\frac{\partial\rho_v}{\partial h_v}\right|_{p}h_v+\rho_v\right)\frac{1}{2}A_{i,c}L_v\frac{dh_{in}}{dt}+\dot{m}_b h_b-\dot{m}_{in}h_{in} \tag{3.50}$$

$$+(\rho_v h_v-\rho_v' h_v')A_{i,c}\frac{dL_v}{dt}=A_{i,s}\frac{L_v}{L_t}\alpha_{i,v}\left(T_{w,v}-T_{r,v}\right),$$

vapor zone: wall energy conservation

$$C_w\rho_w\left(A_{o,c}-A_{i,s}\right)L_v\frac{dT_{w,v}}{dt}=A_{i,s}\frac{L_v}{L_t}\alpha_{i,v}\left(T_{r,v}-T_{w,v}\right)+A_{o,s}\frac{L_v}{L_t}\alpha_o\left(T_a-T_{w,v}\right), \tag{3.51}$$

two-phase zone: refrigerant mass conservation

$$\left(\frac{d\rho_v'}{dp}\bar{\gamma}+\frac{d\rho_l'}{dp}(1\text{-}\bar{\gamma})\right)A_{i,c}L_{tp}\frac{dp}{dt}+\dot{m}_{out}-\dot{m}_b+(\rho_v'-\rho_l')(1-\bar{\gamma})A_{i,c}\frac{dL_v}{dt}=0, \tag{3.52}$$

two-phase zone: refrigerant energy conservation

$$\left(\left(\frac{d\rho_v'}{dp}h_v'+\frac{dh_v'}{dp}\rho_v'\right)\bar{\gamma}+\left(\frac{d\rho_l'}{dp}h_l'+\frac{dh_l'}{dp}\rho_l'\right)(1-\bar{\gamma})-1\right)A_{i,c}L_{tp}\frac{dp}{dt}$$

$$+(\rho_v'h_v'-\rho_l'h_l')(1-\bar{\gamma})A_{i,c}\frac{dL_v}{dt}+\dot{m}_{out}h_{out}-\dot{m}_b h_b \tag{3.53}$$

$$=A_{i,s}\frac{L_{tp}}{L_t}\alpha_{i,tp}\left(T_{w,tp}-T_{r,tp}\right),$$

two-phase zone: wall energy conservation

$$C_w\rho_w\left(A_{o,c}-A_{i,c}\right)L_{tp}\left(\frac{dT_{w,tp}}{dt}-\frac{dL_v}{dt}\frac{T_{w,tp}-T_{wv}}{L_{tp}}\right) \tag{3.54}$$

$$= A_{i,s}\frac{L_{tp}}{L_t}\alpha_{i,tp}\left(T_{r,tp} - T_{w,tp}\right) + A_{o,s}\frac{L_{tp}}{L_t}\alpha_o\left(T_a - T_{w,tp}\right),$$

For both zones: water energy conservation in the condenser volume

$$C_{cw}\rho_{cw}V\frac{dT_{hw}}{dt} = A_{o,s}\frac{L_v}{L_t}\alpha_o\left(T_{w,v} - T_{hw}\right) + A_{o,s}\frac{L_{tp}}{L_t}\alpha_o\left(T_{w,tp} - T_{hw}\right) + \dot{m}_{cw}C_{cw}(T_{cw} - T_{hw}), \tag{3.55}$$

where subscript cw represents inlet cold water, hw represents output hot water.

Expansion Valve

The thermal expansion valve is a device that controls the amount of refrigerant released into the evaporator and is intended to regulate the superheat of the refrigerant that flows out of the evaporator to a steady value [84]. The mass flow rate is calculated from the pressure differences between the input and output with Bernoulli's principle, as in (3.56). Assuming an electronic expansion valve is used, then A_{ev} is decided based on a superheat control logic. In this model, we assume the conventional PI controller is used for superheat control, as shown in (3.57):

$$\dot{m}_{out} = A_c k_2[\rho_{in}(p_{out} - p_{in})], \tag{3.56}$$

$$A_c = k_p(T_{sh}^* - T_{sh}) + k_i\int(T_{sh}^* - T_{sh})dt, \tag{3.57}$$

where subscript sh represents superheat; parameter k_2 is an empirical constant.

3.1.3 Overall Model Structure

After building all component models as multi-input-multi-output (MIMO) systems, the next step is to assemble all MIMOs into the multi-physics ASHP model. The electrical subsystem can be assembled according to the input-output mapping shown in Fig. 3-3, while the thermal subsystem map is shown in Fig. 3-4. The overall model inputs are $v_{g,abc}$, ω_m^*, and operatin condition variables such as T_a, T_{cw}, $\dot{m}_{cw}$, and T_{sh}^*. The overall model outputs include but are not limited to $i_{g,abc}^*$, P_m, and T_{hw}.

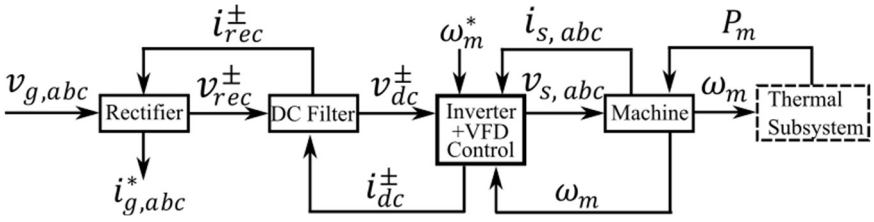

Figure 3-3 An overview of the electrical subsystem structure.

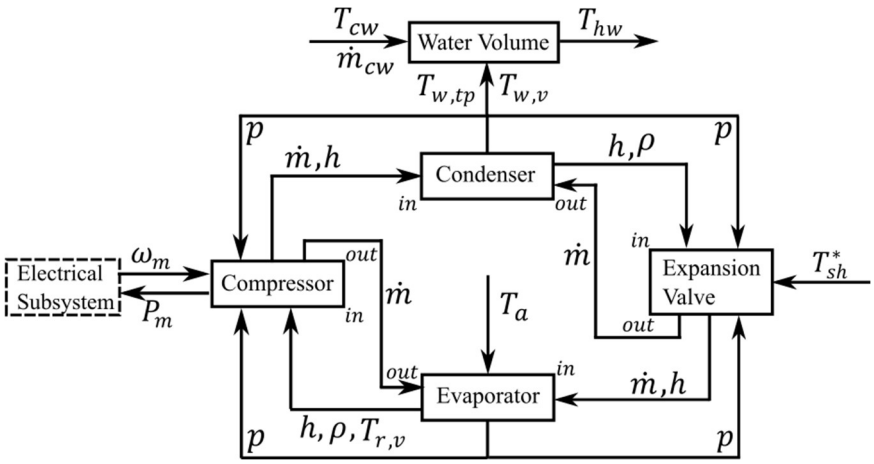

Figure 3-4 An overview of the thermal subsystem structure.

The overall model inputs are $v_{g,abc}$, ω_m^*, and operatin condition variables such as T_a, T_{cw}, $\dot{m}_{cw}$, and T_{sh}^*. The overall model outputs include but are not limited to $i_{g,abc}^*$, P_m, and T_{hw}, which covers both the electrical and thermal domains.

3.2 PHIL Emulation of Heat Pump Dynamics for Control Validation

Scientific Context

Validating FFR controllers of distributed ASHPs in an actual power grid is essential because FFR-level control has strict stability requirements. Traditional power system laboratories, designed primarily for electrical system testing, often face hardware limitations regarding sector coupling systems such as heat pumps [85]. It is noteworthy to mention that while commercial ASHPs can be bought, they come with inherent limitations, such as non-transparent internal controllers, sensing data shortage, and unchangeable slow response speed. These problems undermine their suitability in testing FFR control strategies.

For a thorough assessment of FFR controllers under thermal hardware limitations, realistic dynamic behavior of distributed ASHPs should be produced with emulators that can interface with a real grid. In this context, PHIL systems emerge as an alternative way to emulate physical hardware and test the designed controllers [86]. PHIL emulations overcome the thermal equipment shortage problem by replicating the detailed dynamic behavior of heat pumps in real-time, allowing researchers to observe their performance within actual power grid conditions.

The key to effective emulation is the preservation of the response's non-linearity and accurate replication of the current profile at the grid-interfacing point, while maintaining an acceptable computational burden for real-time implementation. The following paper provides one possible way of real-time implementation of the full dynamic model presented in Section 3.1 with detailed reasoning on platform choices, execution frequencies, and subsystem coupling. The emulation experiments were performed in our active distribution grid laboratory, where the emulation accuracy on grid-interfacing current and real power profiles were examined.

Publication #2: Power-Hardware-in-the-Loop Validation of Air-Source Heat Pump for Fast Frequency Response Applications

Authors: Ruihao Song, Anurag Mohapatra, Thomas Hamacher, Vedran Peric

Publication: Electric Power Systems Research (EPSR)

Digital object identifier: 10.1016/j.epsr.2024.110754

Author	Contribution	Tasks
Ruihao Song	65%	• Conceptualization • Methodology • Investigation • Writing-original draft • Writing-review & editing
Anurag Mohapatra	20%	• Experimental support • Writing-review & editing
Thomas Hamacher	5%	• Supervision • Funding acquisition
Vedran Peric	10%	• Supervision • Writing-review & editing

Electric Power Systems Research 235 (2024) 110754

Contents lists available at ScienceDirect

Electric Power Systems Research

journal homepage: www.elsevier.com/locate/epsr

Power-hardware-in-the-loop validation of air-source heat pump for fast frequency response applications

Ruihao Song *, Anurag Mohapatra, Thomas Hamacher, Vedran S. Perić

Munich Institute of Integrated Materials, Energy, and Process Engineering, Technical University of Munich, Garching, Germany

ARTICLE INFO

Keywords:
air-source heat pump
demand-side response
dynamic modeling
power-hardware-in-the-loop
fast frequency response

ABSTRACT

This paper presents a standard power-hardware-in-the-loop testing platform to simulate detailed air-source heat pump dynamics based on well-established modeling knowledge. Distributed air-source heat pumps can be potentially used for fast frequency response. However, using air-source heat pumps for rapid modulation cannot be based on the current assumptions of linear speed-power transient characteristics developed for low-speed temperature control applications. Customized setups with experimental validation options are needed to design the new fast frequency response compatible heat pump controllers. Most power system laboratories struggle to build a customized air-source heat pump, which hinders research progress. The proposed platform is relatively universal, can fit different heat pumps with minor modifications, and can be implemented on standard PHIL emulators in power system laboratories. Emulation results, real-time implementation details, and model complexity metrics are presented to assist in the transference of the setup to other laboratories.

1. Introduction

1.1. Backgrounds

In the ongoing efforts to curtail greenhouse gas emissions, there is a growing momentum towards electrifying heating in residential structures using air-source heat pump (ASHP) technology [1]. This transition to ASHPs results in tighter power and heating systems integration, enabling combined operations that enhance efficiency and resilience. The fast-responding potential of distributed ASHPs presents numerous opportunities for improving power grid performance by allowing them to operate in high-speed demand-side response (HSDSR) mode for fast frequency response (FFR) ancillary services [2,3]. Thus, the inertia of the power grid can be enhanced, and the expenditure associated with FFR battery systems can be reduced. HSDSR feature is highly demanding on transient performance and requires careful experimental validation. Unfortunately, specialized sector-coupling equipment such as ASHPs are generally unavailable in default power system laboratories, and commercial ASHPs are very expensive and poor in terms of customization capability. Therefore, handling the ASHP equipment shortage problem in power system laboratories is critical before the later FFR controller design stage.

Power Hardware-In-The-Loop (PHIL) experiments are typically carried out to safeguard the electrical grid against the unpredictable behaviors of physical devices under test. However, PHIL systems offer the unique capability to function as "virtual equipment" via dynamic electrical emulation, which has become increasingly popular for sector coupling research [4,5,6]. This innovative approach uses well-accepted physics-based dynamic modeling techniques to determine the virtual equipment's grid-interfacing current, making it adaptable to an extensive range of working conditions and equipment configurations [7]. The generated current reference is then executed by PHIL emulators, effectively mimicking the actual equipment behavior. As a result, from the grid's standpoint, the distinction between actual and virtual equipment becomes indiscernible. Within this context, PHIL is a pivotal technology in overcoming hardware constraints while developing ASHP-based FFR services. Nevertheless, the cornerstone of creating effective virtual equipment lies in dynamic modeling. Since PHIL experiments operate in real-time, developing an HSDSR-compatible ASHP model poses a significant challenge. It necessitates a balance between dynamic accuracy and computational burden.

Despite the growing awareness of the pivotal role of ASHPs, current ASHP models exhibit notable deficiencies in accurately capturing the non-linear power transient characteristics needed by designing HSDSR control, thereby obstructing the utilization of their flexibility potentials. The physical structure of a typical distributed ASHP is shown in Fig. 1,

* Corresponding author.
E-mail address: ruihao.song@tum.de (R. Song).

https://doi.org/10.1016/j.epsr.2024.110754
Received 30 September 2023; Received in revised form 19 February 2024; Accepted 17 June 2024
Available online 4 July 2024

where the system can be divided into electrical and thermal subsystems. On the one hand, most ASHP models used in electrical power systems research are either static or quasi-static, primarily designed for hourly simulation and optimal power-flow calculations. Existing dynamic models often rely on constant linear time-invariant systems to represent both electrical and thermal subsystems in a lumped manner, which fails to capture the non-linear behavior in HSDSR scenarios accurately [8]. On the other hand, in the area of compression-based refrigeration systems, well-established modeling methodologies exist for the non-linear dynamics of the thermal subsystem [9,10,11] in ASHPs. Yet, the electrical subsystem is neglected as the focus of the study is not electrical power.

1.2. Contributions

This paper proposes a PHIL solution that can emulate the non-linear transient behaviors of distributed ASHPs based on fundamental physics and mathematics. We summarize our contributions as follows:

- The developed model is a multi-physics model that incorporates methods that are well-validated in the known literature.
- We used one case study (15 kW, air-to-water type, R134a refrigerant) to show that the developed ASHP model has an acceptable computational burden and can be deployed and simulated in real-time at kHz rate.
- The developed model can run in a standard PHIL platform [12,6] for experiments on an active distribution grid.

The rest of this paper is organized as follows. In section II, we describe the reason for selecting specific modeling methods. In section III, we introduce the complete PHIL implementation process of the constructed model. In section IV, we show the experimental results in our laboratory environment. Finally, we give the conclusion of this paper in section V.

2. Modeling methods

Currently, commercially available modules are designed for maintaining a designated supply water temperature. Therefore, the modulation speed of the variable-frequency drive (VFD) is kept slow as output temperature control does not require rapid modulation. In this context, the non-linear characteristics of the refrigerant circulation system are covered by the slow ramping modulation, thus creating a phenomenon of linear speed-power response characteristics among all working conditions. For example, we tested the speed-power step response of a 4 kW distributed ASHP (WOLF MONOBLOCK) in our laboratory at different working conditions, and the results shown in Fig. 2 suggest linear characteristics, which can justify a transfer function model. However, challenges emerge if the slow ramping style of modulation is insufficient for the application case, such as FFR services.

In the context of FFR, the modulation speed limit of modern ASHPs needs to be removed, and the response will be non-linear at different working conditions. Besides, HSDSR has a harsher transient performance requirement regarding oscillation and stability, as a poorly tuned controller can lead to grid instability. To study how to implement HSDSR on ASHPs, we must carefully model all necessary non-linear behaviors to ensure a feasible controller design. In this paper, we propose to develop a standard ASHP model structure for FFR applications, and the goals are listed as follows.

- The model should be relatively universal and match different ASHPs from simple parameter tuning.
- The model should be physics-based and reflect the ASHP power response non-linearity at different working conditions.

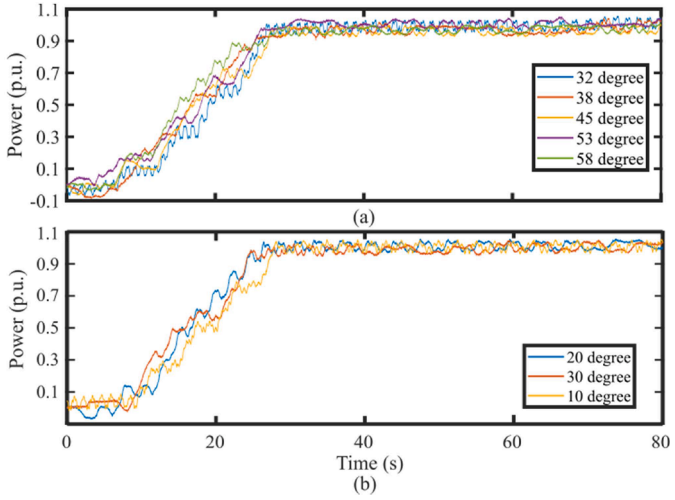

Fig. 2. Speed-power response characteristics of a typical commercial ASHPs (normalized): (a) at different cold water temperatures; (b) at different air temperatures.

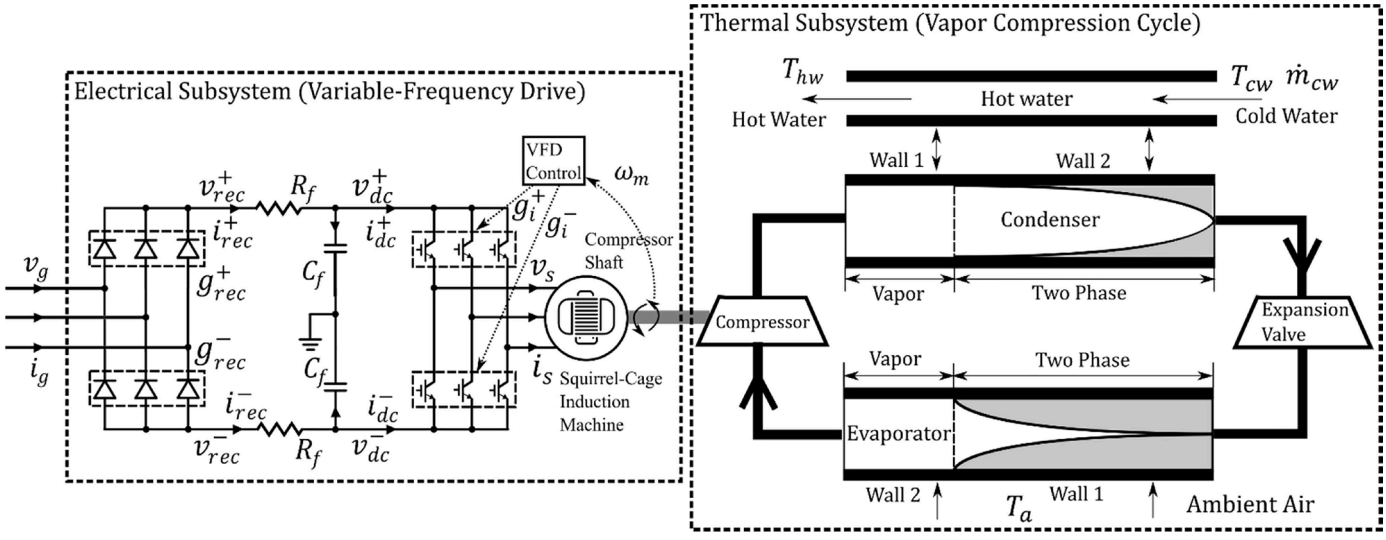

Fig. 1. Physical structure of a typical distributed ASHP (see Appendix for the nomenclature).

- The model should be computationally tractable and be deployed in real-time for HIL and PHIL tests.
- All used modeling methods should originate from the previously validated literature.

We separate the ASHP model into electrical and thermal subsystems to reduce the computational burden due to their different transient rates. Table 1 lists all mainstream methods for the electrical and thermal subsystems separately. The electrical VFD and its modeling are standardized in the power system area, and the differences are only in the level of detail. As we are not interested in the detailed noise profile of the grid-side current, we adopt the KCL/KVL plus switching-function level to model the VFD system [13].

For the thermal subsystem, the choice is between the moving boundary model and the finite volume model because we need an accurate description of mechanical load power transients, which are predominately determined by pressures in the evaporator and condenser. The finite volume method is more precise in refrigerant temperature and specific enthalpy spatial distribution in the condenser and evaporator. Still, that information has little value for the HSDSR controller application. Additionally, one can note that the computational effort needed for the moving boundary model is significantly lower than the finite volume model. A comprehensive comparison between these two modeling methods is done for a 300 kW R134a chiller [16]. The authors mentioned that the moving boundary model executed about three times faster than the finite volume model while maintaining nearly identical accuracy in steady-state and trainset estimations, as shown in Fig. 3. Based on the provided information, the optimal choice is the moving boundary method for the thermal subsystem.

3. PHIL Implementation

3.1. Model building

The detailed model structure is shown in Fig. 4, and all the fundamental equations for model programming can be found in the Appendix. The electrical subsystem requires the mechanical load power from the thermal subsystem to calculate the load torque on the machine shaft. In contrast, the thermal subsystem requires the shaft speed to calculate the mechanical load power; therefore, the two subsystems are coupled. The overall model input is the speed modulation signal, grid-side voltage waveform, working condition measurements, and superheat reference for the thermal expansion valve. The model output contains but is not limited to grid-side current waveform, mechanical load power, and heated water temperature.

Table 1
Existing mainstream models for electrical and thermal subsystems from the literature base.

Electrical subsystem	Machine speed	Grid-side current	Computation
Transfer function	Accurate	N/A	Low
KCL/KVL + switching function [13]	Accurate	Less accurate for the current noise profile	Medium
KCL/KVL + detailed switching	Accurate	Accurate	High
Thermal subsystem	**Mechanical load**	**Internal states**	**Computation**
Single-phase flow model [14]	Less accurate in both dynamics and steady states	N/A	Low
Hammerstein-Wiener model [15]	Less accurate in dynamics, accurate in steady-states	N/A	Low
Moving boundary model [9,10,11]	Accurate	Less accurate with lumped variables	Medium
Finite volume model [16,17]	Accurate	Accurate	High

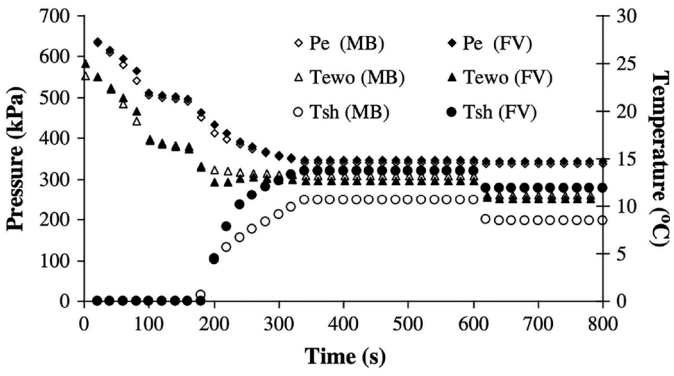

Fig. 3. Finite volume v.s. Moving boundary methods, start-up, and load-change transients [16].

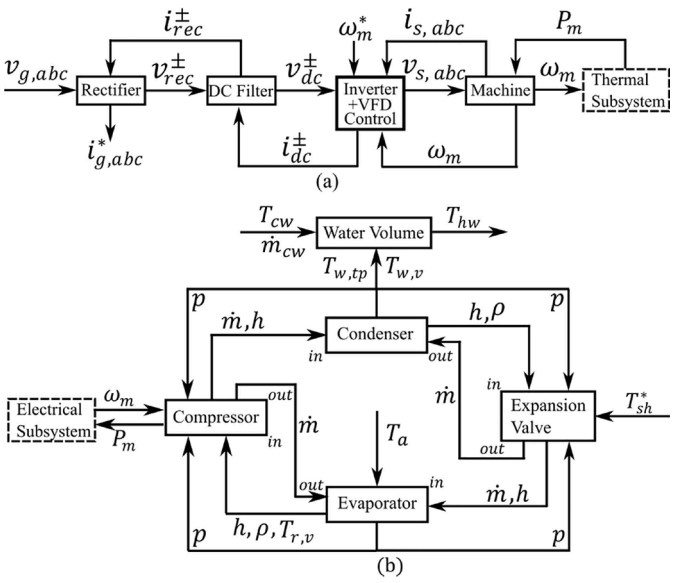

Fig. 4. Model structure of the proposed model (see Appendix for the nomenclature): (a) electrical subsystem; (b) thermal subsystem.

The electrical subsystem is straightforward to construct as the modeling process is already standardized. We chose Matlab/Simulink as the platform to establish the electrical subsystem because it is widely used in power system research areas. We make the model based on the typical physical structure described in Fig. 1a with standard components in the Simscape Specialized Power System Library. Then, we summarize all components with mathematical equations to reduce the computational effort.

The thermal subsystem is relatively complicated to build compared with the electrical subsystem. To model the non-linear flow in the single-cycle refrigerant circulation system, at least mass and energy conservation partial differential equation (PDE) systems need to be solved along the axial direction of the pipe. The moving boundary method simplifies the PDE systems into ordinary differential equation (ODE) systems by dividing the non-linear flow region into length-variant zones where each represents a specific refrigerant state, such as vapor and two-phase mixture zones. This results in a high-order ODE system with coefficients related to media thermal dynamic properties. Modelica

environment (Dymola) is the suitable platform to build such systems for the following two reasons. Firstly, it can solve complex ODE systems without manually combining and arranging all equations. Secondly, it has standard refrigerant media libraries that can work as look-up tables to extract the necessary thermal dynamic property coefficients during real-time model calculation.

3.2. Model deployment

Considering that Matlab/Simulink has better compatibility with standard PHIL setups, we packaged the thermal subsystem model in Dymola with S-function (Dymola block) and coupled these two subsystems on Simulink. This paper uses The Euler solver for both subsystems to lower the computational burden. We must select appropriate computation frequencies for both subsystems to deploy the combined model into the target real-time environment. Choosing a value for the electrical subsystem first is suggested as the non-linear current calculation is more sensitive to the computational frequency. We simulate the electrical subsystem without the thermal subsystem (constant load torque) at several frequencies, as shown in Fig. 5 and Table 2 for time and frequency domain, respectively. The results suggest that the lower threshold to keep a decent accuracy is roughly 8 kHz, while the upper threshold is flexible based on the concerned main harmonic bandwidth. In this paper, 10 kHz is selected for the electrical subsystem.

We tend to choose a slower frequency for the thermal subsystem as the thermal dynamics of ASHP are significantly slower than those of its electrical peers. The combined model has a risk of instability if the frequency for the thermal subsystem is too low, while the model can also exceed real-time capacity if it is too high. Therefore, we choose to deploy it at roughly the minimum frequency to ensure model stability, which is 200 Hz with our parameter set. For other parameter sets, the appropriate frequency can be obtained by simulation tests in the Simulink environment.

After fixing the computational frequencies, both subsystems should be compiled and loaded in the real-time environment through C code DLL files. The execution priority should be configured as thermal over electrical subsystems to ensure a smooth start-up. The mechanical speed ω_m and load power P_m should be exchanged between two subsystems through clocked channels.

3.3. PHIL configuration for the virtual heat pump

The proposed ASHP PHIL emulation platform is used for validating specially designed HSDSR controllers in a realistic grid environment, as shown in Fig. 6a. The developed model is deployed on a NI-PXIe-8880 real-time calculator (Fig. 6b), which runs on PharLap and interfaces with the host PC through the Veristand platform. The calculation result, which is the grid-interfacing current of the virtual heat pump, is sent as a set-point to the Egston (Fig. 6c) COMPISO System Unit (CSU) for execution. During the HSDSR control validation experiment, the controller under test (with the PLL) reads voltage details at the local bus and current shaft power of the virtual ASHP and injects the control signal ω_m^* to the proposed virtual heat pump system. This setup

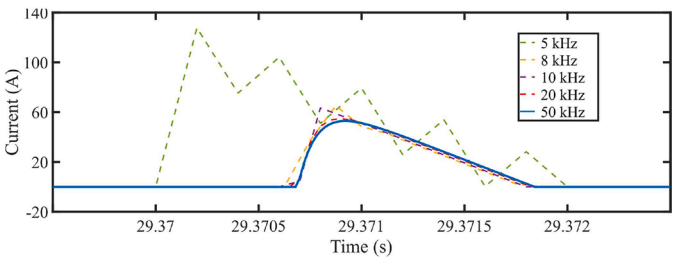

Fig. 5. Grid-side current waveform in the electrical subsystem at different execution frequencies.

Table 2
Main components of grid-side current in frequency domain under different model execution frequencies.

	Funda.	3	5	7	9	11	13
50 kHz	7.098	6.913	6.553	6.042	5.411	4.697	3.946
20 kHz	7.099	6.917	6.564	6.063	5.443	4.742	4.003
10 kHz	7.08	6.908	6.574	6.098	5.506	4.835	4.124
8 kHz	7.109	6.932	6.587	6.097	5.492	4.808	4.089
5 kHz	9.328	8.728	7.615	6.15	4.536	2.997	1.761

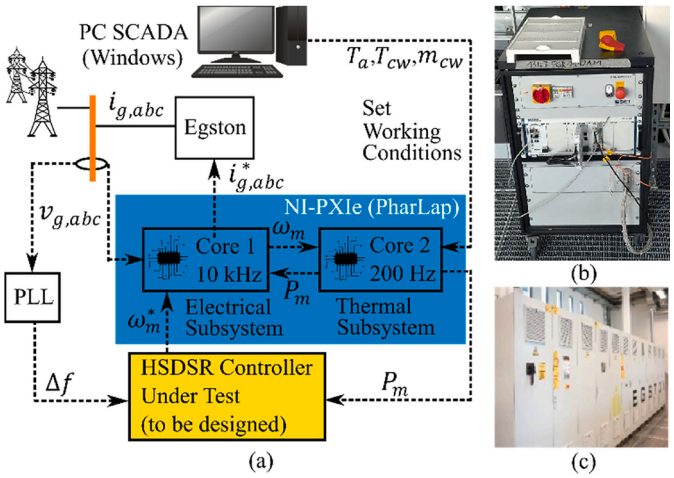

Fig. 6. PHIL emulation of a virtual heat pump for HSDSR design: (a) Setup illustration; (b) NI-PXIe-8880 real-time simulator; (c) Egston CSU;.

establishes a realistic ancillary service test environment. Although the equipment supplier could be diverse, the mentioned application scenario can be migrated to most power system laboratories, generally equipped with real-time simulators and PHIL test beds. Details on our lab specifications and their universality can be found in [6].

4. Results

4.1. Advantages over traditional models

In this subsection, we aim to show that the proposed modeling methodology for ASHP systems offers superior performance to traditional modeling techniques in designing HSDSR controllers. The evaluation of model suitability for FFR services necessitates focusing on power step response analysis instead of the conventional assessment through half-minute or minute-level ramping. This shift in evaluation criterion is attributed to the harsh response time requirements of FFR services, which mandate a response time of 1–2 seconds, in contrast to the more lenient timeframes of 30 seconds and 15 minutes associated with primary and secondary services, respectively. The suitability of ASHP models is assessed from two critical dynamic characteristics of the power response profile: the normalized transient shape and steady-state gain. Moreover, given the variability in working conditions of ASHP systems, specifically fluctuations in air and return water temperatures within specific permissible ranges, it is essential to demonstrate the model's suitability based on an assumption of uncertain working conditions.

We simulate the proposed model for ramping and step responses at four working conditions. In the ramping scenario, the resulting close-to-linear response (Fig. 7a) is similar to what we observed from our commercial ASHP (Fig. 2), which can still be described by traditional models as the response differences between diverse working conditions are negligible. However, in the step response simulation, the proposed model shows strong non-linearity that significantly exceeds the

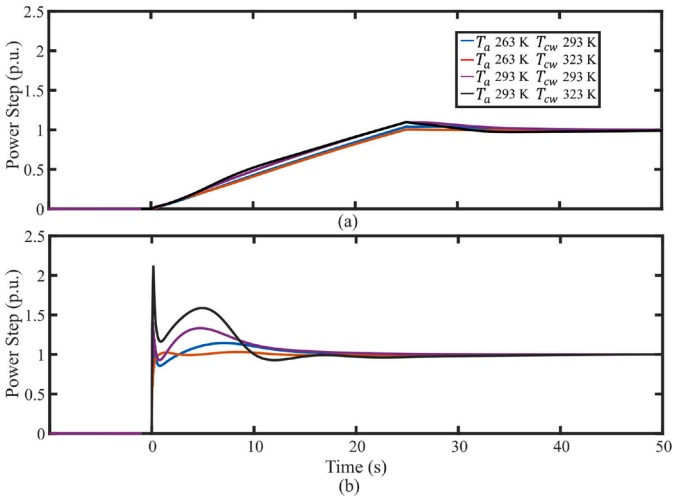

Fig. 7. Speed-power response simulation result of the proposed model at different working conditions (normalized), modulation changing from 50 %-100 %: (a) via a 25 s ramp; (b) via a sudden step.

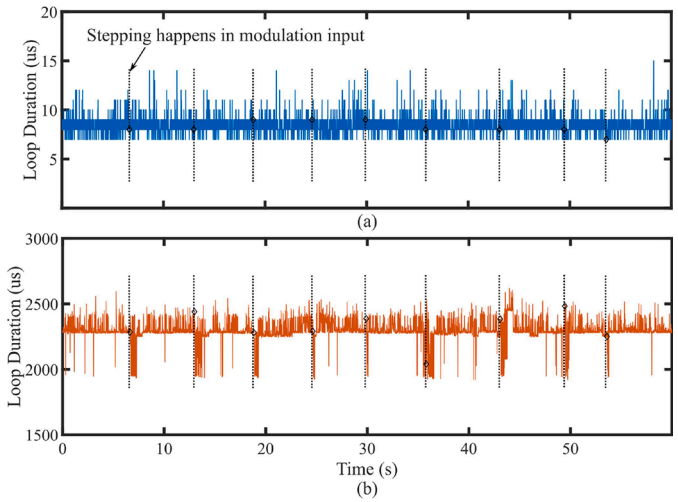

Fig. 8. Actual time to finish one computation step: (a) electrical subsystem; (b) thermal subsystem.

capability of traditional models (Fig. 7b). Table 3 summarizes the performance differences between traditional models and the proposed model under diverse demand-side response scenarios. Based on the presented results, it is apparent that the proposed model provides better insights for the target HSDSR controller design application.

4.2. PHIL results

In this subsection, we aim to show the PHIL emulation results of the virtual heat pump system in our CoSES laboratory. The overall model is deployed with the computation frequencies mentioned in the last section on our PXIe-8880 system, which has Intel(R) Xeon(R) E5–2618 L as CPU at 2.30 GHz and 3 GB of RAM. The actual loop duration to finish every computation iteration is shown in Fig. 8a for the electrical subsystem and Fig. 8b for the thermal subsystem in a one-minute test, where stepping on the modulation input is also applied. With an averaged CPU load of 24 % and 0.5 GB of RAM usage, the electrical subsystem has an average loop time of roughly 8.42 us (< 9 % of target), while the thermal subsystem has an average of 2296.8 us (< 46 % of target). These results indicate a stable real-time operation on the PXIe system, making it eligible for our emulation purposes.

The comparison between the theoretical and experimental current waveform in the time domain is shown in Fig. 9a. We can roughly see that the two waveforms are in similar shapes but with a short delay caused by the Egston CSU internal control system processing. To identify the error, the model output $i^*_{g,abc}$ and experimental result $i_{g,abc}$ are plotted

Table 3
The proposed ASHP model V.S. traditional ASHP models in terms of power response (for uncertain working conditions).

	Step response (HSDSR)	Ramp response (30 s)	Ramp response (mins)
Quasi-static models [18, 19]	Tran.: Mismatch S.S.G: Accurate	Tran.: Mismatch S.S.G: Accurate	Tran.: Accurate S.S.G: Accurate
Constant transfer function/state-space models [20,21]	Tran.: Mismatch S.S.G: Mismatch	Tran.: Accurate S.S.G: Mismatch	Tran.: Accurate S.S.G: Mismatch
Hammerstein-Wiener models [8,22]	Tran.: Mismatch S.S.G: Accurate	Tran.: Accurate S.S.G: Accurate	Tran.: Accurate S.S.G: Accurate
Proposed model	Tran.: Accurate S.S.G: Accurate	Tran.: Accurate S.S.G: Accurate	Tran.: Accurate S.S.G: Accurate

* Tran.: normalized transient shape; S.S.G: steady-state gain;

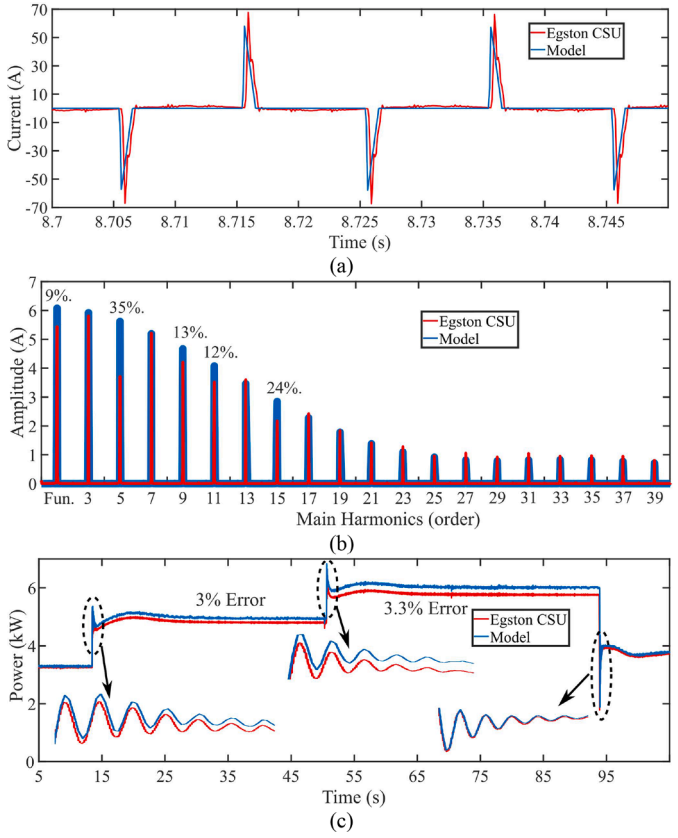

Fig. 9. PHIL performance evaluation: (a) theoretical and experimental current waveform in the time domain; (b) comparison in the frequency domain; (c) real power profile comparison in a modulation period;.

in the frequency domain, as shown in Fig. 9b. We see that the CSU current $i_{g,abc}$ results in an error as the CSU cannot perfectly track the requested current waveform $i^*_{g,abc}$, and most error is on higher order harmonics such as 5th (35 %), 15th (24 %), 9th (13 %), and 11th (12 %). The error can be diverse in other laboratories depending on the tracking speed of the used PHIL hardware.

We then evaluate the ASHP PHIL system performance during a modulation stepping period and check whether the PHIL system can

reproduce the real power profile calculated by the real-time simulator, as shown in Fig. 9c. It is evident that the PHIL system matches the model output with a specific steady-state error, caused by the CSU imperfect current tracking. These problems should be tackled with an equipment-specific compensation factor to adjust the $i^*_{g,abc}$ sent to the hardware. However, we also note that the PHIL system's speed-power transient characteristics are well preserved.

5. Conclusions

This paper identified a gap in ASHP modeling literature that is generally unsuitable for FFR applications in ADG. We proposed a way to simulate the physical non-linear behavior of ASHP during rapid modulation and provide PHIL emulation results. Our model uses existing methods in electrical and mechanical engineering fields to develop a standard physics-based non-linear model that can apply to most distributed ASHPs via parameter tuning. The model was tested with one set of parameters and deployed in the CoSES laboratory PHIL environment. The results suggest that the PHIL experiment can demonstrate the target non-linear behavior on a real active distribution grid with an acceptable real-time computational burden. Our model can be used to mitigate thermal equipment insufficiency in power system laboratories, which generally possess a real-time simulator with PHIL capabilities.

CRediT authorship contribution statement

Ruihao Song: Conceptualization, Data curation, Formal analysis, Investigation, Methodology, Validation, Visualization, Writing – original draft, Writing – review & editing. **Anurag Mohapatra:** Resources, Software, Validation, Writing – review & editing. **Thomas Hamacher:** Funding acquisition, Supervision. **Vedran S. Perić:** Supervision, Writing – review & editing.

Declaration of competing interest

The authors declare that they have no known competing financial interests or personal relationships that could have appeared to influence the work reported in this paper.

Data availability

Data will be made available on request.

Acknowledgment

Ruihao Song is supported by the Bavarian Research Foundation through the project "Secto coupling und Microgrids (STROM, AZ-1473–20)". Dr. Vedran S. Perić is supported by Deutsche Forschungsgemeinschaft (DFG) through the project "Optimal Operation of Integrated Low-Temperature Bidirectional Heat and Electric Grids (IntElHeat, 450821044)".

Appendix

Model equations of the electrical subsystem [11]

Rectifier (Diode)

$$v^+_{rec} = \max\left(v_{g,a}, v_{g,b}, v_{g,c}\right),\ v^-_{rec} = \min\left(v_{g,a}, v_{g,b}, v_{g,c}\right)\ ,\ i^*_{g,abc} = i^+_{rec} g^+_{rec,abc} + i^-_{rec} g^-_{rec,abc},$$

$$g^+_{rec,a} = \begin{cases} 1 & v_{g,a} > v_{g,b} \cap v_{g,a} > v_{g,c} \\ 0 & else \end{cases},\ g^-_{rec,a} = \begin{cases} 1 & v_{g,a} < v_{g,b} \cap v_{g,a} < v_{g,c} \\ 0 & else \end{cases}.$$

Dc filter (RC)

$$R_f i^\pm_{rec} = v^\pm_{rec} - v^\pm_{dc},\ i^+_{rec} \geq 0,\ i^-_{rec} \leq 0,\ C_f \frac{dv^\pm_{dc}}{dt} = i^\pm_{rec} - i^\pm_{dc}.$$

Inverter and Control (Three-level, V/f)

$$v_{s,abc} = \frac{1}{2} g^+_{i,abc} v^+_{dc} + \frac{1}{2} g^-_{i,abc} v^-_{dc},\quad i^+_{dc} = \frac{1}{2}\left(g^+_{i,a} i_{s,a} + g^+_{i,b} i_{s,b} + g^+_{i,c} i_{s,c}\right),\ i^-_{dc} = \frac{1}{2}\left(g^-_{i,a} i_{s,a} + g^-_{i,b} i_{s,b} + g^-_{i,c} i_{s,c}\right),\ g^+_{i,abc} = -g^-_{i,abc},$$

$$f = k_p\left(\omega^*_m - \omega_m\right) + k_i \int \left(\omega^*_m - \omega_m\right) dt,\ \ g^+_{i,a} = \frac{k_\varphi f \sin(2\pi f)}{\bar{v}_{dc}}.$$

Machine (squirrel-cage induction machine)

$$\frac{d\varphi_{s,q}}{dt} = v_{s,q} - R_s i_{s,q} - \omega_e \varphi_{s,d},\quad \frac{d\varphi_{s,d}}{dt} = v_{s,d} - R_s i_{s,d} + \omega_e \varphi_{s,q},\quad \frac{d\varphi'_{r,q}}{dt} = v'_{r,q} - R'_r i'_{r,q},\quad \frac{d\varphi'_{r,d}}{dt} = v'_{r,d} - R'_r i'_{r,d},$$

$$\varphi_{s,q} = \left(L_{l,s} + L_{mg}\right) i_{s,q} + L_{mg} i'_{r,q},\ \varphi_{s,d} = \left(L_{l,s} + L_{mg}\right) i_{s,d} + L_{mg} i'_{r,d},\ \varphi'_{r,q} = \left(L'_{l,r} + L_{mg}\right) i'_{r,q} + L_{mg} i_{s,q},\ \varphi'_{r,d} = \left(L'_{l,r} + L_{mg}\right) i'_{r,d} + L_{mg} i_{s,d},$$

$$J \frac{d\omega_m}{dt} = T_e - k_F \omega_m - T_{load},\ T_e = 1.5p\left(\varphi_{s,d} i_{s,q} + \varphi_{s,q} i_{s,d}\right),\ T_{load} = \frac{P_m}{\omega_m}$$

• **Variables:** v: Voltage; i: Current; g: Gate-equivalent function; R: Resistance; C: Capacitance; ω: Rotational speed; φ: Flux; L: Inductance; p: Pole-pairs; T:Torque; J: Moment of inertia; f: Frequency; k: Constants.

• **Subscripts:** *g*: Grid; *rec*: Rectifier; *f*: Filter; *i*: Inverter; *m* : Mechanical; *e*: Electrical; *c*: Cross-section; *s*: Stator; *r*: Rotor;*mg*: Magnetizing; *F*: Friction; *ls*: Leakage.
• **Superscripts:** *: Reference; ′: Referred to the stator side; +/−: Variable polarity.

Model equations of the thermal subsystem [6]

Eva.	Mass conservation	Energy conservation (refrigerant)	Energy conservation (wall)
Two-phase zone (1^{st})	$\left(\frac{d\rho_v'}{dp}\bar{\gamma}+\frac{d\rho_l'}{dp}(1-\bar{\gamma})\right)A_{i,c}L_{tp}\frac{dp}{dt}+\dot{m}_b-\dot{m}_{in}$ $+\left(\rho_l'-\rho_v'\right)(1-\bar{\gamma})A_{i,c}\frac{dL_{tp}}{dt}=0.$	$\left(\left(\frac{d\rho_v'}{dp}h_v+\frac{dh_v'}{dp}\rho_v\right)\bar{\gamma}+\left(\frac{d\rho_l'}{dp}h_l+\frac{dh_l'}{dp}\rho_l\right)(1-\bar{\gamma})-1\right)$ $A_{i,c}L_{tp}\frac{dp}{dt}+(\rho_l h_l-\rho_v h_v)(1-\bar{\gamma})A_{i,c}\frac{dL_{tp}}{dt}+\dot{m}_b h_b$ $-\dot{m}_{in}h_{in}=A_{i,s}\frac{L_{tp}}{L_t}\alpha_{i,tp}(T_{w1}-T_{r1}).$	$A_{i,s}\frac{L_{tp}}{L_t}\alpha_{i,tp}(T_{r,tp}-T_{w,tp})+A_{o,s}\frac{L_{tp}}{L_t}\alpha_o(T_a-T_{w,tp})$ $=C_w\rho_w(A_{o,c}-A_{i,c})L_{tp}\frac{dT_{w,tp}}{dt}.$
Vapor zone (2^{nd})	$\left(\frac{\partial\rho_v}{\partial p}\|_{h_v}+\frac{1}{2}\frac{\partial\rho_v}{\partial h_v}\|_p\frac{dh_v'}{dp}\right)A_{i,c}L_v\frac{dp}{dt}+\dot{m}_{out}-\dot{m}_b$ $+\left(\rho_v'-\rho_v\right)A_{i,c}\frac{dL_{tp}}{dt}+\frac{1}{2}\frac{\partial\rho_v}{\partial h_v}\|_pA_{i,c}L_v\frac{dh_{out}}{dt}=0.$	$A_{i,c}L_v\frac{dp}{dt}\left(\left(\frac{\partial\rho_v}{\partial p}\|_{h_v}+\frac{1}{2}\frac{\partial\rho_v}{\partial h_v}\|_p\frac{dh_v'}{dp}\right)h_v+\frac{1}{2}\frac{dh_v'}{dp}\rho_v-1\right)$ $+\frac{1}{2}\left(\frac{\partial\rho_v}{\partial h_v}\|_ph_v+\rho_v\right)A_{i,c}L_v\frac{dh_{out}}{dt}+\dot{m}_{out}h_{out}-\dot{m}_bh_b$ $+(\rho_v'h_v'-\rho_vh_v)A_{i,c}\frac{dL_{tp}}{dt}=A_{i,s}\frac{L_v}{L_t}\alpha_{i,v}(T_{w,v}-T_{r,v}).$	$C_w\rho_w(A_{o,c}-A_{i,c})L_v$ $\left(\frac{dL_{tp}}{dt}\frac{T_{w,tp}-T_{w,v}}{L_v}+\frac{dT_{w,v}}{dt}\right)$ $=A_{i,s}\frac{L_v}{L_t}\alpha_{i,v}(T_{r,v}-T_{w,v})$ $+A_{o,s}\frac{L_v}{L_t}\alpha_o(T_a-T_{w,v}).$

Con.	Mass conservation	Energy conservation (refrigerant)	Energy conservation (wall)	Energy conservation (water)
Vapor zone	…	…	…	
Two-phase zone	…	…	…	$C_{cw}\rho_{cw}V_{cw}\frac{dT_{hw}}{dt}=A_{o,s}\frac{L_v}{L_t}\alpha_o(T_{w,v}-T_{hw})$ $+A_{o,s}\frac{L_{tp}}{L_t}\alpha_o(T_{w,tp}-T_{hw})+\dot{m}_{cw}C_{cw}(T_{cw}-T_{hw})$
Comp.	$P_m=\underbrace{\left(\frac{\omega_m}{2\pi}V_{comp}\rho_{in}\eta\right)}_{MassFlow}\underbrace{\left(\frac{k_1RT_{in}}{k_1-1}\left(\left(\frac{p_{out}}{p_{in}}\right)^{\frac{k_1-1}{k_1}}-1\right)\right)}_{\Delta h}$			
Exp. Valve	$\dot{m}_{out}=A_{ori}k_{ev}\sqrt{\rho_{in}(p_{out}-p_{in})}$ $A_{ori}=k_3(T_{sh}^*-T_{sh})+k_4\int(T_{sh}^*-T_{sh})dt+A_{base}$			

• **Abbreviations**: Eva. = Evaporator; Con. = Condenser; Comp. = Compressor; Exp. = Expansion.
• **Variables:** ρ: Density; p: Pressure; h: Specific enthalpy; $\dot{m}$: Massflow; $\bar{\gamma}$: Average vapor fraction; A: Cross-section area; L: Zone length; α: Heat transfer coefficient; C: Specific heat; T: Temperature; P: Power; V: Volume; ω: Speed; η: Efficiency; R: Gas constant; k: Constants.
• **Subscripts**: *v*: Vapor; *l*: Liquid; *c*: Cross-section; *s*: Surface; *i*/*o* : Inner/Outter; *t*: Total; *tp*: Two-phase zone; *r*: refrigerant; *w*: Wall; *a*: Air; *b*: Boundary between two-phase and vapor zone; *in*/*out*: Input/Output; *cw*: Cold water; *hw*: Hot water; *sh*: Superheat, *ori*: Orifice.
• **Superscripts**: $*$: Reference; $'$: Variables in saturation state.

References

[1] International Energy Agency, "The future of heat pumps." [Online]. Available: https://www.iea.org/reports/the-future-of-heat-pumps.
[2] R. Song, T. Hamacher, V. Terzija, V.S. Perić, Potentials of using electric-thermal sector coupling for frequency control: A review, Int. J. Electr. Power Energy Syst. 151 (2023) 109194, https://doi.org/10.1016/j.ijepes.2023.109194. Sep.
[3] Y.-J. Kim, J. Wang, Power hardware-in-the-loop simulation study on frequency regulation through direct load control of thermal and electrical energy storage resources, IEEE Trans. Smart Grid 9 (4) (2018) 2786–2796, https://doi.org/10.1109/TSG.2016.2620176. Jul.
[4] A. Spina, et al., Smart grid technology lab – A full-scale low voltage research facility at tu Dortmund university, in: 2018 AEIT International Annual Conference, IEEE, 2018, pp. 1–6, https://doi.org/10.23919/AEIT.2018.8577378. Oct.
[5] G. De Carne, D. Kottonau, Power hardware in the loop laboratory testing capability for energy technologies, in: 2022 AEIT International Annual Conference (AEIT), IEEE, 2022, pp. 1–5, https://doi.org/10.23919/AEIT56783.2022.9951766. Oct.
[6] A. Mohapatra, T. Hamacher, V.S. Peric, PHIL infrastructure in coses microgrid laboratory, in: 2022 IEEE PES Innovative Smart Grid Technologies Conference Europe (ISGT-Europe), IEEE, 2022, pp. 1–6, https://doi.org/10.1109/ISGT-Europe54678.2022.9960295. Oct.
[7] W. Meesenburg, W.B. Markussen, T. Ommen, B. Elmegaard, Optimizing control of two-stage ammonia heat pump for fast regulation of power uptake, Appl. Energy 271 (April) (2020) 115126, https://doi.org/10.1016/j.apenergy.2020.115126. Aug.
[8] Y.-J. Kim, L.K. Norford, J.L. Kirtley, Modeling and analysis of a variable speed heat pump for frequency regulation through direct load control, IEEE Trans. Power Syst. 30 (1) (2015) 397–408, https://doi.org/10.1109/TPWRS.2014.2319310. Jan.
[9] B.P. Rasmussen, Dynamic modeling for vapor compression systems—Part I: Literature review, HVAC&R Res 18 (2012), https://doi.org/10.1080/10789669.2011.582916.
[10] B.P. Rasmussen, A.G. Alleyne, Control-oriented modeling of transcritical vapor compression systems, J. Dyn. Syst. Meas. Control 126 (1) (2004) 54–64, https://doi.org/10.1115/1.1648312. Mar.
[11] O. Ibrahim, F. Fardoun, R. Younes, H. Louahlia-Gualous, Air source heat pump water heater: dynamic modeling, optimal energy management and mini-tubes condensers, Energy 64 (2014) 1102–1116, https://doi.org/10.1016/j.energy.2013.11.017.
[12] V.S. Peric, et al., CoSES laboratory for combined energy systems at tu munich, in: 2020 IEEE Power & Energy Society General Meeting (PESGM), IEEE, 2020, pp. 1–5, https://doi.org/10.1109/PESGM41954.2020.9281442. Aug.
[13] R.C. Portillo, et al., Modeling strategy for back-to-back three-level converters applied to high-power wind turbines, IEEE Trans. Ind. Electron. 53 (5) (2006) 1483–1491, https://doi.org/10.1109/TIE.2006.882025. Oct.
[14] C. Wu, Z. Xingxi, D. Shiming, Development of control method and dynamic model for multi-evaporator air conditioners (MEAC), Energy Convers. Manag. 46 (3) (2005) 451–465, https://doi.org/10.1016/j.enconman.2004.03.004. Feb.
[15] A. Outtagarts, P. Haberschill, M. Lallemand, The transient response of an evaporator fed through an electronic expansion valve, Int. J. Energy Res. 21 (9) (1997) 793–807, https://doi.org/10.1002/(SICI)1099-114X(199707)21:9<793::AID-ER297>3.0.CO;2-P. Jul.
[16] S. Bendapudi, J.E. Braun, E.A. Groll, A comparison of moving-boundary and finite-volume formulations for transients in centrifugal chillers, Int. J. Refrig. 31 (8) (2008) 1437–1452, https://doi.org/10.1016/j.ijrefrig.2008.03.006. Dec.
[17] TLK-Thermo GmbH, "TIL-model library for thermal components and systems." [Online]. Available: https://www.tlk-thermo.com/index.php/en/til-suite.
[18] F. Fardoun, O. Ibrahim, A. Zoughaib, Quasi-steady state modeling of an air source heat pump water heater, Energy Procedia 6 (2011) 325–330, https://doi.org/10.1016/j.egypro.2011.05.037.
[19] B. Shen, K. Nawaz, V. Baxter, A. Elatar, Development and validation of quasi-steady-state heat pump water heater model having stratified water tank and wrapped-tank condenser, Int. J. Refrig. 87 (2018) 78–90, https://doi.org/10.1016/j.ijrefrig.2017.10.023. Mar.
[20] T.B. Harild Rasmussen, Q. Wu, M. Zhang, Primary frequency support from local control of large-scale heat pumps, Int. J. Electr. Power Energy Syst. 133 (May) (2021) 107270, https://doi.org/10.1016/j.ijepes.2021.107270. Dec.
[21] T.B.H. Rasmussen, Q. Wu, J.G. Moller, M. Zhang, MPC coordinated primary frequency support of small- and large-scale heat pumps, IEEE Trans. Smart Grid 13 (3) (2022) 2000–2010, https://doi.org/10.1109/TSG.2022.3148601. May.
[22] R. Song, G. Yon, T. Hamacher, V.S. Peric, Data-driven model reduction of the moving boundary heat pump dynamic model, in: 2022 IEEE Power & Energy Society General Meeting (PESGM), IEEE, 2022, pp. 1–5, https://doi.org/10.1109/PESGM48719.2022.9916823. Jul.

Concluding Remarks

This paper enabled a conventional power system laboratory to emulate a distributed ASHP's dynamic behavior in terms of current and power profile. This emulation is vital as it provides a platform for close-to-reality validation of ASHP-based FFR when a customized experimental setup is unavailable.

The complete model illustrated in Section 3.1 was chosen for the emulation as it is control-oriented and provides a reference for mimicking the current profile at the grid-interfacing point. The electrical and thermal subsystems were built in Simulink and Dymola, respectively, and the thermal subsystem was then packaged into an S-function and imported into Simulink. The execution frequency of the electrical subsystem was optimized towards the slowest rate that preserves important current harmonics, while the thermal subsystem execution frequency was chosen as the minimum value to stabilize the overall model. The PHIL experiments in our laboratory proved that the developed ASHP emulation could stably run in real-time, and the resulting emulation error on the grid-interfacing current and real power was acceptable.

3.3 Control Strategy Design to Involve Distributed ASHP in FFR

Scientific Context

In Section 3.1, where we delved into the analysis of ASHP dynamic modeling, we acquired a more profound understanding of the dynamic characteristics inherent in ASHP systems. A critical observation from this analysis is the variable nature of ASHP response characteristics, which are not static but fluctuate based on operating conditions such as heat source and sink temperatures. The essential characteristics of the heat pump behavior lie in the refrigeration cycle, which is heavily influenced by the thermodynamic properties of the refrigerant used. Changes in operating conditions lead to shifts in the thermal equilibrium of the refrigeration cycle, which, in turn, directly impacts the power transient behavior during modulation.

Therefore, the primary focus of the following paper was to develop a robust control strategy that integrates distributed ASHPs under uncertain operating conditions into the existing BESS-only FFR services in residential grids. We assumed that each building has a BESS and an ASHP, and we proposed a decentralized coordinative control strategy that synergizes the local ASHP and BESS through a combination of H_∞ and inverse-droop method. We thoroughly assessed the stability of this control strategy through small-signal analysis, paying particular attention to the margins of critical control gains. The performance of the proposed strategy was then validated through co-simulations between Simulink and Dymola.

Publication #3: Integrating Distributed Air-Source Heat Pumps into the Battery-based Fast Frequency Response Service: A Study Based on Thermal Dynamic Uncertainties

Authors: Ruihao Song, Vladimir Terzija, Thomas Hamacher, Vedran Peric

Publication: IEEE Transactions on Sustainable Energy

Digital object identifier: 10.1109/TSTE.2024.3456068

Author	**Contribution**	**Tasks**
Ruihao Song	70%	• Conceptualization • Methodology • Investigation • Writing-original draft • Writing-review & editing
Vladimir Terzija	15%	• Writing-review & editing
Thomas Hamacher	5%	• Supervision • Funding acquisition
Vedran Peric	10%	• Supervision • Writing-review & editing

Integrating Air-Source Heat Pumps into the Demand-side Fast Frequency Response Service: A Study Based on Thermal Dynamic Uncertainty

Ruihao Song, *Member, IEEE,* Vladimir Terzija, *Fellow, IEEE,* Thomas Hamacher, Vedran S. Perić, *Member, IEEE*

***Abstract*--Fast frequency response services, designed to quickly balance the electrical grid within seconds, have a critical importance for managing sudden anomalies in low-inertia power systems. Battery systems often serve as versatile prosumers on the demand side to facilitate fast frequency response services. However, the nature of fast frequency response services leads to a highly fluctuating power profile for batteries, which can shorten their lifetime. In contrast, distributed air-source heat pumps in residential areas have a substantial untapped potential to support fast frequency response services. This paper seeks to integrate them into the existing services through a controller upgrade. We analyze the influence of air-source heat pumps' inherent complex thermal dynamics on fast frequency response services, revealing control challenges posed by unpredictable operating condition changes. Such a challenge is tackled with a standard droop control structure which is tuned through H_∞ method, guaranteeing practical and stable operations within the permitted operating condition range. Finally, the proposed fast frequency response service scheme is tested through multiphysics simulations on a small-size low-inertia residential microgrid. The obtained results strongly supported the proposed new service.**

***Index Terms*-- heat pump, fast frequency response, demand response, thermal dynamics, uncertain system.**

I. Introduction

A critical aspect in maintaining power system stability is to ensure that the grid frequency remains within pre-defined operational and statutory limits (e.g., +/- 0.2 Hz and 0.5 Hz in the U.K., respectively [1]). With the rise of renewable energy sources, the traditional dynamics of power systems have been significantly changed. The intermittent nature of renewable energy sources and their limited contribution to the system inertia, compared to classical synchronous generators, pose serious challenges to the stability of power grids. In order to cope with the inertia shortage, Fast Frequency Response (FFR) services [2][3] are introduced. This type of ancillary service is designed to respond rapidly to frequency anomalies within 1-2 seconds. Related application examples include but are not limited to Dynamic Containment (DC) or Moderation (DM) in the U.K. (1.5s response time) [4], Very Fast Raise/Lower in Australia (1s response time) [5], and Fast Frequency Reserve in Nordic countries [6]. In this paper, we focus on exploring the demand-side opportunities for FFR services.

A common solution for FFR services is to use battery energy storage systems (BESS) [7][8]. BESS-based FFR services normally employ droop control with frequency reaction deadband measures [9][10], state-of-charge (SoC) preservation [11][12], and power ramping limitations [13][14]. In [15], a case study of FFR-level support through BESSs on the French island of Guadeloupe was presented, and the results suggested that a fast-acting storage system can mitigate major wind or solar outages. The authors in [16] demonstrated the feasibility of BESS-based FFR services through hardware-in-the-loop testing, examining the impact of frequency measurement accuracy and latency on frequency regulation performance. Study [17] proposed a model-predictive control (MPC) method for BESS-based FFR services, and the authors claimed that the proposed method achieved a fast response speed while being feasible with low-cost hardware. Although the technological aspects of BESS-based FFR services are mature, they unavoidably result in a volatile BESS power profile. Such a power profile leads to intensive battery heating. Consequently, the lifespan of the BESS is reduced, and the maintenance costs increase, creating a bottleneck for industrial applications. Therefore, there is a need for new FFR service concepts combining BESSs and other flexible equipment at the demand side with a reasonably fast power response.

In current residential power systems, the heating systems constitute a significant proportion of the total load, and this share is anticipated to grow in the future [18][19][20]. Among electric heaters, distributed air-source heat pumps (ASHP) at relatively low power ratings (1-100 kW) can be potentially used in FFR services by rapidly modulating the compressor speed. Their compact size implies a significantly smaller

This work was supported by the Bavarian Research Foundation through the project "Sector Coupling und Microgrids (STROM)" under project number AZ-1473-20, and by the Deutsche Forschungsgemeinschaft (DFG) through the project "Optimal Operation of Integrated Low-Temperature Bidirectional Heat and Electric Grids (IntElHeat)" under project number 450821044.

R. Song and T. Hamacher are with the Munich Institute of Integrated Materials, Energy and Process Engineering, Technical University of Munich, Lichtenbergstr. 4a, 85748, Garching, Germany (e-mail: ruihao.song@tum.de; thomas.hamacher@tum.de).

V. S. Perić was with the Technical University of Munich, Lichtenbergstr. 4a, 85748, Garching, Germany. He is now with the Department of Electrical and Computer Engineering, Aarhus University, Finlandsgade 20, 8200 Aarhus N, Denmark (e-mail: vedran.peric@ece.au.dk).

V. Terzija is with the School of Engineering, Newcastle University, Merz Court, E4.41, Newcastle upon Tyne, NE1 7RU, UK (vladimir.terzija@ncl.ac.uk).

rotational mass compared to conventional gas and steam turbines, enabling them to quickly accelerate or decelerate to adjust power consumption as needed. The consequence of exploiting ASHPs for FFR services is the degradation of heat supply steadiness, which means the actual heat power fluctuates around a designated average value. If this average power is determined by a specific logic, such as an energy management algorithm, it inevitably results in a sub-optimal actual energy consumption. Nevertheless, as the period of FFR services is a matter of seconds, the discrepancy between the actual energy consumption and the scheduled optimum is minor. Furthermore, heat supply systems possess considerable thermal inertia, meaning that any variation in domestic water or air temperature (key indicators of comfort level) caused by power system ancillary services is negligible. These facts indicate that ASHPs have an excellent potential for low-cost demand response [21].

In recent years, different levels of frequency support capabilities of heat pumps have been intensively studied. At the tertiary frequency response level, the scheduling of heat pumps for demand response is discussed in [22], [23], and [24], which is commonly achieved through solving a multi-layer hourly-based optimization problem at the control center. At the secondary frequency response level, direct load control was introduced in [25] and [26], where the base load was determined by the heat demand, and a frequency control reference was incorporated as a short-term input. In [27], the frequency response requirement was integrated into an MPC with 15-minute intervals, where the control goal was to minimize energy consumption while satisfying the frequency response reserve and temperature control goals. At the primary frequency response level, reference [28] investigated the frequency response potentials of large-scale and small-scale heat pumps, where the coordination between them was rule-based. In [29], the MPC method was proposed to control large-scale heat pumps for optimal reference tracking. The MPC controller was located in the grid control center and a bi-directional communication for gathering measurements and distributed control signals was used.

ASHPs are nonlinear in terms of power response [30]. Their nonlinear dynamics result from changes in the thermal equilibrium caused by variations in operating conditions, such as air and water temperatures. A new thermal equilibrium leads to new refrigerant thermal dynamic properties and, eventually, new ASHP power response characteristics. Previous research on primary, secondary, and tertiary response regulations often involved simplification in modeling the dynamic behavior of ASHPs while designing control schemes. These simplifications were often in the form of a data-driven transfer function plus/or an efficiency model, as in [25][26][28][29][31]. This means that errors caused by constant transfer function modeling are considered insignificant in previous research for designing primary, secondary, and tertiary level service controllers. However, FFR service control systems are much faster, suggesting they can impact the transient stability to a larger extent. Therefore, using inaccurate models during the FFR control design phase could result in transient instability, implying the need for careful analysis of components' fast dynamics. As the importance of FFR services continues to rise, the following research gaps are revealed:

- The possibility of using distributed ASHPs in FFR services has not been explored based on fundamental physics.
- We lack appropriate modeling methodologies that can describe ASHP nonlinearities for designing FFR service controllers.
- Although there are standard control strategies for FFR services, there is no available controller tunning method which can address the ASHP nonlinearity problem.
- There are no comparative analyses of the performance of integrated, ASHP-only, and BESS-only FFR services.

In this paper, we look into the dynamics of distributed ASHPs and investigate their potential for FFR services in low-inertia power systems. The highlights and main contributions of the paper can be summarized as follows:

- We demonstrated the feasibility of integrating distributed ASHPs into FFR services through multi-physics analysis. Here, multi-physics denotes the simultaneous simulation of electric power and ASHP thermal dynamics.
- Considering the nonlinearity of ASHP power response in the context of FFR services, we proposed the adoption of a component-level ASHP model derived from fundamental conservation equations. Furthermore, we illustrated potential instabilities arising from traditional ASHP power response modeling through simulations.
- We adopted H_∞ method in designing all controller gains in the standard droop control structure to address the ASHP nonlinearity problem.
- We showed the advantages of the integrated FFR services by comparing the performance of integrated, ASHP-only, and BESS-only FFR services.

This paper is organized as follows: Section II provides the physics-based modeling of distributed ASHPs. Section III presents the control strategy of the proposed FFR service and the related design process. Section IV contains a case study for the proposed FFR service in a microgrid environment through co-simulation between Simulink and Dymola [32]. Finally, Section V gives the conclusion of the paper.

II. Air-source heat pump system modeling

Previous research [28][29][33] often uses a simplified transfer function to represent the whole ASHP system, which leads to control stability risk for FFR services. In this section, we propose a component-level model for ASHP dynamics that is appropriate for designing FFR service controllers. ASHPs are multi-physic systems that can be divided into electrical and thermal subsystems with distinct dynamic characteristics in terms of linearity and time scale. In order to construct an appropriate model for FFR services, a detailed analysis of existing methods for both electrical and thermal subsystems (as shown in Table I) is required to select the most appropriate approach for each. The rule for selecting models is to preserve nonlinear characteristics of the ASHP power response as much

This article has been accepted for publication in IEEE Transactions on Sustainable Energy. This is the author's version which has not been fully edited and content may change prior to final publication. Citation information: DOI 10.1109/TSTE.2024.3456068

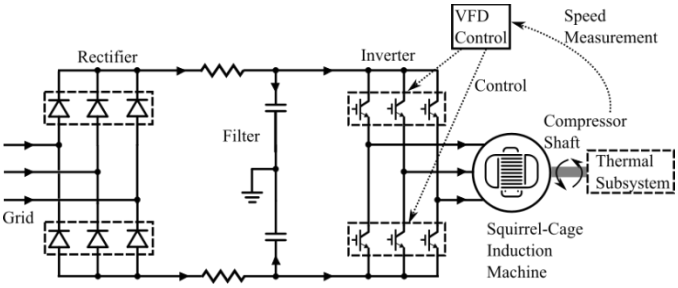

Fig. 1. Physical structure of the electrical subsystem.

as possible while keeping the computation burden and redundant outputs at the minimum level.

A. Electrical subsystem

The electrical subsystem, essentially a variable-speed drive system (VFD), is shown in Fig. 1. It has much faster dynamics than the thermal subsystem, and its modeling is well-established in the field of power systems. In Table I, the mainstream modeling methods for the VFD system are shown. Transfer function models are commonly utilized to represent drive dynamics in system-level analysis, where only input-output characteristics are of interest [34]. While highly focused on control and computationally efficient, they cannot provide information on the drive system's internal states, such as waveforms of grid-side load current and DC-link voltage. These internal states are addressed in physics-based modeling methods, such as KCL/KVL with switching equivalent functions [35] or detailed switching [36]. Among these two methods, the former one is often used to simulate and design drive-level speed and current controllers, provided harmonic distortion is not the primary concern. Conversely, the latter method involving detailed switching is typically employed for designing drive system topology and optimizing efficiency, as it requires a comprehensive understanding of the harmonic spectrum.

For the electrical subsystem of ASHP, this paper only needs to describe how the shaft rotational speed of the drive responds to given speed set points. As the electrical subsystem is relatively linear and significantly faster than the thermal subsystem, we do not need to model detailed internal states or switching to accurately describe the drive speed response. Therefore, a lumped description of the combined dynamics of the machine and its speed controller through a transfer function is the best choice. The input to the transfer function is the speed reference to the drive control system, and the output is the actual produced speed on the machine-compressor shaft.

B. Thermal subsystem

The thermal subsystem of an ASHP, which is essentially a refrigeration loop, contains the dominating dynamics and most of the nonlinearity. Therefore, it should be carefully modeled for rapid modulation scenarios such as FFR services. Unlike drive systems, refrigeration systems are rarely explored in power system fields, resulting in a lack of commonly accepted modeling methods. This paper addresses this gap by reviewing literature from mechanical and thermal dynamics fields and summarizing available methods in Table I. The single-phase

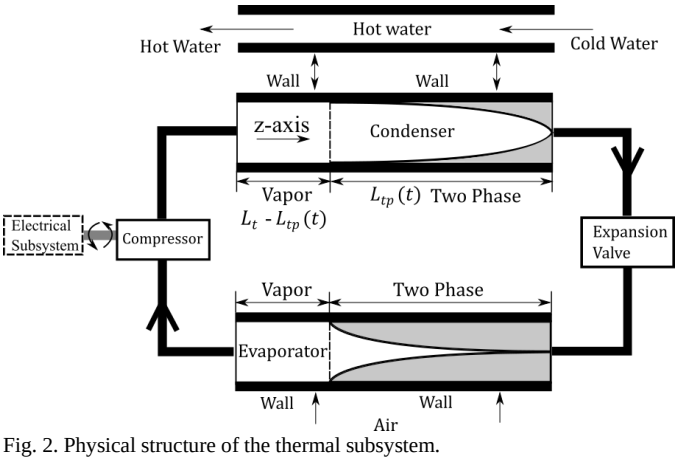

Fig. 2. Physical structure of the thermal subsystem.

TABLE I.
EXISTING MAINSTREAM MODELS FOR ELECTRICAL AND THERMAL SUBSYSTEMS FROM THE LATEST OPEN LITERATURE

Electrical Subsystem	Machine Speed	Internal states	Computation
Transfer function [34]	Accurate	N/A	Low
KCL/KVL with switching equivalent functions [35]	Accurate	Less accurate for the current noise profile	Medium
KCL/KVL with detailed switching [36]	Accurate	Accurate	High

Thermal Subsystem	Mechanical power	Internal states	Computation
Single-phase flow model [37]	Less accurate in both dynamics and steady states	N/A	Low
Hammerstein/Wiener model [38][39]	Less accurate in dynamics, accurate in steady-states	N/A	Low
Moving boundary model [30][40][41]	Accurate	Less accurate with lumped variables	Medium
Finite volume model [42][43]	Accurate	Accurate	High

flow model [37] prioritizes heat transfer modeling accuracy but overlooks the refrigerant phase-shifting in the evaporator and condenser, leading to challenges in capturing the instantaneous mechanical power of the compressor shaft. The Hammerstein/Wiener model [38][39] combines transfer functions with nonlinear polynomials to describe the compressor shaft's instantaneous mechanical power. However, its modeling accuracy in terms of transient characteristics diminishes within the control bandwidth of FFR services. Moving boundary [30][40][41] and finite volume [42][43] modeling methods excel in capturing the nonlinear dynamics of the refrigeration loop, directly addressing fundamental conservation equations of mass, energy, and momentum (optional). However, the moving boundary method, due to variable lumping, exhibits lower accuracy compared to the finite volume method.

With the listed options in Table I, only the moving boundary and finite volume methods fit our requirement as we need to accurately describe both the steady-state and transient characteristics of the nonlinear speed-power response. The moving boundary method is more suitable because the spatial distribution of variables is irrelevant to the scope of this paper. In the thermal subsystem, both the evaporator and condenser

are heat exchangers with refrigerant phase transitions, which are the leading causes of the nonlinear behavior. For example, in the evaporator system, the refrigerant enters the evaporator volume as a saturated mixture of vapor and liquid and then leaves as superheated vapor, as shown in Fig. 2.

Evaporator/Condenser: Generally, if we consider an unidirectional model (*z*-axis, axial) and neglect pressure drop, the modeling of the evaporator system primarily addresses three conservation laws: refrigerant mass (1) and energy (2), and pipe wall energy (3) conservations [44]:

$$A_{i,c}\frac{\partial \rho}{\partial t}+\frac{\partial \dot{m}}{\partial z}=0, \tag{1}$$

$$A_{i,c}\frac{\partial(\rho h-p)}{\partial t}+\frac{\partial(\dot{m}h)}{\partial z}=c_i\alpha_i(T_w-T_r), \tag{2}$$

$$C_w\rho_w\left(A_{o,c}\text{-}A_{i,c}\right)\frac{\partial T_w}{\partial t}=c_i\alpha_i\left(T_{r,tp}-T_w\right)+c_o\alpha_o(T_a-T_w), \tag{3}$$

where variable ρ is the density, $\dot{m}$ is the mass flow, z is the axial direction, h is the specific enthalpy, p is the pressure, T is the temperature; parameter A is the area, c is the circumference, α is the heat transfer coefficient; subscript i represents pipe inner variables, o represents outer variables, c represents cross-section, w represents the pipe wall variables, a represents ambient air, and r represents refrigerant variables.

The moving boundary approach [30][40][41] solves the refrigerant phase transition issue by separating the evaporator and condenser volumes into zones, each representing a specific refrigerant state. In a standard two-zone model, one zone contains a mixed state of vapor and liquid, while the other houses pure vapor. The moving boundary method aims to convert the nonlinear partial differential conservation equations (PDE) into nonlinear ordinary differential equations (ODE) through axial integration. With such a conversion, the resulting system can be friendly to the control system design. For example, the integration process of (1)-(3) for the two-phase zone (0-$L_{tp}(t)$) and vapor zone ($L_{tp}(t)$- L_t) in the evaporator can be described by (4)-(7):

$$A_{i,c}\int_{\kappa_1}^{\kappa_2}\left(\frac{\partial \rho}{\partial t}+\frac{\partial \dot{m}}{\partial z}\right)dz=0, \tag{4}$$

$$A_{i,c}\int_{\kappa_1}^{\kappa_2}\left[\frac{\partial(\rho h-p)}{\partial t}+\frac{\partial(\dot{m}h)}{\partial z}\right]dz=\int_{\kappa_1}^{\kappa_2}c_i\alpha_{i,tp}\left(T_{w,tp}-T_{r,tp}\right)dz, \tag{5}$$

$$C_w\rho_w\left(A_{o,c}-A_{i,c}\right)\int_{\kappa_1}^{\kappa_2}\frac{\partial T_w}{\partial t}dz=\int_{\kappa_1}^{\kappa_2}\left[c_i\alpha_i\left(T_{r,tp}-T_w\right)+c_o\alpha_o\left(T_a-T_w\right)\right]dz, \tag{6}$$

$$\kappa_1=\begin{cases}0, & \textit{two-phase zone}\\ L_{tp}(t), & \textit{vapor zone}\end{cases},\ \kappa_2=\begin{cases}L_{tp}(t), & \textit{two-phase zone}\\ L_t, & \textit{vapor zone}\end{cases} \tag{7}$$

where variable L is the zone length, $\kappa_{1,2}$ are integration limits; subscript tp represents two-phase zone variables, t represents total, and v represents vapor zone variables. The results of these integrations are shown in the Appendix, and full derivation can be found in [45]. As for the condenser, the derivation process is similar, with only an order difference between the two zones.

Compressor: The compressor stage can be modeled with a standard isentropic compression process [46]. Here, the mass flow and specific enthalpy increment can be calculated with (8) and (9), and the required power can be calculated with (10).

$$\dot{m}=\frac{\omega}{2\pi}V_i\rho_{in}\eta, \tag{8}$$

$$\Delta h=\frac{k_1RT_{r,in}}{k_1-1}\left(\left(\frac{p_{out}}{p_{in}}\right)^{\frac{k_1-1}{k_1}}-1\right), \tag{9}$$

$$P_{ASHP}=\dot{m}\Delta h, \tag{10}$$

where variable ω is the rotational speed, and P_{ASHP} is the mechanical power; parameter V is the volume, η is the volumetric efficiency, R is the gas constant, and k_1 is an empirical constant.

Expansion valve: The expansion valve follows the Bernoulli's principle for mass flow calculation as in (11). The valve orifice area is controlled by the superheat controller. If we assume that a standard Proportional-Integral (PI) controller is used, then the orifice area is calculated by (12), where k_2 is also an empirical constant, and subscript sh means the superheat.

$$\dot{m}=A_ck_2\sqrt{\rho_{in}(p_{out}-p_{in})}, \tag{11}$$

$$A_c=k_p(T_{sh}^*-T_{sh})+k_i\int(T_{sh}^*-T_{sh})dt. \tag{12}$$

C. Overall system

One can obtain the overall model of a distributed ASHP by combining all mentioned component models as in Fig. 3, where *cw* represents the cold water and *hw* represents heated water. The overall ω^*-P_{ASHP} response is expressed as in (13):

$$\begin{aligned}&\dot{x}=\varphi(x,\ \underbrace{T_a,T_{cw},\dot{m}_{cw}}_{operating\ conditions})+B\omega^*,\\ &P_{ASHP}=\vartheta(x,T_a,T_{cw},\dot{m}_{cw}),\\ &x=[\underbrace{p,L_{tp},T_{w,tp},T_{w,v},T_{hw}}_{condenser}\ \underbrace{p,h_{r,out},L_{tp},T_{w,tp},T_{w,v}}_{evaporator},\tau,\sigma]^T,\\ &min\le T_{cw},T_a,\dot{m}_{cw}\le max,\end{aligned} \tag{13}$$

where variable $x\in\mathbb{R}^{12\times1}$ is the ASHP state vector, ω^* is the speed reference sent to the drive system, τ is a state related to the superheat PI controller, σ is a state related to the drive system dynamics, φ and ϑ are nonlinear functions, and $B\in\mathbb{R}^{12\times1}$ is the constant input matrix. The nonlinear property of the resulting system is mainly caused by operating conditions (T_a, T_{cw}, assuming constant $\dot{m}_{cw}$) related terms in φ and ϑ. Therefore, the ω^* to P_{ASHP} response characteristics can vary if the ASHP's operating condition is uncertain.

In order to emphasize the importance of the nonlinearity, we compared the power response of the nonlinear model (parameters in the Appendix) and the traditional linear transfer

This article has been accepted for publication in IEEE Transactions on Sustainable Energy. This is the author's version which has not been fully edited and content may change prior to final publication. Citation information: DOI 10.1109/TSTE.2024.3456068

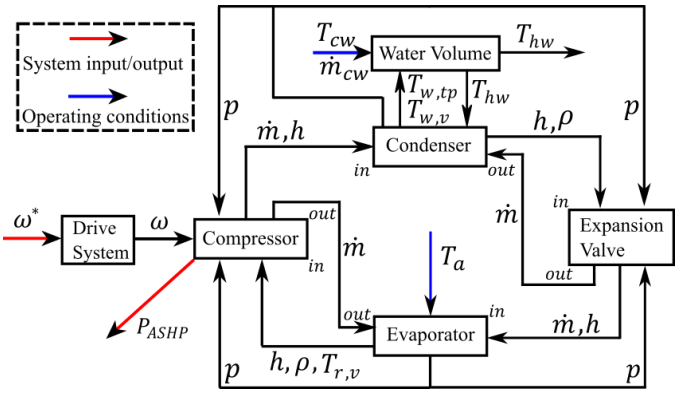

Fig. 3. Overall model structure of a distributed ASHP thermal subsystem.

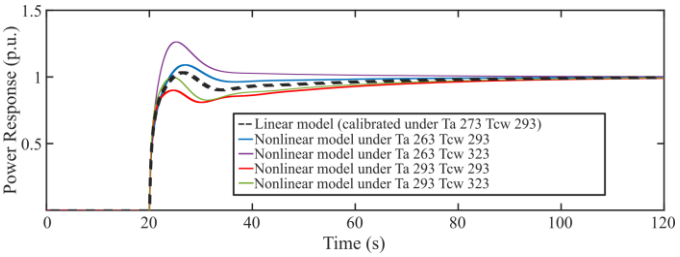

Fig. 4. Power step response comparison between linear and nonlinear models.

function model (calibrated only at one condition) [28][29][33]. From Fig. 4, we see that the linear model identified at a common operating condition can lead to errors in the response peak and settling time. If a traditional linear model is used during the control design of FFR services, the unconsidered behaviors can potentially lead to problems like sub-optimal design, equipment overload, or even frequency instability."

III. PROBLEM FORMULATION OF AN INTEGRATED FFR SERVICE

This paper targets the demand-side FFR services, which were typically achieved with BESSs through common droop control (inversed) [47]. If the basic droop control is considered, traditional FFR services at each unit can be described by (14):

$$\Delta P^*_{BESS} = \frac{1}{N}\Delta P^*_{FFR} = \frac{k_{pf}}{N}\Delta f G_{HPF}(s), \tag{14}$$

where ΔP^*_{BESS} is the individual BESS power response reference, ΔP^*_{FFR} is the FFR service power reference, N is the total number of participation units, k_{pf} is the droop coefficient to be designed, Δf is the measured grid frequency disturbance, and $G_{HPF}(s)$ is a high-pass filter.

In order to reduce the capital and maintenance costs of BESSs, we propose exploiting ASHPs for FFR services as much as possible so that BESSs are used for less time and intensity. However, such a measure cannot fully replace BESSs in FFR services as the response speed of ASHPs cannot independently satisfy the requirement of FFR services. Therefore, BESSs are still needed to support ASHPs as a transient gap filler. An illustration of the proposed FFR control strategy is shown in Fig. 5, where v_{Grid} is the measured grid voltage, $G_{LPF}(s)$ is a low-pass filter, and $G_{HPC}(s)$ is the ASHP power controller to be designed. Compared with (13), the new rule of FFR services is listed in (15) and (16):

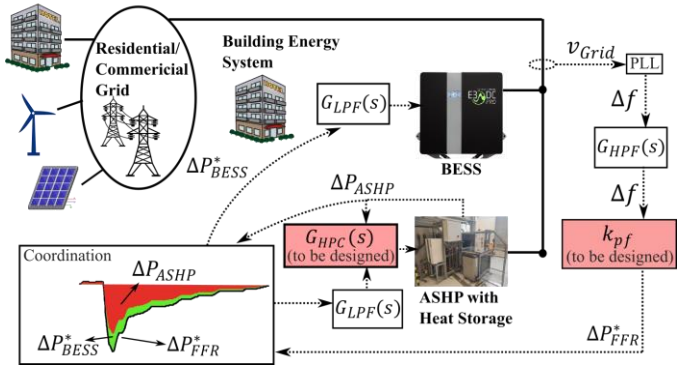

Fig. 5. Overall control strategy of the integrated ASHP-BESS FFR.

$$\Delta P^*_{ASHP} = \frac{1}{N}\Delta P^*_{FFR} = \frac{k_{pf}}{N}\Delta f G_{HPF}(s), \tag{15}$$

$$\Delta P^*_{BESS} = \frac{k_{pf}}{N}\Delta f G_{HPF}(s) - \Delta P_{ASHP}, \tag{16}$$

where ΔP^*_{ASHP} is the power modulation reference sent to the inner power control loop of individual ASHP and ΔP_{ASHP} is the actual measured value. While shifting from the standalone BESS scheme to the proposed integrated scheme, the following two parts of the control system must be carefully designed in a strict order, as the result of the second step is affected by the first one. During the control design, the operating condition uncertainty problem of ASHPs must be appropriately considered.

1) *Heat pump power controller* $G_{HPC}(s)$*:* The goal of the ASHP power controller is to modulate the compressor speed reference ω^* so that ΔP_{ASHP} tracks ΔP^*_{ASHP}. This results in a nonlinear control problem as the characteristic functions φ and ϑ in ASHP power response system (13) change with operating conditions like T_a and T_{cw}.
2) *Droop coefficient* k_{pf} : The margin of k_{pf} must be estimated with a grid-level stability analysis after the heat pump control loop is designed. As the heat pump power control is involved as a subsystem to the grid-level FFR control, the estimation of k_{pf} also becomes nonlinear.

The design of $G_{HPC}(s)$ and k_{pf} is influenced by various aspects of ASHP characteristics, which form fundamental principles for selecting controller gains. In general, we summarize that $G_{HPC}(s)$ and k_{pf} gains are in negative correlation with the following ASHP physical properties.

- *ASHP rating*: Larger ASHP rating typically means increased average mass flow within the refrigeration loop, leading to a heavier compressor and drive rotational mass. Consequently, the ASHP's power response capability reduces, requiring a reduction in controller gains to prevent drive system overcurrent and grid frequency oscillations.
- *Heat transfer coefficients*: Fluctuations in air and water temperatures are the primary drivers of changes in ASHP dynamic characteristics. These fluctuations must propagate through the heat exchanger walls to impact internal refrigerant thermal conditions. Therefore, for equivalent ranges of environmental temperature fluctuations, a more

efficient evaporator and condenser with larger heat transfer capabilities lead to larger variations in ASHP dynamic characteristics. Accordingly, controller gains should be reduced to prevent instability.

- *Refrigerant thermal dynamic coefficients*: The thermal dynamic properties of the refrigerant, such as those described by the derivatives used in the conservation ODE equations ($\partial\rho_v/\partial p|_{h_v}$, $\partial\rho_v/\partial h_v|_p$, and $d\rho_v'/dp$ …, see Appendix), determine the magnitude of variations in characteristics when subjected to thermal operating condition disturbances. Reduced controller gains are necessary to prevent instability if the refrigerant exhibits a larger range of variations in its thermal dynamic properties.

In summary, a larger ASHP rating often suggests a larger average mass flow and more efficient heat exchangers. These features will amplify the uncertainty of the ASHP's transient characteristics, which means the sensitivity of control tunning normally grows with the ASHP rating.

A. Heat pump power control

This paper employs an approximation method that converts the nonlinear control design problem into a linear one with uncertainty. In order to do that, the nonlinear ASHP system (13) is transferred into a discrete set of linear transfer functions (S_{ASHP}) with uncertain coefficients as shown in (17)-(20):

$$\begin{aligned} \dot{x} &= A_{T_{cw},T_a}x + B\omega^*, \\ P_{ASHP} &= C_{T_{cw},T_a}x, \end{aligned} \tag{17}$$

$$A_{T_{cw,},T_a} = \begin{bmatrix} \left.\frac{\partial\varphi_1}{\partial x_1}\right|_{T_{cw},T_a} & \cdots & \left.\frac{\partial\varphi_1}{\partial x_{12}}\right|_{T_{cw},T_a} \\ \vdots & \ddots & \vdots \\ \left.\frac{\partial\varphi_{12}}{\partial x_1}\right|_{T_{cw},T_a} & \cdots & \left.\frac{\partial\varphi_{12}}{\partial x_{12}}\right|_{T_{cw},T_a} \end{bmatrix}, \tag{18}$$

$$C_{T_{cw},T_a} = \begin{bmatrix} \left.\frac{\partial\vartheta}{\partial x_1}\right|_{T_{cw},T_a} & \cdots & \left.\frac{\partial\vartheta}{\partial x_{12}}\right|_{T_{cw},T_a} \end{bmatrix},$$

$$\begin{aligned} G_{ASHP}(s)|_{T_{cw},T_a} &= C_{T_{cw},T_a}(sI - A_{T_{cw},T_a})^{-1}B \\ &= \frac{b_8s^8 + b_7s^7 + \ldots + b_0}{s^{12} + a_{11}s^{11} + \ldots + a_0}, \end{aligned} \tag{19}$$

$$S_{ASHP} = \left\{G_{ASHP}(s)|_{T_{cw},T_a} \;\middle|\; min \le T_{cw}, T_a \le max\right\}, \tag{20}$$

where a and b are coefficients to be calculated. The linearization points are selected from a comprehensive range of potential operational conditions, ensuring a reasonable distance between them. Intuitively, this selection of sparsity involves a trade-off between complexity and approximation accuracy. Once the complete set is obtained, the relationship between each coefficient of the transfer function and the operational condition variables T_{cw} and T_a can be summarized into a nonlinear polynomial ξ via curve fitting, as shown below in (21):

$$\begin{aligned} [a_{0..11}, b_{0..8}]^T &= [\xi_{0..20}(T_{cw}, T_a)]^T, \\ \xi_{0..20}(T_{cw}, T_a) &= \sum_{m,n=0}^{m,n=order} d_{mn}(T_{cw})^m(T_a)^n,\ m, n \epsilon\ Z^+, \end{aligned} \tag{21}$$

where d is the fitted coefficient for each term. With (21), the sparsity of S_{ASHP} can be further reduced by extrapolation between the sampled conditions, which increases the number of samples and increases the approximation accuracy of S_{ASHP}.

After the multi-point linearization, the nonlinear control problem turns into a linear uncertain problem. The H_∞ method is applied in this paper to design the standard ASHP power PI controller (22). It is a well-known approach for handling linear uncertain control problems through optimization methods [48]. The H_∞ method creates controllers that ensure stabilization with confirmed performance levels, which is suitable for our application as we must maintain stability under various operating conditions. When utilizing the H_∞ method, the control designer defines the issue as an optimization problem and proceeds to identify the controller that resolves this optimization. In this way, the impact of uncertainty from operating conditions is minimal. The objective of this optimization is to minimize the gap between the closed-loop response of ASHP power control and a pre-defined target response $G_{tgt}(s)$ (23), while satisfying the constraints of stability, control gains, and overshoot as in (24):

$$G_{HPC}(s) = k_p + k_i\frac{1}{s}, \tag{22}$$

$$G_{tgt}(s) = \frac{1}{1 + T_{tgt}s}, \tag{23}$$

$$\begin{aligned} &\underset{k_p,k_i}{minimize} \quad \left\| G_{tgt}(s) - \frac{G_{LPF}G_{HPC}S_{ASHP}}{1 + G_{LPF}G_{HPC}S_{ASHP}}(s) \right\|_\infty, \\ &s.t. \\ &\quad Re\left\{\lambda\left[\frac{G_{LPF}G_{HPC}S_{ASHP}}{1 + G_{LPF}G_{HPC}S_{ASHP}}(s)\right]\right\}_{max} < 0, \forall\ T_{cw}, T_a, \\ &\quad min \le k_p, k_i \le max, \\ &\quad \left\| \frac{G_{LPF}G_{HPC}S_{ASHP}}{1 + G_{LPF}G_{HPC}S_{ASHP}}(s) \right\|_\infty < 1 + \varepsilon, \forall\ T_{cw}, T_a, \end{aligned} \tag{24}$$

where $k_{p/i}$ are controller gains to be optimized, T_{tgt} is the time constant of the target response, λ is the function to obtain the eigenvalue vector, $Re(z)$ is the function to find the real part of a complex number, and ε is the maximum allowed closed-loop response overshoot in percentage.

B. Droop coefficient

While designing the ASHP power controller, we converted the nonlinear control problem into an uncertain linear problem, and now we can extend it into a grid-level linear uncertain problem for choosing k_{pf}. In this context, small-signal analysis is conducted for an active power disturbance ΔP_{Grid} and the resulting Δf, as shown in Fig. 6, where $G_{Grid}(s)$ is the power-frequency response of the grid and $G_{BESS}(s)$ is the power response of the BESS. Note that the phase-locked loop (PLL) dynamics is included by default in $G_{Grid}(s)$ as we obtain frequency data from a PLL during identifying $G_{Grid}(s)$.

In order to proceed with the analysis, $G_{BESS}(s)$ and $G_{Grid}(s)$ should be obtained for the intended grid environment. If we do not consider the disconnection of grid-forming synchronous generators, $G_{BESS}(s)$ and $G_{Grid}(s)$ are generally

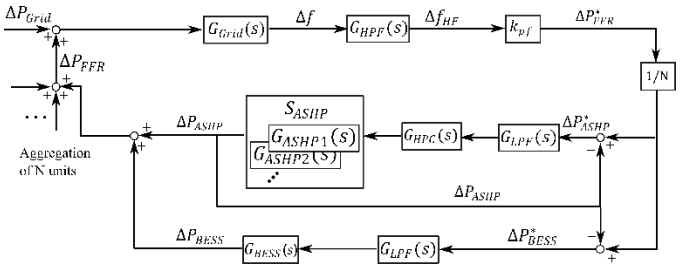

Fig. 6. Block diagram of the grid-level small-signal analysis.

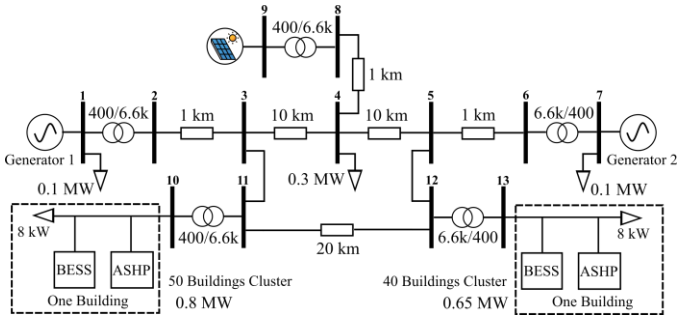

Fig. 7. Overview of the simulated microgrid case study.

linear [49] and constant during normal generation re-dispatching and load change scenarios. Therefore, we simplify them into two constant transfer functions, as in (25) and (26), which can be obtained through standard system identification methods [50][51]:

$$G_{Grid}(s) = \frac{k_{Grid}}{1 + T_{Grid}s}, \tag{25}$$

$$G_{BESS}(s) = \frac{1}{1 + T_{BESS}s}, \tag{26}$$

where T_{Grid} and T_{BESS} are time constants to be identified for the grid and BESS responses, k_{Grid} is a steady-state gain for power-frequency sensitivity. Once the $G_{BESS}(s)$ and $G_{Grid}(s)$ are obtained, we can write the complete closed-loop system transfer function as a set $S_{overall}$, as in (27):

$$\frac{\Delta f}{\Delta P_{Grid}} = S_{overall} = \frac{G_{Grid}(1 + G_{LPF}G_{HPC}S_{ASHP})}{1 + G_{LPF}G_{HPC}S_{ASHP} - k_{pf}G_{Grid}G_{HPF}G_{LPF}(G_{HPC}S_{ASHP} + G_{BESS})}, \tag{27}$$

The margin of k_{pf} can be obtained by finding the maximum value that satisfies the stability condition in (28):

$$Re\{\lambda[S_{overall}]\}_{max} < 0, \qquad \forall\, T_{cw}, T_a. \tag{28}$$

IV. Case Study and Simulations

A. Scenario description

Given the relatively limited scale of inverter-fed renewable sources in modern power systems, urban bulk grids typically exhibit low demand for FFR services due to the substantial inertia provided by synchronous generators. Within current standard power systems, FFR services play a critical role in specific regional grids with high renewable penetration and in remote grids. Therefore, in this paper, we utilize a medium voltage low-inertia microgrid depicted in Fig. 7 to validate the proposed control scheme for integrated FFR services. The test grid is representative of small towns and villages where a main grid connection is infeasible. The technical design process for the proposed FFR services maintains consistency across various scales of power grids, with no significant differences between microgrids and bulk grids.

The power system simulation is conducted in Simulink with the Simscape Power System library, while the ASHP thermal dynamic model was built in Dymola software [32] and imported to Simulink as a Function-Mock-Up Unit (FMU). Detailed specifications of the simulated microgrid are shown in Table II. It is assumed that most of the loads are residential and located in two areas which are filled with buildings of roughly 16 kW load. The heating load fraction for each building is 50% and relies on a distributed ASHP, whose parameters are shown in the Appendix (Table IV). Distributed BESSs are also located in each building together with ASHPs.

TABLE II
Microgrid Specifications

Grid	Islanded, mesh network, 3-phase, medium voltage 400V / 6.6 kV line-line, 50 Hz.
Generation	2 MW generators x 2 (5% droop, inertia constant 0.3072 MWs/MVA, IEEEG3 turbine system, generic power system stabilizers). 0.5 MW inverter-based PV farm x 1 (grid-connected, standard PQ control).
Cables	Medium voltage cable: N2XSEY 6-10 kV.
Load	Balanced loads. Active load: heating ≈ 0.73 MW, other ≈ 1.22 MW. Reactive load: ≈0.14 MVar.

B. Controller design

The first step is to design the heat pump power controller, following the methodology presented in section III. This paper uses the Matlab/Simulink Control System Tunner Toolbox [52] to implement the mentioned controller optimization. Initially, the inner P_{ASHP} control loop is constructed in the Simulink environment. The ASHP target is modeled by a transfer function block, where each coefficient is a polynomial dependent on the operating conditions T_{cw} and T_a. Before proceeding with control optimization, the cutoff frequency of the low-pass filter is selected. Subsequently, after formulating the feedback control loop, the model is imported into the Control System Tuner Toolbox interface, where the controller gains k_p and k_i are designated as the tuned objects. Additionally, the parameter variation ranges and step sizes for T_{cw} and T_a are configured within the toolbox interface. Tuning goals are established through toolbox options for "Tracking of step commands" and "Maximum overshoot." It is noted that the response target transfer function and overshoot constraint are arbitrarily selected here to serve as an example. Finally, appropriate toolbox solver parameters are chosen, leading to the production of optimized results for controller gains k_p and k_i. The result of the optimization in (24) on the studied ASHP is shown in Fig. 8, where we can observe that the tracking objective is achieved as much as possible within the overshoot constraint. We obtain the power control gains from the results (k_p: 0.01, k_i: 0.0443) and plot all possible closed-loop step responses for the ASHP power control

system in Fig. 9. From the figure, the closed-loop transient behavior is quite diverse for different operating conditions, but the response differences between the tests with the linearized set and the nonlinear model are negligible. This proves the accuracy of the linearization process.

The next step is to determine the margin of the droop coefficient k_{pf} through a grid-level small-signal analysis. If we consider a fixed operating condition (T_{cw}: 293 K, T_a: 273 K), the integrated FFR service remains stable for the test microgrid until k_{pf} is over roughly 0.48 MW/Hz, as shown in Fig. 10. However, if we consider all possible operating conditions (entire $S_{overall}$), then the derived stability margin does not hold anymore. In Fig. 11 (a), we can see that the distribution of eigenvalues for all possible operating conditions will cover the right-hand side when k_{pf} equals 0.48 MW/Hz. With uncertain operating conditions considered, the stability margin of k_{pf} is reduced to 0.39 MW/Hz, which is 81.25% of the original margin, as shown in Fig. 11 (b).

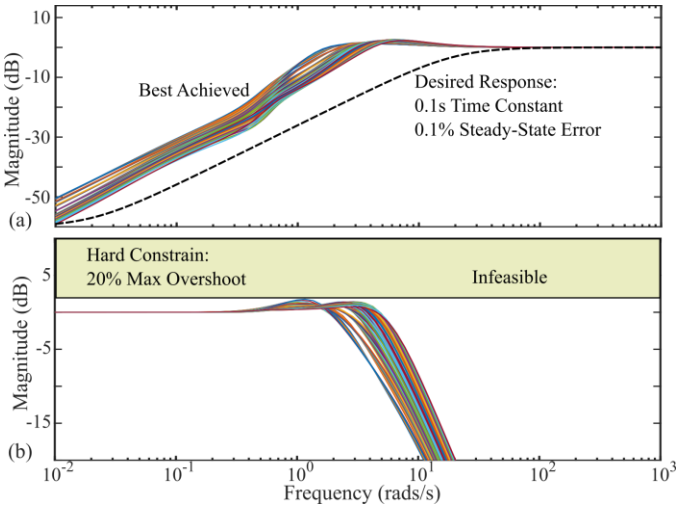

Fig. 8. Bode magnitude plots of the designed ASHP power control loop; (a): tracking error (b): closed-loop function.

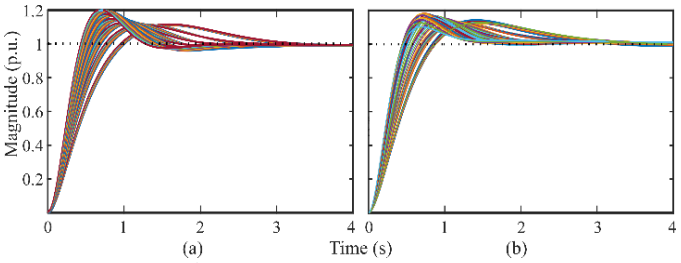

Fig. 9. Comparison of the ASHP closed-loop control response (all operating conditions): (a) with nonlinear model; (b) linearized uncertain model.

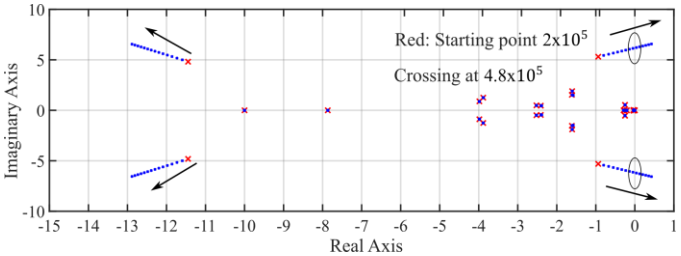

Fig. 10. Eigenvalue movements of integrated FFR system for increasing k_{pf}.

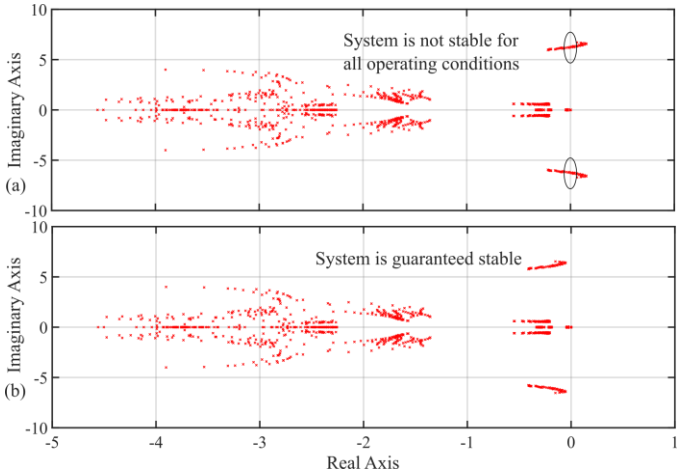

Fig. 11. Eigenvalue distribution for fixed k_{pf} but all operating conditions: (a) k_{pf} = 0.48 MW/Hz; (b) k_{pf} = 0.39 MW/Hz.

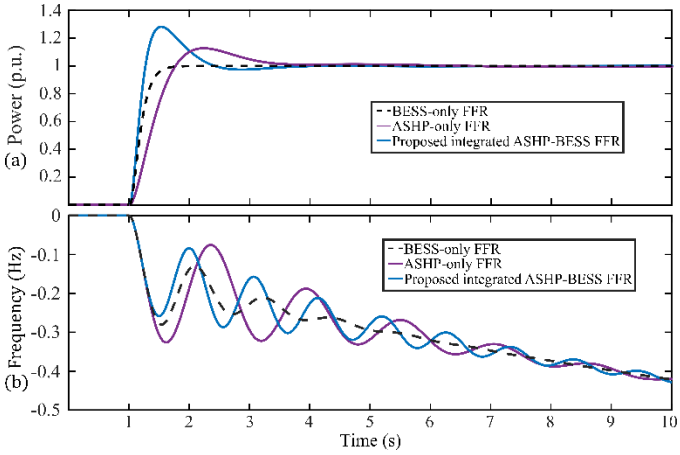

Fig. 12. Step response comparison between the proposed, BESS-only, and ASHP-only FFR services: (a) power control response; (b) grid frequency response (0.1 MW step).

After determining the controller gains, we proceed to test the designed FFR service using step responses and compare it with both BESS-only and ASHP-only FFR services. In Fig. 12 (a), the power response at the equipment level for the integrated FFR service exhibits a settling time between that of BESS-only and ASHP-only services, with a higher overshoot compared to the ASHP-only services. Regarding the grid-level frequency response, $\Delta f/\Delta P_{Grid}$, we observe that the proposed service also yields an oscillation level intermediate to those of all three tested services.

C. *Potential risk of instability*

In this subsection, we aim to show how the FFR service can be affected by the ASHP nonlinearity. We assume the integrated FFR service is designed based on traditional linear assumptions and the ASHP is modeled only for one operating condition (T_{cw}: 293 K, T_a: 273 K). The droop coefficient k_{pf} is set to 0.48 MW/Hz, which is inappropriate because it omits the ASHP-nonlinearity.

Consider that the grid is operating steadily before an operating condition change happens on the ASHP cluster. We then simulate a 10 K increase on T_a and show its impact on the microgrid frequency regulation. In reality, the operating

conditions normally change gradually, such as T_a fluctuation between day and night, T_{cw} fluctuation resulted from thermal storage temperature changes. However, in order to avoid redundant simulation time, we consider the designed T_a change to happen instantaneously from a steady-state operation. Figure 13 (a) shows the microgrid frequency starts to become unstable after the T_a change is injected, causing gradually increased frequency oscillations. The instability will also cause significant power fluctuation on the ASHP, as in Fig. 13 (b), which could damage the equipment.

Before the grid becomes unstable, the frequency response characteristic already experiences a deviation from the designed behavior. Recall that the FFR service is assumed to be designed with the linear method, which only covers one operating condition (T_{cw}: 293 K, T_a: 273 K), where the response is shown in Fig. 14 (a). We list the response difference after a T_a fall (10 K), a T_{cw} rise (10 K), and a T_a rise (10 K) in Fig. 14 (b), (c), and (d), respectively. The results suggest that the rise of T_a and T_{cw} can cause unexpected oscillations in grid frequency, enhancing the crucial role of ASHP nonlinearity in the control design of FFR services.

D. Performance analysis under common disturbances

In this section, we demonstrate the enhancements provided by an integrated ASHP-BESS FFR service as compared to BESS-only and ASHP-only services. The adopted k_{pf} is 0.39 MW/Hz as designed, T_{cw} is 293 K, and T_a is 273 K.

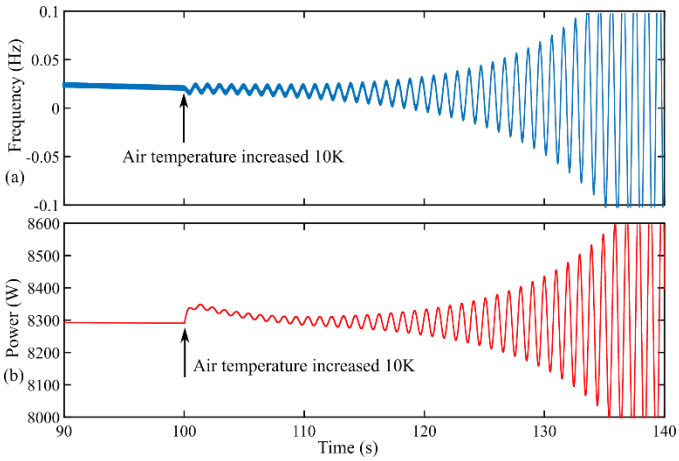

Fig. 13. Frequency instability caused by a sudden 10 K change on T_a: (a) microgrid frequency; (b) individual ASHP power.

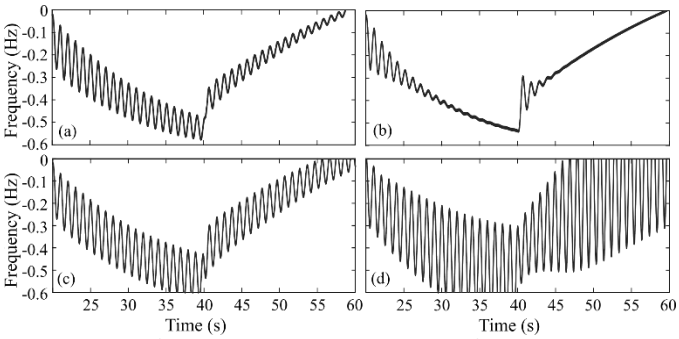

Fig. 14. Impact of ASHP operating condition on grid frequency: (a) designed response with linear assumptions (T_{cw}: 293 K, T_a: 273 K); (b) when T_a falls by 10 K; (c) when T_{cw} increases by 10 K; (d) when T_a increases by 10 K;

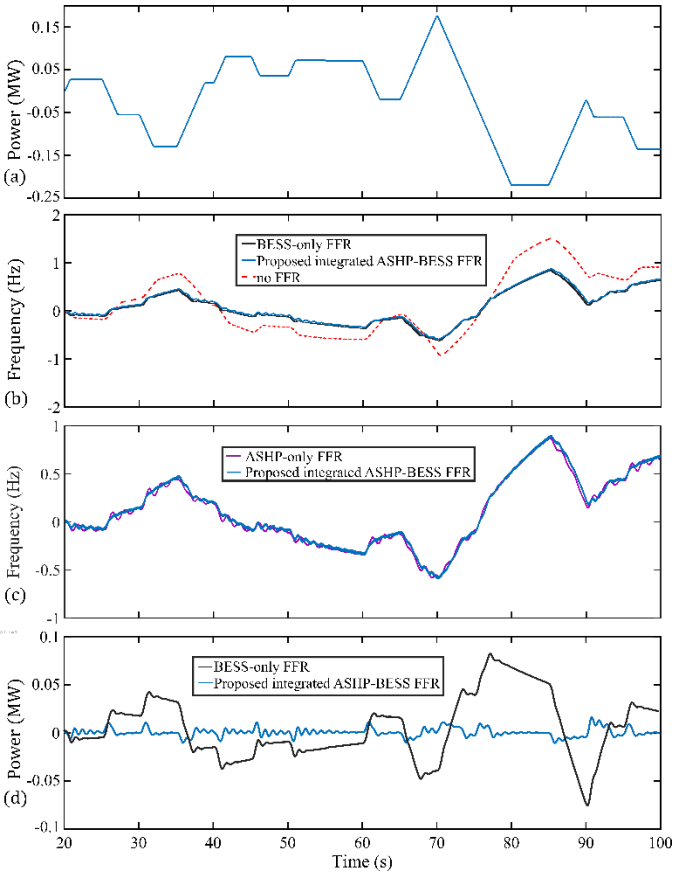

Fig. 15. Ramp power disturbance test results of the simulated grid when T_{cw} is 293 K and T_a is 273 K: (a) power disturbance profile; (b) grid frequency fluctuation comparison with BESS-only service; (c) grid frequency fluctuation comparison with ASHP-only service; (d) BESS power fluctuation comparison.

Our initial test highlights the advantages of the proposed FFR service during a scheduled generation re-dispatch. When this occurs, disturbances in the grid can happen gradually in a ramping manner rather than in abrupt steps. The maximum disturbance (0.25 MW) equals approximately 12.5% of the grid active power consumption, and the ramp rate limit is 4%/s (0.08 MW), as shown in Fig. 15 (a). The reason that we chose this disturbance range is to avoid over-modulation on ΔP_{ASHP}, which is normally caused by the speed limits of the compressor system. If the grid power disturbance is too large and the corresponding ΔP_{FFR}^* exceeds the limits of ΔP_{ASHP}, BESSs will assume full responsibility ($\Delta P_{BESS}^* = \frac{1}{N}\Delta P_{FFR}^*$) for the exceeded portion. As we want to show the integrated system performance under normal conditions, we set the disturbance magnitude to be safe for the proposed integrated FFR service.

In Fig. 15 (b), the integrated service achieves frequency regulation comparable to the standalone BESS service. However, a comparison of the BESS power profile between the integrated and BESS-only services reveals a significant advantage of the integrated service, as shown in Fig. 15 (d). The integrated service shows an 81% reduction in BESS peak power, implying a significant cost cutback. Another comparison with the ASHP-only service is shown in Fig. 15 (c), where both services achieve similar frequency regulation

regarding average value. Yet, the integrated and BESS-only services have lower transient oscillations.

The second test illustrates the advantages of the proposed FFR service during step power imbalances. The disturbance levels are similar to the ramping scenario, as in Fig. 16 (a). The frequency regulation comparison with the BESS-only service is shown in Fig. 16 (b), where we see the integrated service also does not compromise regulation quality under step disturbances. In Fig. 16 (d), we see the BESS power ripples for both services grow larger than in the ramping scenario, but the integrated service still allows an extended duration of near-zero power. As for the comparison with the ASHP-only service, the integrated and BESS-only services maintain their oscillation suppression advantages, as shown in Fig. 16 (c). However, compared with the ramping scenario, the extra oscillation caused by ASHP-only service has increased.

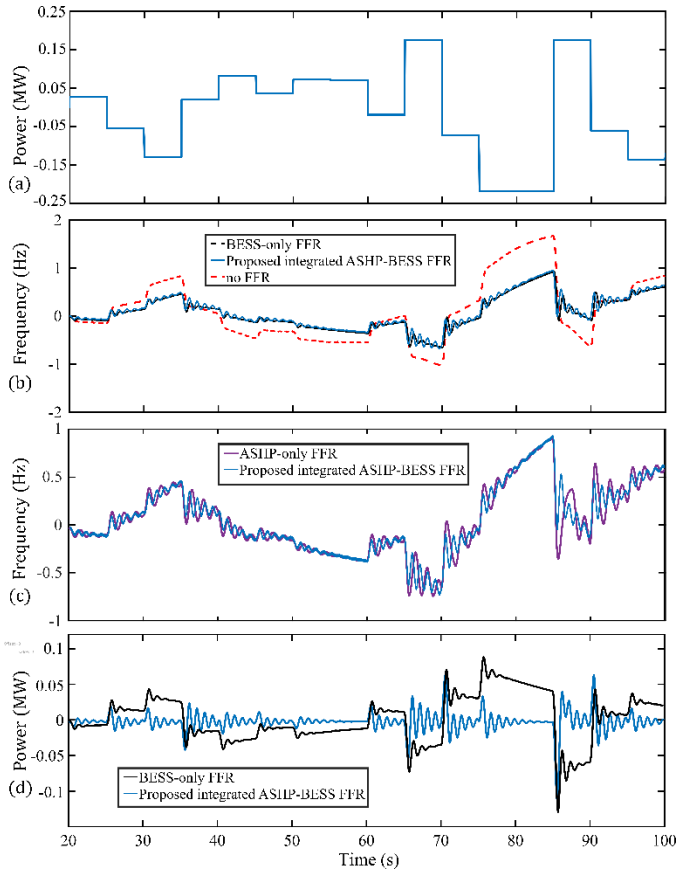

Fig. 16. Step power disturbance test results of the simulated grid when T_{cw} is 293 K and T_a is 273 K: (a) power disturbance profile; (b) grid frequency fluctuation comparison with BESS-only service; (c) grid frequency fluctuation comparison with ASHP-only service; (d) BESS power fluctuation comparison.

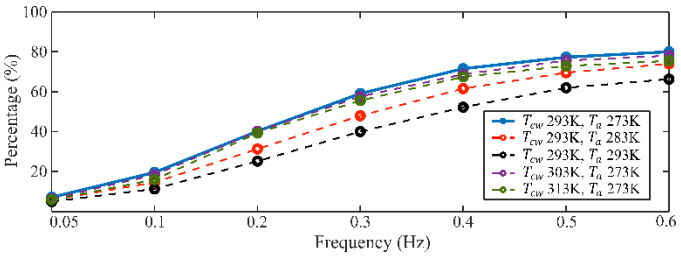

Fig. 17. BESS participation factor in the integrated FFR service system under various disturbance frequencies and operating conditions.

TABLE III
BESS PARTICIPATION RATE (%) IN THE INTEGRATED SYSTEM UNDER VARIOUS DISTURBANCE FREQUENCIES AND OPERATING CONDITIONS

Environment		0.05 Hz	0.1 Hz	0.2 Hz	0.3 Hz	0.4 Hz	0.5 Hz	0.6 Hz
T_{cw}	T_a							
293 K	273 K	7.12	19.57	40.20	59.08	71.51	77.28	79.99
293 K	283 K	5.82	14.59	31.30	47.94	61.55	69.52	73.96
293 K	293 K	4.96	11.32	25.18	40.02	52.23	61.93	66.27
303 K	273 K	6.41	18.38	40.10	57.58	68.74	75.59	78.03
313 K	273 K	5.90	15.96	39.31	55.57	67.43	72.88	75.41

E. Frequency-specific performance analysis

After acknowledging the potential for common scenarios, we also evaluated the performance of the integrated service specified to different oscillation frequencies. This is done by exciting the integrated ASHP-BESS system with sinusoidal references of varying frequencies to determine the BESS participation rate.

Given that both the reference and the resultant responses are close to sinusoidal waveforms, the BESS participation rate can be roughly calculated by comparing the response peak value between the BESS and the integrated system, and a lower value means lower BESS costs. The findings are shown in Fig. 17 and also detailed in Table III. The results show that the integrated service reduces the BESS participation rate when the disturbance frequency is below 0.6 Hz. However, when the disturbance frequency exceeds 0.6 Hz, the integrated system's performance becomes close to a standalone BESS service, as the participation of BESS rises to a level around 80%. This is because the thermal inertia of ASHPs prevents them from ultra-fast power tracking. Moreover, it is evident that T_a can also significantly influence the performance of the integrated system as a higher T_a can also considerably reduce the BESS participation rate.

V. CONCLUSIONS

In the context of declining power system inertia, integrating distributed ASHPs into demand-side, BESS-based FFR services becomes important. This integration not only enhances the FFR services but also reduces the operational demands and associated costs on BESSs. The success of this approach hinges on the development of a precise and rapid control system. Previous studies, which focus on primary and secondary ancillary services, typically employ a linear model for the heat pump power response. This linear approach is adequate for minute-level controller design where the nonlinearity of the heat pump's power response caused by complex thermal dynamics is less significant. However, such nonlinearity in power response leads to potential instability issues in FFR services. To address this challenge, this paper implements a nonlinear physics-based model for the ASHP power response. The subsequent nonlinear FFR control problem is then tackled with a combination of H_∞ and droop control method and controller design steps are provided. Multiphysics simulation results confirm that the proposed method enables ASHPs for FFR services and reduces the

service reliance on BESSs. Furthermore, the results also show that while ASHPs lessen the load on BESSs, they still necessitate BESSs acting as transient boosters in FFR services due to their limited response capabilities.

REFERENCE

[1] National grid ESO, "What is Frequency?" Accessed: Nov. 15, 2023. [Online]. Available: https://www.nationalgrideso.com/electricity-explained/how-do-we-balance-grid/what-frequency

[2] C. Rahmann and A. Castillo, "Fast Frequency Response Capability of Photovoltaic Power Plants: The Necessity of New Grid Requirements and Definitions," *Energies*, vol. 7, no. 10, pp. 6306–6322, Sep. 2014.

[3] R. Eriksson, N. Modig, and K. Elkington, "Synthetic inertia versus fast frequency response: a definition," *IET Renew. Power Gener.*, vol. 12, no. 5, pp. 507–514, Apr. 2018.

[4] National grid ESO, "New Dynamic Services (DC/DM/DR)." Accessed: Nov. 15, 2023. [Online]. Available: https://www.nationalgrideso.com/industry-information/balancing-services/frequency-response-services/new-dynamic-services-dcdmdr

[5] Australian energy market operator, "Fast Frequency Response." Accessed: Nov. 15, 2023. [Online]. Available: https://aemo.com.au/initiatives/major-programs/fast-frequency-response

[6] Fingrid, "Fast Frequency Reserve." Accessed: Nov. 15, 2023. [Online]. Available: https://www.fingrid.fi/en/electricity-market/reserves_and_balancing/fast-frequency-reserve/

[7] L. Meng *et al.*, "Fast Frequency Response From Energy Storage Systems—A Review of Grid Standards, Projects and Technical Issues," *IEEE Trans. Smart Grid*, vol. 11, no. 2, pp. 1566–1581, Mar. 2020.

[8] D. Fernández-Muñoz, J. I. Pérez-Díaz, I. Guisández, M. Chazarra, and Á. Fernández-Espina, "Fast frequency control ancillary services: An international review," *Renew. Sustain. Energy Rev.*, vol. 120, p. 109662, Mar. 2020.

[9] E. Pusceddu, B. Zakeri, and G. Castagneto Gissey, "Synergies between energy arbitrage and fast frequency response for battery energy storage systems," *Appl. Energy*, vol. 283, p. 116274, Feb. 2021.

[10] D. Cirio *et al.*, "Fast Frequency Regulation From a Wind Farm-BESS Unit by Model Predictive Control: Method and Hardware-in-the-Loop Validation," *IEEE Trans. Sustain. Energy*, vol. 14, no. 4, pp. 2049–2061, Oct. 2023.

[11] F. Sanchez, F. Gonzalez-Longatt, A. Rodriguez, and J. L. Rueda, "Dynamic Data-Driven SoC Control of BESS for Provision of Fast Frequency Response Services," in *2019 IEEE Power & Energy Society General Meeting (PESGM)*, pp. 1–5, Aug. 2019.

[12] Z. A. Obaid, L. M. Cipcigan, M. T. Muhssin, and S. S. Sami, "Control of a population of battery energy storage systems for frequency response," *Int. J. Electr. Power Energy Syst.*, vol. 115, p. 105463, Feb. 2020.

[13] U. Akram, M. Nadarajah, R. Shah, and F. Milano, "A review on rapid responsive energy storage technologies for frequency regulation in modern power systems," *Renew. Sustain. Energy Rev.*, vol. 120, p. 109626, Mar. 2020.

[14] J. Tan and Y. Zhang, "Coordinated Control Strategy of a Battery Energy Storage System to Support a Wind Power Plant Providing Multi-Timescale Frequency Ancillary Services," *IEEE Trans. Sustain. Energy*, vol. 8, no. 3, pp. 1140–1153, Jul. 2017.

[15] G. Delille, B. Francois, and G. Malarange, "Dynamic Frequency Control Support by Energy Storage to Reduce the Impact of Wind and Solar Generation on Isolated Power System's Inertia," *IEEE Trans. Sustain. Energy*, vol. 3, no. 4, pp. 931–939, Oct. 2012.

[16] Y. Mitsugi, H. Hashiguchi, T. Shigemasa, Y. Ota, T. Terazono, and T. Nakajima, "Control Hardware-in-the-Loop Simulation on Fast Frequency Response of Battery Energy Storage System Equipped With Advanced Frequency Detection Algorithm," *IEEE Trans. Ind. Appl.*, vol. 57, no. 6, pp. 5541–5551, Nov. 2021.

[17] D. Cirio *et al.*, "Fast Frequency Regulation From a Wind Farm-BESS Unit by Model Predictive Control: Method and Hardware-in-The-Loop Validation," *IEEE Trans. Sustain. Energy*, vol. 14, no. 4, pp. 1–13, Oct. 2023.

[18] P. D. Lund, J. Lindgren, J. Mikkola, and J. Salpakari, "Review of energy system flexibility measures to enable high levels of variable renewable electricity," *Renew. Sustain. Energy Rev.*, vol. 45, pp. 785–807, May 2015.

[19] International Energy Agency, "The future of cooling." Accessed: Nov. 15, 2023. [Online]. Available: https://www.iea.org/reports/the-future-of-cooling

[20] International Energy Agency, "The future of heat pumps." Accessed: Nov. 15, 2023. [Online]. Available: https://www.iea.org/reports/the-future-of-heat-pumps

[21] R. Song, T. Hamacher, V. Terzija, and V. S. Perić, "Potentials of using electric-thermal sector coupling for frequency control: A review," *Int. J. Electr. Power Energy Syst.*, vol. 151, p. 109194, Sep. 2023.

[22] G. Papaefthymiou, B. Hasche, and C. Nabe, "Potential of Heat Pumps for Demand Side Management and Wind Power Integration in the German Electricity Market," *IEEE Trans. Sustain. Energy*, vol. 3, no. 4, pp. 636–642, Oct. 2012.

[23] C. Li, Y. Yao, K. Xie, B. Hu, and T. Niu, "Integrated Electrical, Heating, and Water Distribution System to Accommodate Wind Power," *IEEE Trans. Sustain. Energy*, vol. 12, no. 2, pp. 1100–1114, Apr. 2021.

[24] D. Wang *et al.*, "A Demand Response and Battery Storage Coordination Algorithm for Providing Microgrid Tie-Line Smoothing Services," *IEEE Trans. Sustain. Energy*, vol. 5, no. 2, pp. 476–486, Apr. 2014.

[25] Y.-J. Kim, L. K. Norford, and J. L. Kirtley, "Modeling and Analysis of a Variable Speed Heat Pump for Frequency Regulation Through Direct Load Control," *IEEE Trans. Power Syst.*, vol. 30, no. 1, pp. 397–408, Jan. 2015.

[26] Y.-J. Kim, E. Fuentes, and L. K. Norford, "Experimental Study of Grid Frequency Regulation Ancillary Service of a Variable Speed Heat Pump," *IEEE Trans. Power Syst.*, vol. 31, no. 4, pp. 3090–3099, Jul. 2016.

[27] E. Vrettos and G. Andersson, "Scheduling and Provision of Secondary Frequency Reserves by Aggregations of Commercial Buildings," *IEEE Trans. Sustain. Energy*, vol. 7, no. 2, pp. 850–864, Apr. 2016.

[28] T. B. Harild Rasmussen, Q. Wu, and M. Zhang, "Primary frequency support from local control of large-scale heat pumps," *Int. J. Electr. Power Energy Syst.*, vol. 133, p. 107270, May. 2021.

[29] T. B. H. Rasmussen, Q. Wu, J. G. Moller, and M. Zhang, "MPC Coordinated Primary Frequency Support of Small- and Large-Scale Heat Pumps," *IEEE Trans. Smart Grid*, vol. 13, no. 3, pp. 2000–2010, May 2022.

[30] B. P. Rasmussen, "Dynamic modeling for vapor compression systems—Part I: Literature review," *HVAC&R Res.*, vol. 18, 2012.

[31] M. T. Muhssin, L. M. Cipcigan, N. Jenkins, S. Slater, M. Cheng, and Z. A. Obaid, "Dynamic Frequency Response From Controlled Domestic Heat Pumps," *IEEE Trans. Power Syst.*, vol. 33, no. 5, pp. 4948–4957, Sep. 2018.

[32] Wikipedia, "Dymola." Accessed: Nov. 05, 2023. [Online]. Available: https://en.wikipedia.org/wiki/Dymola

[33] Y.-J. Kim, L. K. Norford, and J. L. Kirtley, "Modeling and Analysis of a Variable Speed Heat Pump for Frequency Regulation Through Direct Load Control," *IEEE Trans. Power Syst.*, vol. 30, no. 1, pp. 397–408, Jan. 2015.

[34] M. Kuschke and K. Strunz, "Energy-Efficient Dynamic Drive Control for Wind Power Conversion With PMSG: Modeling and Application of Transfer Function Analysis," *IEEE J. Emerg. Sel. Top. Power Electron.*, vol. 2, no. 1, pp. 35–46, Mar. 2014.

[35] R. C. Portillo *et al.*, "Modeling Strategy for Back-to-Back Three-Level Converters Applied to High-Power Wind Turbines," *IEEE Trans. Ind. Electron.*, vol. 53, no. 5, pp. 1483–1491, Oct. 2006.

[36] P. Cancelliere, V. D. Colli, R. Di Stefano, and F. Marignetti, "Modeling and Control of a Zero-Current-Switching DC/AC Current-Source Inverter," *IEEE Trans. Ind. Electron.*, vol. 54, no. 4, pp. 2106–2119, Aug. 2007.

[37] C. Wu, Z. Xingxi, and D. Shiming, "Development of control method and dynamic model for multi-evaporator air conditioners (MEAC)," *Energy Convers. Manag.*, vol. 46, no. 3, pp. 451–465, Feb. 2005.

[38] A. Outtagarts, P. Haberschill, and M. Lallemand, "The transient response of an evaporator fed through an electronic expansion valve," *Int. J. Energy Res.*, vol. 21, no. 9, pp. 793–807, Jul. 1997.

[39] R. Song, G. Yon, T. Hamacher, and V. S. Peric, "Data-Driven Model Reduction of the Moving Boundary Heat Pump Dynamic Model," in *2022 IEEE Power & Energy Society General Meeting (PESGM)*, pp. 1–5, Jul. 2022.

[40] B. P. Rasmussen and A. G. Alleyne, "Control-Oriented Modeling of Transcritical Vapor Compression Systems," *J. Dyn. Syst. Meas. Control*, vol. 126, no. 1, pp. 54–64, Mar. 2004.

[41] O. Ibrahim, F. Fardoun, R. Younes, and H. Louahlia-Gualous, "Air source heat pump water heater: Dynamic modeling, optimal energy

management and mini-tubes condensers," *Energy*, vol. 64, pp. 1102–1116, Jan. 2014.
[42] S. Bendapudi, J. E. Braun, and E. A. Groll, "A comparison of moving-boundary and finite-volume formulations for transients in centrifugal chillers," *Int. J. Refrig.*, vol. 31, no. 8, pp. 1437–1452, Dec. 2008.
[43] TLK-Thermo GmbH, "TIL-Model library for thermal components and s ystems." Accessed: Nov. 15, 2023. [Online]. Available: https://www.tlk-thermo.com/index.php/en/til-suite
[44] J. . MacArthur and E. . Grald, "Unsteady compressible two-phase flow model for predicting cyclic heat pump performance and a comparison with experimental data," *Int. J. Refrig.*, vol. 12, no. 1, pp. 29–41, Jan. 1989.
[45] R. Song, G. Yon, T. Hamacher, and V. S. Peric, "Complete derivation of the moving boundary model for an air source heat pump," *TechRxiv*, 2023.
[46] Wikipedia, "Compressor." Accessed: Nov. 15, 2023. [Online]. Available: https://en.wikipedia.org/wiki/Compressor
[47] A. Villa, F. Belloni, R. Chiumeo, and C. Gandolfi, "Conventional and reverse droop control in islanded microgrid: Simulation and experimental test," in *2016 International Symposium on Power Electronics, Electrical Drives, Automation and Motion (SPEEDAM)*, pp. 288–294, Jun. 2016.
[48] L. Xie, M. Fu, and C. E. de Souza, "H_∞ control and quadratic stabilization of systems with parameter uncertainty via output feedback," *IEEE Trans. Automat. Contr.*, vol. 37, no. 8, pp. 1253–1256, Aug. 1992.
[49] I. Serban and C. Marinescu, "Control Strategy of Three-Phase Battery Energy Storage Systems for Frequency Support in Microgrids and with Uninterrupted Supply of Local Loads," *IEEE Trans. Power Electron.*, vol. 29, no. 9, pp. 5010–5020, Sep. 2014.
[50] L. Lennart, *System identification: theory for the user*. Upper Saddle River, NJ: PTR Prentice Hall, 1999.
[51] Mathwork, "System identification toolbox." Accessed: Dec. 06, 2023. [Online]. Available: https://ch.mathworks.com/products/sysid.html
[52] MathWorks, "Tune a Control System Using Control System Tuner." Accessed: Apr. 23, 2024. [Online]. Available: https://ww2.mathworks.cn/help/control/ug/tuning-control-systems-with-control-system-tuner.html

APPENDIX

A. Air-source heat pump parameters

TABLE IV
AIR-SOURCE HEAT PUMP THERMAL SUBSYSTEM PARAMETERS (12 KW)

Evaporator (Copper, fin-tube, 5 tubes)	$A_{i,c}$	$8.553e^{-4}\ m^2$	L_t	$15\ m$
	$A_{o,c}$	$1.134e^{-3}\ m^2$	$\alpha_{i,tp}$	$2000\ W/m^2K$
	$\alpha_{i,v}$	$400\ W/m^2K$	α_o	$50\ W/m^2K$
	$\bar{\gamma}$	0.894	$A_{o,s}$	$53\ m^2$
Condenser (Copper, shell-tube, 5 tubes)	$A_{i,c}$	$1.662e^{-3}\ m^2$	L_t	$15\ m$
	$A_{o,c}$	$1.963e^{-3}\ m^2$	$\alpha_{i,tp}$	$2000\ W/m^2K$
	$\alpha_{i,v}$	$400\ W/m^2K$	α_o	$2000\ W/m^2K$
	V_{cw}	$0.01\ m^2$	$\dot{m}_{cw}$	$0.5\ kg/s$
	$\bar{\gamma}$	0.771	$A_{o,s}$	$11.78\ m^2$
Compressor (R134a)	R	$81.49\ J/kg{\cdot}K$	V_{cm}	$2.5e^{-3}\ m^3$
	k_1	1.2		
Expansion Valve	k_2	1.414	k_p	$-1e^{-7}$
	k_i	$-3.3\ e^{-8}$		

B. Integration results of conservation equations

All integration of conservation laws of the evaporator system is shown here, note that the bolded parts are thermal dynamic property coefficients determined by a media (R-134a in this paper) look-up table. If the refrigerant is in saturation state, then the index variable for saturation dynamic property coefficients ($d\rho_v'/dp$, $d\rho_l'/dp$, $dh_v'/dp\ldots$) is pressure only. For non-saturation properties, the index variable is written as a footnote, such as h_v for $\partial\rho_v/\partial p|_{h_v}$. For detailed derivation process of all listed integration results, please refer to [45].

The integration result of refrigerant mass conservation in the two-phase zone of the evaporator system:

$$\left(\frac{\boldsymbol{d\rho_v'}}{\boldsymbol{dp}}\bar{\gamma}+\frac{\boldsymbol{d\rho_l'}}{\boldsymbol{dp}}(1-\bar{\gamma})\right)A_{i,c}L_{tp}\frac{dp}{dt}+(\boldsymbol{\rho_l'}-\boldsymbol{\rho_v'})(1-\bar{\gamma})A_{i,c}\frac{dL_{tp}}{dt}+\dot{m}_b\text{-}\dot{m}_{in}=0. \tag{29}$$

The integration result of refrigerant energy conservation in the two-phase zone of the evaporator system:

$$\begin{aligned}A_{i,c}L_{tp}\frac{dp}{dt}\left(\frac{\boldsymbol{d\rho_v'}}{\boldsymbol{dp}}\boldsymbol{h_v'}+\frac{\boldsymbol{dh_v'}}{\boldsymbol{dp}}\boldsymbol{\rho_v'}\right)\bar{\gamma}&\\+A_{i,c}L_{tp}\frac{dp}{dt}\left(\left(\frac{\boldsymbol{d\rho_l'}}{\boldsymbol{dp}}\boldsymbol{h_l'}+\frac{\boldsymbol{dh_l'}}{\boldsymbol{dp}}\boldsymbol{\rho_l'}\right)(1-\bar{\gamma})-1\right)&\\+(\boldsymbol{\rho_l'h_l'}-\boldsymbol{\rho_v'h_v'})(1-\bar{\gamma})A_{i,c}\frac{dL_{tp}}{dt}+\dot{m}_bh_b&\\-\dot{m}_{in}h_{in}=A_{i,s}\frac{L_{tp}}{L_t}\alpha_{i,tp}(T_{w,tp}-T_{r,tp}).&\end{aligned} \tag{30}$$

The integration result of wall energy conservation in the two-phase zone of the evaporator system:

$$\begin{aligned}&C_w\rho_w(A_{o,c}-A_{i,c})L_{tp}\frac{dT_{w,tp}}{dt}\\&=A_{i,s}\frac{L_{tp}}{L_t}\alpha_{i,tp}(T_{r,tp}-T_{w,tp})+A_{o,s}\frac{L_{tp}}{L_t}\alpha_o(T_a-T_{w,tp}).\end{aligned} \tag{31}$$

The integration result of refrigerant mass conservation in the vapor zone of the evaporator system:

$$\begin{aligned}\left(\boldsymbol{\frac{\partial\rho_v}{\partial p}}\Big|_{\boldsymbol{h_v}}+\frac{1}{2}\boldsymbol{\frac{\partial\rho_v}{\partial h_v}}\Big|_{\boldsymbol{p}}\boldsymbol{\frac{dh_v'}{dp}}\right)A_{i,c}L_v\frac{dp}{dt}+\dot{m}_{out}-\dot{m}_b&\\+(\boldsymbol{\rho_v'}-\rho_v)A_{i,c}\frac{dL_{tp}}{dt}+\frac{1}{2}\boldsymbol{\frac{\partial\rho_v}{\partial h_v}}\Big|_{\boldsymbol{p}}A_{i,c}L_v\frac{dh_{out}}{dt}=0.&\end{aligned} \tag{32}$$

The integration result of refrigerant energy conservation in the vapor zone of the evaporator system:

$$\begin{aligned}\left(\left(\boldsymbol{\frac{\partial\rho_v}{\partial p}}\Big|_{\boldsymbol{h_v}}+\frac{1}{2}\boldsymbol{\frac{\partial\rho_v}{\partial h_v}}\Big|_{\boldsymbol{p}}\boldsymbol{\frac{dh_v'}{dp}}\right)h_v+\frac{1}{2}\boldsymbol{\frac{dh_v'}{dp}}\rho_v-1\right)&\\A_{i,c}L_v\frac{dp}{dt}+\frac{1}{2}\left(\boldsymbol{\frac{\partial\rho_v}{\partial h_v}}\Big|_{\boldsymbol{p}}h_v+\rho_v\right)A_{i,c}L_v\frac{dh_{out}}{dt}&\\+\dot{m}_{out}h_{out}-\dot{m}_bh_b+(\boldsymbol{\rho_v'h_v'}-\rho_vh_v)A_{i,c}\frac{dL_{tp}}{dt}&\\=A_{i,s}\frac{L_v}{L_t}\alpha_{i,v}(T_{w,v}-T_{r,v}).&\end{aligned} \tag{33}$$

The integration result of wall energy conservation in the vapor zone of the evaporator system:

$$\begin{aligned}&C_w\rho_w(A_{o,c}-A_{i,c})L_v\left(\frac{dL_{tp}}{dt}\frac{T_{w,tp}-T_{w,v}}{L_v}+\frac{dT_{w,v}}{dt}\right)\\&=A_{i,s}\frac{L_v}{L_t}\alpha_{i,v}(T_{r,v}-T_{w,v})+A_{o,s}\frac{L_v}{L_t}\alpha_o(T_a-T_{w,v}).\end{aligned} \tag{34}$$

C. *Summary of physical variables:*

- Variables & Parameters: ρ: Density; p: Pressure; h: Specific enthalpy; $\dot{m}$: Mass flow; $\bar{\gamma}$: Average vapor fraction; A: Cross-section area; L: Zone length; α: Heat transfer coefficient; C: Specific heat; c: Circumference; T: Temperature; P: Power; V: Volume; ω: Speed; η: Efficiency; R: Gas constant; κ: Integration limit; k: Constants.
- Subscripts: v: Vapor; l: Liquid; c: Cross-section; s: Surface; i/o: Inner/Outer; t: Total; tp: Two-phase zone; r: refrigerant; w: Wall; a: Air; b: Boundary between two-phase and vapor zone; in/out: Input/Output; cw: Cold water; sh: Superheat.
- Superscripts: $*$: Reference; $'$: Variables in saturation state.

BIOGRAPHIES

Ruihao Song (Member, IEEE) received the B.Eng. degree from Donghua University, Shanghai, China, in 2016, and the M.Phil. degree from the University of New South Wales, Sydney, Australia, in 2019. He is currently working towards the Ph.D. degree with the Technical University of Munich, Garching, Germany. His research interests include power systems operation and control, renewable energy, microgrids, ancillary services, battery energy storage systems, and integrated energy systems.

Vladimir Terzija (Fellow, IEEE) received the Dipl-Ing., M.Sc., and Ph.D. degrees in electrical engineering from the University of Belgrade, Belgrade, Serbia, in 1988, 1993, and 1997, respectively. Since 2023, he has been a Professor of energy systems and networks with Newcastle University. From 2021 to 2023, he was a Full Professor and the Head of Laboratory of Modern Energy Systems, Skoltech, Russia. From 2006 to 2020, he was the EPSRC Chair Professor in power system engineering with the Department of Electrical and Electronic Engineering, The University of Manchester, Manchester, U.K. From 1997 to 1999, he was an Assistant Professor with the University of Belgrade. From 2000 to 2006, he was a Senior Specialist for switchgear and distribution automation with ABB, Ratingen, Germany. His research interests include smart grid applications, wide-area monitoring, protection and control, multi-energy systems, switchgear and transient processes, ICT, data analytics, and digital signal processing applications in power systems. He was a recipient of the prestigious Alexander von Humboldt Fellow. He is the Editor-in-Chief of the International Journal of Electrical Power and Energy Systems.

Thomas Hamacher received the Ph.D. degree from the University of Hamburg, Hamburg, Germany, in 1994, for his work on baryonic beta decay after studying physics at the University of Bonn, Bonn, Germany, RWTH Aachen University, Aachen, Germany, and Columbia University, New York, NY, USA. He has been with the Max Planck Institute for Plasma Physics, Garching, Germany, since 1996, most recently as the Head of the Energy and System Studies Group. From 2010 to 2013, he was the Acting Head of the Chair of the Energy Management and Application Technology, Technical University of Munich (TUM), Munich, Germany. In 2013, he was appointed as a Full Professor of renewable and sustainable energy systems at TUM. He is the Director of the Munich School of Engineering, Garching. He is a member of the Environmental Science Centre (WZU), University of Augsburg, Augsburg, Germany. His research interests include energy and systems analysis, urban energy systems, integration of renewable energy into power grids, and innovative nuclear systems (including fusion). His additional research interest includes methods and fundamentals of energy models. He is also a member of the Energy Working Group of the European Physical Society (EPS).

Vedran S. Perić (Member, IEEE) received the M.S. degree in power systems and power electronics from the University of Novi Sad, Serbia, and the joint Ph.D. degree from the KTH Royal Institute of Technology, Stockholm, Sweden (primary institution), the Delft University of Technology, Delft, The Netherlands, and Comillas Pontifical University, Madrid, Spain, in 2016. He was a Research and Teaching Assistant with the University of Novi Sad and Visiting Researcher with the Delft University of Technology. He held positions of Senior Power System Engineer with GE Grid Solutions Research and Development Department, Senior Power System Consultant at GE Energy Consulting, and as a Senior Business Analyst with Regional Security Coordinator, TSCNET Services GmbH. He was a Head of Research Center for Combined Smart Energy Systems (CoSES) at the Munich Institute of Integrated Materials, Energy and Process Engineering at Technical University of Munich, Germany. Since 2024, he has been an Associated Professor of electrical energy technology at Aarhus University, Denmark. His research interests include power system operation and control, with the focus on commercial application of innovative technologies.

Concluding Remarks

This paper explored the challenges and theoretically validated the feasibility of integrating ASHP in the existing BESS-based FFR services, which is particularly valuable due to the increasing demand for FFR capacity and the high costs of BESS. In summary, FFR-compatible ASHP controllers are much more complex to design than PFR and SFR controllers because the non-linear power response behaviors of ASHP start to impact control stability significantly.

The model used for referencing distributed ASHP behavior originates from Section 3.1. In order to conduct small-signal analysis efficiently, we simplified the electrical subsystem into a linear transfer function to reduce the model size and cut the redundant information on the grid-interfacing current. On top of that, we applied the H_∞ method [87][88][89] for the ASHP power control loop to handle the dynamic behavior uncertainty problem. The coordination between the local ASHP and BESS in each building was designed such that the ASHP takes the body part of the FFR responsibility, and the BESS was controlled to fill the response gap between the total calculated FFR demand and measured contribution from the ASHP.

The overall closed-loop stability was examined with the root-locus method [90]. Finally, we simulate the proposed FFR strategy in a low-inertia medium voltage microgrid, and the resulting data theoretically confirmed our hypothesis that integrating ASHP in the FFR services can reduce the pressure on BESSs and thus reduce the overall service costs. Besides, we also proved that ASHPs cannot solely satisfy the requirement of FFR services, and they need BESSs to help during transients.

Chapter 4: Economic Frequency Recovery: the PFR and SFR Services Scenario

This Chapter focuses on how to model and design controllers for heat pumps to enable them for PFR and SFR services. With the current stage of REG penetration level in power systems, PFR and SFR services still dominate the market of frequency ancillary services. The response time requirements for these services are much more relaxed than those for FFR services, and the reduced response requirement opens up the possibility for a broad spectrum of heat pumps to be utilized in PFR and SFR services. In this context, we present the modeling and controller design results in this section with two publications.

4.1 Data-driven Modeling of Commercial Heat Pumps

Scientific Context

To effectively harness the potential of various commercial heat pumps for an economic frequency recovery stage, it is essential to develop a modeling method that is both practical and adaptable. This method should be specially tailored for PFR and SFR services in order to balance the computation and accuracy, and it should be capable of accommodating a wide range of heat pump systems. Similar problems were studied in [91][92], where the focus was the temperature response modeling for a wide range of heat pumps. For our application, we can summarize the following three key features for the target modeling scenario.

- The physical structure of heat pumps can vary significantly for different power ratings. Large-scale heat pumps at the centralized level generally have more components than domestic and community levels.
- Commercial modules do not guarantee access to internal measurements and detailed physical parameters. Typically, we can only study the target heat pump through input-output testing.
- Compared with the modeling requirement of FFR services, the role of non-linear dynamics is weakened for PFR and SFR services. This means we can replace the previous non-linear transient characteristics with a single linear approximation, significantly reducing the modeling complexity.

Publication #4: Data-Driven Model Reduction of the Moving Boundary Heat Pump Dynamic Model

Authors: Ruihao Song, Guillaume Yon, Thomas Hamacher, Vedran Peric

Publication: 2022 IEEE Power & Energy Society General Meeting (PESGM).

Digital object identifier: 10.1109/PESGM48719.2022.9916823.

Author	**Contribution**	**Tasks**
Ruihao Song	65%	• Conceptualization • Methodology • Investigation • Writing-original draft • Writing-review & editing
Guillaume Yon	20%	• Methodology
Thomas Hamacher	5%	• Writing-review & editing
Vedran Peric	10%	• Supervision • Writing-review & editing

Data-Driven Model Reduction of the Moving Boundary Heat Pump Dynamic Model

Ruihao Song
School of Engineering and Design
Technical University of Munich
Munich
ruihao.song@tum.de

Guillaume Yon
Energy Production and Management
ENSTA ParisTech
Paris
guillaume.yon@ensta-paris.fr

Thomas Hamacher
School of Engineering and Design
Technical University of Munich
Munich
thomas.hamacher@tum.de

Vedran S Perić
School of Engineering and Design
Technical University of Munich
Munich
vedran.peric@tum.de

***Abstract*— Heat pump systems have the potential to be used as controllable load to compensate for the uncertainties in modern power systems. The moving boundary model for heat pumps is known for its accuracy and acceptable computational burden. However, this model is sometimes impractical because it requires detailed information on the mechanical structure of the internal loops and the thermal state of the refrigerant. A data-driven method based on the cascaded wiener model is proposed in this paper to simplify the moving boundary model. The proposed model is developed from an observation that the dynamic behavior of the heat pump is relatively linear over a large range of operation states, while the static behavior is very nonlinear. Through comparison of simulation results, the proposed model has close accuracy to the moving boundary model and can be a viable alternative for control design purposes.**

***Keywords*— heat pump, dynamic modelling, moving boundary model, wiener model, controllable load, data-driven modelling.**

NOMENCLATURE

Variables		Subscripts	
L	Effective length	ini	Initial condition
A	Area	v	Vapor in saturation state
ρ	Density	l	Liquid in saturation state
$\dot{m}$	Massflow	i	Inner
P	Pressure	o	Outer
h	Specific enthalpy	w	Wall
T	Temperature	a	Ambient Air
α	Heat transfer coefficient	r	Refrigerant
p	Perimeter	t	Total
ω	Rotational speed	c	Cross-section
η	Volumetric efficiency	s	Surface
γ	Vapor fraction	cw	Condensing water
k	Empirical constant	cm	Compressor
R	Gas constant	ev	Expansion valve
		sh	Superheat

I. INTRODUCTION

Heat and electricity are the two major sectors of the modern energy system [1]. The coupling between these sectors can mitigate the power system flexibility challenges of renewable energy penetration or bring collateral damage by introducing cross-sector faults [2]. Therefore, it is important to carefully study the coupling equipment and control them in an appropriate way. The heat pump system is a representative system that can bridge the heat and electricity sectors because it converts electricity into heat efficiently. It has great potential to be used as a flexible load in microgrids to maintain the stability of the power supply [3]. Therefore, there is a motivation for developing accurate and practical heat pump dynamic models for control design purposes.

The moving boundary model [4][5][6] is a well-known physics-based model for heat pump dynamics. It tackles the refrigerant phase-changing problem by dividing the evaporator/condenser volumes into different zones, where each zone represents a specific refrigerant state. More researchers followed this modelling philosophy and developed advanced versions, which include features such as mode switching [7] (one, two, or three-zone modes) and pressure drop [8]. Although the moving boundary model is well-validated and well-accepted due to its accuracy, the need for relatively detailed information about the refrigerant loop undermines its practicality. Data-driven modelling approaches are alternatives that can provide similar accuracy, while do not require knowledge about the refrigerant loop. The Hammerstein-wiener model structure is potentially a suitable modeling approach for this application, because the dynamic behavior of the heat pump is relatively linear throughout the operation range, while the static behavior is very nonlinear. Researchers in [9] used the Hammerstein-wiener model for geothermal borefields, which shows an example for using such model structure in thermal system modelling. In [10], the Hammerstein-wiener model is applied for modelling a ground source heat pump. However, the electrical characteristics are not considered in this research.

In this paper, a data-driven cascaded wiener model is proposed for the dynamic modelling of an air source heat pump for both electrical and thermal characteristics. The model contains three branches to consider the impact of compressor speed, condensing water temperature, and air temperature inputs, where each branch is characterized by a wiener model. The coupling effect between inputs is described by a set of nonlinear functions. Both the traditional moving boundary model and the cascaded wiener model are built in Modelica environment [11] for performance comparison. The presented results show that the proposed model has resembled performance with the moving boundary model and can be calibrated easily without any sensors in the refrigerant loop.

This paper is organized as follows. Firstly, Section II presents the traditional moving boundary model. Secondly, Section III introduces the detailed structure and calibration procedure of the data-driven cascaded wiener model. Thirdly, an experiment is shown in Section IV, where the performance of the moving boundary model and the proposed model are compared for two different scenarios. Finally, Section V gives the conclusion of this paper.

II. MOVING-BOUNDARY MODEL

The overall structure of the moving boundary model for an air-source heat pump is shown in Fig. 1. The model consists of 4 components (Fig.1: A, B, C, D), which will be discussed in detail. The inputs to this model are the speed (ω), air temperature (T_a), and condensing water temperature ($T_{cw,in}$) while the outputs are electrical power (P_{ele}) and output water temperature (T_{out}). For a typical two-zone type model, one zone contains refrigerant in a mixture state of vapor and liquid, and the other contains refrigerant in a pure vapor. All modelling assumptions are listed as follows.

2022 IEEE Power & Energy Society General Meeting (PESGM) | 978-1-6654-0823-3/22/$31.00 ©2022 IEEE | DOI: 10.1109/PESGM48719.2022.9916823

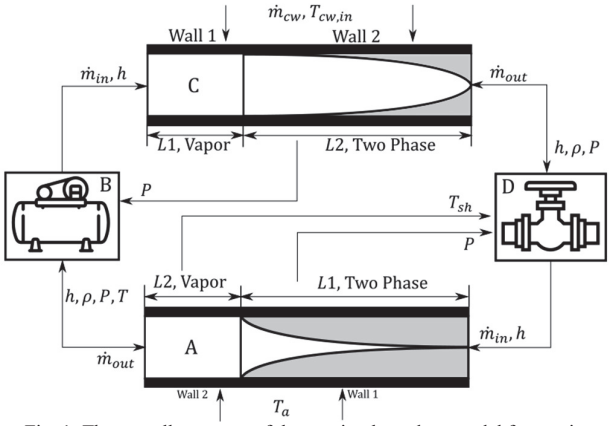

Fig. 1. The overall structure of the moving boundary model for an air-source heat pump. A: Evaporator; B: Compressor; C: Condenser; D: Expansion valve.

Evaporator and Condenser:

- Cross-section area is constant in pipes;
- Momentum conservation and pressure drop are neglected;
- Only the axial flow dynamics are considered;
- Fluid is at equilibrium in the two-phase zone;
- Variable and parameters are averaged in each zone;
- Refrigerant boundary state between one and the two-phase zone is in thermal equilibrium;
- Boundary temperature between wall zones is equal to the temperature of the two-phase zone;
- Vapor fraction is constant in both exchangers.

Compressor:

- Actuation dynamics are neglected;
- Process is isentropic.

Expansion Valve:

- Actuation dynamics are neglected;
- Process is adiabatic.

A. Evaporator

The refrigerant enters the evaporator as a saturated mixture of vapor and liquid, and then leaves as superheated vapor, as shown in part A of Fig. 1. Eq. (1)-(6) gives all the evaporator's conservation equations. The detailed derivation of the conservation equations is shown in [12].

1) Mass Conservation

In the two-zone, the equation is:

$$\left(\frac{d\rho_v}{dP}\bar{\gamma}+\frac{d\rho_l}{dP}(1-\bar{\gamma})\right)A_{ci}L_1\frac{dP}{dt}+\dot{m}_b-\dot{m}_{in} +(\rho_l-\rho_v)(1-\bar{\gamma})A_{ci}\frac{dL_1}{dt}=0. \quad (1)$$

In the vapor zone, the equation is:

$$\left(\frac{\partial\rho_2}{\partial P}\Big|_{h_2}+\frac{1}{2}\frac{\partial\rho_2}{\partial h_2}\Big|_P\frac{dh_v}{dP}\right)A_{ci}L_2\frac{dP}{dt}+\dot{m}_{out}-\dot{m}_b +(\rho_v-\rho_2)A_{ci}\frac{dL_1}{dt}+\frac{1}{2}\frac{\partial\rho_2}{\partial h_2}\Big|_P A_{ci}L_2\frac{dh_{out}}{dt}=0. \quad (2)$$

2) Energy Conservation

In the two-phase zone, the equation for the refrigerant is:

$$\left(\left(\frac{d\rho_v}{dP}h_v+\frac{dh_v}{dP}\rho_v\right)\bar{\gamma}+\left(\frac{d\rho_l}{dP}h_l+\frac{dh_l}{dP}\rho_l\right)(1-\bar{\gamma})-1\right)A_{ci}L_1\frac{dP}{dt}+(\rho_l h_l-\rho_v h_v)(1-\bar{\gamma})A_{ci}\frac{dL_1}{dt}+\dot{m}_b h_b -\dot{m}_{in}h_{in}=A_{si}\frac{L_1}{L_t}\alpha_{i,tp}(T_{w1}-T_{r1}). \quad (3)$$

In the two-phase zone, the equation for the wall is:

$$A_{si}\frac{L_1}{L_t}\alpha_{i,tp}(T_{r1}-T_{w1})+A_{so}\frac{L_1}{L_t}\alpha_o(T_a-T_{w1}) =C_w\rho_w(A_{co}-A_{ci})L_1\frac{dT_{w1}}{dt}. \quad (4)$$

In the vapor zone, the equation for the refrigerant is:

$$A_{ci}L_2\frac{dP}{dt}\left(\left(\frac{\partial\rho_2}{\partial P}\Big|_{h_2}+\frac{1}{2}\frac{\partial\rho_2}{\partial h_2}\Big|_P\frac{dh_v}{dP}\right)h_2+\frac{1}{2}\frac{dh_v}{dP}\rho_2-1\right) +\frac{1}{2}\left(\frac{\partial\rho_2}{\partial h_2}\Big|_P h_2+\rho_2\right)A_{ci}L_2\frac{dh_{out}}{dt}+\dot{m}_{out}h_{out}-\dot{m}_b h_b +(\rho_v h_v-\rho_2 h_2)A_{ci}\frac{dL_1}{dt}=A_{si}\frac{L_2}{L_t}\alpha_{i,v}(T_{w2}-T_{r2}). \quad (5)$$

In the vapor zone, the equation for the wall is:

$$C_w\rho_w(A_{co}-A_{ci})L_2\left(\frac{dL_1}{dt}\frac{T_{w1}-T_{w2}}{L_2}+\frac{dT_{w2}}{dt}\right) =A_{si}\frac{L_2}{L_t}\alpha_{i,v}(T_{r2}-T_{w2})+A_{so}\frac{L_2}{L_t}\alpha_o(T_a-T_{w2}). \quad (6)$$

In all the derived equations, P, L_1, h_{out}, T_{w1}, and T_{w2} are state variables. $\frac{d\rho_{v,l}}{dP}$, $\frac{\partial\rho}{\partial P}\Big|_h$, $\frac{\partial\rho}{\partial h}\Big|_P$, $\frac{dh_{v,l}}{dP}$, ρ_v, and ρ_l are parameters calculated dynamically from state variables.

B. Compressor

The specific enthalpy increment and the massflow of the compressor can be calculated with Eq. (7). The massflow is calculated with a dynamic volumetric efficiency, which is a function of the pressure ratio between the input and output. Finally, the compressor power can be obtained by multiplying the massflow and the specific enthalpy increment.

$$P_{shaf}=\underbrace{\left(\frac{\omega}{2\pi}V_{cm}\rho_{in}\eta\right)}_{MassFlow}\underbrace{\left(\frac{kRT_{in}}{k-1}\left(\left(\frac{P_{out}}{P_{in}}\right)^{\frac{k-1}{k}}-1\right)\right)}_{\Delta h}. \quad (7)$$

C. Condenser

As shown in the condenser part of Fig. 1, the first zone is now the vapor zone, which causes the resulting system to be slightly different from the evaporator. In addition, since the condenser has a volume for the water, one additional energy conservation equation is needed for the condensing water volume. Interested readers can also refer to [12] for the complete condenser model equations and derivation.

D. Expansion Valve

The massflow rate of the expansion valve is calculated from the pressure differences between the input and output, as in (10). Since electronic expansion valves have been widely used for modern heat pumps, a PI-based superheat control mechanism is implemented in the model, as illustrated in (11).

$$\dot{m}_{ev}=A_{ev}C_{ev}[\rho_{in}(P_{out}-P_{in})], \quad (10)$$

$$A_{ev}=kp(T_{sh}^*-T_{sh})+ki\int(T_{sh}^*-T_{sh})dt+A_{ev,base}. \quad (11)$$

978-1-6654-0823-3/22/$31.00 ©2022 IEEE

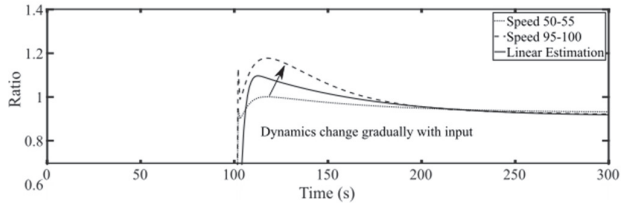

Fig. 2. Electric power response (normalized) with respect to different speed step changes.

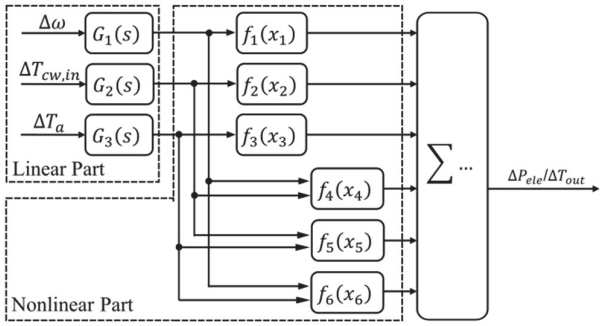

Fig. 3. Cascaded wiener model for air source heat pump.

III. Proposed Data-Driven Cascaded Wiener Model

To simplify the traditional moving boundary model, we propose a data-driven cascaded wiener model. The reason for choosing such model type is explained as follows. Although the dynamics of the heat pump is mathematically nonlinear for different input ranges, we observed from the simulation results that the dynamical behavior changes are relatively small. For example, Fig. 2 shows how the power response changes for different speed input ranges. It is obvious that a linear transfer function can provide sufficient accuracy even though the curve characteristic changes with the speed input range. Thus we choose to use a transfer function based system to approximate the dynamic behavior. However, we find serious steady-state mismatch problems if only transfer functions are used for the dynamic model. Therefore, an extra gain function is needed for steady-state calibration. A typical wiener model contains two parts: a linear dynamics part and a nonlinear function part, which makes it very suitable for this application. The input to the system goes through the linear dynamics first and then through nonlinear functions, as shown in Fig. 3.

The inputs (ω, $T_{cw,in}, T_a$) and outputs (P_{ele}, T_{out}) of the cascaded wiener model are the same as the moving boundary model. All dynamics are represented by transfer functions. Note that extra correlation terms are added to the model to describe the coupling between system inputs. In this paper, the correlations are described by regression surfaces. The reason for using three correlation functions instead of one is to avoid unnecessary complexity in calibration. Through the designed structure, we can bring the regression problem from four-dimension to three-dimension without losing much accuracy. The data used for calibration can either be taken from a detailed model simulation or a real system experiment. The detailed model calibration is explained in five main steps.

- Step 1: Choose a base operating point that is defined by system inputs and outputs data. The base point determines the offset in all inputs and outputs. In this paper, the base operating point is the minimum values in the operating ranges.
- Step 2: Calibrate G_1, G_2, G_3 based on error minimization according to the measured responses. Since the steady-state values are addressed in the nonlinear functions, the results from this step should be transfer functions with unity gain in the steady-state.
- Step 3: Calibrate f_1, f_2, f_3 based on error minimization according to steady-state output data from single-input tests. The input data should be selected evenly from the input ranges.
- Step 4: Calibrate f_4, f_5, f_6 based on error minimization according to the steady-state correlation error from dual-input tests. After finishing step 3, a base part model can be established, which should be used to identify the correlation error.
- Step 5: Combine all parts and build the complete cascaded wiener model.

IV. Experiments and Results Comparison

The introduced moving boundary model is implemented in Modelica environment in the same way as shown in Fig. 1. The parameters used for simulation are shown in Table I. The refrigerant fluid type is R134a (tetrafluoroethane), and all its thermal dynamic properties are calculated in a numerical way through Modelica R134a media library. The data needed for calibrating the cascaded wiener model is taken from the simulation results. The operation range of the heat pump is set to 50-100 rads/s (ω), 293.15-323.15 K ($T_{cw,in}$), and 273.15-303.15 K (T_a). The increment for speed, air temperature, and water temperature is chosen as 5 rads/s, 3 degrees, and 3 degrees. Time-domain simulations are used to identify the dynamic part of the cascaded wiener model, and steady-state points are used for the regression of nonlinear functions.

A. Step 1: Finding offsets from the base operating point

The moving boundary model is initialized and then injected with base point inputs (50 rads/s, 293.15 K, 273.15 K). The resulting P_{ele} is 991.85 W and T_{out} is 299.24 K.

TABLE I
Moving Boundary Model Parameters

Symbol	Quantity	Symbol	Quantity
	$Evaporator\ (Copper)$		
A_{ci}	$2.138e^{-4}\ m^2$	L_t	$15\ m$
A_{co}	$2.835e^{-4}\ m^2$	α_{i1}	$2000\ W/m^2K$
A_{si}	$0.7775\ m^2$	α_{i2}	$400\ W/m^2K$
A_{so}	$0.8954\ m^2$	α_o	$300\ W/m^2K$
$L_{1,ini}$	$7.938\ m$	P_{ini}	$1.8\ bar$
$h_{out,ini}$	$403690\ J/kg$	$T_{w1,ini}$	$262.365\ K$
$T_{w2,ini}$	$270.388\ K$	$\bar{\gamma}$	0.894
	$Condenser\ (Copper)$		
A_{ci}	$4.155e^{-4}\ m^2$	L_t	$15\ m$
A_{co}	$4.909e^{-4}\ m^2$	α_{i1}	$400\ W/m^2K$
A_{si}	$1.084\ m^2$	α_{i2}	$2000\ W/m^2K$
A_{so}	$1.178\ m^2$	α_o	$2000\ W/m^2K$
V_{cw}	$0.005\ m^2$	P_{ini}	$7.5\ bar$
$h_{out,ini}$	$335640\ J/kg$	$T_{w1,ini}$	$302.293\ K$
$T_{w2,ini}$	$301.1\ K$	$\dot{m}_{cw}$	$0.1\ kg/s$
$T_{water,ini}$	$300.035\ K$	$\bar{\gamma}$	0.771
	$Compresser\ (R134a)$		
	$\eta = 1 - 0.043\frac{P_{out}}{P_{in}}$		
R	$81.49\ J/kgK$	V_{cm}	$50e^{-5}\ m^3$
k	1.2		
	$Expansion\ Valve$		
	$C_{ev} = 3 + 5\,e^{-6}(P_{out} - P_{in})$		
$A_{ev,base}$	$5e^{-7}\ m^2$	kp	$-1e^{-6}$
ki	$-2e^{-7}$	T^*_{sh}	$15\ K$

978-1-6654-0823-3/22/$31.00 ©2022 IEEE

TABLE II
POLE-ZERO SELECTION DATA FOR $G_{1,2,3}$

	P_{ele}		T_{out}	
G_1	2 poles 1 zero	86.96%*	**2 poles 1 zero**	99.68%
	3 poles 1 zero	88.06%	3 poles 1 zero	99.92%
	3 poles 2 zeros	89.07%	3 poles 2 zeros	99.95%
G_2	**2 poles 1 zero**	98.97%	**2 poles 1 zero**	99.88%
	3 poles 1 zero	98.97%	3 poles 1 zero	99.88%
	3 poles 2 zeros	99.01%	3 poles 2 zeros	99.88%
G_3	**2 poles 1 zero**	98.86%	**2 poles 1 zero**	99.77%
	3 poles 1 zero	98.97%	3 poles 1 zero	99.82%
	3 poles 2 zeros	98.98%	3 poles 2 zeros	99.82%

*: poorly matched with overshoot. bold: chosen ones.

TABLE III
REGRESSION MODEL PARAMETERS

	P_{ele}		T_{out}	
G_1	$a_2 = 4.89$ $a_1 = 0.71$ $a_0 = 9.50e^{-3}$	$b_2 = 5.34$ $b_1 = 0.64$ $b_0 = 9.50e^{-3}$	$a_1 = 0.0653$ $a_0 = 7.59e^{-4}$	$b_1 = 0.0168$ $b_0 = 7.59e^{-4}$
G_2	$a_1 = 0.0886$ $a_0 = 1.12e^{-3}$	$b_1 = 6.032e^{-3}$ $b_0 = 1.12e^{-3}$	$a_1 = 0.173$ $a_0 = 2.4e^{-3}$	$b_1 = 0.0173$ $b_0 = 2.4e^{-3}$
G_3	$a_1 = 0.101$ $a_0 = 1.29e^{-3}$	$b_1 = 0.0396$ $b_0 = 1.29e^{-3}$	$a_1 = 0.1086$ $a_0 = 1.39e^{-3}$	$b_1 = -5.27e^{-3}$ $b_0 = 1.39e^{-3}$
f_1	$c_1 = 21.08;\ c_2 = -0.021$ $c_3 = -2.59e^{-4}$		$c_1 = 0.12;\ c_2 = -3e^{-4}$	
f_2	$c_1 = 18.6;\ c_2 = -0.19$ $c_3 = -8.93e^{-4}$		$c_1 = 1;\ c_2 = -9.61e^{-4}$	
f_3	$c_1 = 17.5;\ c_2 = -0.107$ $c_3 = 3.067e^{-3}$		$c_1 = 0.197;\ c_2 = 1.73e^{-3}$	
f_4	$d_{11} = 0.3;\ d_{12} = -5e^{-3}$ $d_{21} = -2.54e^{-3}$		$d_{11} = -1.99e^{-4};\ d_{12} = -2.4e^{-5}$ $d_{21} = 6.53e^{-6}$	
f_5	$d_{11} = 0.84$		$d_{11} = 3.58e^{-4};\ d_{12} = 3.15e^{-5}$ $d_{21} = 1.72e^{-5}$	
f_6	$d_{11} = 0.605;\ d_{12} = 3.75e^{-3}$ $d_{21} = -2.17e^{-3}$		$d_{11} = 3.76e^{-3};\ d_{12} = 2.35e^{-5}$ $d_{21} = -3.12e^{-5}$	

B. Step 2: Dynamic Behaviour Calibration

The data used in dynamic behavior calibration are sampled from single-input, 10% range, step responses with a 2 Hz sampling frequency. All tests start from steady-states that refers to the mid-point of the input range. To calibrate the unity gain transfer functions, it is important to normalize (to 1) the data first and then apply the prediction error method (PEM) to find the best fit for the dynamic response. In this paper, the MATLAB System Identification toolbox is used for transfer function calibration. All the resulted functions are in a common form, as shown in (12). Numbers of poles and zeros are selected based on the data in Table II. It is intended that the number of zeros is less than the poles to keep the attenuation on high-frequency noise components. All parameters of the transfer functions can be found in Table III.

$$G_{1,2,3}(s) = \frac{\sum b_j s^j + b_{j-1}s^{j-1} + \cdots + b_0 s^0}{\sum s^i + a_{i-1}s^{i-1} + \cdots + a_0 s^0},\ i,j \epsilon \mathbf{Z}^+. \quad (12)$$

C. Step 3: Individual Nonlinearity Calibration

Each input of the heat pump system has its own nonlinearity, which means the individual input-output relationship when other inputs are kept at 0. Discrete steady-state output data from various single-input tests is used for the calibration. For each input, one possible test sequence can be incremental from the lower to the upper boundary and have a reasonable increment between points. The higher the increment is, the larger the regression error will be. After integrating the resulting polynomials, the empirical model should be able to match the moving boundary model in all single-input tests. All the resulted functions are in a common form as shown in (13), and all related parameters are shown in Table II.

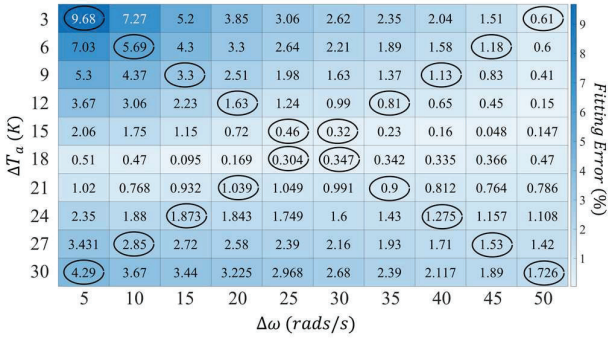

Fig. 4. Resulted map of the fitting error (f_6) in surface regression

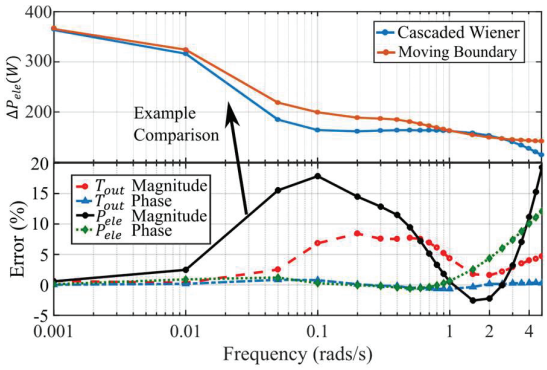

Fig. 5. Error statistics for different input sine frequencies.

$$f_{1,2,3}(x_{1,2,3}) = \sum_{i=1}^{\cdots} c_i (x_{1,2,3})^i,\quad i \epsilon \mathbf{Z}^+, \quad (13)$$

$$x_1 = \Delta\omega G_1(s), x_2 = \Delta T_{cw,in} G_2(s), x_3 = \Delta T_a G_3(s).$$

D. Step 4: Correlation Nonlinearity Calibration

The next step is to study the coupling effects based on dual-input tests. However, the function now represents a surface in the coordinate system, and it is not efficient to include all input combinations for surface regression. In this paper, we choose both diagonals in the combination table to be used in the regression. The resulting surface of f_6 and an error map for all speed and air temperature input combinations is shown in Fig. 4, which suggests that the diagonal-based regression has reasonable accuracy. According to the data, a set of suitable regression results are in the form of (14)-(16), whose parameters are shown in Table III.

$$f_4(x_1, x_2) = \sum_{i,j=1}^{\cdots} d_{ij} (x_1)^i (x_2)^j,\quad i,j \epsilon \mathbf{Z}^+, \quad (14)$$

$$f_5(x_2, x_3) = \sum_{i,j=1}^{\cdots} d_{ij} (x_2)^i (x_3)^j, \quad (15)$$

$$f_6(x_1, x_3) = \sum_{i,j=1}^{\cdots} d_{ij} (x_1)^i (x_3)^j. \quad (16)$$

E. Results comparison

In this section, the moving boundary model and the data-driven cascaded wiener model are simulated together. Two scenarios are designed for verifying the cascaded wiener model's performance.

1) Scenario 1: Frequency Range Test

In this scenario, the inputs are sine waves with different frequencies. The purpose is to find out the frequency limit for the proposed model to have satisfactory matching with the moving boundary model. Detailed information about magnitude and phase error is shown in Fig. 5 for both outputs.

978-1-6654-0823-3/22/$31.00 ©2022 IEEE

The test starts from the midpoint for all three inputs. The magnitudes of all sine inputs are fixed at 10% of each input range, while the frequencies change from 0.001 to 5 rads/s simultaneously. The results show that the magnitude accuracy of the proposed model is generally accurate in the test range. However, there is an error spike around 0.1 rads/s, which is the result of poles/zeros of $G_{1,2,3}$. As shown in Fig. 6, the bode plot suggests that the power magnitude error peak around 0.1 rads/s can be explained by the coupling of $G_{1,2,3}$' frequency characteristics. Unfortunately, the performance of G_1 around 0.1 rads/s is partially sacrificed here for better matching in the low-frequency range. Besides, the power phase is getting distorted after 1 rads/s. This is because G_1 dominates the dynamics around 1 rads/s, and the slope of its phase shift starts to increase from this point, which causes the overall phase error to rise quickly. To sum up, the model is very close to the moving boundary model in terms of frequency response in the low-frequency range, but the matching accuracy starts to degrade and vary after 0.02 rads/s.

2) Scenario 2: Sluggish Ramping Test

In this scenario, the inputs are simulated to mimic real applications. The water temperature changes slowly due to the inertia of the thermal storage or the heat network. Ambient temperature also changes slowly but in a random manner. These two temperature curves are shown in Fig. 7 (a). Besides, speed step changes (ramping time 5s) happen every 600s. The FFT (fast Fourier transform) of all input signals are shown in Fig. 7 (b), suggesting that the majority components of input signals are in a range of 0 to 0.02 rads/s, which fits the accurate range of the proposed model. From Fig. 8, although there are mismatches when speed changes, these two models still have a high level of consensus on both model outputs. It is clear that the proposed model has similar accuracy with the moving boundary model in a relatively realistic scenario.

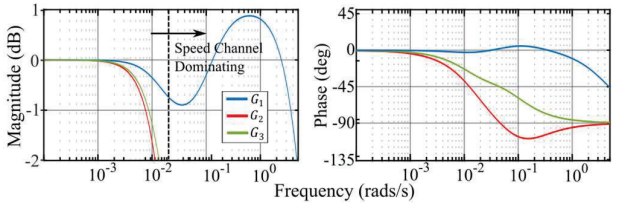

Fig. 6. Bode plot of $G_{1,2,3}$

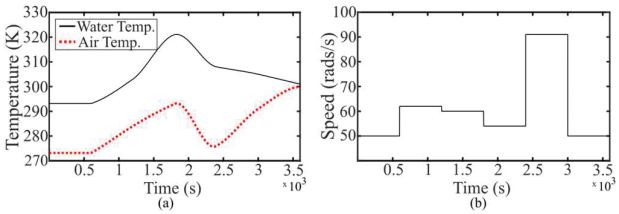

Fig. 7. Input signals to both models. (a): Temperature (Water and Air) inputs. (b): Speed input.

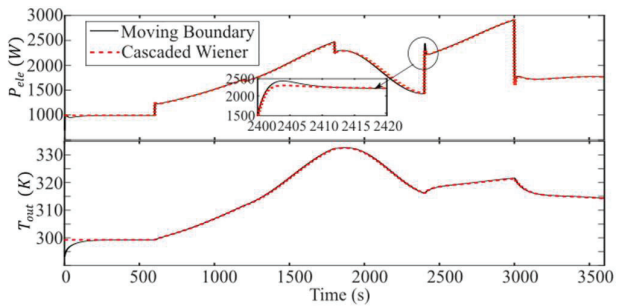

Fig. 8. Model output comparison: output water temperature, scenario 2.

V. Conclusion

The traditional moving boundary model is accurate for heat pump system modelling. However, this model structure requires knowledge of the internal refrigerant loop and the refrigerant's thermal state. In this paper, a traditional moving boundary model and a novel cascaded wiener model are built in Modelica environment for performance comparison. The results suggest that the proposed model is a useful alternative for heat pump dynamic modelling for relatively low-frequency inputs.

Acknowledgement

The work of Dr. Vedran S. Perić was supported by Deutsche Forschungsgemeinschaft (DFG) through the project "Optimal Operation of Integrated Low-Temperature Birdirectional Heat and Electric Grids (IntElHeat)" under Project number 450821044.

Reference

[1] T. M. D. Mohr, "Fuel poverty in the US: Evidence using the 2009 Residential Energy Consumption Survey," *Energy Econ.*, vol. 74, pp. 360–369, 2018, doi: 10.1016/j.eneco.2018.06.007.

[2] R. Song, T. Hamacher, and V. S. Perić, "Impact of hydraulic faults on the electric system in an integrated multi-energy microgrid," in *Proc. of the 9th Workshop on Modeling and Simulation of Cyber-Physical Energy Systems*, May 2021, pp. 1–6, doi: 10.1145/3470481.3472709.

[3] Y.-J. Kim, L. K. Norford, and J. L. Kirtley, "Modeling and Analysis of a Variable Speed Heat Pump for Frequency Regulation Through Direct Load Control," *IEEE Trans. Power Syst.*, vol. 30, no. 1, pp. 397–408, Jan. 2015, doi: 10.1109/TPWRS.2014.2319310.

[4] X. He, S. Liu, and H. Asada, "Modeling of vapor compression cycles for advanced controls in HVAC systems," in *Proc. of 1995 American Control Conf.*, vol. 5, pp. 3664–3668, doi: 10.1109/ACC.1995.533821.

[5] D. Leducq, J. Guilpart, and G. Trystram, "Low order dynamic model of a vapor compression cycle for process control design," *J. Food Process Eng.*, vol. 26, no. 1, pp. 67–91, Oct. 2002, doi: 10.1111/j.1745-4530.2003.tb00590.x.

[6] B. P. Rasmussen and A. G. Alleyne, "Control-oriented modeling of transcritical vapor compression systems," *J. Dyn. Syst. Meas. Control. Trans. ASME*, vol. 126, no. 1, pp. 54–64, Mar. 2004, doi: 10.1115/1.1648312.

[7] J. Bonilla, S. Dormido, and F. E. Cellier, "Switching moving boundary models for two-phase flow evaporators and condensers," *Commun. Nonlinear Sci. Numer. Simul.*, vol. 20, no. 3, pp. 743–768, Mar. 2015, doi: 10.1016/j.cnsns.2014.06.035.

[8] H. Qiao, C. R. Laughman, V. Aute, and R. Radermacher, "An advanced switching moving boundary heat exchanger model with pressure drop," *Int. J. Refrig.*, vol. 65, pp. 154–171, Jan. 2016, doi: 10.1016/j.ijrefrig.2016.01.026.

[9] E. Atam, D. O. Schulte, A. Arteconi, I. Sass, and L. Helsen, "Control-oriented modeling of geothermal borefield thermal dynamics through Hammerstein-Wiener models," *Renew. Energy*, vol. 120, pp. 468–477, May 2018, doi: 10.1016/j.renene.2017.12.105.

[10] A. Kose and E. Petlenkov, "System identification models and using neural networks for Ground Source Heat Pump with Ground Temperature Modeling," in *2016 Int. Joint Conf. on Neural Networks*, Jul. 2016, pp. 2850-2855, doi: 10.1109/IJCNN.2016.7727559.

[11] *Modelica Language.*, Modelica Association, Accessed on: Oct. 1998, [Online]. Available: https://www.modelica.org/modelicalanguage.

[12] *Complete Derivation of the Moving Boundary Model for an Air Source Heat Pump,* Ruihao Song, Guillaume Yon, Thomas Hamacher, and V. S. Perić, Accessed on: Nov. 2021, [Online]. Available: https://www.researchgate.net/publication/356388007_Complete_Derivation_of_the_Moving_Boundary_Model_for_an_Air_Source_Heat_Pump.

Concluding Remarks

This publication aimed to find a model structure for modeling general heat pump systems for PFR and SFR applications. We focused on the practical feasibility and model versatility for a wide range of types and power ratings to maintain accuracy in minute-level modulation scenarios.

As heat pump non-linearity only causes a trivial impact on PFR and SFR services, this paper proposed a data-driven model structure based on Wiener models, which is a combination of linear dynamics and non-linear steady-state algebraic functions, to compute the power and output temperature responses from the speed modulation input and operating condition measurements. The proposed model was derived by summarizing the key characteristics observed in the fundamental physics-based model presented in Section 3.1, and the accuracy of the model was proved by comparing it with the physics-based model through PFR and SFR modulation simulations.

Follow-up Experimental Work

The derived model structure has been implemented in our laboratory to reproduce the dynamic behavior of the installed commercial ASHP module (WOLF, CHA-10 MONOBLOCK), which is shown in Fig. 4-1. Through experimental observations, we noticed that standard commercial modules have manually programmed acceleration limits, leading to a ramping modulation behavior. Besides, the input delay due to internal controller processing is also significant. Based on this information, we slightly revised the model structure to adapt to this reality, as shown in Fig. 4-2.

The model is calibrated with the steps mentioned in the paper, and the resulting model parameters are shown in Table 4-1. The result was validated through modulation experiments that mimic a PFR-level modulation scenario. The speed modulation reference was a step signal that randomly changes between 30% to 90% every 15 seconds. The return cold water and air temperatures continuously changed with a stochastic pattern. The model outputs and experimental measurements on power and output water temperatures are compared in Fig. 4-3, where results show a satisfactory matching.

Figure 4-1 The WOLF ASHP and its associated testing setup in our laboratory.

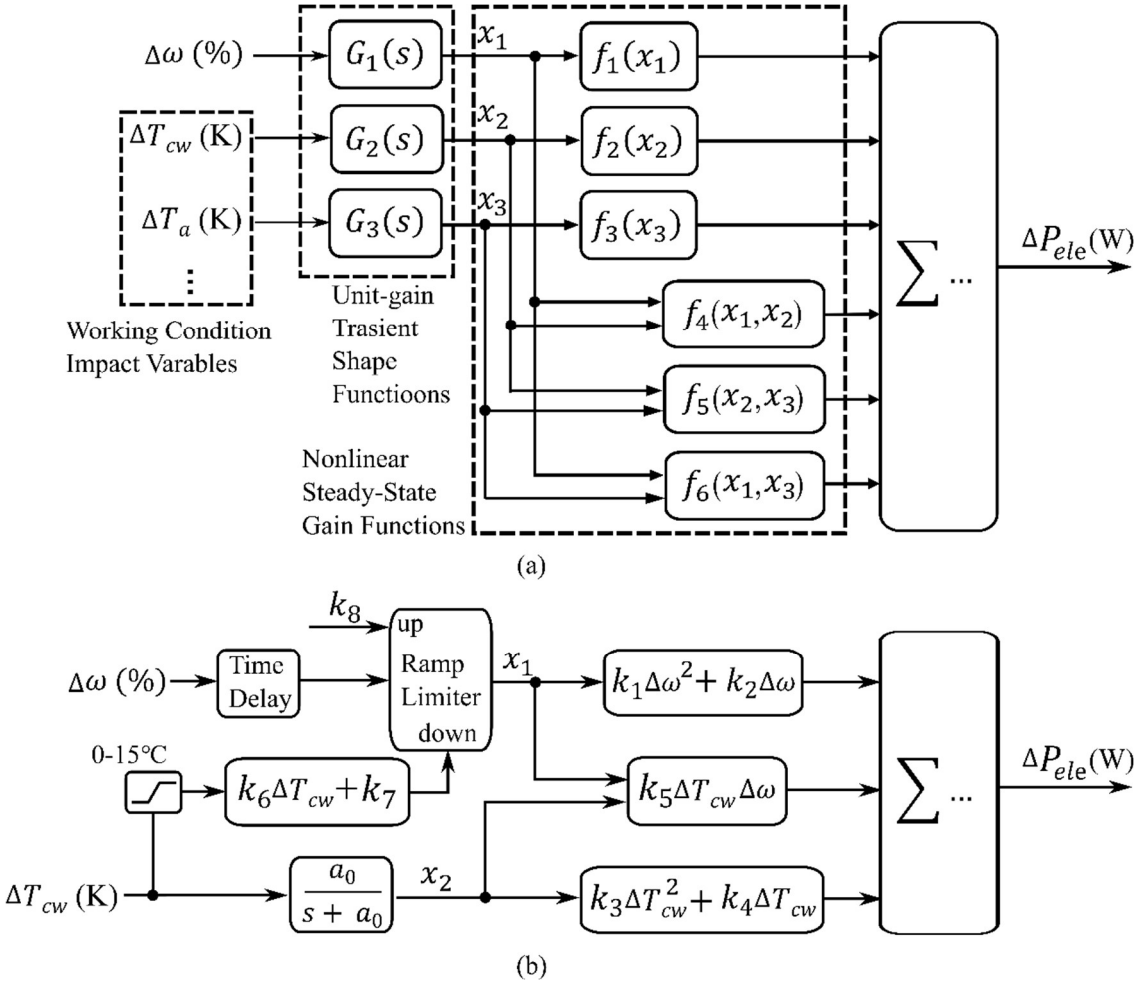

Figure 4-2 Heat pump model structure: (a) a general cascaded wiener model structure; (b) modified structure for the ASHP in our laboratory.

Table 4-1 Identified heat pump model parameters

Parameter	Value	Parameter	Value	Parameter	Value
a_0	0.046	k_1	0.07564	k_2	18.02
k_3	0.2339	k_4	10.81	k_5	0.4625
k_6	-0.005	k_7	-0.38	k_8	1.5
Time Delay	7s				

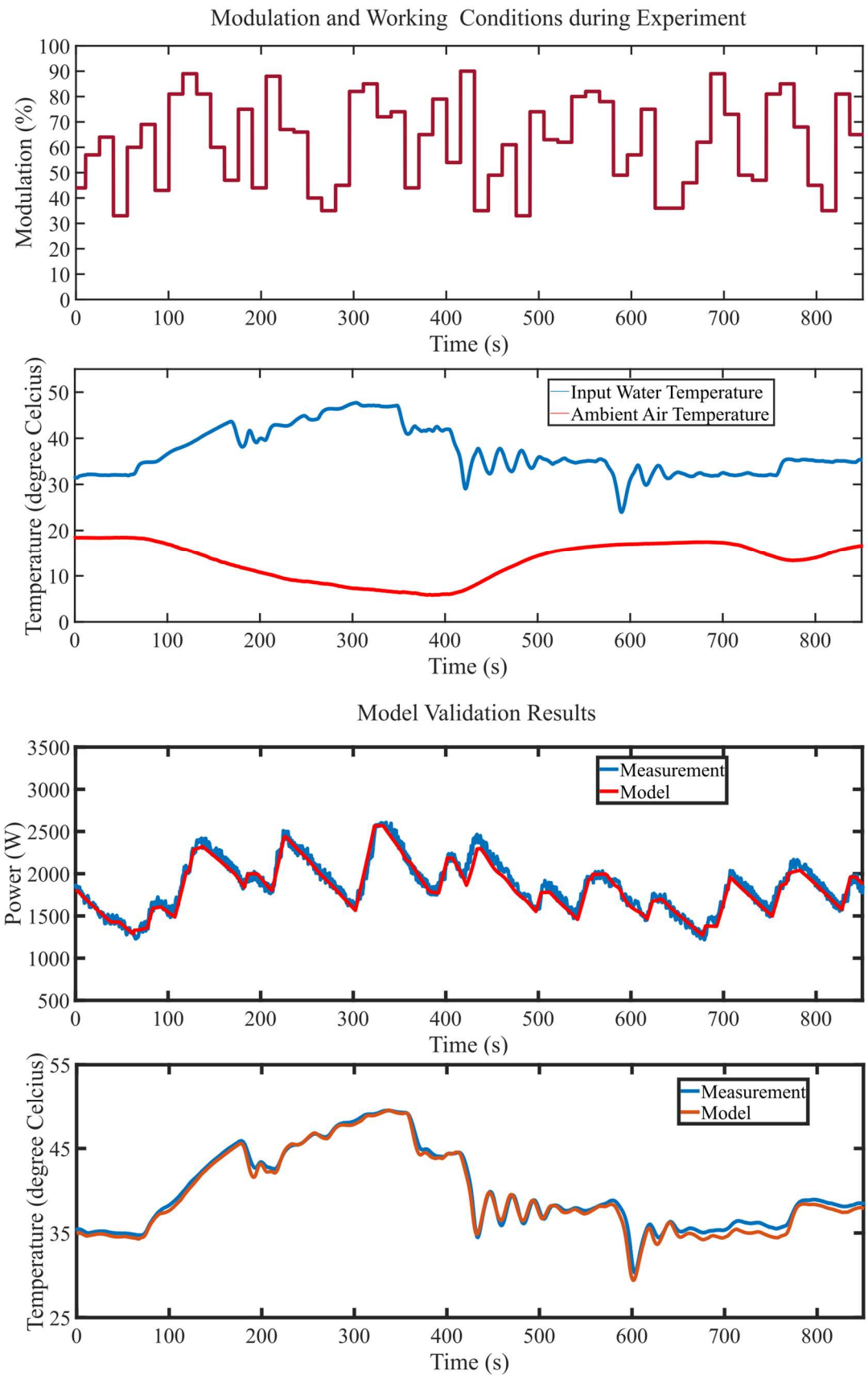

Figure 4-3 Experimental conditions and validation results of the derived model structure in our laboratory.

4.2 Adaptive Control of Heat Pumps for PFR and SFR services

Scientific Context

Due to the absence of standardized internal control systems, current commercial heat pumps often exhibit varied dynamic behavior. From our experiments, we noted that a significant portion of commercial heat pump systems modulate at a constant but possibly asymmetric ramping speed. Furthermore, they often have notable and uncertain input delays due to internal processing. These characteristics can be specific to certain brands or even particular modules. The diversity in behavior makes traditional feedback power controllers such as PI hard to design and perform terribly. In this context, a tailored control strategy is imperative for commercial heat pumps to be effectively integrated into PFR and SFR services. Such a strategy should address and mitigate the challenges above, ensuring reliable performance across various commercial heat pump types.

In this context, open-loop strategies, which were extensively used for electrical system control [93][94][95], emerge as potential solutions. However, employing open-loop control necessitates a comprehensive understanding of the subject heat pump's behavior. Without this, the controller induces significant steady-state errors, compromising its effectiveness. Open-loop controllers require a pre-established knowledge of the target equipment to calculate the required input with the power reference from PFR and SFR service dispatches and operating condition measurements. Consequently, a pivotal phase in the control design is establishing the dynamic behavior knowledge. In the following paper, we introduced the design process of such an open-loop controller for the commercial ASHP in our laboratory, and the control performance was evaluated by comparing with traditional PI controller through simulations under a typical PFR-level modulation scenarios.

Publication #5: Adaptive Control of Practical Heat Pump Systems for Power System Flexibility based on Reinforcement Learning

Authors: Ruihao Song, Daniel Zinsmeister, Thomas Hamacher, Haoran Zhao, Vladimir Terzija, Vedran Peric

Publication: 2023 International Conference on Power System Technology (PowerCon)

Digital object identifier: 10.1109/PowerCon58120.2023.10331231

Author	Contribution	Tasks
Ruihao Song	60%	• Conceptualization • Methodology • Investigation • Writing-original draft • Writing-review & editing
Daniel Zinsmeister	15%	• Experimental setup building • Writing-review & editing
Thomas Hamacher	5%	• Supervision • Funding acquisition
Haoran Zhao	5%	• Writing-review & editing
Vladimir Terzija	5%	• Writing-review & editing
Vedran Peric	10%	• Supervision • Writing-review & editing

Adaptive Control of Practical Heat Pump Systems for Power System Flexibility based on Reinforcement Learning*

1st Ruihao Song
School of Engineering and Design
Technical University of Munich
Garching, Germany
ruihao.song@tum.de

2nd Daniel Zinsmeister
Professorship of Energy Management Technologies
Technical University of Munich
Munich, Germany
d.zinsmeister@tum.de

3rd Thomas Hamacher
School of Engineering and Design
Technical University of Munich
Garching, Germany
thomas.hamacher@tum.de

4th Haoran Zhao
School of Electrical Engineering
Shandong University
Jinan, China
hzhao@sdu.edu.cn

5th Vladmir Terzija
School of Engineering
Newcastle University
Newcastle upon Tyne, United Kingdom
vladimir.terzija@newcastle.ac.uk

6th Vedran Peric
School of Engineering and Design
Technical University of Munich
Garching, Germany
vedran.peric@tum.de

***Abstract*—Modern power systems are under flexibility shortage because of high renewable penetration. As heating systems are increasingly integrated with electric power systems, heat pumps have become a valuable source of power system flexibility. However, utilizing the flexibility of heat pumps necessitates additional regulation system on the heat pump, which complicates their design. Many commercially available heat pump systems modulate through a relatively slow ramping process and suffer from significant input transport delays. Due to complex dynamical process in heat pumps, a traditional model-free closed-loop power controller, such as the proportional-integral-derivative type, may result in poor transient performance. In contrast, an open-loop control may provide faster transient response at the expense of significant steady-state error. The steady state error is especially problematic due to high non-linearity of heat pump power consumption with respect to working condition variables, such as source and sink media temperatures and mass flow levels. This paper proposes an reinforcement learning based open-loop control system that provides fast transient response but is adaptive in nature to compensate for the non-linearities arisen from changing working conditions. The impact of working condition changes is captured with the trained deep neural network that modifies the modulation input to minimize potential steady-state power tracking error.**

Keywords—heat pump, power system flexibility, adaptive control, reinforcement learning

I. INTRODUCTION

With the increasing use of renewable energy sources in modern power systems [1]-[3], there is a growing trend towards reducing emissions in district heating systems. In the residential sector, it is expected that combustion-based heating equipment such as gas or coal boilers and combined-heat-and-power (CHP) systems will gradually be replaced by heat pumps [4]. The increasing level of electrification of heat sources allows new opportunities for integrated operations between power and heat grids. For example, the abundant flexibility of heat grids can be used to attenuate frequency fluctuations in power grids [5]-[7] or achieve optimal multi-grid-level dispatching [8], [9]. However, utilizing heat pump power flexibility requires a relatively fast and accurate power regulation system, which can be difficult to achieve with common commercially available heat pumps, especially at domestic and community levels.

Commercially available heat pump systems often have power transient behaviors that differ from theoretically possible dynamic response due to practical limitations such as transport delay, drive operation limitations, and internal control, etc.. Compared to theoretical behaviors without drive limitations, the transient characteristic in commercial heat pumps exhibits much slower response, often taking minutes to settle. Additionally, significant reference transport delays are also common, which further deteriorates the power modulation dynamics. In this context, traditional model-free power control methods, such as proportional-integral-derivative (PID) control, may result in worse transient behavior than open-loop control. However, the heat pump's power consumption may be affected by source and sink media temperatures, mass flow levels, etc., depending on the internal design of the specific heat pump. Estimating the impact of all possible working condition variables through conventional methods, such as polynomial fitting, can be complicated and laborious since the effects can be correlated and intertwined, making open-loop methods unattractive.

The work of Mr. Ruihao Song was supported by the Bavarian Research Foundation through the project "Sector coupling und Microgrids (STROM)" under project number AZ-1473-20. The work of Daniel Zinsmeister was funded by the Federal Ministry for Economic Affairs and Climate Action, Germany (FKZ: 03EN3032A). The construction of the CoSES laboratory was supported by Deutsche Forschungsgemeinschaft (DFG) through the project "Flexible reconfigurable microgrid laboratory" under project number 350746631. The work of Dr. Vedran S. Perić was supported by Deutsche Forschungsgemeinschaft (DFG) through the project "Optimal Operation of Integrated Low-Temperature Bidirectional Heat and Electric Grids (IntElHeat)" under project number 450821044.

2023 International Conference on Power System Technology (PowerCon) | 979-8-3503-0022-2/23/$31.00 ©2023 IEEE | DOI: 10.1109/POWERCON58120.2023.10331231

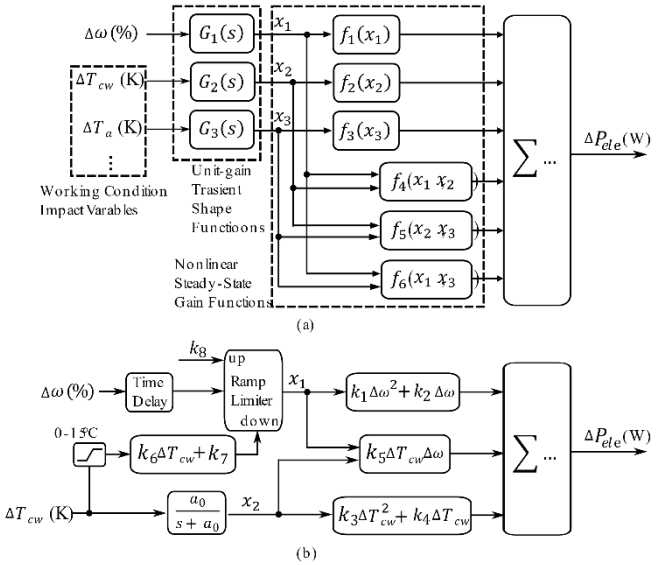

Fig. 1. Heat pump model structure: (a) a general cascaded Wiener model structure; (b) model structure identified for the heat pump in the CoSES labortory.

Artificial intelligence (AI)-based methods, such as deep neural networks (DNNs), are increasingly popular for modeling multi-input complex behaviors in power systems, including load modeling, stochastic renewable forecasting, and fault diagnostics [10]-[12]. In this context, we opt to use a DNN to describe the impact of working condition variables on heat pump power consumption for improved accuracy. We assume that there is no prior knowledge or data regarding the working condition impact, and thus propose employing reinforcement learning (RL) to calibrate the DNN through an equipment-learning process. In this paper, the training is conducted based on a simulation model that has been experimentally verified in the CoSES laboratory [13], [14]. The trained DNN is subsequently deployed in the adaptive open-loop controller for simulation tests. The performance of the proposed controller is then compared to a traditional PID controller under various scenarios for a comprehensive evaluation.

This paper is organized as follows. Section II describes the simulation model and the its validation on the heat pump system in the CoSES laboratory. Section III presents the proposed adaptive open-loop controller structure and the RL-based training algorithm. Section IV presents the training results and compares the performance of the proposed controller with the traditional PID controller. Finally, Section V provides the conclusion of this paper.

II. System Modeling

In this paper, we use a simulation model to generate training data and test the proposed controller. The adopted heat pump model structure is inherited from a previously proposed cascaded Wiener modeling technique [15] with modifications to address the input delay and ramping limitations, as shown in in Fig. 1 (a) and (b). The general model structure separates the modeling process into parts of unit-gain transient shape functions and steady-state gains functions. The transient shape is described by transfer functions while the steady-state is described by nonlinear polynomials, as described in (1)-(3),

Fig. 2. Experimental setup for calibrating the cascaded Wiener model.

$$G_{1,2,3\ldots} = \frac{b_j s^j + b_{j-1} s^{j-1} + \cdots + b_0 s^0}{s^i + a_{i-1} s^{i-1} + \cdots + a_0 s^0}, i,j \in \mathcal{Z}^+, \quad (1)$$

$$f_{1,2,3}(x_{1,2,3}) = \sum_{i=1}^{\cdots} c_i \, (x_{1,2,3})^i, i \in \mathcal{Z}^+, \quad (2)$$

$$f_4(x_{1,2}) = \sum_{i,j=1}^{\cdots} d_{ij} \, (x_1)^i (x_2)^j, i,j \in \mathcal{Z}^+,$$

$$f_5(x_{2,3}) = \sum_{i,j=1}^{\cdots} d_{ij} \, (x_2)^i (x_3)^j, \quad (3)$$

$$f_6(x_{1,3}) = \sum_{i,j=1}^{\cdots} d_{ij} \, (x_1)^i (x_3)^j,$$

where a, b, c, d are empirical coefficients. Normally, the model has three inputs: modulation percentage (compressor speed), source media temperature, and sink media temperature; one output of power consumption. However, there could be more or less working condition variables as inputs for specific commercial heat pump models, as the system internal design varies with manufacturers.

The heat pump model used in this paper is calibrated on a 5 kW (electrical) air-source heat pump experimental setup in the CoSES laboratory, which is shown in Fig. 2. The transient shape function is calibrated from step response data, while the polynomials are fitted with steady-state measurements. We validate the obtained model through experimental results, as shown in Fig. 3. The modulation reference is set as a random step-change signal between 30% to 90% with a time interval of 15 seconds, while the cold water and air temperatures are continuously changing. The results suggest that the model is accurate in the low-frequency range, which fits for simulation in target scenarios of minute-level energy management system. All resulted model parameters from experimental calibration (from Fig. 1 (b)) is shown in Table I.

TABLE I. Heat Pump Model Parameters

Parameter	Value	Parameter	Value	Parameter	Value
a_0	0.046	k_1	0.07564	k_2	18.02
k_3	0.2339	k_4	10.81	k_5	0.4625
k_6	-0.005	k_7	-0.38	k_8	1.5
Time Delay = 7s					

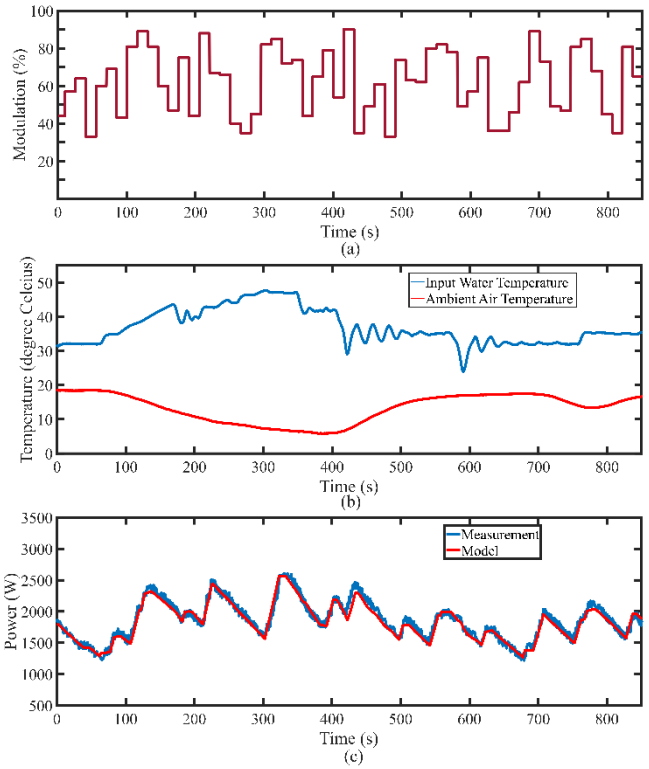

Fig. 3. Validation results of the simulation model: (a) modulation input; (b) cold water and air temperature profiles; (c) predicted power data compared with measurements.

III. Proposed Method

We introduce an adaptive open-loop control method for heat pump power regulation, which is developed based on the inversion of the general cascaded Wiener model structure discussed in Section II. Generally, the control inputs consist of the power reference ΔP_{ele}^{ref} and working condition variables $\Delta T_{cw,a}$, ..., while the output is represented as the post-transient modulation impact x_1^{ref}, as shown in Fig. 4. The controller can be characterized by solving (4) in real-time, with the post-transient working condition impacts $x_{2,3}$ computed from the measured working condition variables.

$$x_1^{ref} = argmin_{\hat{x}_1} |\Delta P_{ele}^{ref} - f_1(\hat{x}_1) - f_{2,3}(x_{2,3}) - f_4(\hat{x}_1, x_2) - f_5(x_2, x_3) - f_6(\hat{x}_1, x_3)|. \quad (4)$$

In this paper, we replace the calculation of (4) with a DNN trained through RL. We utilize the trained DNN to establish the open-loop controller, as illustrated in Fig. 4. Once the DNN is trained, it can be implemented as a fixed policy for generating $\hat{x}_1$ with a low computational burden. As a summary, we list the steps for implementing the proposed controller as follows.

- Step 1: Identify the ASHP single-channel dynamic response $G_{1,2,3}(s)$ with experimental data.
- Step 2: Formulate a RL-based training environment for ASHP static behavior with chosen training parameters..
- Step 3: Start training experiments and wait until the reward converge to a stable value.

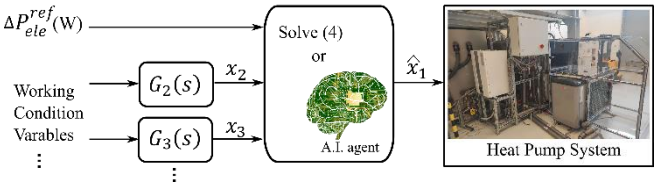

Fig. 4. Control structure illustration.

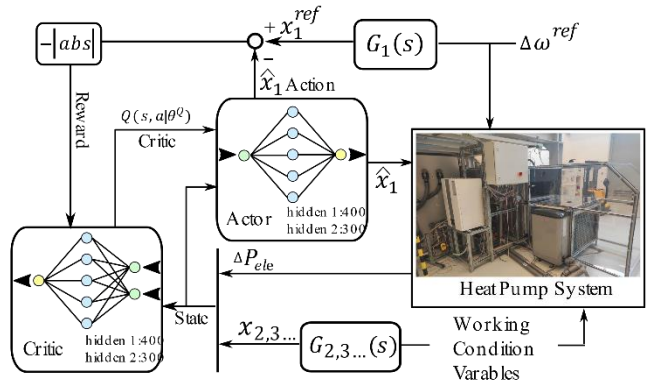

Fig. 5. Training configuration of the DNN agent for modeling the working condition effect on the target heat pump.

- Step 4: Generate the trained policies from step 2, and then implement the controller. If the resulted control accuracy is not satisfactory, iterate from step 2.

We adopt the Deep Deterministic Policy Gradient (DDPG) algorithm [16] for RL, as the action space of the desired control system is continuous rather than discrete. The DDPG algorithm is based on an actor-critic dual-DNN learning structure, and the detailed training setup and algorithm for the heat pump is outlined in Fig. 5 and Algorithm 1. At each time step t during training, the actor network, denoted by $\mu(s|\theta^\mu)$, receives an observation of system states s_t (5) and takes an action a_t (5). To explore a wide range of possibilities, the action sent to the target environment is not only the current actor network output but also includes sampled noise from a specific model. The noise model can vary with applications, and in this paper, we employ the Ornstein-Uhlenbeck Noise Model. The performance of such action is assessed by the critic network, denoted by $Q(s,a|\theta^Q)$, based on the received next step observation of system states s_{t+1} and a reward r_t derived from a reward function in (5). Note that $s_{t,t+1}, a_t, r_t \in \mathbb{R}^N$. The trial-reward-evaluation cycle is conducted multiple times at every time step until a memory buffer B is fully populated with trial transition tuples (s_t, a_t, r_t, s_{t+1}). If B is already full, then the newly generated tuples will overwrite and replace the oldest one.

Both the actor and critic networks are updated at each time step, with the critic network being updated before the actor network. To enhance the critic network, a random batch of N transition tuples is sampled from B, and a cumulative loss L is calculated, as in (6). The critic network weights θ^Q are then updated based on finding the optimal θ^Q that minimizes the cumulative losses L, with a reward discount factor γ and a learning rate η_Q. On the other hand, the actor network weights θ^μ are updated by adding a gradient $\nabla_{\theta^\mu} J$, as in (7), to the current θ^μ with a learning rate η_μ. Finally, the target critic network weights $\theta^{Q'}$ and target actor network weights $\theta^{\mu'}$ are softly updated, as demonstrated in Algorithm 1.

Algorithm 1: Training algorithm of the heat pump adaptive control agent based on DDPG

Initialize: Apply ω_{base} to the heat pump
Initialize: Set a base working conditions
Initialize: randomly generate weight vectors θ^{μ} and θ^{Q}.
Initialize: $\theta^{\mu'} = \theta^{\mu}, \theta^{Q'} = \theta^{Q}$
Initialize: B
for episode = 1, M (maximum episode number) **do**
  Apply a random ω_{ref} to the heat pump
  Set a random working condition within limits
  for step t = 1, T (maximum step number) **do**
  Generate one transition tuple (s_t, a_t, r_t, s_{t+1}) with:

$$\boldsymbol{a_t = \mu(s_t|\theta_t^{\mu}) + \mathcal{N}}.$$

  Store the generated tuple in B.
  Sample a random K of transitions from B.
  Calculate θ^{Q} based on minimizing L, (6)

$$\theta^{Q} = \text{argmin}_{\theta^{Q}} L_t|_{\eta_Q}$$

  Calculate θ^{μ} based on sampled policy gradient, (7)

$$\theta^{\mu} = \theta^{\mu} + \eta_{\mu} \Delta_{\theta^{\mu}} J$$

  Softly update the target weight vectors ($\tau = 0.001$):

$$\theta^{Q'} \longleftarrow \tau\theta^{Q} + (1-\tau)\theta^{Q'}$$

$$\theta^{\mu'} \longleftarrow \tau\theta^{\mu} + (1-\tau)\theta^{\mu'}$$

  end for
end for

$$s_t = [\Delta P_{ele,t}, x_{2,t}, x_{3,t}, \dots]^T, a_t = \hat{x}_{1,t}, \quad r_t(a_t) = -|x_{1,t}^{ref} - \hat{x}_{1,t}|. \tag{5}$$

$$L = \frac{1}{K}\sum_{i}^{K}(r_i(a_i) + \gamma Q'(s_{i+1}, \mu'(s_{i+1}|\theta^{\mu'})|\theta^{Q'}) - Q(s_i, a_i|\theta^{Q})). \tag{6}$$

$$\nabla_{\theta^{\mu}} J = \frac{1}{K}\sum_{i=1}^{K} \nabla_a Q(s, a|\theta^{Q})|_{s_i, \mu(s_i)} \nabla_{\theta^{\mu}} \mu(s|\theta^{\mu})|_{s_i}. \tag{7}$$

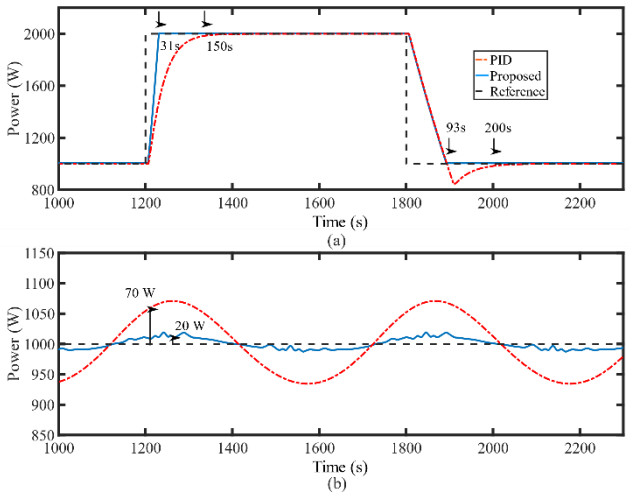

Fig. 7. Comparison between the proposed and conventional PID controller: (a) step response; (b) Disturbance rejection with sinusoidal cold water temperature disturbance.

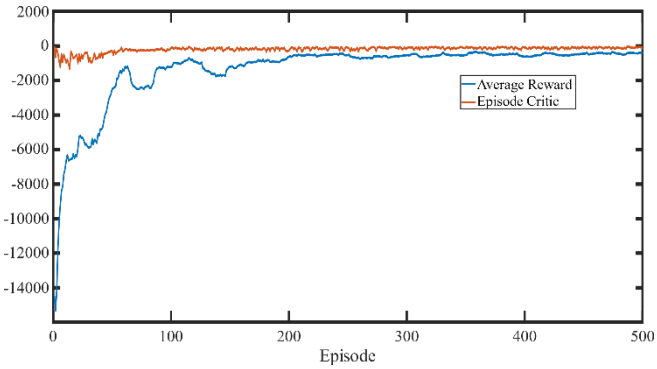

Fig. 6. The training result of the DNN agent through DDPG-RL

TABLE II. DDPG RL TRAINING PARAMETERS

Parameter	Value	Parameter	Value
Discount factor	0.99	Sampling time	1s
Maximum step	600	Maximum episode	500
Critic learning rate	1e-3	Actor learning rate	1e-4
Actor gradient threshold	1	Critic gradient threshold	1
Critic optimizer	adam	Noise variance	4
Noise decay rate	1e-3	Minibatch size	64
Reply buffer size	1e6	Steps to look ahead	32

IV. SIMULATION RESULTS

In this paper, both training and testing of the proposed controller is conducted through the presented simulation model in Section II. We employ the MATLAB Reinforcement Learning Toolbox [17] and Simulink to execute the required algorithm. The RL training process is heavily influenced by the chosen learning parameters, which should be tuned iteratively to enhance learning performance. The training results of the DNN agent are displayed in Fig. 6, with all related training parameters presented in Table II. We demonstrate the improvement of the designed adaptive open-loop controller by comparing it to the traditional PID controller. Generally, the proposed controller can settle much faster than the traditional PID controller. However, the estimation error from the DNN inevitably leads to a small power regulation steady-state error, which is normally negligible if properly trained. The PID controller is tuned such that the overshoot for both upward and downward regulations is within 15%. We conducted in total of three tests to compare controller performance, where the scenario descriptions and results are listed in the following subsections.

A. Scenario 1: step response

The first test assumes the heat pump system receives power step change commands from the energy management system approximately every 10 minutes, with the response results displayed in Fig. 7 (a). It is evident that the power settling time is significantly reduced by 80% for upward regulation and 50% for downward regulation.

B. Scenario 2: disturbance rejection

The second test aims to demonstrate the capability of disturbance rejection with a sinusoidal cold water temperature input (our heat pump in the laboratory is only affected by cold water temperature). Fig. 7 (b) shows that the resulting power disturbance from the proposed controller is only 30% of that from the conventional PID controller.

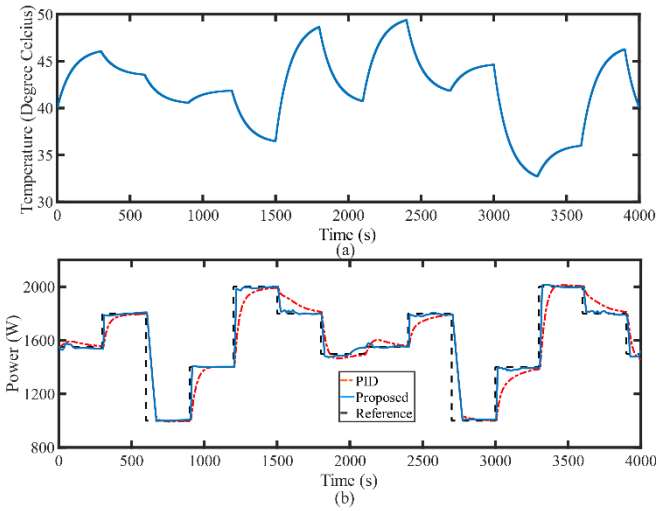

Fig. 8. Power tracking performance under disturbances: (a) cold water temperature profile; (b) power tracking response with reference of 10 minutes period; (c) power tracking response with reference of 5 minutes period.

C. *Scenario 3: complex tracking*

Finally, the last test simulates a complex scenario in which the heat pump must track the reference from the energy management system while contending with random cold water temperature disturbances. The applied cold water temperature profile is illustrated in Fig. 8 (a). We initially simulate a reference that changes every 5 minutes, with the tracking result shown in Fig. 8 (b), where significant tracking improvement is observed with the proposed method. To provide a more comprehensive comparison, we subsequently simulate longer reference intervals ranging from 10 to 30 minutes, with each simulation lasting for 5 step cycles. The results are documented in Table III. It is shown that for all tested reference intervals, the proposed method can improve performance by approximately 50% compared to the conventional PID method, leading to significantly reduced economic losses from derailing the power dispatch commands.

V. Conclusion

This paper presents an adaptive open-loop control system for practical heat pumps, designed to improve tracking of dispatch commands from higher-level energy management systems. The proposed method employs a DNN trained by DDPG-RL to generate the required heat pump modulation signal based on the observation of the dispatched power reference and measured working condition variables. Comparative simulations demonstrate that the proposed method outperforms the conventional PID control for a commercial heat pump system in the CoSES laboratory.

TABLE III. Energy Mismatch Percentage due to Inaccurate Power Tracking

	5 (minutes)	10	15	20	30
PID	23.3%	15.94%	13.28%	11.85%	10.3%
Proposed	13.03%	7.69%	6.026%	5.30%	4.87%
Improvement	44.07%	51.72%	54.62%	55.29%	52.77%

References

[1] Eurostat, "Renewable energy statistics in EU.", url: https://ec.europa.eu/eurostat/statistics explained/index.php?title=Renewable_energy_statistics.

[2] Wikipedia, "Renewable energy in China.", url: https://en.wikipedia.org/wiki/Renewable_energy_in_China.

[3] U.S. Energy Information Administration, "US renewable energy sources.", url: https://www.eia.gov/tools/faqs/faq.php?id=92&t=4#:$\sim$:text=In 2020%2C renewable energy sources,about 19.8%25 of electricity generation.

[4] J. Rosenow, D. Gibb, T. Nowak, and R. Lowes, "Heating up the global heat pump market," *Nature Energy*, pp. 10–13, sep 2022.

[5] Z. A. Obaid, L. Cipcigan, M. T. Muhssin, and S. S. Sami, "Development of a water heater population control for the demand-side frequency control," in *2017 IEEE PES Innovative Smart Grid Technologies Conference Europe (ISGT-Europe)*, vol. 2018-Jan, pp. 1–6, sep 2017..

[6] Y.-J. Kim, E. Fuentes, and L. K. Norford, "Experimental Study of Grid Frequency Regulation Ancillary Service of a Variable Speed Heat Pump," *IEEE Transactions on Power Systems*, vol. 31, pp. 3090–3099, jul 2016..

[7] Y.-J. Kim and J. Wang, "Power Hardware-in-the-Loop Simulation Study on Frequency Regulation Through Direct Load Control of Thermal and Electrical Energy Storage Resources," *IEEE Transactions on Smart Grid*, vol. 9, pp. 2786–2796, jul 2018.

[8] D. Testi, L. Urbanucci, C. Giola, E. Schito, and P. Conti, "Stochastic optimal integration of decentralized heat pumps in a smart thermal and electric micro-grid," *Energy Conversion and Management*, vol. 210, p. 112734, 2020.

[9] M. Zhang, Q. Wu, J. Wen, X. Xue, Z. Lin, and F. Fang, "Real-time optimal operation of integrated electricity and heat system considering reserve provision of large-scale heat pumps," *Energy*, vol. 237, p. 121606, 2021.

[10] V. N. Nguyen, R. Jenssen, and D. Roverso, "Intelligent monitoring and inspection of power line components powered by uavs and deep learning," *IEEE Power and Energy Technology Systems Journal*, vol. 6, no. 1, pp. 11–21, 2019.

[11] M. S. Ibrahim, W. Dong, and Q. Yang, "Machine learning driven smart electric power systems: Current trends and new perspectives," *Applied Energy*, vol. 272, p. 115237, 2020.

[12] M. Khodayar, G. Liu, J. Wang, and M. E. Khodayar, "Deep learning in power systems research: A review," *CSEE Journal of Power and Energy Systems*, vol. 7, no. 2, pp. 209–220, 2021

[13] V. S. Peri ´c, T. Hamacher, A. Mohapatra, F. Christiange, D. Zinsmeister, P. Tzscheutschler, U. Wagner, C. Aigner, and R. Witzmann, "Coses laboratory for combined energy systems at tu munich," in *2020 IEEE Power & Energy Society General Meeting (PESGM)*, pp. 1–5, 2020.

[14] D. Zinsmeister, T. Lickleder er, S. Adldinger, F. Christange, P. Tzscheutschler, T. Hamacher, and V. S. Peri ´c, "A prosumer-based sector-coupled district heating and cooling laboratory architecture," *Smart Energy*, vol. 9, p. 100095, 2023.

[15] R. Song, G. Yon, T. Hamacher, and V. S. Peri ´c, "Data-driven model reduction of the moving boundary heat pump dynamic model," in *2022 IEEE Power & Energy Society General Meeting (PESGM)*, pp. 1–5, 2022.

[16] T. P. Lillicrap, J. J. Hunt, A. Pritzel, N. Heess, T. Erez, Y. Tassa, D. Silver, and D. Wierstra, "Continuous control with deep reinforcement learning," *arXiv preprint arXiv:1509.02971*, 2015.

[17] MathWorks, "Reinforcement Learning ToolBox", url: https://ch.mathworks.com/products/reinforcement-learning.html.

Concluding Remarks

In this paper, we introduced a novel open-loop control strategy to regulate the power of general heat pump systems with minute-level response speeds, particularly for PFR services, SFR services, and other energy management applications. This controller is tailored to overcome common power response limitations in commercial heat pumps and is adaptable to various heat pump types and power ratings.

The proposed open-loop controller calculates the required command signal with a given power reference and operating condition measurements. In this paper, we adopted a deep neural network (DNN) for such a calculation process. This allows for the automation of a significant portion of the design process using Deep Deterministic Policy Gradient (DDPG) reinforcement learning [96][97][98]. Random modulation inputs and operating conditions are applied to the heat pump during the learning phase. The DNN-based controller then attempts to predict the applied modulation levels using current power reference and operating condition readings. Within each iteration, the accuracy of these predictions is assessed, and adjustments are made to the DNN to minimize the error.

The trained DNN-based open-loop controller was compared with traditional PI controllers in minute-level power-tracking scenarios with uncertain operating conditions. The results showed that the DNN-based open-loop controller substantially outperforms a well-tuned PI controller regarding the reference tracking performance.

Chapter 5: Conclusion & Outlook

5.1 Conclusion

The power system worldwide is shifting into a new era where power electronic converters are replacing the majority of SGs. While beneficial for the environment, this transition brings challenges for power system stability and reliability, especially concerning system inertia and the need for rapid balancing capabilities. The need for generation-demand balancing motivates researchers to look for power flexibility opportunities, especially from the demand side. The ongoing trend of heating sector electrification with different kinds of heat pumps provides abundant power flexibility on the demand side in residential grids. However, exploiting these flexibility opportunities requires appropriate modeling and control strategies for heat pump systems, which becomes the focus of this thesis. The following paragraphs provide summaries of the raised research questions in Chapter 1.

Research question 1: What is the state-of-the-art in using heating systems for frequency response services and the related future trends?

In Chapter 2, we explored the potential of CHP and PtH systems in regulating power system frequency. This Chapter, presented as a review paper (Publication #1), analyzed how quickly and effectively each type of sector coupling equipment can respond to changes in frequency and determines which frequency response services they are best suited for. Additionally, we reviewed existing algorithms designed for frequency response services. Our investigation into current literature revealed that CHPs are primarily used for PFR services at the centralized level, often through inherent droop control. However, there was limited discussion on the use of CHPs at both community and domestic levels. Regarding PtH systems, most studies focused on their application at community and domestic levels. These systems were typically managed either through rule-based switching or droop algorithms for PFR services, while SFR services were usually implemented by centralized control via radial communication. The paper also highlighted a noticeable trend: the shift from CHP units to heat pumps. This change was motivated by the desire to integrate more REGs into power grids and reduce overall emissions. On the algorithm side, existing applications focused heavily on decentralized methods that do not use communications. With the advancement of communication technologies, the future of control algorithms appears to be leaning towards distributed multi-agent control, as it offers more coordination potentials and better transient performance.

Research question 2: How to model the heat pump systems for different frequency response services that have diverged design focus?

In this thesis, we focused on creating heat pump models tailored to specific objectives, leading to three models suitable for different uses. The first one was a physics-based model that thoroughly reflects the drive system's electrical dynamics and the refrigeration loop's thermal dynamics, as shown in Section 3.1. The model provides detailed information on all physical variables, such as grid-interfacing current, compressor speed, and pressures, and it is used as the basis of this thesis for understanding heat pump dynamics. We applied this detailed model in Publication #2, where we emulated the heat pump behavior within a standard power system laboratory through PHIL technology. In Publication #3, we introduced the second model, which was developed to design an FFR control strategy that integrates distributed ASHPs. Here, the model's complexity was reduced by summarizing the electrical drive system's behavior with a linear transfer function. This simplification is possible because the current profile of the ASHP system is not needed for control design analysis, and we were only interested in the dominant non-linearity of the refrigeration loop. The third model was designed for PFR and SFR services, as detailed in Publication #4. In this context, the focus of the modeling shifts away from the heat pump's transient non-linearity into versatility and practicality due to the significantly reduced control bandwidth. We employed a data-driven cascaded Wiener model structure that reduces the transient shape into a linear representation and keeps the non-linearity in steady-state gains.

Research question 3: How to design stable and robust heat pump controllers for future FFR services in order to provide inertia support in a low-inertia power grid?

FFR services pose harsh requirements on controller performance as the control bandwidth is significantly higher than PFR and SFR services. With FFR services, an inappropriate controller can potentially trigger a grid-level frequency instability. In this context, the non-linearity of the refrigeration loop in heat pump systems becomes critical and should be carefully considered during the control design process. In Publication #3, through non-linear physics-based modeling, we identified that the dynamic characteristics of heat pump systems can vary for different operating conditions. In order to design a robust heat pump power controller, the H_∞ method is applied as it is known for its ability to handle system parameter uncertainties. Once the heat pump power controller was designed, a grid-level small-signal analysis was conducted to design the FFR inverse-droop gain. Again, the heat pump operating condition factor was considered, which resulted in a more conservative choice of the inverse-droop gain than the traditional method.

Research question 4: How to design relatively universal and practical heat pump controllers for PFR and SFR services in order to perform economical frequency recovery?

Power reference tracking is normally conducted through conventional PI control for most real-world applications. However, existing commercial heat pump systems often have unknown internal controllers and response delays that deteriorate the performance of conventional PI controllers. Unfortunately, these internal characteristics are often sealed as a black box system that we cannot change. In order to tackle this problem, an DNN-

based open-loop controller is proposed in Publication #5. This control strategy uses a DNN to generate the desired control input signal with measured operating conditions and a given power reference, where the DNN is acquired through a training process based on DDPG reinforcement learning. In this way, the controller design process becomes versatile and is standardized for all commercial heat pump types.

5.2 Outlook

Impact of Frequency Response Actions on Heat Pump Life Expectancy

This thesis focused mainly on how heat pumps can contribute to different levels of power system frequency response by analyzing the benefits on the grid side. However, we have not yet analyzed how frequency response actions impact the life expectancy of heat pumps. Typically, the frequency response function is achieved through frequent compressor speed modulations, which often exceed the consideration of heat pump manufacturers. Rapid compressor speed modulations can sometimes cause mechanical stress spikes that damage moving parts in the compressor and expansion valve. In addition, frequent modulations can also cause metal and plastic parts to suffer from fatigue due to temperature cycling, potentially leading to cracks and breaks. Future research in this interdisciplinary field is essential to ensure the sustainable integration of heat pumps in smart grid environments, balancing the benefits of grid stability with the longevity and reliability of heat pump systems.

Business Model at Community and Domestic Levels

Currently, the requirements for entering the frequency response services market are usually set at the MW level. This high threshold makes it challenging for community and domestic heat pumps to participate, especially when compared to larger CHP stations or major heat pump stations, which are typically designed to be involved in the grid planning stage. As a result, there is often a lack of policies and regulations that would enable domestic and community-level heat pump owners to earn profit by providing frequency response services. Given this situation, heat pump manufacturers are generally hesitant to upgrade their products to include frequency response capabilities, not to mention that there could be the potential risk of lowering equipment life expectancy. To encourage investment in improving heat pump controllers, it is crucial to develop a practical business model that would allow domestic and community-level heat pump owners to profit from helping in frequency ancillary services.

Abbreviations

REG	Renewable energy generation
PV	Photovoltaic
IRENA	International renewable energy agency
SG	Synchronous generator
AEMO	Australian energy market operator
ENTSO-e	European network of transmission system operators for electricity
GW	Gigawatt
MW	Megawatt
FFR	Fast frequency response
PFR	Primary frequency response
SFR	Secondary frequency response
TFR	Tertiary frequency response
BESS	Battery energy storage system
DSR	Demand side response
FCR	Frequency containment reserve
AGC	Automatic generation control
aFRR	Automated Frequency Restoration Reserve
mFRR	Manual Frequency Restoration Reserve
PJM	Pennsylvania-New Jersey-Maryland (the United States)
kW	kilowatt
IEA	International energy agency
PHIL	Power-hardware-in-the-loop
PI	Proportional-integral
CHP	Combined-heat-and-power
PtH	Power-to-heat
ASHP	Air-source heat pump
VFD	Variable-frequency drive
DC	Direct current
PWM	Pulse-width modulation
SCIM	Squirrel-cage induction machine
PDE	Partial differential equation
ODE	Ordinary differential equation
MIMO	Multi-input-multi-output
DNN	Deep neural network
DDPG	Deep deterministic policy gradient

Bibliography

[1] R. Quadrelli and S. Peterson, “The energy–climate challenge: Recent trends in CO2 emissions from fuel combustion,” *Energy Policy*, vol. 35, no. 11, pp. 5938–5952, Nov. 2007, doi: 10.1016/j.enpol.2007.07.001.

[2] International renewable energy agency, “Renewable power generation cost in 2019,” Accessed: Nov. 15, 2023. [Online]. Available: https://www.irena.org/-/media/Files/IRENA/Agency/Publication/2020/Jun/IRENA_Power_Generation_Costs_2019.pdf.

[3] Enerdata, “Share of renewables in electricity production,” Accessed: Nov. 15, 2023. [Online]. Available: https://yearbook.enerdata.net/renewables/renewable-in-electricity-production-share.html.

[4] A. Mullane, G. Bryans, and M. O’Malley, “Kinetic energy and frequency response comparison for renewable generation systems,” in *2005 International Conference on Future Power Systems*, 2005, pp. 6 pp. – 6, doi: 10.1109/FPS.2005.204252.

[5] G. Cai, B. Wang, D. Yang, Z. Sun, and L. Wang, “Inertia Estimation Based on Observed Electromechanical Oscillation Response for Power Systems,” *IEEE Trans. Power Syst.*, vol. 34, no. 6, pp. 4291–4299, Nov. 2019, doi: 10.1109/TPWRS.2019.2914356.

[6] R. K. Panda, A. Mohapatra, and S. C. Srivastava, “Online Estimation of System Inertia in a Power Network Utilizing Synchrophasor Measurements,” *IEEE Trans. Power Syst.*, vol. 35, no. 4, pp. 3122–3132, Jul. 2020, doi: 10.1109/TPWRS.2019.2958603.

[7] ENTSO-e, “Future system inertia 2,” Accessed: Nov. 15, 2023. [Online]. Available: https://www.statnett.no/globalassets/for-aktorer-i-kraftsystemet/utvikling-av-kraftsystemet/nordisk-frekvensstabilitet/future-system-inertia-phase-2.pdf.

[8] S. C. Johnson, D. J. Papageorgiou, D. S. Mallapragada, T. A. Deetjen, J. D. Rhodes, and M. E. Webber, “Evaluating rotational inertia as a component of grid reliability with high penetrations of variable renewable energy,” *Energy*, vol. 180, pp. 258–271, Aug. 2019, doi: 10.1016/j.energy.2019.04.216.

[9] Australian energy market operator, “2022 Inertia report,” Accessed: Nov. 15, 2023. [Online]. Available: https://aemo.com.au/-/media/files/electricity/nem/planning_and_forecasting/operability/2022/2022-inertia-report.pdf?la=en.

[10] National grid ESO, “National trends and insights,” Accessed: Nov. 15, 2023. [Online]. Available: https://www.nationalgrideso.com/document/190151/download.

[11] ENTSO-e, “Future system inertia,” Accessed: Nov. 15, 2023. [Online]. Available: https://eepublicdownloads.entsoe.eu/clean-documents/Publications/SOC/Nordic/Nordic_report_Future_System_Inertia.pdf.

[12] European network of transmission system operators for electricity, “ENTSO-E balancing report 2022,” Accessed: Nov. 15, 2023. [Online]. Available: https://eep

ublicdownloads.entsoe.eu/clean-documents/nc-tasks/2022_ENTSO_E_Balancing_Report_Web_2bddb9ad4f.pdf.

[13] F. Sanchez, F. Gonzalez-Longatt, A. Rodriguez, and J. L. Rueda, "Dynamic Data-Driven SoC Control of BESS for Provision of Fast Frequency Response Services," in *2019 IEEE Power & Energy Society General Meeting (PESGM)*, Aug. 2019, pp. 1–5, doi: 10.1109/PESGM40551.2019.8973551.

[14] R. Hollinger, A. M. Cortes, and T. Erge, "Fast Frequency Response with BESS: A Comparative Analysis of Germany, Great Britain and Sweden," in *2018 15th International Conference on the European Energy Market (EEM)*, Jun. 2018, pp. 1–6, doi: 10.1109/EEM.2018.8469998.

[15] E. Pusceddu, B. Zakeri, and G. Castagneto Gissey, "Synergies between energy arbitrage and fast frequency response for battery energy storage systems," *Appl. Energy*, vol. 283, p. 116274, Feb. 2021, doi: 10.1016/j.apenergy.2020.116274.

[16] Y. Mitsugi, H. Hashiguchi, T. Shigemasa, Y. Ota, T. Terazono, and T. Nakajima, "Control Hardware-in-the-Loop Simulation on Fast Frequency Response of Battery Energy Storage System Equipped With Advanced Frequency Detection Algorithm," *IEEE Trans. Ind. Appl.*, vol. 57, no. 6, pp. 5541–5551, Nov. 2021, doi: 10.1109/TIA.2021.3107223.

[17] C. Rahmann and A. Castillo, "Fast Frequency Response Capability of Photovoltaic Power Plants: The Necessity of New Grid Requirements and Definitions," *Energies*, vol. 7, no. 10, pp. 6306–6322, Sep. 2014, doi: 10.3390/en7106306.

[18] S. Wang, S. Duan, G. Mi, and Y. Lu, "Optimized Power Distribution Technology for Fast Frequency Response in Photovoltaic Power Stations," *Energies*, vol. 15, no. 23, p. 8923, Nov. 2022, doi: 10.3390/en15238923.

[19] V. D. Paduani, H. Yu, B. Xu, and N. Lu, "A Unified Power-Setpoint Tracking Algorithm for Utility-Scale PV Systems With Power Reserves and Fast Frequency Response Capabilities," *IEEE Trans. Sustain. Energy*, vol. 13, no. 1, pp. 479–490, Jan. 2022, doi: 10.1109/TSTE.2021.3117688.

[20] S. Homan, N. Mac Dowell, and S. Brown, "Grid frequency volatility in future low inertia scenarios: Challenges and mitigation options," *Appl. Energy*, vol. 290, p. 116723, May 2021, doi: 10.1016/j.apenergy.2021.116723.

[21] T.-H. Jin, K.-Y. Shin, M. Chung, and G.-P. Lim, "Development and Performance Verification of Frequency Control Algorithm and Hardware Controller Using Real-Time Cyber Physical System Simulator," *Energies*, vol. 15, no. 15, p. 5722, Aug. 2022, doi: 10.3390/en15155722.

[22] Fingrid, "Fast Frequency Reserve," Accessed: Nov. 15, 2023. [Online]. Available: https://www.fingrid.fi/en/electricity-market/reserves_and_balancing/fast-frequency-reserve/.

[23] National grid ESO, "New Dynamic Services (DC/DM/DR)," Accessed: Nov. 15, 2023. [Online].Available: https://www.nationalgrideso.com/industry-information/balancing-services/frequency-response-services/new-dynamic-services-dcdmdr.

[24] Australian energy market operator, "Fast Frequency Response," Accessed: Nov. 15, 2023. [Online]. Available: https://aemo.com.au/initiatives/major-programs/fast-frequency-response.

[25] L. Wozniak and T. L. Filbert, “Speed loop cancellation governor for hydrogenerators. I. Development,” *IEEE Trans. Energy Convers.*, vol. 3, no. 1, pp. 85–90, Mar. 1988, doi: 10.1109/60.4204.

[26] İ. Eker, “Governors for hydro-turbine speed control in power generation: a SIMO robust design approach,” *Energy Convers. Manag.*, vol. 45, no. 13–14, pp. 2207–2221, Aug. 2004, doi: 10.1016/j.enconman.2003.11.008.

[27] N. Kariminejad, S. A. Taher, M. Shahidehpour, and K. Khateri, “A Hierarchical Governor/Turbine and Electric Vehicles Optimal Control Framework for Primary Frequency Support in Power Systems,” *IEEE Trans. Smart Grid*, vol. 9, no. 6, pp. 6702–6712, Nov. 2018, doi: 10.1109/TSG.2017.2718557.

[28] Choi, Kook, and Yu, “Control Strategy of BESS for Providing Both Virtual Inertia and Primary Frequency Response in the Korean Power System,” *Energies*, vol. 12, no. 21, p. 4060, Oct. 2019, doi: 10.3390/en12214060.

[29] V. Prakash *et al.*, “Primary frequency response with stochastic scheduling under uncertain photovoltaic generation,” in *2017 IEEE Power & Energy Society General Meeting*, Jul. 2017, pp. 1–5, doi: 10.1109/PESGM.2017.8273730.

[30] A. Molina-Garcia, F. Bouffard, and D. S. Kirschen, “Decentralized Demand-Side Contribution to Primary Frequency Control,” *IEEE Trans. Power Syst.*, vol. 26, no. 1, pp. 411–419, Feb. 2011, doi: 10.1109/TPWRS.2010.2048223.

[31] C. Liu and P. Du, “Participation of Load Resources in Day-Ahead Market to Provide Primary-Frequency Response Reserve,” *IEEE Trans. Power Syst.*, vol. 33, no. 5, pp. 5041–5051, Sep. 2018, doi: 10.1109/TPWRS.2018.2818948.

[32] W. Li, P. Du, and N. Lu, “Design of a New Primary Frequency Control Market for Hosting Frequency Response Reserve Offers From Both Generators and Loads,” *IEEE Trans. Smart Grid*, vol. 9, no. 5, pp. 4883–4892, Sep. 2018, doi: 10.1109/TSG.2017.2674518.

[33] Regelleistung.Net, “Europäische Kooperationen,” Accessed: Nov. 15, 2023. [Online]. Available: https://www.regelleistung.net/de-de/Europäische-Kooperationen.

[34] Australian energy market operator, “Guide to ancillary services in the national electricity market,” Accessed: Nov. 15, 2023. [Online]. Available: https://www.aemo.com.au/Electricity/National-Electricity-Market-NEM/Security-and-reliability/-/media/2C771C82C8054929B16E4545216ACE03.ashx.

[35] Y. Xu, H. Sun, W. Gu, Y. Xu, and Z. Li, “Optimal Distributed Control for Secondary Frequency and Voltage Regulation in an Islanded Microgrid,” *IEEE Trans. Ind. Informatics*, vol. 15, no. 1, pp. 225–235, Jan. 2019, doi: 10.1109/TII.2018.2795584.

[36] X. Yang, Y. Du, J. Su, L. Chang, Y. Shi, and J. Lai, “An Optimal Secondary Voltage Control Strategy for an Islanded Multibus Microgrid,” *IEEE J. Emerg. Sel. Top. Power Electron.*, vol. 4, no. 4, pp. 1236–1246, Dec. 2016, doi: 10.1109/JESTPE.2016.2602367.

[37] K. Ullah, A. Basit, Z. Ullah, S. Aslam, and H. Herodotou, “Automatic Generation Control Strategies in Conventional and Modern Power Systems: A Comprehensive Overview,” *Energies*, vol. 14, no. 9, p. 2376, Apr. 2021, doi: 10.3390/en14092376.

[38] M. Dong *et al.*, "A Distributed Secondary Control Algorithm for Automatic Generation Control Considering EDP and Automatic Voltage Control in an AC Microgrid," *Energies*, vol. 11, no. 4, p. 932, Apr. 2018, doi: 10.3390/en11040932.

[39] S. Zhang, H. Liu, F. Wang, T. Yan, and K. Wang, "Secondary frequency control strategy for BESS considering their degree of participation," *Energy Reports*, vol. 6, pp. 594–602, Dec. 2020, doi: 10.1016/j.egyr.2020.11.183.

[40] X. Wang, X. Li, W. Ni, and F. Wen, "A Model Predictive Control Based Optimal Task Allocation among Multiple Energy Storage Systems for Secondary Frequency Regulation Service Provision," *Energies*, vol. 16, no. 3, p. 1228, Jan. 2023, doi: 10.3390/en16031228.

[41] V. Lakshmanan, M. Marinelli, J. Hu, and H. W. Bindner, "Provision of secondary frequency control via demand response activation on thermostatically controlled loads: Solutions and experiences from Denmark," *Appl. Energy*, vol. 173, pp. 470–480, Jul. 2016, doi: 10.1016/j.apenergy.2016.04.054.

[42] Y. Bao *et al.*, "Provision of secondary frequency regulation by coordinated dispatch of industrial loads and thermal power plants," *Appl. Energy*, vol. 241, pp. 302–312, May 2019, doi: 10.1016/j.apenergy.2019.03.025.

[43] X. Fang, H. Yuan, and J. Tan, "Secondary Frequency Regulation from Variable Generation Through Uncertainty Decomposition: An Economic and Reliability Perspective," *IEEE Trans. Sustain. Energy*, vol. 12, no. 4, pp. 2019–2030, Oct. 2021, doi: 10.1109/TSTE.2021.3076758.

[44] European network of transmission system operators for electricity, "Electricity Balancing," Accessed: Nov. 15, 2023. [Online]. Available: https://www.entsoe.eu/network_codes/eb/.

[45] PJM Interconnection, "Regulation market," Accessed: Nov. 15, 2023. [Online]. Available: https://learn.pjm.com/three-priorities/buying-and-selling-energy/ancillary-services-market/regulation-market.

[46] International energy agency, "Heating," Accessed: Nov. 15, 2023. [Online]. Available: https://www.iea.org/energy-system/buildings/heating.

[47] International energy agency, "Buildings," Accessed: Nov. 15, 2023. [Online]. Available: https://www.iea.org/energy-system/buildings.

[48] S. Yuan *et al.*, "Future energy scenarios with distributed technology options for residential city blocks in three climate regions of the United States," *Appl. Energy*, vol. 237, pp. 60–69, Mar. 2019, doi: 10.1016/j.apenergy.2019.01.048.

[49] International Energy Agency, "heat pumps," Accessed: Nov. 15, 2023. [Online]. Available: https://www.iea.org/energy-system/buildings/heat-pumps.

[50] N. J. Hewitt, M. J. Huang, M. Anderson, and M. Quinn, "Advanced air source heat pumps for UK and European domestic buildings," *Appl. Therm. Eng.*, vol. 31, no. 17–18, pp. 3713–3719, Dec. 2011, doi: 10.1016/j.applthermaleng.2011.02.005.

[51] T. Brown, D. Schlachtberger, A. Kies, S. Schramm, and M. Greiner, "Synergies of sector coupling and transmission reinforcement in a cost-optimised, highly renewable European energy system," *Energy*, vol. 160, pp. 720–739, Oct. 2018, doi:10.1016/j.energy.2018.06.222.

[52] J. Hong, N. J. Kelly, I. Richardson, and M. Thomson, "Assessing heat pumps as

flexible load," *Proc. Inst. Mech. Eng. Part A J. Power Energy*, vol. 227, no. 1, pp. 30–42, Feb. 2013, doi: 10.1177/0957650912454830.

[53] L. Sun, J. Qiu, X. Han, X. Yin, and Z. Y. Dong, "Capacity and energy sharing platform with hybrid energy storage system: An example of hospitality industry," *Appl. Energy*, vol. 280, p. 115897, Dec. 2020, doi: 10.1016/j.apenergy.2020.115897.

[54] R. Hemmati, H. Mehrjerdi, M. Shafie-khah, P. Siano, and J. P. S. Catalao, "Managing Multitype Capacity Resources for Frequency Regulation in Unit Commitment Integrated With Large Wind Ramping," *IEEE Trans. Sustain. Energy*, vol. 12, no. 1, pp. 705–714, Jan. 2021, doi: 10.1109/TSTE.2020.3017231.

[55] D. Fernández-Muñoz, J. I. Pérez-Díaz, I. Guisández, M. Chazarra, and Á. Fernández-Espina, "Fast frequency control ancillary services: An international review," *Renew. Sustain. Energy Rev.*, vol. 120, p. 109662, Mar. 2020, doi: 10.1016/j.rser.2019.109662.

[56] Y.-J. Kim, L. K. Norford, and J. L. Kirtley, "Modeling and Analysis of a Variable Speed Heat Pump for Frequency Regulation Through Direct Load Control," *IEEE Trans. Power Syst.*, vol. 30, no. 1, pp. 397–408, Jan. 2015, doi: 10.1109/TPWRS.2014.2319310.

[57] Y.-J. Kim, E. Fuentes, and L. K. Norford, "Experimental Study of Grid Frequency Regulation Ancillary Service of a Variable Speed Heat Pump," *IEEE Trans. Power Syst.*, vol. 31, no. 4, pp. 3090–3099, Jul. 2016, doi: 10.1109/TPWRS.2015.2472497.

[58] W. Gu, J. Wang, S. Lu, Z. Luo, and C. Wu, "Optimal operation for integrated energy system considering thermal inertia of district heating network and buildings," *Appl. Energy*, vol. 199, pp. 234–246, Aug. 2017, doi: 10.1016/j.apenergy.2017.05.004.

[59] Y. Chen, Y. Xu, Z. Li, and X. Feng, "Optimally coordinated dispatch of combined-heat-and-electrical network with demand response," *IET Gener. Transm. Distrib.*, vol. 13, no. 11, pp. 2257–2267, Jun. 2019, doi: 10.1049/iet-gtd.2018.6992.

[60] Z. Li, Y. Xu, L. Wu, and X. Zheng, "A Risk-Averse Adaptively Stochastic Optimization Method for Multi-Energy Ship Operation Under Diverse Uncertainties," *IEEE Trans. Power Syst.*, vol. 36, no. 3, pp. 2149–2161, May 2021, doi: 10.1109/TPWRS.2020.3039538.

[61] Z. Li, Y. Xu, S. Fang, X. Zheng, and X. Feng, "Robust Coordination of a Hybrid AC/DC Multi-Energy Ship Microgrid With Flexible Voyage and Thermal Loads," *IEEE Trans. Smart Grid*, vol. 11, no. 4, pp. 2782–2793, Jul. 2020, doi: 10.1109/TSG.2020.2964831.

[62] W. Gu *et al.*, "Modeling, planning and optimal energy management of combined cooling, heating and power microgrid: A review," *Int. J. Electr. Power Energy Syst.*, vol. 54, no. 2014, pp. 26–37, Jan. 2014, doi: 10.1016/j.ijepes.2013.06.028.

[63] J. Wang, S. You, Y. Zong, C. Træholt, Z. Y. Dong, and Y. Zhou, "Flexibility of combined heat and power plants: A review of technologies and operation strategies," *Appl. Energy*, vol. 252, no. January, p. 113445, Oct. 2019, doi: 10.1016/j.apenergy.2019.113445.

[64] MathWorks, "Simscpe Electrical," Accessed: Nov. 15, 2023. [Online]. Available: https://ch.mathworks.com/products/simscape-electrical.html.

[65] R. C. Portillo *et al.*, "Modeling Strategy for Back-to-Back Three-Level Converters Applied to High-Power Wind Turbines," *IEEE Trans. Ind. Electron.*, vol. 53, no. 5, pp. 1483–1491, Oct. 2006, doi: 10.1109/TIE.2006.882025.

[66] P. Mitra, D. Ramasubramanian, A. Gaikwad, and J. Johns, "Modeling the Aggregated Response of Variable Frequency Drives (VFDs) for Power System Dynamic Studies," *IEEE Trans. Power Syst.*, vol. 35, no. 4, pp. 2631–2641, Jul. 2020, doi: 10.1109/TPWRS.2020.2966820.

[67] Wikipedia, "Kirchhoff's circuit laws," Accessed: Nov. 15, 2023. [Online]. Available: https://en.wikipedia.org/wiki/Kirchhoff%27s_circuit_laws.

[68] Wikipedia, "Pulse-width modulation," Accessed: Nov. 15, 2023. [Online]. Available: https://en.wikipedia.org/wiki/Pulse-width_modulation.

[69] A. Munoz-Garcia, T. A. Lipo, and D. W. Novotny, "A new induction motor V/f control method capable of high-performance regulation at low speeds," *IEEE Trans. Ind. Appl.*, vol. 34, no. 4, pp. 813–821, 1998, doi: 10.1109/28.703982.

[70] MathWorks, "Asynchronous Machine," Accessed: Nov. 15, 2023. [Online]. Available: https://ch.mathworks.com/help/sps/powersys/ref/asynchronousmachine.html.

[71] T. B. Harild Rasmussen, Q. Wu, and M. Zhang, "Primary frequency support from local control of large-scale heat pumps," *Int. J. Electr. Power Energy Syst.*, vol. 133, no. May, p. 107270, Dec. 2021, doi: 10.1016/j.ijepes.2021.107270.

[72] T. B. H. Rasmussen, Q. Wu, J. G. Moller, and M. Zhang, "MPC Coordinated Primary Frequency Support of Small- and Large-Scale Heat Pumps," *IEEE Trans. Smart Grid*, vol. 13, no. 3, pp. 2000–2010, May 2022, doi: 10.1109/TSG.2022.3148601.

[73] Y.-J. Kim, L. K. Norford, and J. L. Kirtley, "Modeling and Analysis of a Variable Speed Heat Pump for Frequency Regulation Through Direct Load Control," *IEEE Trans. Power Syst.*, vol. 30, no. 1, pp. 397–408, Jan. 2015, doi: 10.1109/TPWRS.2014.2319310.

[74] S. Bendapudi, J. E. Braun, and E. A. Groll, "A comparison of moving-boundary and finite-volume formulations for transients in centrifugal chillers," *Int. J. Refrig.*, vol. 31, no. 8, pp. 1437–1452, Dec. 2008, doi: 10.1016/j.ijrefrig.2008.03.006.

[75] TLK-Thermo GmbH, "TIL-Model library for thermal components and systems." Accessed: Nov. 15, 2023. [Online]. Available: https://www.tlk-thermo.com/index.php/en/til-suite.

[76] B. P. Rasmussen and A. G. Alleyne, "Control-Oriented Modeling of Transcritical Vapor Compression Systems," *J. Dyn. Syst. Meas. Control*, vol. 126, no. 1, pp. 54–64, Mar. 2004, doi: 10.1115/1.1648312.

[77] B. P. Rasmussen, "Dynamic modeling for vapor compression systems — Part I: Literature review," *HVAC&R Res.*, vol. 18, 2012, doi: 10.1080/10789669.2011.582916.

[78] O. Ibrahim, F. Fardoun, R. Younes, and H. Louahlia-Gualous, "Air source heat pump water heater: Dynamic modeling, optimal energy management and mini-

tubes condensers," *Energy*, vol. 64, pp. 1102–1116, 2014, doi: 10.1016/j.energy.2013.11.017.

[79] J. . MacArthur and E. . Grald, "Unsteady compressible two-phase flow model for predicting cyclic heat pump performance and a comparison with experimental data," *Int. J. Refrig.*, vol. 12, no. 1, pp. 29–41, Jan. 1989, doi: 10.1016/0140-7007(89)90009-1.

[80] Wikipedia, "Leibniz integral rule," Accessed: Nov. 15, 2023. [Online]. Available: https://en.wikipedia.org/wiki/Leibniz_integral_rule.

[81] Wikipedia, "Chain rule," Accessed: Nov. 15, 2023. [Online]. Available: https://en.wikipedia.org/wiki/Chain_rule.

[82] Wikipedia, "Vapor–liquid equilibrium," Accessed: Nov. 15, 2023. [Online]. Available: https://en.wikipedia.org/wiki/Vapor–liquid_equilibrium.

[83] Wikipedia, "Compressor," Accessed: Nov. 15, 2023. [Online]. Available: https://en.wikipedia.org/wiki/Compressor.

[84] Wikipedia, "Thermal expansion valve," Accessed: Nov. 15, 2023. [Online]. Available: https://en.wikipedia.org/wiki/Thermal_expansion_valve.

[85] W. El-Baz, L. Mayerhofer, P. Tzscheutschler, and U. Wagner, "Hardware in the Loop Real-Time Simulation for Heating Systems: Model Validation and Dynamics Analysis," *Energies*, vol. 11, no. 11, p. 3159, Nov. 2018, doi: 10.3390/en11113159.

[86] G. Lauss and K. Strunz, "Accurate and Stable Hardware-in-the-Loop (HIL) Real-Time Simulation of Integrated Power Electronics and Power Systems," *IEEE Trans. Power Electron.*, vol. 36, no. 9, pp. 10920–10932, Sep. 2021, doi: 10.1109/TPEL.2020.3040071.

[87] T. Başar and P. Bernhard, *H-infinity optimal control and related minimax design problems: a dynamic game approach*. Boston, Birkhäuser Boston, MA.

[88] Shengyuan Xu and Tongwen Chen, "Robust H∞ control for uncertain stochastic systems with state delay," *IEEE Trans. Automat. Contr.*, vol. 47, no. 12, pp. 2089–2094, Dec. 2002, doi: 10.1109/TAC.2002.805670.

[89] MathWorks, "Robust Control Toolbox," Accessed: Nov. 15, 2023. [Online]. Available: https://ch.mathworks.com/products/robust.html.

[90] Wikipedia, "Root locus analysis," Accessed: Nov. 15, 2023. [Online]. Available: https://en.wikipedia.org/wiki/Root_locus_analysis.

[91] Z. E. Lee and K. M. Zhang, "Scalable identification and control of residential heat pumps: A minimal hardware approach," *Appl. Energy*, vol. 286, p. 116544, Mar. 2021, doi: 10.1016/j.apenergy.2021.116544.

[92] A. Kose and E. Petlenkov, "System identification models and using neural networks for Ground Source Heat Pump with Ground Temperature Modeling," in *2016 International Joint Conference on Neural Networks (IJCNN)*, Jul. 2016, vol. 2016-Octob, pp. 2850–2855, doi: 10.1109/IJCNN.2016.7727559.

[93] C. R. Knospe, R. W. Hope, S. J. Fedigan, and R. D. Williams, "Experiments in the control of unbalance response using magnetic bearings," *Mechatronics*, vol. 5, no. 4, pp. 385–400, Jun. 1995, doi: 10.1016/0957-4158(95)00015-W.

[94] S. Jain and V. Garg, "A review of open loop control strategies for shades, blinds and integrated lighting by use of real-time daylight prediction methods," *Build. Environ.*, vol. 135, pp. 352–364, May 2018, doi: 10.1016/j.buildenv.2018.03.018.

[95] G. Orekhov, J. Luque, and Z. F. Lerner, "Closing the Loop on Exoskeleton Motor Controllers: Benefits of Regression-Based Open-Loop Control," *IEEE Robot. Autom. Lett.*, vol. 5, no. 4, pp. 6025–6032, Oct. 2020, doi: 10.1109/LRA.2020.3011370.

[96] Y. Du *et al.*, "Intelligent multi-zone residential HVAC control strategy based on deep reinforcement learning," *Appl. Energy*, vol. 281, p. 116117, Jan. 2021, doi: 10.1016/j.apenergy.2020.116117.

[97] L. Luo, J. Zhang, S. Chen, X. Zhang, B. Ai, and D. W. K. Ng, "Downlink Power Control for Cell-Free Massive MIMO With Deep Reinforcement Learning," *IEEE Trans. Veh. Technol.*, vol. 71, no. 6, pp. 6772–6777, Jun. 2022, doi: 10.1109/TVT.2022.3162585.

[98] Y. Ma, W. Zhu, M. G. Benton, and J. Romagnoli, "Continuous control of a polymerization system with deep reinforcement learning," *J. Process Control*, vol. 75, pp. 40–47, Mar. 2019, doi: 10.1016/j.jprocont.2018.11.004.